Exploiting Interfacial Water Properties for Desalination and Purification Applications

Randall T. Cygan, Todd M. Alam, C. Jeffrey Brinker, Bruce C. Bunker, Jacalyn S. Clawson, Louise J. Criscenti, Paul S. Crozier, Darcie Farrow, Peter J. Feibelman, Benjamin L. Frankamp, Greg P. Holland, Jack E. Houston, Dale L. Huber, Ying-Bing Jiang, Kevin Leung, Christian D. Lorenz, Tina M. Nenoff, May D. Nyman, Nathan W. Ockwig, Christopher J. Orendorff, Jason D. Pless, Susan B. Rempe, Seema Singh, Mark J. Stevens, Konrad Thuermer, Frank B. van Swol, Sameer Varma, Ryan C. Major, Matthew J. McGrath, J. Ilja Siepmann, Xiaoyang Zhu, Joseph L. Cecchi, Zhu Chen, Darren R. Dunphy, Henry Gerung, David J. Kissel, Nanguo Liu, George K. Xomeritakis, Joshua A. Anderson, Alex Travesset, Luke L. Daemen, Monika A. Hartl, and Hongwu Xu

Sandia National Laboratories

Exploiting Interfacial Water Properties for Desalination and Purification Applications

Randall T. Cygan, Todd M. Alam, C. Jeffrey Brinker, Bruce C. Bunker, Jacalyn S. Clawson, Louise J. Criscenti, Paul S. Crozier, Darcie Farrow, Peter J. Feibelman, Benjamin L. Frankamp, Greg P. Holland, Jack E. Houston, Dale L. Huber, Ying-Bing Jiang, Kevin Leung, Christian D. Lorenz, Tina M. Nenoff, May D. Nyman, Nathan W. Ockwig, Christopher J. Orendorff, Jason D. Pless, Susan B. Rempe, Seema Singh, Mark J. Stevens, Konrad Thuermer, Frank B. van Swol, and Sameer Varma

Sandia National Laboratories
Albuquerque, New Mexico 87185

Ryan C. Major, Matthew J. McGrath, J. Ilja Siepmann, and Xiaoyang Zhu

University of Minnesota
Minneapolis, Minnesota 55455

Joseph L. Cecchi, Zhu Chen, Darren R. Dunphy, Henry Gerung, David J. Kissel, Nanguo Liu, and George K. Xomeritakis

University of New Mexico
Albuquerque, New Mexico 87131

Joshua A. Anderson and Alex Travesset

Iowa State University
Ames, Iowa 50011

Luke L. Daemen, Monika A. Hartl, and Hongwu Xu

Los Alamos National Laboratory
Los Alamos, New Mexico 87545

Abstract

A molecular-scale interpretation of interfacial processes is often downplayed in the analysis of traditional water treatment methods. However, such an approach is critical for the development of enhanced performance in traditional desalination and water treatments. Water confined between surfaces, within channels, or in pores is ubiquitous in technology and nature. Its physical and chemical properties in such environments are unpredictably different from bulk water. As a result, advances in water desalination and purification methods may be accomplished through an improved analysis of water behavior in these challenging environments using state-of-the-art microscopy, spectroscopy, experimental, and computational methods.

Acknowledgements

Contents

Introduction

Water confined between surfaces, within channels, or in pores is ubiquitous in technology and nature. Its physical and chemical properties in such environments are unpredictably different from bulk water, however. As a result, advances in water desalination and purification technologies have been slow, and—more importantly—inadequate to meet the anticipated international demand for safe, potable water. The research accomplished through this Laboratory Directed Research and Development project have addressed three key areas: (1) identify those properties of interfacial water whose better scientific understanding could lead to new desalination/purification technology opportunities; (2) define the new experimental, theoretical, and simulation approaches to predictive understanding of these key properties; and (3) provide a plan that links research successes in these areas to market-based technology opportunities. Sandia's expertise in surface science and chemistry, theory and simulation, in situ characterization, and the synthesis of well-defined porous materials and fluidic architectures has provided an opportunity to succeed in a science-based approach to engineering improved desalination membranes, urgently needed to alleviate the worldwide potable water supply crisis.

Significant improvements in traditional water treatment processes require novel approaches based on a fundamental understanding of nanoscale and atomic interactions at interfaces between aqueous solution and materials. To better understand these critical issues in support of this project and to promote an open dialog among leading international experts in water-related specialties, Sandia National Laboratories sponsored a workshop in April, 2005 in Santa Fe, New Mexico. The "Frontiers of Interfacial Water Research Workshop" provided attendees with a critical review of water technologies and emphasized the new advances in surface and interfacial microscopy, spectroscopy, diffraction, and computer simulation needed for the development of new materials for water treatment. A summary report including the critical findings of the workshop was published in 2005:

Cygan, R.T. and Greathouse, J.A. (2005) Frontiers of interfacial water research: Workshop report. Report, SAND2005-6220, p. 40. Sandia National Laboratories, Albuquerque.

The present report includes the results of multiple tasks relating to water behavior on external surfaces, within model organic membranes, and in the pores of complex mesopororous materials. Most of this work has been published in the open literature or is in technical review. The first paper (Cygan et al., 2008) includes a general summary of these efforts plus some additional studies relating to biofilms and viral disinfection. The subsequent articles address more specific topics and provide greater analytical, experimental, and computational detail of the role of water and its interactons with materials and material surfaces.

Cygan, R.T., Brinker, C.J., Nyman, M.D., Leung, K., and Rempe, S.B. (2008) A molecular basis for advanced materials in water treatment. *Materials Research Society Bulletin*, 33(1), 42-47. (Expanded from published version with contributions from Bunker, B.C., Orendorff, C.J., and Huber, D.L.)

Orendorff, C.J., Alam, T.M., Frankamp, B.L., Clawson, J.S., Holland, G.P., Huber, D.L., and Bunker, B.C. (2008) Model Nylon 6,6 thin films: Synthesis and characterization. *Langmuir*, submitted.

Orendorff, C.J., Huber, D.L., and Bunker, B.C. (2008) Effects of water and temperature on conformational order in model Nylon thin films. *Journal of Physical Chemistry B*, submitted.

Feibelman, P.J. (2006) Lubrication theory of drag on a scanning probe in structured water, near a hydrophilic surface. *Langmuir*, 22(5), 2136-2140.

Feibelman, P.J. and Houston, J.E. (2006) Does exceptional viscous drag impede flow through a nano-sieve's pores? In *Proceedings of the Materials Research Society*, Volume 930E.

Feibelman, P.J. (2005) Stress correction for slab asymmetry in supercell calculations. *Physical Review B*, 72(15), 153408.

Feibelman, P.J. (2007) Substitutional NaCl hydration in ice. *Physical Review B*, 75(21), 214113.

Feibelman, P.J. (2007) Comment on "Free energy of solvation of simple ions: Molecular dynamics study of solvation of Cl^- and Na^+ in the ice/water interface". *Journal of Chemical Physics*, 126, 237101.

Leung, K., Rempe, S.B., and Lorenz, C.D. (2006) Salt permeation and exclusion in hydroxylated and functionalized silica pores. *Physical Review Letters*, 96(9), 095504.

Varma, S, and Rempe, S.B. (2006) Coordination numbers of alkali metal ions in aqueous solutions. *Biophysical Chemistry*, 124(3), 192-199**.**

Varma, S, and Rempe, S.B. (2007) Tuning ion coordination architectures to enable selective partitioning. *Biophysical Journal*, 93(4), 1093-1099**.**

Major, R.C., Houston, J.E., McGrath, M.J., Seipmann, J.I., and Zhu, X.-Y. (2006) Viscous water meniscus under nanoconfinement. *Physical Review Letters*, 96(17), 177803.

Singh, S., Houston, J.E., van Swol, F., and Brinker, C.J. (2006) Drying transition of confined water. *Nature*, 442(7102), 526-526.

Jiang, Y.-B., Liu, N., Gerung, H., Cecchi, J.L., and Brinker, C.J. (2006) Nanometer-thick conformal pore sealing of self-assembled mesoporous silica by plasma-assisted atomic layer deposition. *Journal of the American Chemical Society*, 128(34), 11018-11019.

Jiang, Y.-B., Xomeritakis, G., Chen, Z., Dunphy, D., Kissel, D.J., Cecchi, J.L., and Brinker, C.J. (2007) Sub-10 nm thick microporous membranes made by plasma-defined atomic layer deposition of a bridged silsesquioxane precursor. *Journal of the American Chemical Society*, 129(50), 15446-15447.

Lorenz, C.D., Crozier, P.S., Anderson, J.A., and Travesset, A. (2008) Molecular dynamics of ionic transport and electrokinetic effects in realistic silica channels. *Journal of Physical Chemistry C*, 112(27), 10222-10232.

Nenoff, T.M., Ockwig, N.W., Cygan, R.T., Alam, T.M., Leung, K., Pless, J.D., Xu, H., Hartl, M.A., and Daemen, L.L. (2007) Role of water in selectivity of niobate-based octahedral molecular sieves. *Journal of Physical Chemistry C*, 111(35), 13212-13221.

Ockwig, N.W., Cygan, R.T., Criscenti, L.J., and Nenoff, T.M. (2008) Molecular dynamics studies of nanoconfined water in clinoptilolite and heulandite zeolites. *Physical Chemistry Chemical Physics*, 10, 800-807.

Ockwig, N.W., Cygan, R.T., Hartl, M.A., Daemen, L.L., and Nenoff, T.M. (2008) Incoherent inelastic neutron scattering studies of nanoconfined water in clinoptilolite and heulandite zeolites. *Journal of Physical Chemistry C*, in press.

A Molecular Basis for Advanced Materials in Water Treatment

Abstract

A molecular-scale interpretation of interfacial processes is often downplayed in the analysis of traditional water treatment methods; however, such a fundamental approach is perhaps critical for the realization of enhanced performance in traditional desalination and related treatments, and in the development of novel water treatment technologies. Specifically, we have examined the molecular-scale processes that affect water at a model membrane, the behavior of a model polysaccharide as a biofilm, ion selectivity at the nanopore scale as inspired by nature, and the use of cluster-surfactant flocculants in viral sequestration.

Introduction

The past twenty years have seen only nominal improvements in the flux of polymeric reverse osmosis (RO) membranes, in which, by exceeding the osmotic pressure of a saltwater solution, water is transported against concentration gradients through a semi-permeable membrane that removes most salts. These improvements have relied on engineering solutions (for example, corrugation of the membrane to enhance its effective surface area) rather than improving material properties to increase flux and selectivity of the membrane itself. The same can be said for ion exchangers, a related class of materials that are proven for both RO membranes and brackish water desalination through ion exchange, and can be tuned for specific toxic elements such as lead, selenium, and radionuclides. Further progress in desalination demands a scientific understanding of the water-membrane interface and the transport of water molecules in confined geometries. Only then can membranes be intelligently engineered for both high-chemical selectivity and fast transport of pure water. Several examples of water treatment studies that incorporate a molecular-based strategy are discussed in the following sections.

Thin Film Models of Reverse Osmosis Membranes

Polyamide RO membranes are a ubiquitous component of many water desalination and remediation systems. Although reverse osmosis membranes are starting to capture key markets for converting salt water into fresh water, the performance of RO systems is limited by the performance characteristics of membrane materials. One critical factor that governs overall performance of these membrane materials involves the complex interactions that occur at the RO membrane interface. These interactions include polymer-water, polymer-contaminant, and polymer-electrolyte interactions, all of which affect operating pressures and membrane susceptibility to fouling.[1–8] Unfortunately, commercial polymeric membranes are complex materials, containing multiple layers, compositions, and domain structures, many of which are amorphous. The goal of this work is to create polymer thin films to serve as experimental models to study fundamental interfacial interactions of RO systems. In turn, a more in-depth understanding of separation and fouling mechanisms will guide the development and optimization of future membrane materials.

One key for understanding how polymeric materials interact with water and dissolved components, such as salt, involves creating model polymers in which the composition and structure of the polymer is controlled and characterized at a molecular level. We are creating such model polymers by growing polymeric self-assembled monolayers on planar substrates. For initial studies, we have developed a synthetic procedure for producing thin films of the model polyamide Nylon 6,6 with well-defined composition and structure.[9] Nylon 6,6 films can be prepared by stepwise surface polymerization of polyamide repeat units from amine-terminated alkylsilane monolayers. Polyamide growth occurs via the stepwise reactions of amine-terminated monolayers with adipoly chloride and 1,6-hexamethylenediamine. Reactions with the diacid chloride and diamine are cycled sequentially to generate precise chain lengths and film thicknesses ranging from 1–10 nm.[9] Below, we highlight how we have characterized the structure of these Nylon 6,6 films and their interactions with water and salt water solution using a range of techniques including solid-state nuclear magnetic resonance (NMR) spectroscopy, Fourier transform infrared (FT-IR) spectroscopy, Raman spectroscopy, sum frequency generation (SFG) spectroscopy, ellipsometry, interfacial force microscopy (IFM), and neutron reflectivity.[9,10] The results show that when the model polymer films are exposed to water, a complex interfacial region is established within which water imposes dramatic changes in the structure and properties of the polymer, while the polymer imposes dramatic changes in the structure and properties of water and dissolved solutes within nanometers of the polymer surface.

Prior to water exposure, the model Nylon films are highly ordered and rigid (based on interactions with scanning probe tips in the IFM). Although semi-crystalline, vibrational and NMR spectra reveal that a significant fraction of Nylon chains are present in a completely straight, all-trans configuration as in bulk crystalline Nylon.[11,12] It appears that extensive interactions between the Nylon 6,6 chains are dominated by inter-chain hydrogen-bonding between adjacent amine and carbonyl groups, analogous to the α and β crystalline phases of bulk Nylon 6,6 materials.[11,12] The resulting lateral network of hydrogen bonds results in limited chain mobility and appreciable conformational order (both apparent in NMR results).[9,10]

When the native Nylon film adsorbs as little as 8 wt% water (as measured on a quartz crystal microbalance), it is transformed from a rigid, semi-crystalline material into a soft, amorphous material. Raman spectra show a decrease in the number of all-trans, hydrogen-bonded chains, resulting in chains with greater rotational and conformational disorder, shown in Figure 1.[10] NMR measurements indicate that in contrast to their immobile, native state, the Nylon chains are now highly mobile and fluxional. IFM measurements indicate that the water-induced increase in chain fluxionality is accompanied by a dramatic increase in film softness (a lowering of the modulus by over a factor of three). These results suggest that water has a high affinity for the amide and carbonyl groups and disrupts the hydrogen bonds between the chains; inducing a transition between semi-crystalline and amorphous states. The more open and fluxional amorphous state is expected to facilitate transport of water and other species relative to the densely-packed crystalline state. These results show that it is probably inappropriate to infer polymer properties for water-based applications, such as reverse osmosis membranes, based on the properties of the native polymer. Studies such as this need to be performed to quantify how key polymer properties change in response to water-polymer interactions.
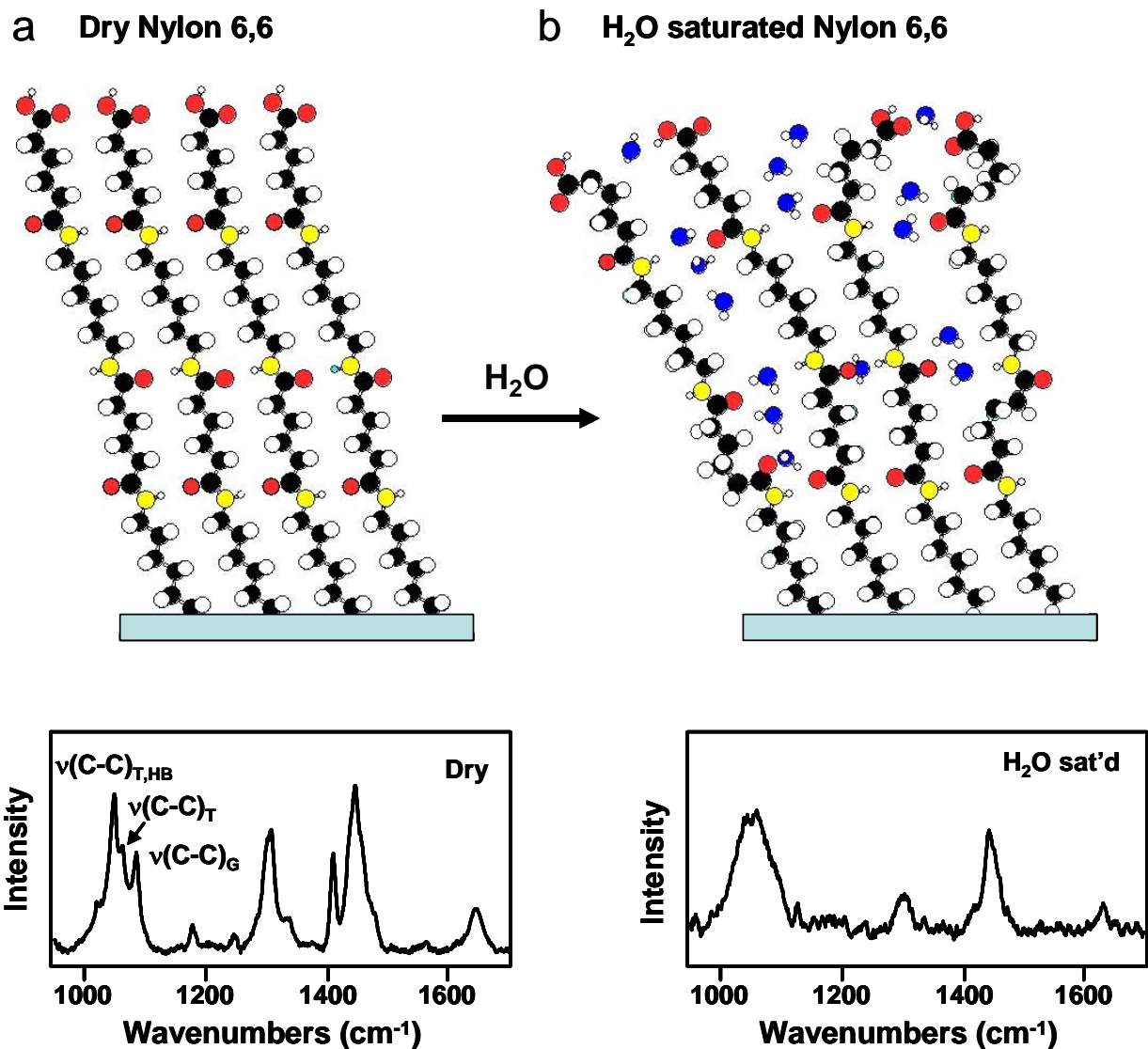
Figure 1. Molecular configurations and the corresponding Raman spectra of the dry (a) and water saturated (b) Nylon 6,6 thin film. Raman spectra show a decrease in the relative intensities of the hydrogen-bonded and all-trans modes [$v(C-C)_T$, $v(C-C)_{T,HB}$] upon water exposure; an indication of a transition between semi-crystalline, ordered to more amorphous, disordered Nylon 6,6. The atoms are colored by element and environment for clarity: carbon (black), hydrogen (white), nitrogen (yellow), carbonyl oxygen (red), and water oxygen (blue).

While it is clear that water can dramatically restructure polymers, it is equally clear that the polymer can restructure the water, at least within a few nanometers of the surface. Evidence for the restructuring of interfacial water is provided by neutron reflectivity, vibrational spectroscopy via SFG, and property measurements obtained via the interfacial force microscope (IFM). In deionized water, neutron reflectivity reveals the presence of an interfacial water layer that is 4–5 nm thick and has a density on the order of 90% that of bulk water (i.e. similar to that of ice). SFG vibrational spectra obtained in the O-H stretching region confirm that the model nylon film generates an overlayer of water that contains much more "ordered" or "ice-like" water than bulk

water. IFM measurements on the model Nylon film immersed in water detect a repulsive hydration force that is associated with a high-viscosity interfacial water layer that is 4 nm thick, consistent with the neutron scattering results. This layer exhibits some of the attributes seen previously in IFM measurements on classical "anti-fouling" surfaces such as polyethylene oxide, where interfacial viscosities up to ten million times the viscosity of bulk water have been measured.[13]

Exposure of model nylon surfaces to salt water reveals that dissolved species can compete with the polymer in terms of ordering and restructuring the hydrogen bonding networks found in water. SFG measurements indicate that the fraction of "ordered water" at the interface decreases as the salt content of the solution increases. Neutron scattering results indicate that as ions are added, salts can displace and/or eventually eliminate the low-density interfacial water layer observed in deionized water. While water is present at the immediate surface, it appears that this water is involved in solvating interfacial cations and anions rather than forming extended H-bonded networks in response to water-polymer interactions.

In summary, systematic experiments on model Nylon thin films suggest that a wide range of interesting phenomena can occur at the interface between polymers and aqueous solutions, impacting the structure and properties of both the polymer and the water. Understanding the structural changes in this interfacial region could have a direct impact on water treatment technologies including separation processes based on reverse osmosis membranes. Water can greatly mediate the interactions between polymer chains, resulting in the creation of more open, amorphous, and fluxional structures which influences the transport of both water and dissolved solutes. Polymers can locally promote the formation of new hydrogen-bonded networks within water, within a few nanometers of the water-polymer interface. Potential consequences of such ordering could include the expulsion of salts (as in ice or at the air-water interface) leading to enhanced water-salt separations, or undesired increases in interfacial viscosity (increasing rather than decreasing the pressure required to drive water through reverse osmosis membranes). In terms of membrane fouling, the presence of interfacial water layers is known to inhibit protein adsorption and other biofouling processes.[14–18] By systematically varying the structure and composition of the tethered polymers, we can start to determine how each of the above phenomena are influenced by the polymer. The understanding obtained on water-polymer interactions could impact the development of polymeric materials for many applications in addition to reverse osmosis membranes, ranging from proton conduction membranes for fuel cells, to anti-stiction and anti-friction coatings to designer materials for the biomedical community.

Molecular Models for Biofilms and Organic Fouling

Alginate is a relatively simple compound that represents the complex chemistries and structures associated with natural microbial extracellular polymeric substances (EPS). Microbial exudates typically include straight chains of polysaccharide material that are structurally complex and extremely difficult to characterize. With time, EPS exuded by microorganisms often result in the formation of biofilms that can associate with polyamide and polyimide materials and ultimately reduce the efficacy of the RO and nanofiltration processes. Organic fouling accelerates the deterioration of the membrane materials and significantly shortens the membrane life.[1,7] Recent

experimental and theoretical studies have attempted to elucidate the binding mechanisms of alginate to various cations and to organic membranes.[19–23] In particular, divalent cations such as Ca^{2+} react with the exudate to form metal-organic complexes that create a highly compacted fouling layer that ultimately leads to substantial reduction in permeate flux.[3,7,22]

Alginic acid is a straight-chain, hydrophilic, colloidal, polyuronic acid typically arranged in three combinations of disaccharide subunits (mannuronic, *M;* guluronic, *G*). Approximately 20–50% of polysaccharides produced in a wide sampling of marine and terrestrial bacteria were uronic acids.[24] Alginic acid is a dominant environmental polymer produced by seaweed in marine environments, and by environmental bacteria including *Azotobacter vinelandii* and *Pseudomonas aeruginosa.*[25,26] The deprotonated alginate ion complexes aqueous cations including Ca^{2+} and binds to membrane functional groups, although the exact mechanisms are not well understood. The structural flexibility of the alginic acid (or alginate) polymer is the result of torsions (measured as angles φ and ψ) about the ether linkage that exists between disaccharide subunits.[23] Functional groups such as carboxylate and alcohol groups on either subunit will inhibit the torsions and limit the number of possible polymer conformers. Ultimately, the proportion of *MM* and *GG* subunits and their macromolecular conformation will determine the affinity of alginate for cation binding.

Molecular simulations, using both classical and electronic structure methods, have determined the relative stability of various alginic acid and alginate structures, and the optimum binding sites and binding energy of each structure with Ca^{2+}.[23] Figure 2 presents some of the simulation results from an analysis of disaccharide structures and 20-unit polymer chains. Optimum binding of Ca^{2+} is observed for the *GG-D* conformation (one of several initial configurations) which is consistent with the egg-box model proposed previously for gelation processes involving alginate and related polysaccharides.[27] To date, limited effort has been expended on investigations of the more complex nature of organic fouling (biofilms and natural organic matter) of polyamide RO membranes. However, recent atomic force microscopy (AFM) measurements of adhesion forces between membrane or organic foulant and a modified AFM tip have provided considerable evidence toward elucidating the detailed mechanisms and interactions.[28,29] It would be beneficial to provide a theoretical basis using appropriate molecular models to validate these experimental findings and to probe possible membrane modifications that may mitigate organic fouling.
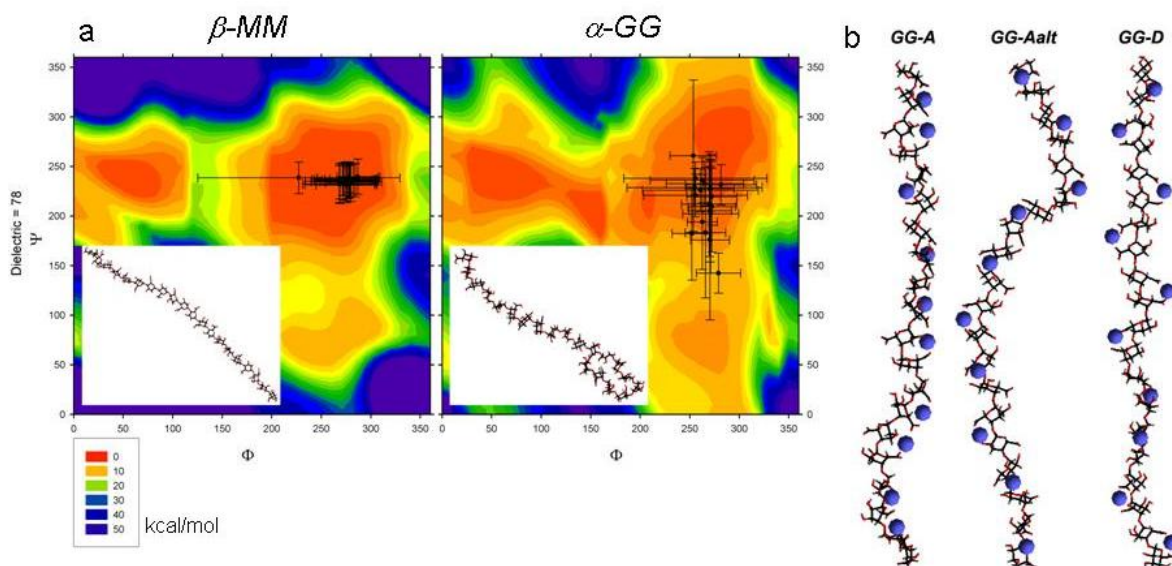
Figure 2. (a) Potential energy maps of the variation in the torsion angles associated with the ether linkage of two 20-unit polysaccharides (*MM* and *GG* alginic acids) derived from molecular simulation using a dielectric value that is consistent with an aqueous environment.[23] The error bars denote the variation of the torsion angles during a 300 K molecular dynamics simulation. The insets show the final conformation of the polymer at the end of the simulation. (b) Energy-optimized configurations of three *GG* alginate 20-unit polymers associated with calcium ions derived from molecular simulation.[23]

Novel Nanoporous Biomimetic Silica-Based Membranes

The permeation and exclusion of salt in nano-confined aqueous media are central to both selective ion transport and purification/desalination of sea and brackish water. Recently, highly ordered, nanoporous, silica thin films with tailor-made interior pore surfaces have been synthesized.[30–32] These membranes can be exploited as experimental platforms that help elucidate the roles of pore surface chemistry and confinement on salt hydration and permeation. The design of efficient ion exclusion membranes may benefit from the study of biology. For example, the aquaporin transmembrane channels present in our kidneys utilize their unique structural motifs to achieve high water flux and quantitative rejection of Na^+ and Cl^- ions with only small pressure gradient and energy input.[33] Other transmembrane channels, such as the potassium channels of nerve and muscle, are designed to permit rapid permeation of only select ions.[34] Harnessing these basic physical and biomimetic principles will potentially lead to robust solid state membranes in reverse-osmosis processes, a water purification technology essential to solving water shortage problems in the 21st century. In this section, we briefly describe our combined experimental[30–32] and multiscale modeling[35,36] exploration of the structure-function relationship pertinent to this effort. We note that electrolyte transport in synthetic nanopores has been a subject of experimental[37-39] and modeling[40-42] work elsewhere, but that water treatment has not been a main focus of this research except in zeolite membranes[43] where the pore diameter is much smaller. In contrast to our own work,[36,44] early efforts to understand the determinants of rapid permeation of select ions in biological channels[34] do not apply quantum mechanical methods principally to interrogate ion selectivity in the interior binding sites of potassium channels.

Figure 3a illustrates the thermodynamic conditions under which various ordered mesophases appear within the surfactant-water-oil detergent phase diagram. In our work, polysilicic acid is included as a secondary hydrophilic component and the evaporation-induced self-assembly technique we pioneered[30] is used to direct the formation of thin film silica mesophases on porous supports with cubic or bicontinuous nanostructures. Surfactant calcinations or extraction results in mesoporous films characterized by a continuous 3D network of connected pores with ~2-3 nm diameter (depending on choice of surfactant template). Both the pore interior and the thin film ("membrane") surfaces can be functionalized to achieve design functions. For example, we have previously synthesized hybrid organic-inorganic thin films with an approximately $2/nm^2$ surface density of $-(CH_2)_3NH_2$ groups. They have been characterized using Fourier-transform infrared (FTIR), transmission electron microscopy (TEM), and grazing incidence small angle x-ray scattering (GISAXS) techniques, and have been successfully demonstrated as selective nitrogen gas permeation membranes.[31] A high resolution TEM image depicting the highly order 2-nm diameter pore structure is shown in Figure 3b.

We have also applied plasma-assisted atomic layer deposition (ALD) to coat the pore surface of silica membranes with silicon dioxide or titanium oxide.[32] This technique yields precisely controlled pore diameters, and its utility has been demonstrated in sealing membrane surfaces in order to synthesize low k dielectric materials for optoelectronic applications.[32] But ALD treatment of silica membranes, combined with organic group functionalization, has the potential to create extremely versatile and well-controlled patch-clamp platforms. Patch clamp techniques are used traditionally to measure ion transport rates through individual biological ion channels. Our platform allows measurements of ion currents through synthetic nanopores. These platforms will for the first time allow systematic investigations of the effect of pore diameter, structure, and chemistry on water flux, ion permeation and exclusion as functions of the pressure gradient across the membrane. The resulting insight will help the design of the next generation of robust, solid state reverse osmosis membranes for large scale desalination purposes.
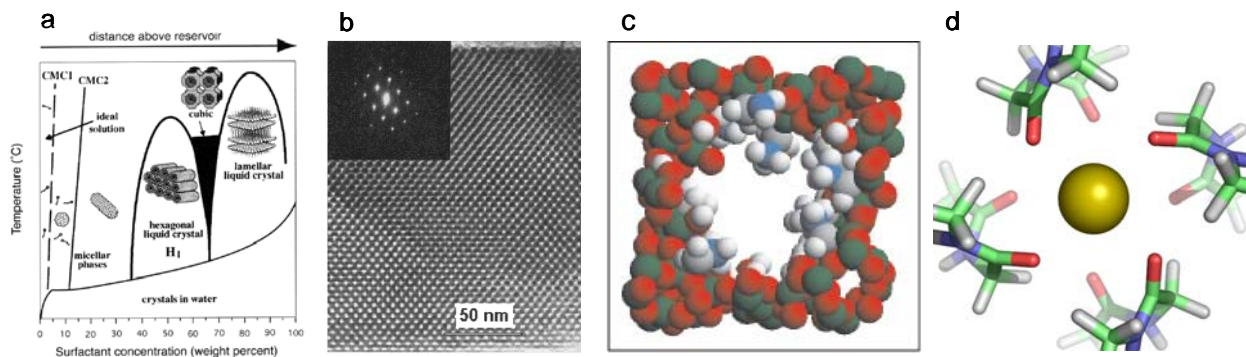
Figure 3. (a) Synthetic phase diagram for porous silica membranes.[30] (b) Snapshot of AIMD simulation of–CH_2NH_2 functionalized silica nanopore; protons are almost quantitatively transferred from silanol to the amine groups.[35] (c) TEM images of nanoporous silica thin films depicting the highly ordered 2-nm diameter pore structure.[30] (H_2O molecules omitted for clarity.) (d) 8-carbonyl binding site made of diglycine molecules and occupied by a permeant K^+ ion from quantum chemical study of a biological potassium channel.[36]

To accompany the experiments, we have also conducted simulations of water-filled silica nanopores.[45] Our theoretical work has emphasized highly accurate density functional theory (DFT) calculations. DFT explicitly accounts for the valence electrons of both water and solid substrates, and has proved successful in predicting chemical reactions in water and the electronic polarizability of materials. Thus, we have applied the *ab initio* molecular dynamics (AIMD) technique, which propagates molecular dynamics trajectories using DFT-derived forces, to examine the surface chemistry of narrow (~1.2 nm diameter) pores (Figure 3c). Under conditions that are close to room temperature, no chemical reactions are observed in water-filled hydroxylated silica pores. However, at the pH of zero charge (the aqueous solution pH at which the material has on average an equal number of positively charged and negatively charged surface sites and thus becomes electrostatically charge neutral) model silica pores functionalized with $-CH_2NH_2$ groups are found to extract protons from nearby silanol (-SiOH) groups in picosecond time scales and produce positively charged $-NH_3^+$ headgroups that protrude into the pore interior. This leads to large changes in the surface charge distributions. While silanol and amine groups are known to be acidic and basic, respectively, this is a non-trivial finding because an ammonium group generally requires three water molecules to hydrate it—more than is available inside our narrow model pore. Instead, silanol groups themselves are found to provide a hydrogen bonding environment that stabilizes the $-NH_3^+$ groups.[30]

The consequences of surface chemistry on ion permeation are significant. Using classical force fields fitted with DFT-derived electrostatic potentials, hydroxylated silica pores are found to be intrinsically attractive to Na^+ and repulsive to Cl^-—even at the pH of zero charge. Amine group functionalized pores exhibit the opposite trend, favoring anions while also introducing ion traps at the pore surface.[35] This is due to the electrostatic dipole distribution on the pore interior surface, and is reminiscent of the carbonyl dipole layer in the narrow filter region of high-selectivity biological potassium channels (see Figure 3d), which allows K^+ ions to pass through rapidly.[34]

The mechanism for potassium channel ion selectivity, which not only differentiates between cations and anions, but also differentiates between small and large cations, is found to be dependent on other parameters as well. Quantum chemical studies[36,44] indicate that rapid, selective K^+ transport combined with exclusion of the smaller Na^+ ion arises from binding sites in the filter containing high numbers of carbonyl ligands (>6) and surrounded by a special local environment electrostatically equivalent to a low dielectric phase. While no restrictions on the binding site cavity size are necessary, limitations on ligand flexibility are required to maintain high ion coordinations.

Properties of the channel change with alterations in the number of ion-coordinating ligands. Reduction in coordination can occur when chemical groups, specifically hydrogen-bond donors, in the nearby environment compete with an ion for its ligands. Further, selectivity is significantly reduced in binding sites with fewer ion-coordinating ligands. This implies that selectivity of a channel can be tuned, either by modifying the local solvation phase or the binding site itself such that the high ion coordinations necessary for highly selective channels are no longer enforced.[36,37,44] A complete mechanistic view of ion permeation will treat not only properties in and around pore binding sites, but also properties on the membrane surface. These mechanistic predictions will be tested and exploited using functionalized synthetic silica pores;

they demonstrate the utility of AIMD and DFT simulations on water-filled, complex, hybrid, organic-inorgainc nanopores.

Finally, we have used DFT to compute the intrinsic energies of Na^+ and Cl^- inside metallic carbon nanotube (CNT) arrays.[45] We predict large binding energies, on the order of an electron volt, due to the nanotube electronic polarizability. This effect is missing in almost all classical force field simulations, which instead predict small binding energies and that ions are excluded inside narrow water-filled CNT. This example emphasizes the importance of incorporating electronic structure effects when modeling the ion permeability in artificial synthetic nanoporous membranes.

Cluster-Surfactant Flocculent Chemistry for Treatment of Viruses

Cluster-surfactant flocculents for virus sequestration are composed of inorganic metal-oxo polynuclear ions plus surfactants or amphiphiles of an opposite charge. Separately as salts or acids, the components are hydrophilic and water soluble; but when combined they form a hydrophobic floc, or precipitate, that is capable of sequestering and separating contaminants such as viruses from aqueous media. The precipitation of the floc occurs via self-assembly of the cluster and surfactant components. The floc components generally assemble to form lamellae of interdigitated surfactant tails alternating with layers of inorganic clusters that are associated with charged surfactant heads. The lamellae range from flat ordered layers to buckled and distorted layers, to complete spherical enclosure of the clusters by a hydrophobic surfactant layer (Figure 4).[46-49]
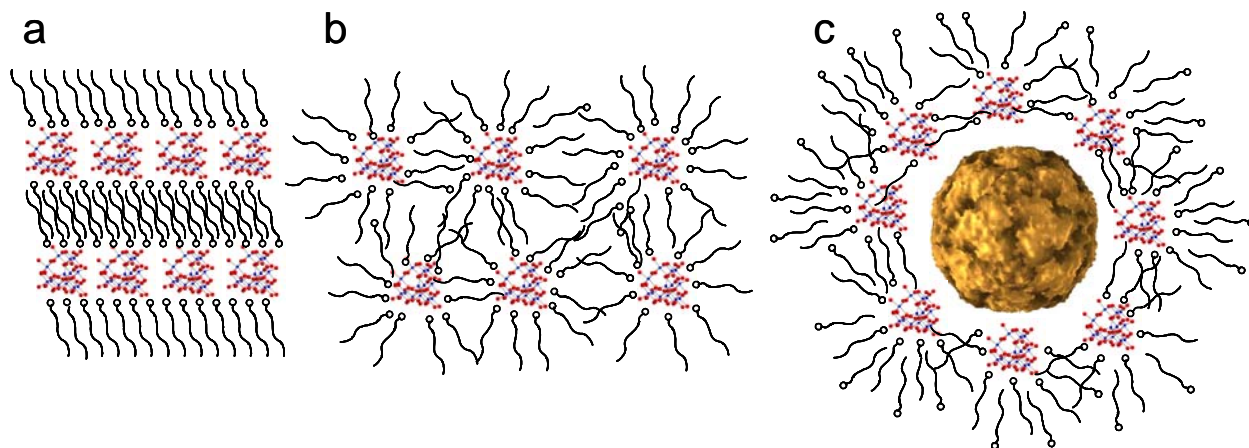
Figure 4. Schematics of cluster-surfactant self-assembled phases using the Al_{13} ε-Keggin ion for illustration; (a) represents a well-ordered phase with alternating layers of clusters and interdigitated surfactant tails; (b) represents a phase with clusters completely enclosed by surfactants and the enclosed clusters ordered in approximate layers. The (a) assembly is formed with lower-charged clusters (i.e. ≤ 4) while the (b) assembly is formed with higher-charged clusters. (c) Schematic of a cluster-surfactant phase enmeshing a virus (bovine enterovirus).

The variation in cluster-surfactant ordering is influenced by cluster charge, size and geometry, surfactant tail length and surfactant charge. These characteristics can be varied in order to optimize virus sequestration ability. Understanding and optimizing the virus sequestration

processes may impact a number of applications where removal of viruses from aqueous media is desired including water re-use, water clarification (alum or ferric process), wastewater treatment, detection, or diagnostics.

We have investigated virus sequestration capabilities of cluster-surfactant phases that contain 1) cationic clusters plus anionic surfactants or 2) anionic clusters plus cationic surfactants. The main cationic cluster of interest is the ε-Keggin aluminum tridecamer, $[Al_{13}O_4(OH)_{24}(H_2O)_{12}]^{7+}$($Al_{13}^{7+}$), a component of the alum flocculation process that is recognized to play a key role in effective removal of a variety of contaminants including microorganisms and anthropogenic organic pollutants.[50-64] This cluster is combined with sodium dodecylsulfate (SDS), an anionic surfactant, or soluble silicate plus cationic surfactant dodecyltrimethylamine ($C_{12}Si$). Anionic clusters known as polyoxometalates (POMs) are based on early d^0 transition metals including W, Nb, Mo, and V. POMs included in this study are $[Nb_6O_{19}]^{8-}$ (Nb_6), $[SiW_{11}O_{39}]^{8-}$ (SiW_{11}), $[PW_{12}O_{40}]^{3-}$ (PW_{12}), and $[SiW_{12}O_{40}]^{4-}$ (SiW_{12}). These are coupled with cationic surfactants hexadecyltrimethylammonium chloride ($C_{16}Cl$), dodecyltrimethylammonium chloride ($C_{12}Br$) or $C_{12}Si$.

In a typical experiment to test virus sequestration efficacy of a cluster-surfactant floc, the water-soluble components (10^{-6} to 10^{-4} molar concentration) are added to an aqueous media that is spiked with a virus titer (Bovine enterovirus, BEV, or Influenza A; a representative non-enveloped and enveloped virus, respectively). The precipitate forms, adhering and enmeshing the viruses in the process, which is subsequently filtered. The aqueous media is then analyzed by rRT-PCR (reverse transcriptase polymer chain reaction) for virus concentration remaining. Virus sequestration efficacy of a series of cluster-surfactant phases is summarized in the bar graph of Figure 5a.[65] Overall, these results indicate that: (1) the efficacy of the POM-surfactant phases depends more on the surfactant than the cluster and the order of POM-surfactant efficacy is POM-$C_{12}Si$ > POM-C_{12} > POM-C_{16}; (2) for Al_{13}^{7+}, the $C_{12}Si$ is much more effective than either SDS or NaOH (analogous to alum flocculation). Cluster-surfactant colloids were characterized in aqueous media by dynamic light scattering (DLS) and in the solid-state by powder x-ray diffraction. These results show that larger colloids (Figure 5b) and poorer long-range ordering of the clusters and surfactants corresponded with better virus sequestration efficacy. It is somewhat surprising that the more hydrophobic C_{16} surfactant forms more soluble and less effective virus sequestration phases with smaller average colloid size than less hydrophobic C_{12}, when combined with POMs. The POM-C_{16} phases also exhibit better long-range order than POM-C_{12} phases. We attribute these results to the better interdigitating ability of C_{16} compared to C_{12}. This results in more ordered precipitates in the solid-state and probably offers stabilization in aqueous solution. On the other hand, the shorter C_{12} chain cannot interdigitate as well, and thus more readily precipitates with the POM since the hydrophobic tail region has more contact with the aqueous media.[65]
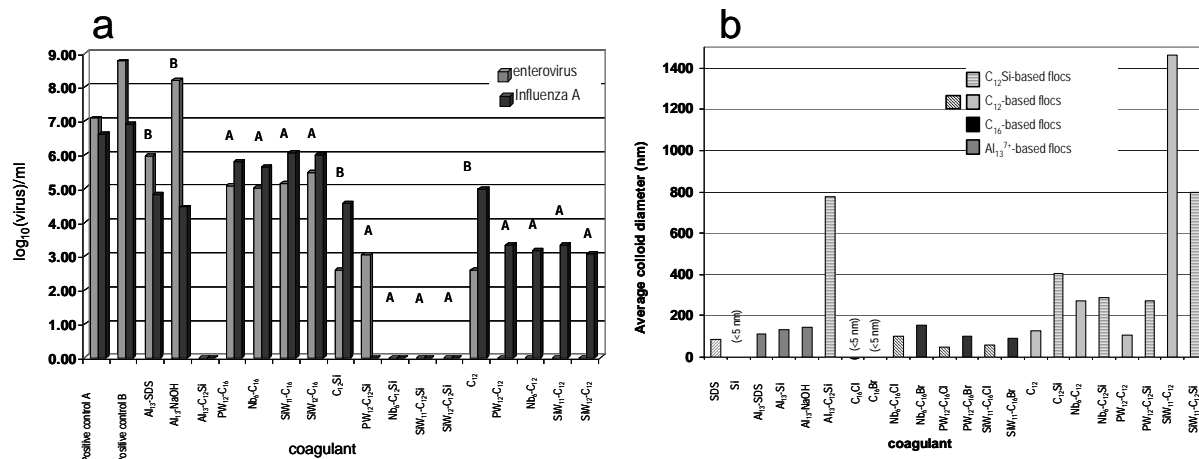
Figure 5. (a) Graph showing efficacy of various cluster-surfactant phases via concentration ($\log_{10}$/ml—vertical axis) of virus remaining in solution, post-coagulation treatment, and filtration.[65] Detection limit of virus by *r*RT-PCR is 10^1 TCID50/ml (tissue culture infectious dose). Positive controls **A** and **B** are the initial virus concentrations without treatment. Each experiment is labeled **A** or **B**, pertaining to the control concentrations utilized. The concentration of each inorganic cluster is 10^{-6} M. (b) Average colloidal diameter of cluster-surfactant phases in aqueous solution determined by Dynamic Light Scattering. Concentration of inorganic cluster is 10^{-5} M for each experiment.

Overall, the Al_{13}^{7+}-$C_{12}Si$ and the POM-$C_{12}Si$ flocculents are most effective for virus sequestration, reducing the virus titer of both influenza A and BEV to below detection limit by *r*RT-PCR (10^1 virus/ ml). The dissolved silicate polymerizes with the Al_{13}^{7+} cluster to form anionic aluminosilicate clusters, which then precipitate with the cationic surfactants. The role of the dissolved silicate is not clear in the case of the POM-$C_{12}Si$ flocculents, since silicate is not a significant component of the precipitates. Perhaps it serves to slow down the precipitation of the floc since $C_{12}Si$ is stable in aqueous solution, and thus allows more complete adhesion and enmeshment of the viruses.

Ongoing challenges of this work are both fundamental and applied. The Al_{13}^{7+}-$C_{12}Si$ flocculent, along with the hypothetical analogous Fe_{13}^{7+}-$C_{12}Si$, are related to alum or ferric flocculent chemistries utilized in municipal water treatment plants, and will be investigated in further detail for practical use in water treatment applications with improved pathogen removal capabilities. Other ongoing studies involve probing the interactions of viruses with individual floc components (clusters, surfactants, dissolved silicate) to discern enmeshment and adhesion mechanisms of virus sequestration, and to also explore selectivity for specific viruses in the interest of detection technologies.

References

1. S.K. Hong, M. Elimelech, J. Membr. Sci. 132, 159 (1997).

2. J.S. Baker, L.Y. Dudley, Desalination 118, 81 (1998).

3. W. Yuan, A.L. Zydney, Desalination 122, 63 (1999).

4. J.W. Cho, G. Amy, J. Pellegrino, Y.M. Yoon, Desalination 118, 101 (1998).

5. W.H. Peng, I.C. Escobar, D.B. White, J. Membr. Sci. 238, 33 (2004).

6. K. Riedl, B. Girard, R.W. Lencki, J. Membr. Sci. 139, 155 (1998).

7. A.E. Childress, M. Elimelech, J. Membr. Sci. 119, 253 (1996).

8. T. Knoell, J. Safarik, T. Cormack, R. Riley, S.W. Lin, H. Ridgway, J. Membr. Sci. 157, 117 (1999).

9. C.J. Orendorff, B.L. Frankamp, T.C. Monson, T.M. Alam, J. Majewski, D.L. Huber, B.C. Bunker, Langmuir (2008) submitted.

10. C.J. Orendorff, D.L. Huber, B.C. Bunker, *Langmuir* (2008) submitted.

11. C.W. Bunn, E.V. Garner, *Proc. R. Soc. Lond. Math. Phys. Sci.* **189**, 39 (1947).

12. H.W. Starkweather, D.R. Johnson, J.F. Whitney, *J. Polym. Sci. A* **1**, 715 (1963).

13. H.I. Kim, J.G. Kushmerick, J.E. Houston, B.C. Bunker, *Langmuir* **19**, 9271 (2003).

14. C. Palegrodsdemange, E.S. Simon, K.L. Prime, G.M. Whitesides, *J. Am. Chem. Soc.* **113**, 12 (1991).

15. K.L. Prime, G.M. Whitesides, *Science* **252**, 1164 (1991).

16. P. Harder, M. Grunze, R. Dahint, G.M. Whitesides, P.E. Laibinis, *J. Phys. Chem. B* **102**, 426 (1998).

17. K. Feldman, G. Hahner, N.D. Spencer, P. Harder, M. Grunze, *J. Am. Chem. Soc.* **121**, 10134 (1999).

18. S.I. Jeon, J.H. Lee, J.D. Andrade, P.G. de Gennes, *J. Colloid Interface Sci.* **142**, 149 (1991).

19. C.M. DeRamos, A.E. Irwin, J.L. Nauss, B.E. Stout, *Inorg. Chim. Acta* **256**, 69 (1997).

20. N. Emmerichs, J. Windgender, H.-C. Flemming, C. Mayer, *Int. J. Biol. Macromol.* **34**, 73 (2004).

21. P. Le-Clech, Y. Marselina, Y. Ye, R.A. Stuetz, V. Chen, *J. Membr. Sci.* **290**, 36 (2007).

22. Q.L. Li, Z.H. Xu, I. Pinnau, *J. Membr. Sci.* **290**, 173 (2007).

23. T.D. Perry, R.T. Cygan, R. Mitchell, *Geochim. Cosmochim. Acta* **70**, 3508 (2006).

24. A.F.D. Kennedy, I.W. Sutherland, *Biotechnol. Appl. Biochem. 9,* 12 (1987).

25. T.A. Davis, F. Llanes, B. Volesky, A. Mucci, *Environ. Sci. Technol.* **37**, 261 (2003).

26. A. Boyd, A.M. Chakrabarty, *J. Ind. Microbiol. Biotechnol.* **15**, 162 (1995).

27. I. Braccini, S. Pérez, *Biomacromolecules* **2**, 1089 (2001).

28. Q. Li, M. Elimelech, *Environ. Sci. Technol.* **38**, 4683 (2004).

29. S. Lee, M. Elimelech, *Environ. Sci. Technol.* **40**, 980 (2006).

30. C.J. Brinker, Y.F. Lu, A. Sellinger, H.Y. Fan, *Adv. Mater.* **11**, 579 (1999).

31. N.G. Liu, R.A. Assink, B. Smarsly, C.J. Brinker, *Chem. Commun.* **10**, 1146 (2003).

32. Y.-B. Jiang, N. Liu, H. Gerung, J.L. Cecchi, C.J. Brinker, *J. Am. Chem. Soc.* **128**, 11018 (2006).

33. S. Holmann, S. Nielsen, P. Agre, *Aquaporins* (Academic Press, San Diego, 2001).

34. B. Hille, *Ionic Channels of Excitable Membranes* (Third edition of Sinauer Associates, Sunderland, MA, 2001).

35. K. Leung, S.B. Rempe, C.D. Lorenz, *Phys. Rev. Lett.* **96**, 095504 (2006).

36. S. Varma, S.B. Rempe, *Biophys. J.* **93**, 1093 (2007).

37. P.C. Jordan, *Biophys. J.* **93**, 1091 (2007).

38. J. Goldberger, R. Fan, P.D. Yang, *Acc. Chem. Res.* **39**, 239 (2006).

39. F.H.J. van der Heyden, D. Stein, K. Besteman, S.G. Lemay, C. Dekker, *Phys. Rev. Lett.* **96**, 224502 (2006).

40. G. Hummer, *Mol. Phys.* **105**, 201 (2007).

41. E.R. Cruz-Chu, A. Aksimentiev, and K. Schulten, *J. Phys. Chem. B* **110**, 21497 (2006).

42. C.Y. Won and N.R. Aluru, *J. Am. Chem. Soc.* **129**, 2748 (2007).

43. J.D. Pless, M.L.F. Philips, J.A. Voigt, D. Moore, M. Axness, J.L. Krumhansl, T.M. Nenoff, *Industrial. Engr. Chem. Res.* **45**, 4752 (2006).

44. S. Varma, D. Sabo, S.B. Rempe, *J Mol. Bio.* **374** (2007).

45. K. Leung, M. Marsman, *J. Chem. Phys.* **127**, 154722 (2007)..

46. M. Nyman, D. Ingersoll, S. Singh, F. Bonhomme, T.M. Alam, C.J. Brinker, M.A. Rodriguez, *Chem. Mater.* **17**, 2885 (2005).

47. T. Ito, H. Yashiro, T. Yamase, *Langmuir* **22**, 2806 (2006).

48. D.G. Kurth, P. Lehmann, D. Volkmer, H. Colfen, M.J. Koop, A. Muller, A. Du Chesne, *Chem. Eur. J.* **6**, 385 (2000).

49. D. Volkmer, A. Du Chesne, D.G. Kurth, H. Schnablegger, P. Lehmann, M.J. Koop, A. Muller, *J. Am. Chem. Soc.* **122**, 1995 (2000).

50. B.D. Ballard, A.A. MacKay, *J. Environ. Eng.* **108**, 131 (2005).

51. P. Paton-Morales, F.I. Talens-Alesson, *Colloid Polym. Sci.* **278**, 697 (2000).

52. M. Porras, F.I. Talens, *Sep. Sci. Technol.* **34**, 2679 (1999).

53. F.I. Talens-Alesson, S. Anthony, M. Bryce, *Water Res.* **38**, 1477 (2004).

54. M. Abbaszadegan, B.K. Mayer, H. Ryu, N. Nwachuku, *Environ. Sci. Technol.* **41**, 971 (2007).

55. H.A. Bustamante, S.R. Shanker, R.M. Pashley, M.E. Karaman, *Water Res.* **35**, 3179 (2001).

56. L. Fiksdal, T. Leiknes, *J. Membr. Sci.* **279**, 364 (2006).

57. Y. Matsui, T. Matsushita, S. Sakuma, T. Gojo, T. Mamiya, H. Suzuoki, T. Inoue, *Environ. Sci. Technol.* **37**, 5175 (2003).

58. T. Matsushita, Y. Matsui, N. Shirasaki, Y. Kato, *Desalination* **178**, 21 (2005).

59. M. Suwa, Y. Suzuki, *Water Sci. Tech.* **47**, 45 (2003).

60. B.T. Zhu, D.A. Clifford, S. Chellam, *Water Res.* **39**, 5153 (2005).

61. H.J. Liu, J.H. Qu, C.Z. Hu, S.J. Zhang, *Colloids Surf., A* **216**, 139 (2003).

62. C.Z. Hu, H.J. Liu, J.H. Qu, D.S. Wang, J. Ru, *Environ. Sci. Technol.* **40**, 325 (2006).

63. B.Y. Gao, Q.Y. Yue, B.J. Wang, *Chemosphere* **46**, 809 (2002).

64. D.S. Wang, Z.K. Luan, H.X. Tang, *J. Am. Water Works Assoc.* **95**, 79 (2003).

65. M. Nyman, J.M. Bieker, S.G. Thoma, D.E. Trudell, *J. Colloid Interfac. Sci.*, **316**, 968 (2007).

Model Nylon 6,6 Thin Films: Synthesis and Characterization

Introduction

Polymer thin films on surfaces are widely used in controlling interfacial materials properties for areas including biocompatibility, anti-fouling coatings, and corrosion resistance. Such films can be created by numerous approaches from simple spray coating to more complex surface-initiated polymerization techniques.[1,2] For studying the fundamental interfacial interactions and structure/function relationships in thin films, it would be ideal if the thin films were produced with well-defined structure, density, and composition.

Polymer coatings prepared by spray or spin coating from solution are generally randomly oriented polymer films that are physisorbed to the substrate. Methods to prepare thin films that are chemisorbed to the substrate and, therefore, exhibit greater mechanical strength, are divided into two designations; "grafting to" (GT) and "grafting from" (GF) approaches.[3] In the GT approach, polymers are grown in solution with reactive end groups. A surface is modified with monolayers of complimentary reactive terminal groups. Upon reaction with a solution polymer, a chemical bond is formed; covalently attaching the polymer to the substrate. While the GT technique is experimentally relatively simple, it is limited to low graft densities because of steric effects at the surface, where the film thickness is controlled by the molecular weight of the polymer formed under solution polymerization conditions.[4,5]

The GF approach, also referred to as surface initiated polymerization, takes place from initiator groups covalently bound to the surface. Typically, an initiator is tethered to a molecule that can form a self-assembled monolayer (SAM) (e.g. alkanethiols or alkylsilanes). A SAM of the initiator is immobilized on a substrate of choice, followed by exposure of the modified-substrate to a monomer and catalyst resulting in polymer growth from the proximal surface initiator outward.[6-8] This technique is more challenging than GT, however, it produces surfaces of higher graft density with precise control over film thickness and functionality with ideal surface confinement.

Interfacial interactions with polymer surfaces govern the function of polymeric materials in numerous applications from medical device implants to adhesive coatings. One such application of interest is polymer membranes in reverse osmosis (RO) or nanofiltration (NF) systems.[9] The interactions between these membrane surfaces, typically polyamide (nylon) or cellulose acetate polymers, and water and saltwater govern their desalination performance.[10-12] In addition, bio- and abiotic fouling known to plague these systems from brackish water is also dictated by surface phenomena.[13,14] While studying the bulk membrane properties is beneficial, creating thin film mimics of these membrane materials would provide a model for surface characterization studies to better understand the structure-function relationships at the RO interface.

In this report, we present a GF stepwise approach to synthesizing Nylon 6,6 thin films. We apply this polyamide sequential growth procedure[15] to give thin polymer films with discretely defined film thickness and structure. This work is the first in a series of reports to use these well-

defined films as experimental models to study fundamental interfacial interactions at complex polymer interfaces. The structure and properties of these model thin films are characterized by ellipsometry, FT-IR spectroscopy, and solid state NMR.

Experimental

Materials
Adipoyl chloride, 1,6-hexamethylene diamine, 3-aminopropyltrimethoxysilane (APTES), 1.0 M N,N'-dicyclohexyl-carbodiimide (DCC) in dichloromethane, 4-dimethylamminopyridine (DMAP), dichloromethane, 11-mercaptoundecanoic acid (11-MUA), and anhydrous toluene were purchased from Aldrich. Ethanol (200 proof) was purchased from Aaper. All chemicals were used as received. Silicon wafers (100 mm diameter, one polished side) and quartz substrates (100 mm diameter, one polished side) were purchased from Wafer World. Fumed silica (14 nm dia., 200 m^2/g) was purchased from Aldrich. Gold substrates were prepared by the vapor deposition of 5 nm chromium as an adhesion layer followed by 100 nm gold on clean silicon wafers.

Methods
Surface grafted Nylon 6,6 films were prepared on piranha-cleaned (3:1 conc. H_2SO_4: 30% H_2O_2) silicon, quartz, and gold substrates and on as-received silica particles. On silicon and quartz, APTES monolayers were prepared using a generalized vapor deposition procedure.[16,17] Silicon (1 cm^2) or quartz (100 mm dia.) substrates were sealed in a clean, dry glass cell containing 0.4 mL neat APTES at the bottom of the cell for >2 h at 25°C. The resulting APTES monolyers were rinsed with toluene and ethanol and dried with N_2. Efforts to prepare APTES monolayers from solution using a 2% solution of APTES in toluene [v/v] consistently resulted in APTES multilayers films with a film thickness of 2-3 nm. Therefore, the vapor deposition of APTES on silicon is used throughout. Nylon 6,6 films were prepared using a stepwise growth procedure in alternating diamine and diacid solutions. APTES-modified substrates were immersed in 0.1 M adipoyl chloride in dry toluene for 45 min. Substrates were removed, rinsed with toluene, dried with a stream of N_2 gas, and immersed in a 0.1 M 1,6-hexamethylene diamine solution in dry toluene for 10 min. Substrates were removed from solution, rinsed with ethanol, and dried using N_2. This alternating diacid/diamine procedure was repeated with 10 min incubation times until film growth reached the desired thickness. On silica particles, the procedure was analogous with the exception that between diacid/diamine reactions, particles were vacuum filtered followed by washing and drying steps on the filtration apparatus.

Nylon 6,6 thin films were prepared on gold substrates for reflectance-absorbance FT-IR measurements. Gold substrates were cleaned with piranha, rinsed with copious amounts of H_2O, and immersed in a 2 mM 11-MUA solution in ethanol for >12 h. The resulting carboxylic acid-terminated SAMs were modified with the diamine by carbodiimide coupling chemistry. 11-MUA SAMs were washed with ethanol, dried with N_2 and immersed in a solution containing 10 mM N,N'-dicyclohexyl-carbodiimide (DCC), 0.1 M 1,6-hexamethylene diamine, and 10 mg 4-dimethylamminopyridine (DMAP) in dry dichloromethane for 4 h. Substrates were washed with dichloromethane, toluene, and ethanol and dried with N_2. The resulting films are designated $Nylon_{0.5}$. From this point, additional polyamide growth steps we performed following the same procedure used on silicon or quartz.

Instrumentation

Ellipsometric measurements were made with a DRE Dr.-Riss EL X-01R ellipsometer using a HeNe laser (3 mW) at an incident angle of 70°. Initial readings were taken on clean, bare silicon to establish the thickness of the native oxide. The ellipsometry results were used to calculate the corresponding film thickness using the DRE ELX1 software program.

The solid state one dimensional (1D) ^{29}Si magic angle spinning (MAS) NMR spectra were obtained on a Bruker Avance 400 instrument at 79.50 MHz using a 7 mm broadband probe, a 4 kHz sample spinning speed and ^{1}H TPPM decoupling (77 kHz). For the direct Bloch decay experiments a 240 s recycle delay was used, while for the ^{1}H-^{29}Si cross polarization (CP) MAS NMR experiments a 5 ms contact time and a 10 s recycle delay was utilized. For all ^{29}Si NMR experiments air was used as the carrier gas to reduce the relaxation time of the silicon. The two dimensional (2D) ^{1}H-^{29}Si HETCOR NMR experiments were performed on a 4 mm broadband MAS probe using both Lee-Goldberg (LG) CP and LG decoupling during the indirect dimension, using 1024 scan averages and 64 t_1 increments. The ^{29}Si NMR chemical shifts were referenced to the secondary external standard Q_8M_8 (δ = +11.5 ppm with respect to TMS δ = 0.0 ppm). The 1D ^{13}C CPMAS NMR spectra were obtained using a 4 mm broadband probe on either a Bruker Avance 400 or an Avance 600 instrument operating at 100.1 and 150.9 MHz, respectively. Standard CPMAS NMR experiments with a 1 ms contact time and a 10 s recycle delay were utilized. The ^{13}C NMR chemical shifts were referenced to the carbonyl resonance of a secondary external glycine reference (δ = 176.0 ppm wrt to TMS).

Infrared spectra were acquired with a Bruker IFS 66v/s FT-IR spectrometer (Bruker). Thin film spectra were obtained using p-polarized light at an incident angle of 85° with respect to the surface normal using a Harrick Seagull™ variable reflection accessory (Harrick). All spectra are the average of 3000 scans of both the sample and the reference. Spectra were acquired at 2 cm^{-1} resolution and Blackman-Harris apodization using a liquid N_2-cooled MCT-D316 detector. Spectra are reported as –log (R/R_0), where R is the reflectance of the sample and R_0 is the reflectance of the reference.

Results and Discussion

This stepwise GF approach offers unique control of Nylon 6,6 film thickness and uniformity of surface-bound oligomers. A schematic of the surface-grafting reaction to form Nylon 6,6 on silicon is shown in Figure 1. The native oxide of a silicon substrate is functionalized with a primary amine using 3-aminopropyltrimethoxysilane (APTES). Amide bond formation is achieved by the reaction of the amine-terminated APTES monolayer with adipoyl chloride. The resulting film is designated Nylon$_{1.0}$. Each subsequent reaction with the diamine and diacid chloride results in one complete Nylon 6,6 repeat unit. Complete diamine/diacid repeat units that are acid-terminated are given the whole number designation Nylon$_{2.0}$, Nylon$_{3.0}$, etc.; while amine-terminated half repeat units are designated Nylon$_{1.5}$, Nylon$_{2.5}$, etc.
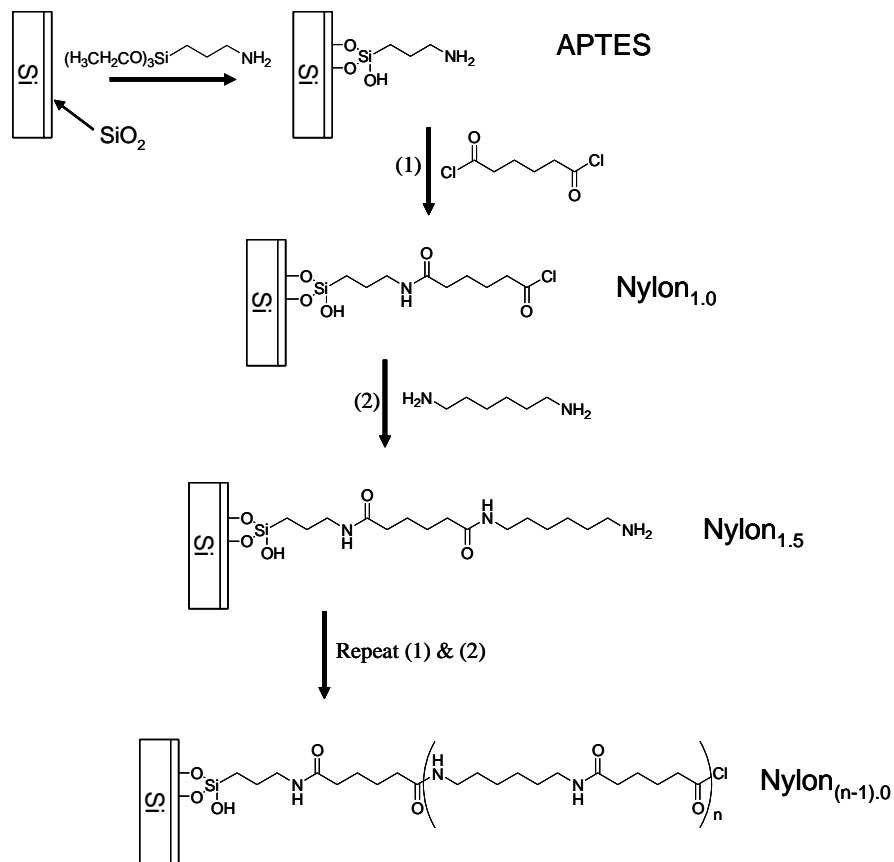
Figure 1. Schematic of the step-wise surface growth of Nylon 6,6 on silicon substrates.

Nylon film thickness is monitored using ellipsometry to investigate the effect of each growth step on the final film thickness. Film thickness values are given in Table 1. The thickness of the APTES monolayer is measured to be 0.97 ± 0.18 nm, which is in good agreement with that measured by Bein et al.[17] After the first addition of the acid chloride, the film thickness increased to 1.75 ± 0.17 nm. For a total of 7 additions of diamine and diacid, the film thickness follows a linear trend, with an increasing slope of ~0.7 nm per subunit, plotted in Figure 2. However, a closer look at the film thickness change with increasing oligomer subunit in Table 1 shows that for each diacid addition after the first, the film thickness increases only an average of 0.27 nm, while the length of an adipoly chloride molecule is ~0.7 nm. Moreover, each diamine addition after the initial diamine coupling results in a disproportionately large film thickness change, 1.4 and 1.0 nm for a molecule that is ~0.7 nm in length. Moreover, the Nylon$_{4.0}$ sample has a measured film thickness of 5.77 ± 0.71 nm, which is ~20% shorter than the expected length of the all-trans, fully extended conformation, a 4-repeat unit Nylon 6,6 oligomer (~7 nm). If the negative deviation from the expected film thickness for the adipoyl chloride reactions to make Nylon$_{2.0}$, Nylon$_{3.0}$, and Nylon$_{4.0}$ were a result of incomplete diacid to diamine conversion, the film thickness would roll over and plateau to show no increase with subsequent diacid/diamine reactions. However, upon the addition of diamine to make Nylon$_{2.5}$ and Nylon$_{3.5}$, the measured film thickness continues to increase and not roll over. Then, the differences between the observed and theoretical film thickness change for each growth step must be a consequence of the structure and conformation of the growing polymer chain.

Table 1. Nylon 6,6 film thickness values determined by ellipsometry.

# of Nylon 6,6 Repeat Units[a]	Total Film Thickness (nm)
APTES[b]	0.97 ± 0.18
1.0	1.75 ± 0.17
1.5	2.19 ± 0.35
2.0	2.58 ± 0.39
2.5	4.40 ± 0.38
3.0	4.28 ± 0.28
3.5	5.33 ± 0.85
4.0	5.77 ± 0.71

[a]Repeat unit is an addition of both diamine and diacid
[b]3-aminopropyltrimethoxysilane
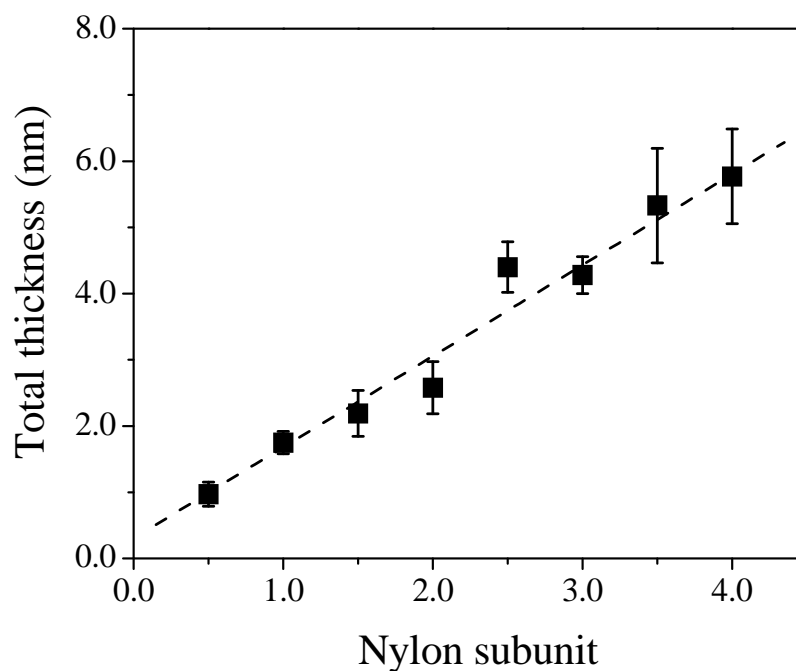
Figure 2. Linear fit to nylon film thickness with subsequent additions of nylon subunits measured by ellipsometry.

It is well understood that the structure of bulk crystalline α and β Nylon 6,6 is governed by inter-chain hydrogen bonding of amide groups.[18,19] Consider the example of adipoly chloride reacting with the amine-terminated Nylon$_{1.5}$ sample to give Nylon$_{2.0}$. As the diacid couples one end to the amine-terminated surface to form an amide, there is inter-chain hydrogen bonding at that

amide end of the terminal diacid, but not at the distal free acid chloride end if the molecular orientation is parallel to the surface normal. Then, it is more energetically favorable for the diacid to be tilted with respect to the surface normal, or even lay flat in order to maximize hydrogen-bonding interactions with the newly formed amide groups (5-6 kcal/mol); opposed to standing parallel to the surface normal and only being stabilized by weaker chain-chain van der Waals interactions of a four-methylene long molecule (2-3 kcal/mol).

In the following diamine reaction to give $Nylon_{2.5}$, the diamine couples to the surface-terminal acid chloride to make another amide. The new amide (formerly the acid terminal group of the film) can reorient in order to hydrogen bond with neighboring Nylon chains in a different minimum energy conformation, as opposed being tilted or lying flat on the surface. Then, the positive deviation from the expected film thickness for the diamine reactions to make $Nylon_{2.5}$ and $Nylon_{3.5}$ is observed because the film thickness increases by the length of the added diamine and the reorientation or configuration of the adjacent diacid subunit in order to maximize hydrogen bonding. In the final film, sample $Nylon_{4.0}$, the measured film thickness is ~20% shorter than expected for the all-trans conformation. This indicates that the aliphatic chains must have kinks, gauche conformers, or a twisted structure throughout the length of the chains, in order to facilitate inter-chain hydrogen bonding. In the case of bulk α and β Nylon 6,6, chains are offset to align neighboring amide groups and accommodate hydrogen bonds.[18,19] In the surface-confined case, chains are restricted from a chain offset structure and an alternative minimum energy conformation to maximize hydrogen-bonding interactions must be achieved.

Reflectance-Absorbance Infrared Spectroscopy (RAIRS) is used to gain more insight into the chemistry of the stepwise growth process and to study the structural behavior of these Nylon thin films. IR spectra for Nylon 6,6 films at various points in the growth process, shown in Figure 3. The corresponding vibrational assignments and peak frequencies are given in Table 2. In order to make reflectance measurements on these Nylon thin films, they must be prepared on a reflective substrate, such as gold. An important distinction between the IR and other experiments presented in this work is that Nylon 6,6 is grafted from a reflective gold substrate via 11-mercaptoundecanoic acid (11-MUA) monolayers for the IR experiments instead of the APTES monolayer on silicon or silica. On gold, the amide coupling is carried out under carboiimide coupling conditions; which is different to the acid chloride/amine coupling chemistry used on silicon. While this is a discrepancy between the acid chloride/APTES coupling described above, the IR data provide important chemical characterization of these Nylon 6,6 thin films.
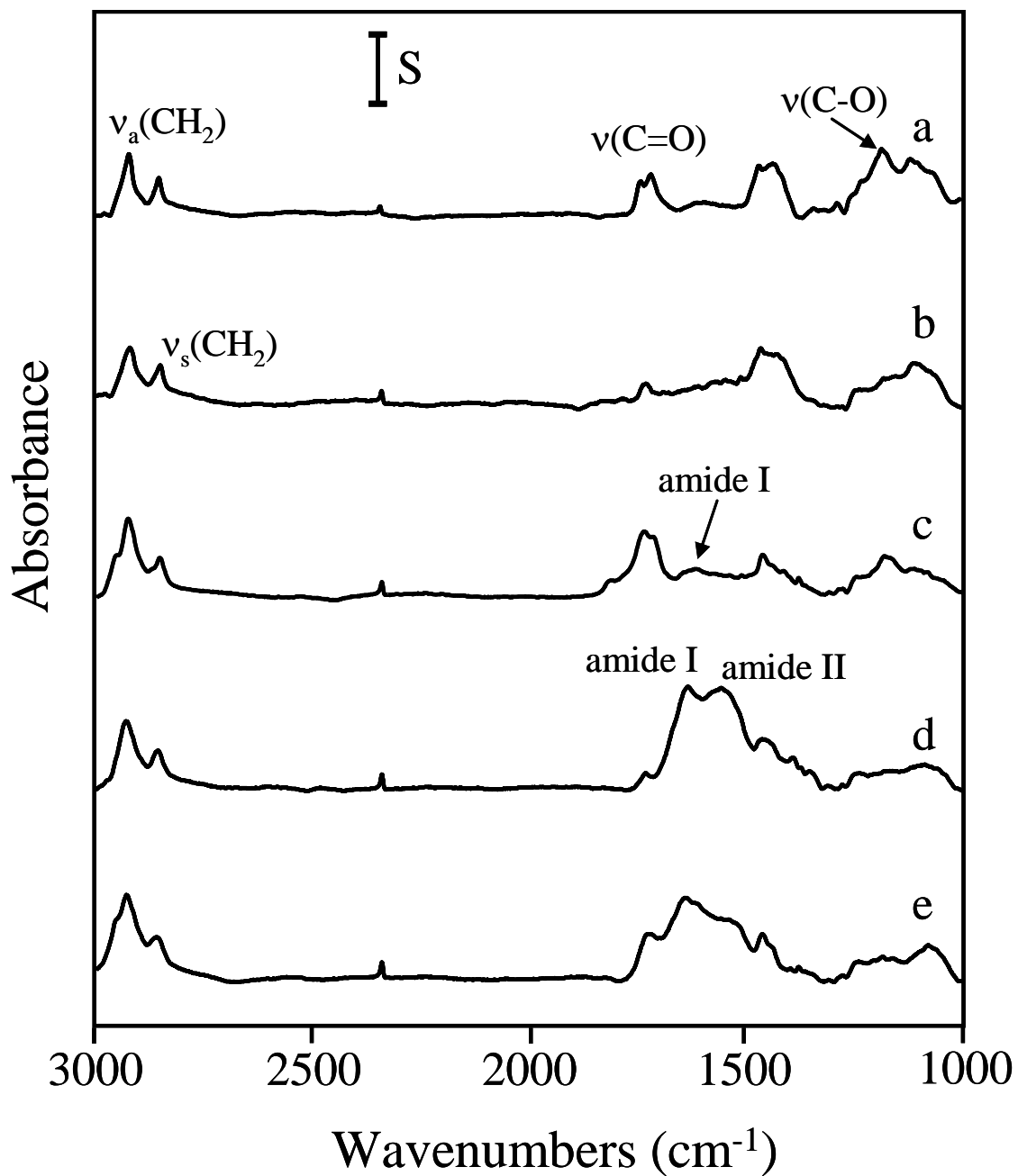
Figure 3. RAIRS spectra of (a) 11-mercaptoundecanoic acid (11-MUA) SAM, (b) Nylon$_{0.5}$, (c) Nylon$_{1.0}$, (d) Nylon$_{2.5}$ and (e) Nylon$_{4.0}$ on gold substrates. S = 2.5 x 10^{-3} a.u. for all spectra.

Table 2. Peak Frequencies (cm^{-1}) and assignments for 11-mercaptoundecanoic acid (11-MUA) and Nylon 6,6 on gold substrates.

Peak Frequency (cm^{-1})					Assignment[a,b]
11-MUA[c]	**Nylon$_{0.5}$**	**Nylon$_{1.0}$**	**Nylon$_{2.5}$**	**Nylon$_{4.0}$**	
2920	2920	2925	2929	2929	$\nu_a(CH_2)$
2850	2851	2852	2857	2857	$\nu_s(CH_2)$
1740	NO[d]	1737	NO	NO	$\nu(C=O)$, free acid
NO	1733	NO	1733	NO	$\nu(C=O)$
1717	NO	1717	NO	1721	$\nu(C=O)$, H-bonded
NO	NO	1626	1634	1636	$\nu(C=O)$, amide I
NO	1560sh[e]	1553sh	1558	1554	$\delta(N-H)$, amide II
1466	1466	1464	1464	1463	$\delta(CH_2)$
1440	1440	1440	1440	1440	$\delta (CH_2)$
1181	1181	1180	NO	1180	$\nu(C-O)$
1114	1114	1112	1112	1112	$\nu(C-C)$
1061	1061	1060sh	1060	1060	$\nu(C-C)$

[a]ν = stretch; δ = bend and/or scissor
[b]Assignments were made from References 20-23
[c]11-mercaptoundecanoic acid
[d]Not observed
[e]Shoulder

For the 11-MUA SAM on gold, methylene vibrational modes are observed at 2920 (stretch), 2850 (stretch), and 1466 cm^{-1} (scissor), carbonyl modes for the free and hydrogen-bonded carboxylic acid are observed at 1740 and 1717 cm^{-1}, respectively, and the carboxyl C-O stretch is observed at 1181 cm^{-1} (Figure 3a). For each diamine or diacid subunit addition, there are specific chemical markers of polyamide growth one would expect to observe. Upon the addition of the first diamine, the free carbonyl stretch (1717 cm-1) and carboxyl C-O stretch (1181 cm^{-1}) should disappear and the characteristic amide modes including the amide carbonyl stretch (~1635 cm^{-1}) and amide N-H bend (~1560 cm^{-1}) should appear. After the subsequent diacid addition, one would expect to observe the reemergence of the free and hydrogen-bonded carbonyl stretches (~1740 cm^{-1} and ~1720 cm^{-1}) resulting from the acid-terminal functional group. In addition, the intensities of the amide modes (amide carbonyl and amide N-H) should all increase with increasing diacid/diamine subunit reactions. However, as stated previously, it should be noted that these RAIRS spectra are collected with p-polarization. Then, any perturbations to the polyamide structure may change the intensity or even the presence of a mode depending on its orientation to the s- and p-planes.

After the first diamine reaction, sample Nylon$_{0.5}$ (Figure 3b), carbonyl modes at 1717 and 1740 cm^{-1} almost completely disappear from the spectra and what intensity remains has shifted to 1730 cm^{-1}. In addition, the intensity of the carboxyl C-O stretch at 1181 cm^{-1} is significantly less

than observed for the 11-MUA monolayer. There is also the addition of a broad shoulder that appears between 1550 and 1650 cm^{-1} in Figure 3b. After the first diacid reaction (sample Nylon$_{1.0}$ shown in Figure 3c) the free and hydrogen-bonded carbonyl modes and the carboxyl C-O stretch mode reappear in the IR spectrum and have comparable intensities to those modes observed for the 11-MUA SAM. The amide carbonyl mode (1635 cm^{-1}), often referred to as the amide I, is also observed in the spectrum of Nylon$_{1.0}$. In addition, the methylene deformation mode intensity decreases at 1440 cm^{-1}. For the amine-terminated Nylon$_{2.5}$ sample, both the amide carbonyl and the amide N-H bend at 1558 cm^{-1} (amide II) modes are readily observable, while the intensities of the acid carbonyl and carboxyl C-O stretching modes are diminished. After the final diacid addition (sample Nylon$_{4.0}$ in Figure 3e), the amide II mode intensity decreases slightly, but the bulk of the spectrum remains unchanged. There is a spurious shoulder peak observed for samples Nylon$_{2.5}$ and Nylon$_{4.0}$ (Figures 3c and 3e) that can only be assigned to the asymmetric methyl stretch (2960 cm^{-1}). Since there are no methyl groups in the reactive subunits, it is likely due to residual wash solvent (acetone or ethanol) associated with or trapped in the films. It should be noted that spectral data above 3000 cm^{-1}, including the terminal amine N-H stretch at ~3150 cm^{-1}, are inaccessible due to spectral interference from water ice from the liquid N_2-cooled detector.

The vibrational modes observed for the 11-MUA SAM are characteristic of acid terminated monolayers described in the literature.[20-23] Once the terminal-acid group is reacted with the diamine to make sample Nylon$_{0.5}$, the carbonyl modes are almost completely disappear from the spectrum, but some intensity remains at a mode shifted to 1730 cm^{-1}. This suggests that the terminal carboxylic acid has reacted, but not to completion. Comparing the integrated peak areas of the ν(C=O) modes in Figures 3a and b, we estimate that ~10% of residual free carboxylic acid remains unreacted. In addition, the intensity of the carboxyl C-O stretch (1181 cm^{-1}) is significantly decreased after the first diamine reaction, which is additional evidence to support the free carboxylate reaction. Incomplete coupling is typical of carboiimide chemistry,[20] however, in this case it is not significant enough to prohibit comparisons of film structure and behavior between these films on gold and others on silicon.

While it is clear that the free carboxylate has reacted, the expected amide product of that reaction is not clearly discernable in the spectral data (Figure 3b). There is a shoulder of the amide II mode at 1560 cm^{-1}, but the intensity of that mode and the amide I peak are significantly less than expected, compared to previous reports.[20] In fact, the intensity of both the amide I and II modes after the second stepwise reaction with the diacid (Figure 3c) are less than expected. Despite the difference in expected intensity, there is clearly amide coupling at the surface during the first two surface grafting steps. In addition, the reemergence of the terminal acid carbonyl modes at 1717 and 1737 cm^{-1} in the Nylon$_{1.0}$ spectrum (Figure 3c) is direct evidence that one end of the diacid is coupled to the surface while the other functional acid group is distal on the surface. After additional acid chloride-amine coupling cycles to make samples Nylon$_{2.5}$ and Nylon$_{4.0}$, amide I (~1635 cm^{-1}) and amide II (~1556 cm^{-1}) modes are readily observable in the IR spectra (Figures 3d and e).

The diminished intensity of the amide I and II modes in the Nylon$_{0.5}$ and Nylon$_{1.0}$ is likely the result from two contributing sources. As stated above, the carboiimide coupling chemistry is incomplete, leading to submonolayer surface-grafted polyamide and less amide vibrational mode

intensity in the IR spectra. However, given the ~90% efficiency of the initial amide coupling, this is not likely to be the primary contribution to the attenuated amide I and II absorbance. Another factor contributing to the observed decreased amide I and II intensity is the orientation and structure of coupled diamine and diacid molecules. As observed in the ellipsometry measurements, the orientation and conformation of added diacid and diamine subunits is dynamic and will change in order to maximize hydrogen bonding. The first diacid addition to make $Nylon_{1.0}$ results in a linear increase in the film thickness that is roughly proportional to the length of an all-trans diacid molecule (Table 1). Then, if the surface-bound diacid is approximately perpendicular to the surface, or in the p-plane, then the amide I carbonyl and amide II N-H groups will both be in the s-plane. The result is attenuated absorbance of these modes in the IR spectrum of $Nylon_{1.0}$ (Figure 3c) because these measurements are acquired in the p-polarization.

As additional diacid/diamine reactions give amine-terminated $Nylon_{2.5}$ and acid-terminated $Nylon_{4.0}$ samples, there are more amide bonds on the surface, which will contribute to greater IR absorbance of amide I and II modes observed in Figures 3d and e. These additional amide linkages throughout the length of the aliphatic chains must also be rotated slightly out of the s-plane to account for the significantly greater intensity of the amide I and II modes in Figures 3d and 3e. However, these chains remain kinked, bent or twisted to facilitate chain-chain hydrogen bonding which agrees well with the measured ellipsometric film thickness of $Nylon_{4.0}$ sample being ~20% less than that of the all-trans conformer.

The peak frequencies of the methylene symmetric ($\nu_s(CH_2)$, ~2850 cm^{-1}) and asymmetric ($\nu_a(CH_2)$, ~2920 cm^{-1}) stretching modes in $\nu(C-H)$ region (2800-3000 cm^{-1}) can also be used as a spectral indicator of Nylon 6,6 chain order.[23] For the 11-MUA SAM, the symmetric and asymmetric methylene stretching peak frequencies are observed at 2850 and 2920 cm^{-1}, respectively. These vibrational frequencies are consistent with crystalline-like, all-trans closely packed monolayers.[21] Increasing polyamide growth from $Nylon_{0.5}$ to $Nylon_{4.0}$, both methylene stretching modes shift to higher frequency (Table 2). While the frequencies of these modes are not direct indicators of chain conformation,[24] the methylene peak frequencies suggest that the 11-MUA SAM is well ordered and that the final long-chain $Nylon_{4.0}$ sample has more disorder in system.

A variety of solid state NMR techniques can be utilized to interrogate the Nylon 6,6 structure and the nature of the interaction with the substrate. It is important to note that solid state NMR experiments performed herein are for on $Nylon_{4.0}$-modified silica particles (14 nm, 200 m^2/g), not on planar silicon. However, the initial condensation step of APTES and subsequent Nylon 6,6 growth on silica particles and on the native oxide of planar silicon are analogous. Solid state ^{29}Si cross polarization (CP) and direct polarization (DP) MAS NMR are well suited for studying organosilane condensation on silica. ^{29}Si CPMAS NMR spectra show several different silicon chemical environments for unmodified silica, APTES-, and $Nylon_{4.0}$-modified silica samples shown in Figures 4a-c. For a reference, these different silicon environments are also illustrated in Figure 4. For unmodified silica, disilanol (Q^2), silanol (Q^3), and siloxane (Q^4) environments are observed. The reduced signal intensity in the CPMAS NMR of unmodified silica results from the reduced hydrogen concentration in this material. Partially cross-linked (T^2) and completely cross-linked (T^3) silyl environments are observed for APTES and $Nylon_{4.0}$ samples.
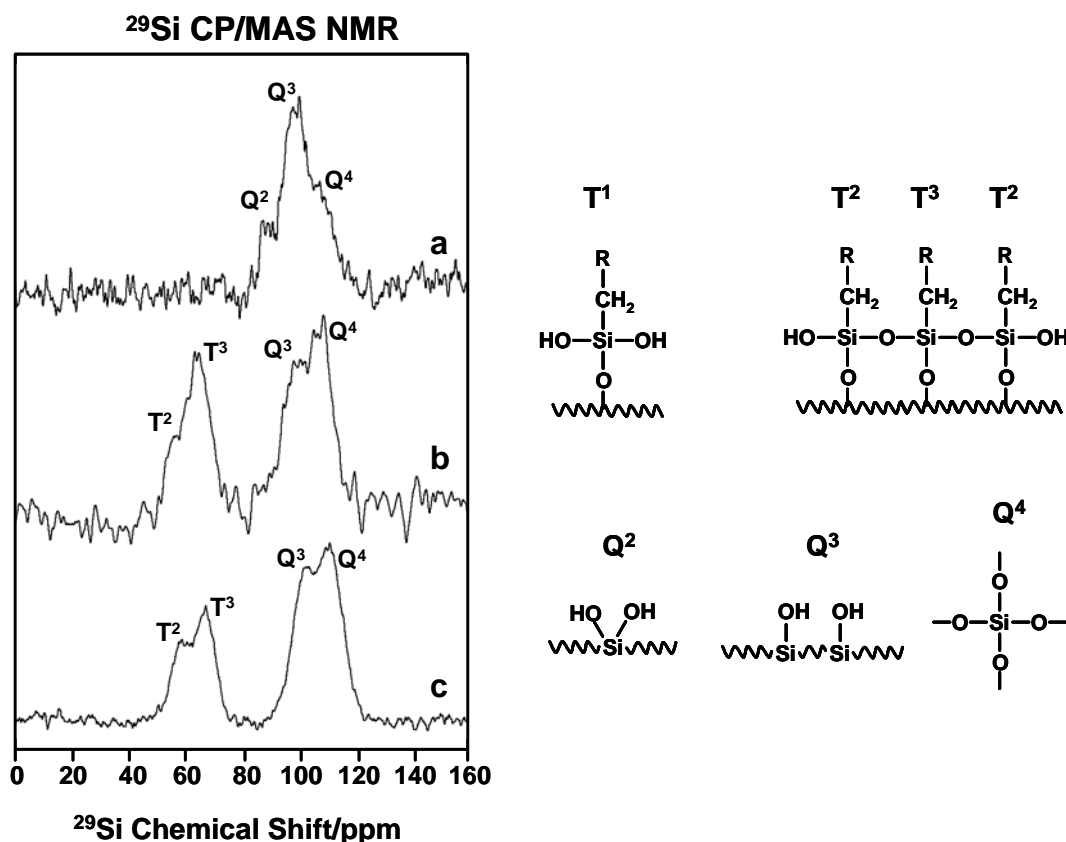
Figure 4. ^{29}Si CPMAS NMR spectra of (a) unmodified silica, (b) APTES-, and (c) Nylon$_{4.0}$-modified silica. Structural elements of different silicon species observed during the Nylon 6,6 modification procedure.

The presence of T-groups clearly shows that both the APTES modifier and the Nylon 6,6 oligomers are covalently attached to the substrate. The absence of uncross-linked (T^1) silyl modes in both the APTES and Nylon$_{4.0}$ spectra indicate that these films are significantly cross-linked with relatively high surface coverage. The lack of a ^{29}Si NMR signal at $\delta = 45.6$ ppm confirms that the lack of unreacted APTES within the final material. The extent of cross-linking for Nylon 6,6 (based on the integration of the DP ^{29}Si NMR spectra) is calculated to be 85%, using the following T-group relationship:[25]

$$\% \text{ cross-linked} = 1/3 \; T^1 \; (\%) + 2/3 \; T^2 \; (\%) + T^3 \; (\%) \tag{1}$$

Using the percent cross-linked and the measured T:Q ratio, we can estimate a Nylon 6,6 surface coverage. Using the $Q^2 + Q^3 : Q^4$ ratio measured in the DP ^{29}Si spectrum, approximately 14% of the total Si-O species are surface accessible groups. If 14% of the silicon atom are accessible for condensation and the final silane is 85% cross-linked, then the maximum theoretical T:Q ratio should be 9.1% for a complete monolayer. The measured T:Q ratio is 8.5% for the Nylon$_{4.0}$ sample, or an estimated Nylon 6,6 coverage of 93%.

The Nylon 6,6 structure is interrogated by the solid state ^{13}C and ^{1}H NMR. The ^{13}C DPMAS NMR spectrum of Nylon$_{4.0}$ is shown in Figure 5a and can be use to determine if the expected

43

Nylon 6,6 chemical composition has be synthesized. ^{13}C NMR is extremely useful for determining material composition because each chemically distinct carbon atom will have a unique resonance and those resonances are quantitative. For the Nylon$_{4.0}$ sample the ^{13}C CPMAS NMR spectrum shown in Figure 5a reveals a series of resonances between 25 and 50 ppm due to the different methylene environments that are differentiated by their relative positions to the amide nitrogen (α_N, β_N, and γ_N) or their relative positions to the amide carbonyl (α_C and β_C). These ^{13}C resonances have been assigned to amorphous (A) or crystalline (C) conformational states of the polyamide chains in previous studies in bulk polyamides.[26] However, in our case, polyamide are surface-confined and it would be difficult to assign chemical shifts as having analogous bulk-like crystalline or amorphous environments. Moreover, the peak intensities can be split depending on the polymer conformation can chemical environment, further complicating the interpretation of these results.[26,27] For the purposes of this report, the discussion will focus on the primary intense modes: α_N (39.7 ppm), α_C (39.3 ppm), β_C (26.5 ppm) and overlapping β_N/γ_N (25.2 ppm). The integrated intensities of these modes are expected to be 5:6:6:10, respectively (since the β_N and γ_N peaks overlap). The measured ratios of these modes from the DP spectrum are 5:3.7:6:10. In general, the integrations are in good agreement with the theoretical values which is direct evidence that we have a 4-repeat Nylon 6,6 film. However, there is some discrepancy in the integration of the α_C peak. This deviation is not surprising, since the α_C peak is adjacent to the α_N and its integration depends on a mathematical fit to these data.

The ^{1}H MAS NMR spectra of APTES and Nylon$_{4.0}$ samples are shown in Figures 5b and 5c. There are distinctive differences in the ^{1}H spectra for APTES-modified silica and Nylon$_{4.0}$, most notably in the N-H region (2-8 ppm). Qualitatively, the predominant free amine N-H resonance in the APTES spectra at ~6.5 – 7 ppm (Figure 5b) is shifted to the amide N-H ~8.3 ppm for Nylon$_{4.0}$ (Figure 5c). However, broad line widths and the overlap with residual water make these assignments difficult. Broad line widths along with associated spinning sidebands are observed for both APTES and Nylon 6,6 modified silica are indicative of significant residual ^{1}H-^{1}H dipolar coupling due to restricted chain mobility, analogous to observation made previously for densely-packed alkylsilane films on silica.[25]

The two dimensional (2D) ^{1}H-^{29}Si heteronuclear correlation (HETCOR) MAS NMR spectra are shown in Figure 6. For APTES and Nylon$_{4.0}$, there is a CH$_2$ correlation with the T^2 and T^3 silica species as would be expected for APTES. There are also strong correlations between CH$_2$ and OH protons and Q^3 and Q^4 silicon species, clearly demonstrating that APTES is covalently attached to the silica surface. Also of interest is the observation of Si-NH correlations for the Nylon$_{4.0}$ material, while this correlation is missing in the APTES material. This suggests that for APTES-modified silica the terminal primary amine is not strongly associated or near the silica surface, or that there are significant chain dynamics to prevent efficient CP between the NH and ^{29}Si. On the other hand the similarity in the line width of the ^{1}H MAS NMR spectra in the dry state would argue against huge differences in chain dynamics. For Nylon$_{4.0}$ the observation of this Si-NH contact suggest that the aliphatic chains are kinked, twisted or bent, putting an amide group near the surface silicon atoms.[28] The presence of Si-NH surface interaction and a kinked-type chain conformation agrees well with the ellipsometry and IR results, suggesting that the polyamide chains are not all-trans and completely perpendicular to the surface, but that they have kinked or bent conformers that facilitate inter-chain hydrogen bonding.
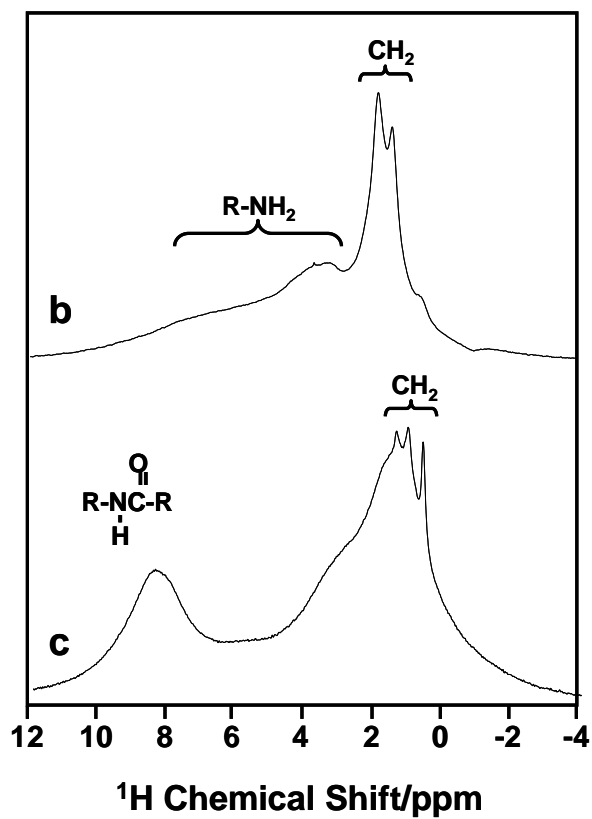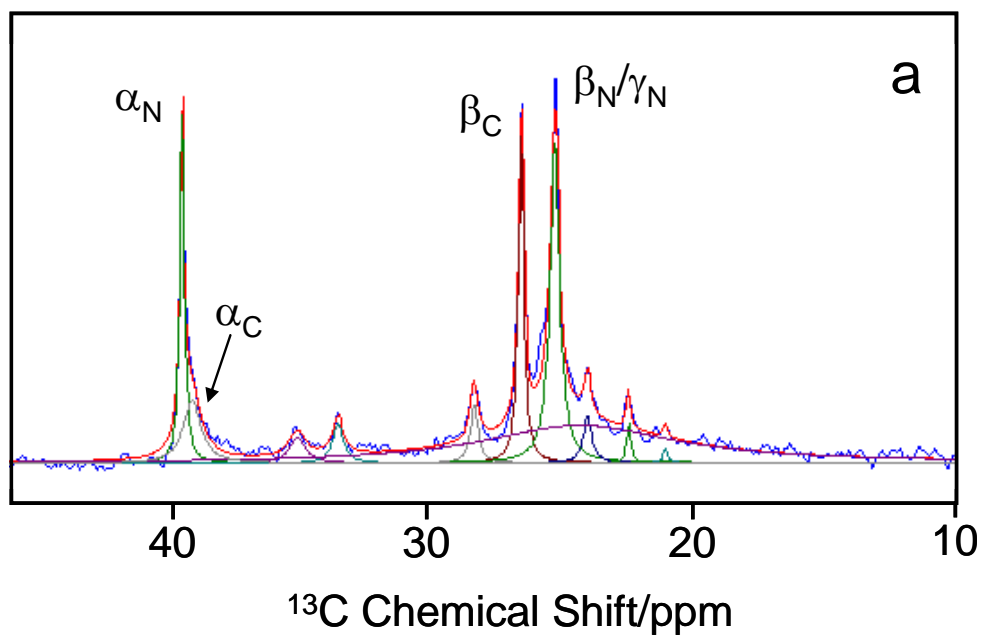
Figure 5. ^{13}C DPMAS NMR spectra of (a) Nylon[4.0]-modified silica and ^{1}H MAS NMR spectra of (b) APTES- and (c) Nylon[4.0]-modified silica.
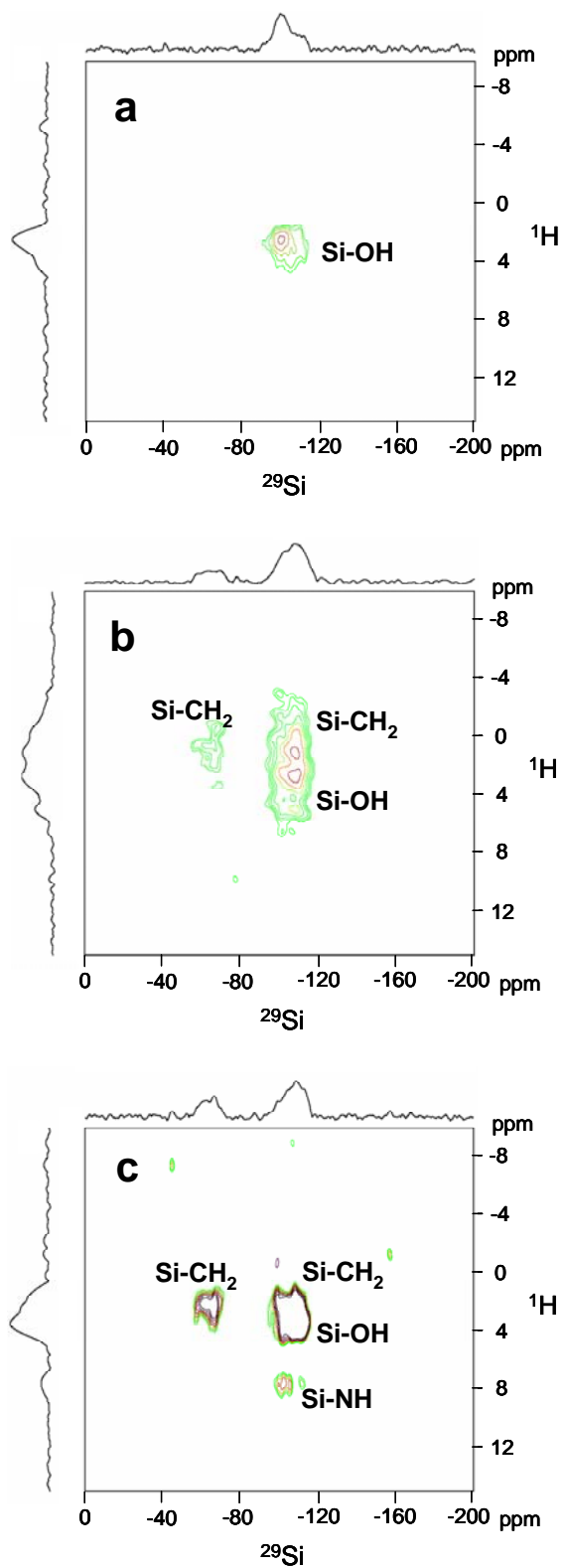
Figure 6. ^{1}H-^{29}Si LG CPMAS HETCOR spectra of (a) unmodified silica, (b) APTES-, and (c) Nylon$_{4.0}$-modified silica.

Conclusions

The synthesis of surface-bound Nylon 6,6 films via a step growth polymerization process is presented as a method to create model polymer surfaces. These Nylon thin-films are grown in a stepwise fashion allowing discrete control of terminal functionality and film thickness, determined by ellipsometry. The ellipsometry results also suggest that hydrogen bonding within the aliphatic chains and at the terminal functional groups significantly impacts the final film thickness. Amide coupling reactions between diacid and diamine precursors at individual film growth steps are confirmed by IR spectroscopy and the composition of the final 4-repeat Nylon 6,6 film is confirmed by ^{13}C NMR. Moreover, the IR spectral data are in good agreement with ellipsometry results and provide some structural evidence that the Nylon chains are not in the all-trans, fully extended conformation, but exist in a kinked or twisted structure to facilitate inter-chain hydrogen bonding. This kinked-type chain conformation is also supported by 2-D HETCOR ^{1}H-^{29}Si NMR which shows a fraction of amide coupling to the underlying substrate. There is evidence in the literature to support a kinked or bent Nylon 6,6 conformation from the bulk γ-phase of Nylon 6,6 and Nylon 6 which contains distorted amide conformers to make a pleated sheet-type bulk structure.[29-31] Additional experiments are currently underway to elucidate the structure of surface-tethered Nylon 6,6 using Raman spectroscopy and will be reported at a later date.

References

1. Halperin, A.; Tirrell, M.; Lodge, T. P. Adv. Polym. Sci. 1992, 100, 31-71.

2. Fleer, G. J.; Cohen-Stuart, M. A.; Scheutjens, J. M. H. M.; Cosgrove, T.; Vincent, B.; Polymers at Interfaces; Chapman & Hall: London, 1993.

3. Edmondson, S.; Osborne, V. L.; Huck, W. T. S. Chem. Soc. Rev. 2004, 33, 14-22.

4. Milner, S. T. Science 1991, , 251, 905-914.

5. Rühe, J.; Knoll, W. J. Macromol. Sci.: Polym. Rev. 2002, C42, 91-138.

6. Prucker, O.; Rühe, J. Mater. Res. Soc. Symp. Proc. 1993, 304, 1675-1677.

7. Dyer, D. J. Adv. Funct. Mater. 2003, 13, 667-670.

8. Chechik, V.; Crooks, R. M.; Stirling, C. J. M. Adv. Mater. 2000, 12, 1161-1171.

9. Peng, W.; Escobar, I. C.; White, D. B. J. Membrane Sci. 2004, 238, 33-46.

10. Riedl, K.; Girard, B.; Lencki, R. W. *J. Membrane Sci.* **1998**, *139*, 155-166.

11. Childress, A. E.; Elimelech, M. *J. Membrane Sci.* **1996**, *119*, 253-268.

12. Knoell, T.; Safarik, J.; Cormack, T.; Riley, R.; Lin, S. W.; Ridgway, H. *J. Membrane Sci.* **1999**, *157*, 117-138.

13. Hong, S. K. Elimelech, M. *J. Membrane Sci.* **1997**, *132*, 159-181.

14. Baker, J. S.; Dudley, L. Y. *Desalination* **1998**, *118*, 81-90.

15. Aberem, M .B.; Feng, W.; Kadi, A. A-. Riedl, B.; Brisson, J. *Composite Interfaces* **2005**, *12*, 425-433.

16. Cai, M.; Ho. M.; Pemberton, J. E. *Langmuir* **2000**, *16*, 3446-3453.

17. Kurth, G.; Bein, T. *Langmuir* **1993**, *9*, 2965-2973.

18. Fuller, C. S.; Baker, W. O.; Pape, N. R. *J. Am. Chem. Soc.* **1940**, *62*, 3275-3281.

19. Danford, M. D.; Spruiell, J. E.; White, J. L. *J. Appl. Polym. Sci.* **1978**, *22*, 3351-3361.

20. Frey, B. L.; Corn, R. M. *Anal. Chem.* **1996**, *68*, 3187-3193.

21. Chidsey, C. E. D.; Loiacono, D. N. *Langmuir* **1990**, *6*, 682-691.

22. Smith, E. L.; Alves, C. A.; Anderegg, J. W.; Porter, M. D.; Siperko, L. M. *Langmuir* **1992**, *8*, 2707-2714.

23. Nuzzo, R. G.; Dubois, L. H.; Allara, D. L. *J. Am. Chem. Soc*. **1990**, *112*,558-569.

24. Orendorff, C. J.; Ducey, M. W.; Pemberton, J. E. *J. Phys. Chem. A* **2002**, *106*, 6991-6998.

25. Pursch, M.; Sander, L. C.; Albert, K. *Anal. Chem.* **1996**, *68*, 4107-4113.

26. Kubo, K.; Ando, I.; Shiibashi, T.; Yamanobe, T.; Komoto, T.. *Polymer Sci. B* **1991**, *29*, 57-66.

27. Caravajal, G. S.; Leyden, D. E.; Quinting, G. R.; Maciel, G. E. *Anal. Chem.* **1988**, *60*, 1776-1786.

28. Wiench, J. W.; Avadhut, Y. S.; Maity, N.; Bhaduri, S.; Lahiri, G. K.; Pruski, M.; Ganapathy, S. *J. Phys. Chem. B* **2007**, *111*, 3877-3885.

29. Starkweather, H. W.; Whitney, J. F.; Johnson, D. R. *J. Polym. Sci.* **1963**, *1*, 715.

30. Starkweather, H. W.; Jones, G. A. *J. Polym. Sci.* **1981**, *19*, 467.

31. Stephens, J .S.; Chase, D. B.; Rabolt, J. F. *Macromolecules* **2004**, *37*, 877.

Effects of Water and Temperature on Conformational Order in Model Nylon Thin Films

Abstract

Nylon 6,6 thin films have been examined by Raman spectroscopy to determine how chain conformation is influenced by environmental parameters such as exposure to water and temperature variations. The motivation for this work is to elucidate how interactions between water and the model polymers mediate polymer structures in applications such as the removal of salt from water in reverse osmosis membranes. Raman spectra show that model self-assembled monolayers containing Nylon 6,6 chains are semi-crystalline under ambient conditions. The native chains adopt an unusual kinked and folded conformation related to that found in γ-Nylon 6,6. The regular chain deformations allow adjacent tethered chains to maximize hydrogen-bonding between neighboring amide groups under the constraints imposed by surface tethering. With increasing temperature, the films undergo a phase transition associated with the disruption of hydrogen bonds leading to structures containing more linear regions that are closer to the "all trans" case. Similar structural changes are observed on exposing the Nylon films to water. The salt content of the water does not appear to have a significant impact on the structure or phase transition in the Nylon 6,6. These results suggest that while inclusion of water has a profound effect on the polymer structure, either salt is excluded from the polymer or there is sufficient free volume with in the films to accommodate hydrated ions with our inducing further structural changes.

Introduction

Structure-function relationships at polymer interfaces and organic thin films directly impacts the material performance in several technologies including the biocompatibility of medical implant devices,[1] adsorption resistance of antifouling coatings,[2] and charge transports across heterojunctions in organic electronics.[3,4] One of our interests in polymer interfaces is in the area of reverse osmosis (RO) or nanofiltration (NF) systems. It is well known that the characteristics of polyamide membranes, commonly used for RO systems, at the interface govern their desalination and remediation capabilities.[5-8] In these systems water-polymer, polymer-polymer, and dissolved species-polymer interactions all directly contribute to the overall material performance.

Much of the early work to elucidate bulk polyamide structure was determined by X-ray diffraction.[9-13] Crystalline Nylon 6,6 is known to exist in one of three phases, triclinic zigzag sheets (α or β), or pseudohexagonal (γ). In α and β phase, Nylon chains are hydrogen-bonded in a regular zigzag pattern, without any intrasheet hydrogen-bonding. While there is some debate if intrasheet hydrogen bonding exists in the γ phase, it is well understood that the aliphatic chains are distorted to give a pseudohexagonal, pleated sheet phase. Due to the regular periodic spacing of hydrogen bonding amide and carbonyl groups in Nylon 6,6 the crystalline to amorphous phase transition occurs at relatively high temperatures (~250°C). In other polyamides, including some even-even numbered Nylons (Nylon 2,6, Nylon 2,8, etc.) and odd-odd numbered Nylons (Nylon 5,5), the hydrogen-bond donor and acceptor positions are either off-set or have irregular spacing,

giving rise to notably lower phase transition temperatures.[14,15] In all cases, chain-chain hydrogen-bonding interactions in polyamides are the dominating force that defines their structure in the solid state.

In recent years, Raman spectroscopy has proven to be a powerful tool for giving detailed structural information for various phases of polyamides. Most of the Raman phase behavior investigations have been carried out for Nylon 6 materials (films or fibers) because of its unique α- to γ- phase transition.[16,17] Polarized Raman spectra of oriented Nylon 6 fibers provide spectroscopic evidence for the phase transition between the extended sheet α-form to the pleated sheet parallel chain γ-phase.[16] Moreover, Stephens et al.[17] have shown that electrospinning Nylon 6 into fibers imparts conformational stress to the polymer, observing a phase transition from bulk and γ-phases to more disordered electrospun phase.

We have developed methodology for creating model Nylon 6,6 thin films as experimental models of the RO membrane surface.[18] One goal of this work is to use Raman spectroscopy to elucidate the temperature-dependent phase behavior of these model Nylon thin films. Once the phase behavior of these films is established, we aim to use that information to study how water and salt water interactions impact the interfacial Nylon structure. This information will be used to relate these structural changes to develop a detailed understanding of interactions at the RO membrane interface.

Experimental

Materials
Adipoyl chloride, 1,6-hexamethylene diamine, 3-aminopropyltrimethoxysilane (APTES), bulk Nylon 6,6, and anhydrous toluene were purchased from Aldrich. Ethanol (200 proof) was purchased from Aaper. Sodium chloride was purchased from Fisher Scientific. All chemicals were used as received. Kromasil silica (Krom-100-10, 309 m^2/g) was obtained from Akzo Nobel.

Methods
Surface-grafted Nylon 6,6 films were prepared on silica particulate substrates as described previously.[18] Briefly, 3 g silica was added to a clean, dry round bottom flask containing 2% [v/v] 3-aminopropyltimethoxysilane (APTES) in anhydrous toluene and stirred under N_2 for 4 h at 25°C. The resulting APTES-modified silica was filtered and washed with toluene and ethanol. Nylon 6,6 films were prepared using a stepwise growth procedure in alternating diamine and diacid solutions. APTES-modified silica was added to 10 mL 0.1 M adipoyl chloride in dry toluene and stirred under N_2 for 45 min. Particles were vacuum filtered, washed with toluene, and added to 10 mL 0.1 M 1,6-hexamethylene diamine solution in dry toluene and stirred under N_2 for 30 min. The alternating filtration and diacid/diamine reactions were repeated to increase the Nylon 6,6 chain growth. In total, three adipoyl chloride and two 1,6-hexamethylene diamine steps were used to prepare the samples used in all experiments. The result is a three-repeat unit, acid terminated Nylon 6,6 oligomer-modified silica substrate, referred to as Nylon$_{3.0}$; the chemical structure of which is shown in Figure 1.
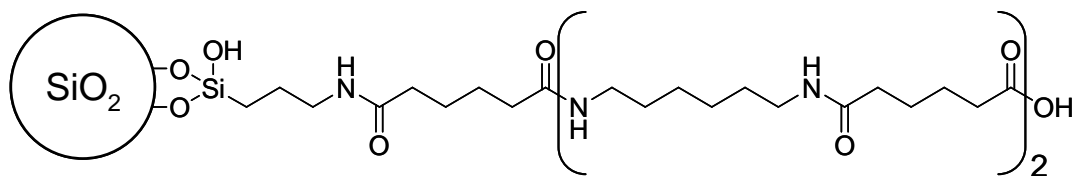
Figure 1. A schematic of surface-bound Nylon$_{3.0}$ on silica.

Instrumentation

Samples for Raman spectroscopy were prepared by adding 50 mg of polyamide-modified silica to a quartz NMR tube (Wilmad Glass). Temperature control was achieved using a copper block sample holder fitted with either a resistive heater or a well for ice and the temperature was monitored with a K-type thermocouple. At each temperature, samples were equilibrated for 30 min prior to spectral acquisition. Raman spectra were collected using 25 mW of 785 radiation from diode laser in a commercial Thermo-Nicolet Almega Dispersion Raman spectrometer. Slit settings were 100 μm for all experiments and a spectral bandpass of 5.4 cm^{-1}. The total carbon content of the polyamide-modified silica was determined using a Perkin-Elmer 2400 Series II CHNS elemental analyzer (Desert Analytics, Tucson, AZ).

Results and Discussion

Raman Spectral Indicators of Conformational Order in Alkanes

Raman spectroscopy has proven to be a useful tool for determining structure and order of bulk aliphatic organic materials and organic thin films including lipid bilayers and self-assembled monolayers.[19-23] Perhaps the most significant body of recent work is focused on using Raman spectroscopy to determine the rotational and conformational order of alkylsilane-modified silica stationary phases for reversed-phase liquid chromatography (RPLC); materials that are closely related to our aliphatic Nylon 6,6-modified silicas.[24-27] These reports have identified several spectral indicators of rotational and conformational order. Examples include the asymmetric and symmetric methylene stretching frequencies, $\nu_a(CH_2)$ and $\nu_s(CH_2)$, which are an indicator of alkyl chain-chain coupling. The intensity ratio of the $\nu_a(CH_2)$ to the $\nu_s(CH_2)$, is an empirical measure of rotational disorder, while the intensity ratio of the gauche carbon-carbon stretch, $\nu(C\text{-}C)_G$, to the trans carbon-carbon stretch, $\nu(C\text{-}C)_T$, is a direct measure of gauche conformers in the material. While there are many more vibrational modes that provide valuable structural information for alkanes, these listed are examples of the types of spectral data used and their relationship to structure that can be obtained by Raman spectroscopy.

Conformational Order in Bulk Nylon 6,6 and Surface-Confined Nylon 6,6

Raman spectra of a commercial bulk Nylon 6,6 polymer and surface-bound Nylon$_{3.0}$ are shown in Figure 2. The corresponding peak frequency assignments are given in Table 1. While vibrational modes for polyamides can be use for simple identification, specifically amide I (1635 cm^{-1}) and amide II (1444 cm^{-1}) modes, the vibrational spectra contains a plethora of information on their physical structural and chemical environment. For bulk Nylon 6,6 in the $\nu(C\text{-}C)$ region, the $\nu(C\text{-}C)_{T,HB}$ (1046 cm^{-1}) and $\nu(C\text{-}C)_T$ (1063 cm^{-1}) modes correspond to trans conformers within the aliphatic chains. The $\nu(C\text{-}C)_{T,HB}$ also indicates intermolecular (i.e. chain-chain) hydrogen-bonding in a crystalline "zigzag" pattern, or α-phase-like environment.[28-30] The

absence of ν(C-C)$_G$ (1080 cm^{-1}) for bulk Nylon 6,6 suggests that the Nylon chains are in the all-trans crystalline phase. The bulk Nylon 6,6 spectrum also has a pronounced methylene deformation mode, designated δ(CH$_2$), at 1428 cm^{-1}. For bulk polyethylene (PE), this mode referred to previously as δ(CH$_2$)$_{ORTHO}$, is a direct measure of the polymer chain-chain coupling in the crystalline orthrorhombic phase.[20] For Nylons, the relative intensity of the 1428 cm^{-1} δ(CH$_2$) can also be used as a chain-chain coupling spectral indicator analogous to that for the PE case. There is also a δ(C-N-H) bending mode observed at 1480 cm^{-1} for bulk Nylon 6,6, which indicates a trans amide group.[17,31]
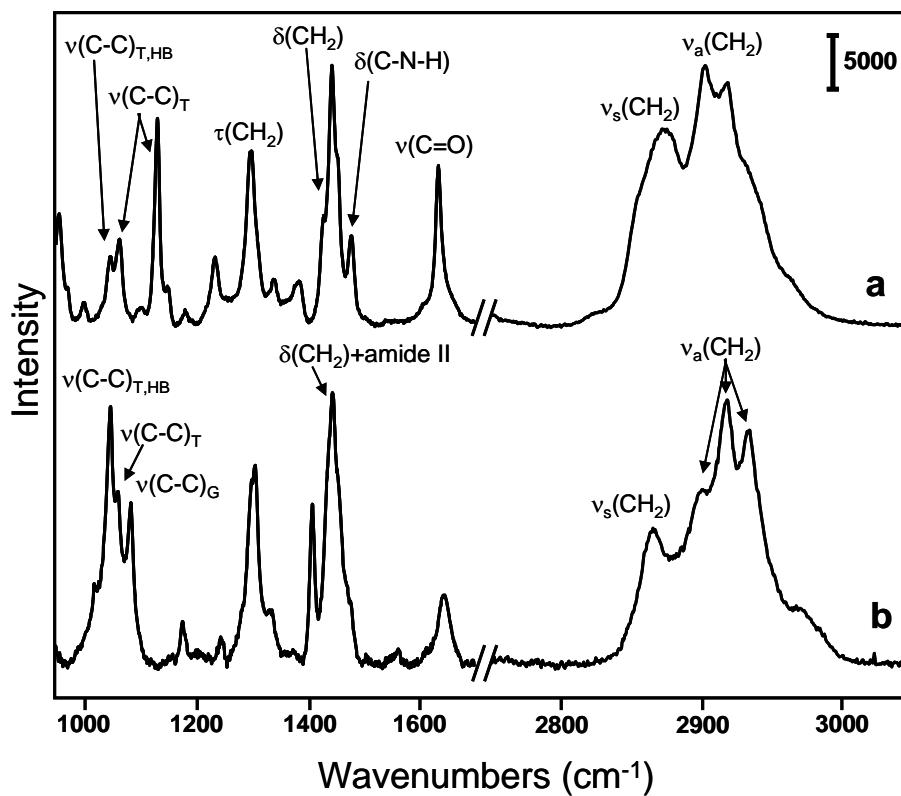
Figure 2. Raman spectra of (a) bulk Nylon 6,6 and (b) surface-tethered Nylon$_{3.0}$. Acquisition times are (a) 2 min and (b) 5 min.

The ν(C-H) region in both Nylon 6,6 spectra is comprised of a broad, complex envelop of asymmetric and symmetric methylene modes with discrete contributions from chemically distinct methylene groups α and β to the carbonyl group and α, β, and γ to the amide N-H, listed in Table 1.[32] It is important to note that for alkane containing materials, the spectral indicator I[ν_a(CH$_2$)]/I[ν_s(CH$_2$)] is used extensively as a sensitive empirical marker of rotational and conformational order.[20,25,26] However, in the case of polyamides, the complexity of the ν(CH$_2$) envelope will likely correspond to a change in the behavior and physical meaning of the I[ν_a(CH$_2$)]/I[ν_s(CH$_2$)]. Then, for the purposes of this discussion, qualitative references to spectral changes in the ν(C-H) region will be address and the more quantitative discussion of structural changes in Nylon 6,6 will be focused on the ν(C-C) and δ(C-H) spectral regions.

Table 1. Peak frequencies (cm^{-1}) and assignments for bulk Nylon 6,6 and Nylon$_{3.0}$.

Peak Frequency (cm^{-1})			Assignment[a,b,c,d]
Bulk Nylon 6,6	**Nylon$_{3.0}$ at 23°C**	**Nylon$_{3.0}$ at 90°C**	
2933sh	2930	2934sh	ν_a(CH$_2$)/α-NH, β-NH, β-CO
2919	2918	2924	ν_a(CH$_2$)/α-CO
2903	2903	2904sh	ν_a(CH$_2$)/β-CO, γ-NH
2873	2860	2865	ν_s(CH$_2$)
1635	1650	1641	ν(C=O), amide I
1480			δ(C-N-H)
1444	1444	1446	δ(CH$_2$), δ(N-H), amide II
1428	1410		δ(CH$_2$)
1298	1302	1308	τ(CH$_2$)
1131			ν(C-C)$_T$
	1082	1084sh	ν(C-C)$_G$
1063	1060	1060	ν(C-C)$_T$
1046	1042	1047	ν(C-C)$_{T,HB}$

[a]ν = stretch; δ = bend and/or scissor; τ = twist
[b]α, β, and γ are methylene positions relative to NH and CO functional groups
[c]Assignments were made from references 28-31
[d]G = gauche; T = trans; T,HB = trans/hydrogen-bonded described in text

There are a number of interesting spectral differences between surface-bound Nylon$_{3.0}$ (Figure 3a) and bulk Nylon 6,6 (Figure 2a) at ambient temperature. Nylon$_{3.0}$ has an appreciable ν(C-C)$_G$ mode (1082 cm^{-1}), indicating gauche conformers, while bulk Nylon 6,6 appears to be in the all-trans conformation. The ν(C-C)$_T$ mode at 1131 cm^{-1} is not observed in the Nylon3.0 spectrum and amide I and II modes are also much more pronounced in the bulk Nylon 6,6 spectrum. This is likely due to the fact that the amide species are so few in number for Nylon$_{3.0}$ that their intensity relative to the methylene and carbon skeletal modes is diminished when compared to the bulk. In addition, the relative intensity of the δ(C-N-H) bend observed at 1480 cm^{-1} decreases to a shoulder in Raman spectrum of the Nylon$_{3.0}$ sample. This suggests that not only are their methylene gauche conformers, but that the amide groups are primarily gauche conformers in the surface-confined Nylon. The aliphatic chains are also highly coupled, indicated by the peak frequencies of the ν_a(CH$_2$) and ν_s(CH$_2$) modes at 2918 and 2860 cm^{-1}, respectively, and the intense δ(CH$_2$) mode at 1410 cm^{-1} and ν(C-C)$_{T,HB}$ mode at 1040 cm^{-1} .[17,20]
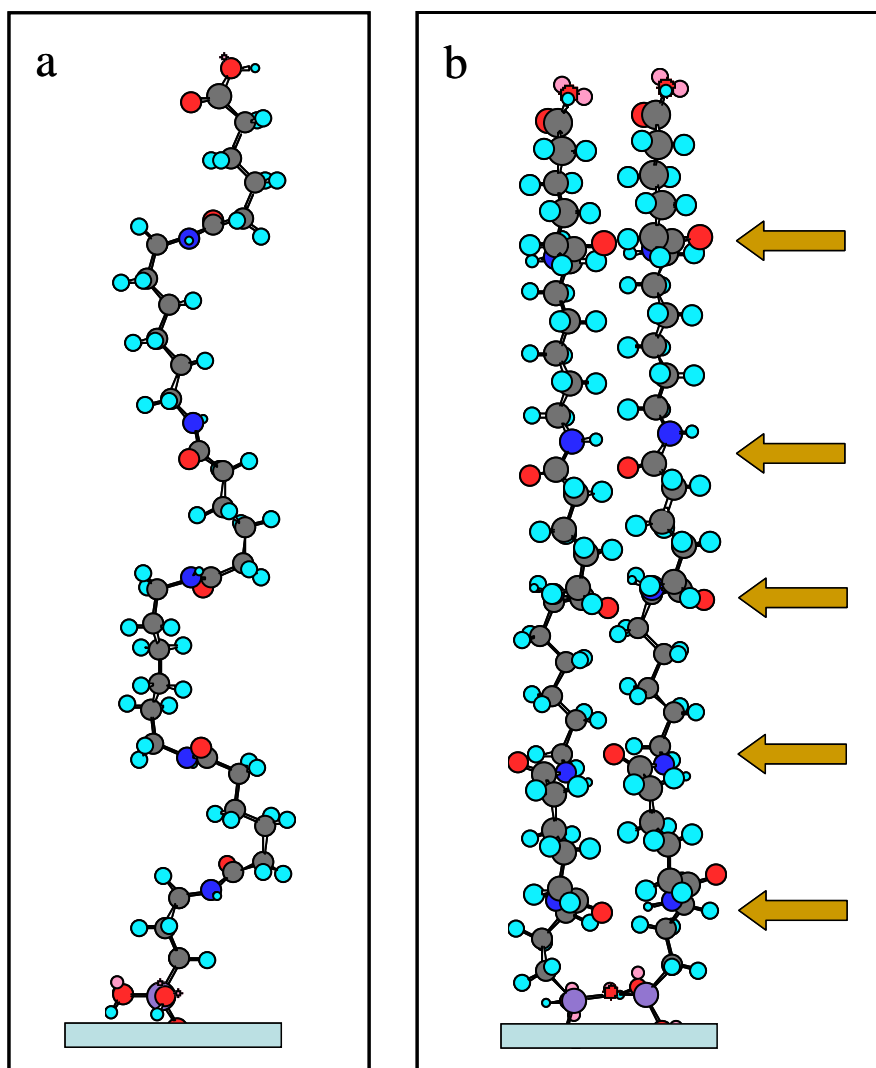
Figure 3. A molecular picture of surface-confined Nylon$_{3.0}$ at ambient temperature for (a) a single Nylon3.0 chain and (b) a 90° rotated view of adjacent Nylon$_{3.0}$ chains. Arrows highlight hydrogen-bonded amide groups. Models are energy minimized using the MM2 (Molecular Modeling 2) calculation. Structures are colored by atom: carbon atoms are pink, oxygen atoms are red, nitrogen atoms are blue, and hydrogen atoms are pale blue.

In order to determine the structure of Nylon$_{3.0}$ at ambient temperature, the surface coverage of surface-bound polyamide must be determined. Elemental analysis shows the weight percentage of carbon on Nylon$_{3.0}$ to be 13.2%, which can be used to calculate a polyamide surface coverage. The surface coverage, Γ, of polyamide on Nylon$_{3.0}$ is estimated to be 1.35 μmol/m^2; determined from the weight percentage carbon, P_c, the number of carbons, n_c, the oligomer molecular weight, MW, and the surface area of the silica substrate, S, using the following relationship:[33]

$$\Gamma(\mu mol/m^2) = \frac{10^6 P_c}{1200 n_c - P_c(MW-1)} x \frac{1}{S} \qquad (1)$$

54

For Nylon$_{3.0}$ samples, there are 33 carbon atoms, the molecular weight is 618 g/mole and the surface area of the silica substrates is 309 m^2/g. Assuming every surface silicon atom was an accessible silanol, the theoretical maximum surface coverage for a three-repeat unit Nylon 6,6 monolayer would be 2.83 μmol/m^2. Then, Nylon$_{3.0}$ coverage is estimated to be approximately half of the theoretical maximum.

These spectral data and the surface coverage of Nylon chains are used to create a molecular picture of the Nylon$_{3.0}$ thin film shown in Figure 3. In bulk α and β crystalline Nylon 6,6, aliphatic chains are off-set from one another in order to maximize hydrogen bonding interactions.[9,10] In the γ-phase of bulk Nylon 6, the amide group is twisted into a gauche conformer in order to facilitate inter-chain hydrogen-bonding, forming a pleated sheet.[17] In either case, chain-chain hydrogen-bonding interactions dictate the ultimate structure. In the surface-bound Nylon 6,6 case, chains are physically restricted from the off-set conformation observed for bulk α− and β-phases. At half the theoretical maximum surface coverage, Nylon$_{3.0}$ chains have enough free volume to accommodate gauche methylene and amide conformers in order maximize chain-chain hydrogen-bonding interactions. Introducing gauche conformers into the Nylon 6,6 structure aligns neighboring amide groups and facilitates inter-chain hydrogen bonding, analogous to the structure of γ-Nylon 6. In addition, methylene gauche conformers create bends and kinks in the aliphatic chains that enable chain-chain coupling. Other structures including helical Nylon were candidates to rationalize the gauche conformers and high degree of chain coupling, however, the 2-D footprint of these structures would be larger than the available space for this surface coverage material and it is possible for a helix to form by twisting the methylene groups without introducing gauche conformers.[17] This proposed kinked chain structure in Figure 3 is also consistent with the ellipsometry and IR spectral data acquired for similar surface-bound Nylon 6,6 materials in previous reports.[18]

Conformational Order in Surface-Bound Nylon 6,6 as a Function of Temperature
Raman spectra of Nylon 6,6-modified silica, referred to as Nylon$_{3.0}$, at 23, 60, and 90°C are shown in Figure 4. The peak frequency assignments are given in Table 1. Qualitatively there are appreciable spectral changes for Nylon$_{3.0}$ as a function of temperature. As temperature increases, the intensity of the $\nu(C-C)_{T,HB}$ and $\nu(C-C)_G$ modes decrease relative to the $\nu(C-C)_T$ mode, the $\tau(CH_2)$ peak frequency shifts to higher frequency and the intensity ratio of the $\delta(CH_2)$ mode (1410 cm^{-1}) to the $\delta(CH_2)$+amide II mode (1444 cm^{-1}) decreases. In the $\nu(C-H)$ region, the primary $\nu_a(CH_2)$ (2918 cm^{-1}) mode shift to higher frequency and the relative intensities of all $\nu_a(CH_2)$ modes (2903, 2918, and 2930 cm^{-1}) appear to decrease and become a part of a broad $\nu_a(CH_2)$ envelope at elevated temperature.
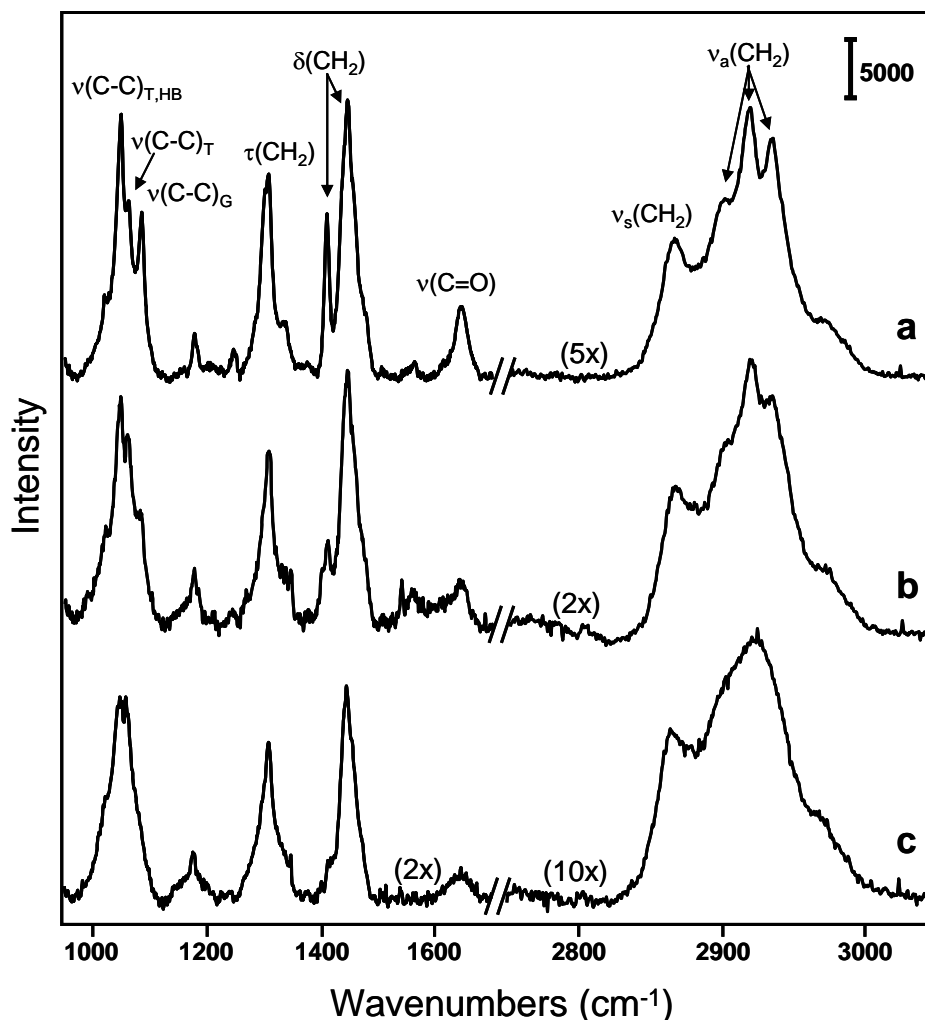
Figure 4. Raman spectra of Nylon$_{3.0}$ at (a) 23, (b) 60, and (c) 90°C. Acquisition times are 5 min for all spectra.

These temperature-dependent conformational order changes in Nylon$_{3.0}$ are highlighted in Figure 5 with plots of $I[\nu(C\text{-}C)_{T,HB}]/I[\nu(C\text{-}C)_T]$, $I[\nu(C\text{-}C)_G]/I[\nu(C\text{-}C)_T]$, $I[\delta(CH_2)]/I[\delta(CH_2)+\text{amide II}]$ verses temperature. As Nylon$_{3.0}$ undergoes a temperature-induced phase transition, chain-chain hydrogen-bonding is disrupted, shown by a decrease in $\nu(C\text{-}C)_{T,HB}$ intensity with temperature (Figure 4a) as the value of $I[\nu(C\text{-}C)_{T,HB}]/I[\nu(C\text{-}C)_T]$ decreases from ~1.5 at 0°C to ~1.05 at 90°C. This observation of thermal hydrogen-bond breaking is consistent with those made previously for bulk Nylon 6,6.[28] This also suggests that the Nylon$_{3.0}$ exhibits less α-phase character at elevated temperature. The diminishing crystalline-like nature of Nylon$_{3.0}$ with temperature is shown explicitly in Figure 5b. It is clear that the intensity of the $\delta(CH_2)$ mode decreases relative to the intensity of the $\delta(CH_2)+\text{amide II}$ mode from a value of ~0.6 to ~0.2. This is consistent with previous observations made for the solid-liquid phase transition of polyethylene, where the intensity ratio of the $\delta(CH_2)_{ORTHO}$ (1420 cm^{-1}) to the $\delta(CH_2)$ (1440 cm^{-1}) decreases during the melting transition.[20]

56
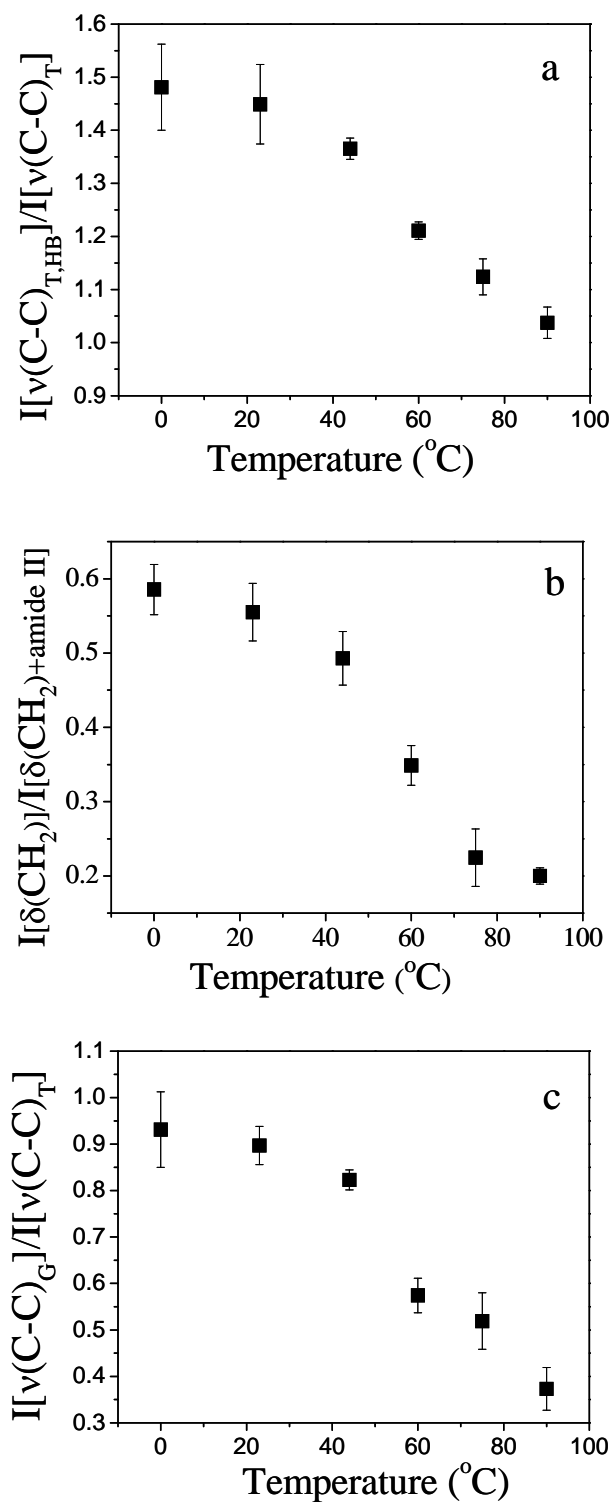
Figure 5. Plots of (a) $I[\nu(C\text{-}C)_{T,HB}]/I[\nu(C\text{-}C)_T]$, (b) $I[\delta(CH_2)]/I[\delta(CH_2)+\text{amide II}]$, and (c) $I[\nu(C\text{-}C)_G]/I[\nu(C\text{-}C)_T]$ as a function of temperature. Error bars represent one standard deviation.

Perhaps the most interesting observation in the phase transition is decrease in the relative gauche conformers with increasing temperature (Figure 4c). The value of $I[\nu(C-C)_G]/I[\nu(C-C)_T]$ decreases from ~0.95 at 0^oC to ~0.4 at 90^oC. This observations is counter intuitive because melting of bulk aliphatic materials generally results in increased numbers of gauche conformers.[19,20,34] At ambient temperature, chain-chain interactions are the dominant driving force and results in chains that are kinked and bent in order to maximize hydrogen-bonding interactions (Figure 3). During the phase transition, hydrogen-bonding is disrupted and the free volume of the material increases. In order to accommodate the free volume change and reestablish a new lowest energy conformation, the number of methylene gauche conformers decreases as Nylon chains begin to decoupled and become more upright from the surface. It is interesting to note, that there is not significant change in the $\delta(C-N-H)$ region, indicating that the amide bond remains gauche, even at high temperature. This is somewhat surprising since the methylene gauche component decreases with increasing temperature. However, their remains an appreciable amount of hydrogen-bonded aliphatic chains (indicated by the $I[\nu(C-C)_{T,HB}]/I[\nu(C-C)_T]$) and it is likely that even at high the amide gauche conformation is the most energetically favorable conformation to facilitate amide hydrogen-bonding.

Water and Saltwater Interactions with Nylon 6,6 Thin Films
In the interest of using these Nylon 6,6 thin films as experimental models for RO membranes, we have investigated how water effects the conformation and structure of these materials. Raman spectra of $Nylon_{3.0}$ dosed with 5, 10 and 100% [wt] water are shown in Figure 6. For all samples, the weight percent water is mass of deionized water per total mass of $Nylon_{3.0}$ sample. For example, $Nylon_{3.0}$ dosed with 100% water is 50 μL water added to 50 mg $Nylon_{3.0}$. In 5% water, the Raman spectrum of $Nylon_{3.0}$ is similar to that of dry $Nylon_{3.0}$ at 23^oC, with the exception of a slight decrease in the intensity of the $\nu(C-C)_{T,HB}$ mode and an increase in the relative $\nu(C-C)_G$ intensity. In 10% water, there is a significant decrease in the relative intensity of the $\nu(C-C)_{T,HB}$, $\nu(C-C)_G$, and $\delta(CH_2)$ modes compared to $Nylon_{3.0}$ in 5% water, while the $\nu(C-H)$ region remains relatively unchanged. In 100% water, the water saturated case, $\nu(C-C)_{T,HB}$, $\nu(C-C)_G$, and $\delta(CH_2)$ modes all decrease in intensity and the $\nu_a(CH_2)$ modes decrease in intensity and become a part of the broad $\nu_a(CH_2)$ envelope. Spectroscopically, the effect of increasing hydration appears to be very similar to the effect of increasing temperature on the structure and conformational order of $Nylon_{3.0}$.
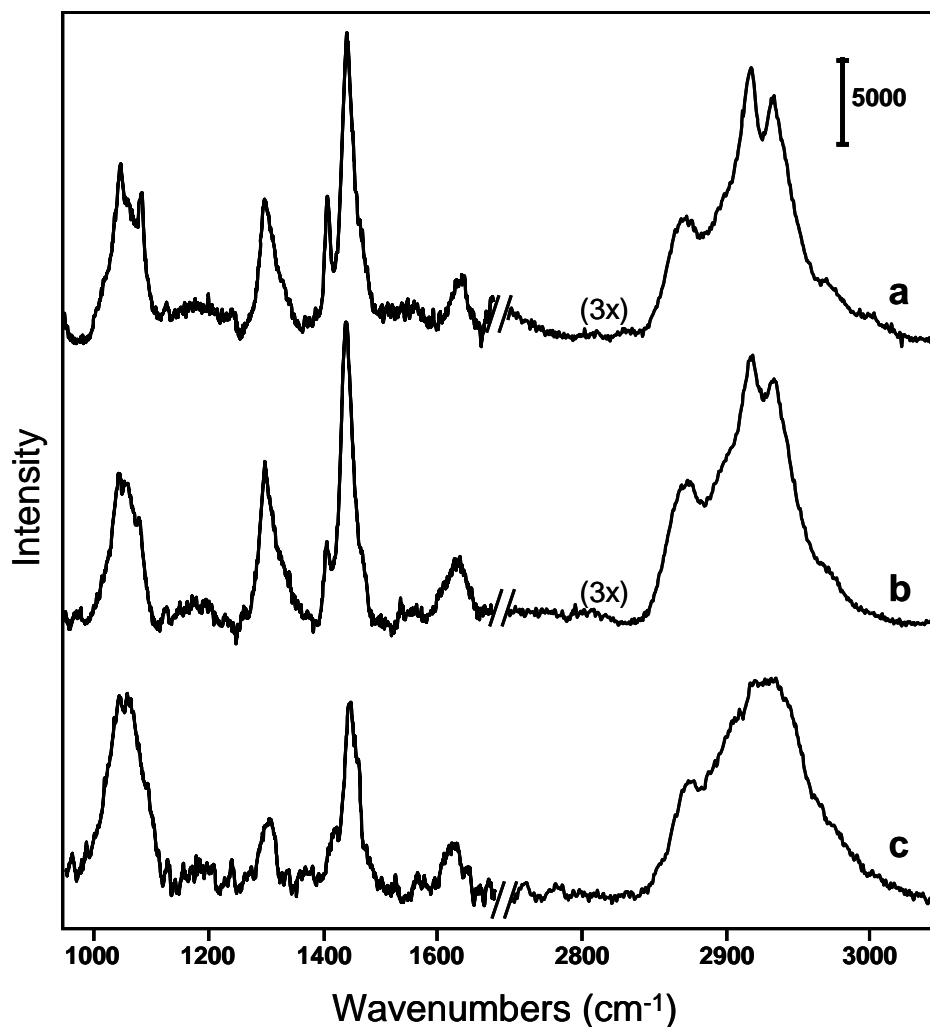
Figure 6. Raman spectra of Nylon$_{3.0}$ dosed with (a) 0, (b) 5, (c) 10 and (d) 100% [wt] water. Acquisition times are 5 min for all spectra.

At the onset of water interactions with Nylon$_{3.0}$, there is an immediate competition between hydrating forces and intermolecular Nylon chain hydrogen-bonding interactions. For Nylon$_{3.0}$ undergoing a transition from the dry to the 5% water state, there is an appreciable decrease in the I[ν(C-C)$_{T,HB}$]/I[ν(C-C)$_T$] ratio shown in Figure 7a. This is attributed to hydrating water molecules disrupting intermolecular hydrogen-bonding. In addition, the relative number of gauche conformers increases slightly in 5% water compared to the dry Nylon$_{3.0}$ sample. This is distinctly different than the temperature-induced phase transition behavior, which only shows a systematic decrease in numbers of gauche conformers (Figure 5c). Then, the hydration mechanism and water-polymer interactions are unique for these materials. It is likely that initial hydration or solvation with a small fraction of water occurs at the distal end of the Nylon 6,6 chains by breaking terminal chain-chain hydrogen-bonds, as observed for the solvation of alkylsilane thin films.[26,35] Then, it is reasonable to expect an increase in end-gauche conformers or other rotational disorder if hydration is localized to the distal terminal groups and not homogeneous down the length of the aliphatic chains.[36] As the amount of water increases to 10 and 100%, there is a significant decrease in chain-chain hydrogen bonding (Figure 7a).

However, just as observed with increasing temperature the relative number of gauche conformers decreases for Nylon$_{3,0}$ in 100% water. As the Nylon chains become fully hydrated it becomes more energetically favorable for water molecules to occupy the free volume between the chains and hydrogen-bond to amine and carbonyl groups. Then, as the free volume is filled with water molecules the number of gauche conformers decreases to allow for Nylon chains to spread out, become hydrated, and take on a new equilibrium conformation.
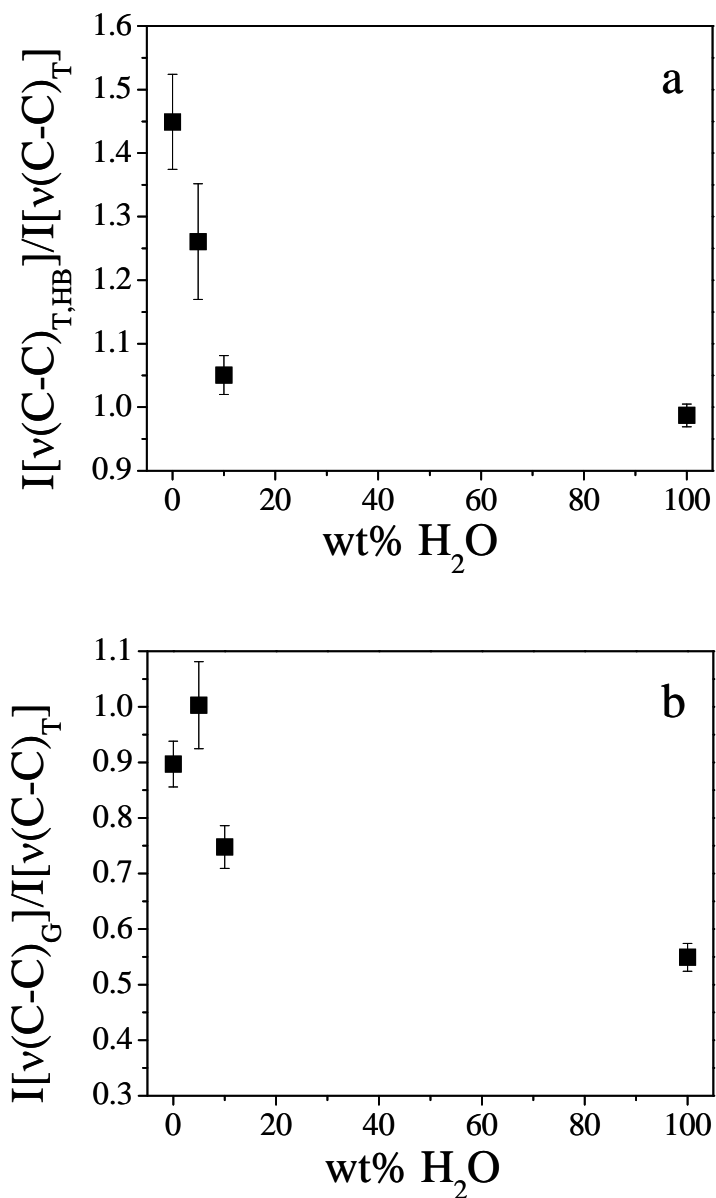
Figure 7. Plot of (a) I[ν(C-C)$_{T,HB}$]/I[ν(C-C)$_T$] and (b) I[ν(C-C)$_G$]/I[ν(C-C)$_T$] as a function of wt% water. Error bars represent one standard deviation.

The effects of hydration of the conformational order of this model Nylon 6,6 film are significant. These results suggest that for water-based applications, such as RO separation systems, understanding water-polymer interactions are critical. In addition, detailed investigations of the structure-function relationships of these materials should be carried out using the hydrated thin film model, since the native polymer thin film structure would be an inappropriate control for water-based applications. With this information, we can begin to investigate the interfacial interactions of more complex solutions containing dissolved species (e.g. salts, minerals, and known fouling materials) by studying changes to the hydrated Nylon structure.

Our initial studies on more complex RO interfaces are focused on desalination systems by investigating Nylon$_{3.0}$ structure in aqueous NaCl solutions. The Raman spectra of Nylon$_{3.0}$ in 10^{-4} M and 1 M NaCl is shown in Figure 8. It is clear that the Raman spectra are independent of salt concentration over this range and are identical to that for Nylon$_{3.0}$ saturated with water (Figure 7c). Then, the presence of NaCl, even at 1 M, has no observable effect on the structure of Nylon$_{3.0}$. While this is only a limited data set, these data suggest that either; (1) salt is excluded from the Nylon/salt solution interface and only water interacts with the Nylon chains or (2) there is enough free volume between the Nylon chains in the water saturated case to accommodate hydrated ions within Nylon chains without disrupting their hydrated structure. There is sufficient evidence to support the salt exclusion scenario from bulk polyamide RO membrane literature.[37-40] Moreover, using the Nylon surface coverage (1.35 μmol/m^2), a Nylon:salt mole ratio is estimated to be 1000 in 10^{-4} M NaCl and 0.1 in 1 M NaCl, respectively. Then, if hydrated ions do interact with the Nylon chains, one might expect the Nylon structure to change over the four orders of magnitude change in Nylon:salt ratio. No observed structural change with salt concentration could be additional support for the salt excluded case from the Nylon 6,6 thin film. However, given that the surface coverage of Nylon$_{3.0}$ is approximately half of the theoretical maximum ($\Gamma_{max} = 2.83$ μmol/m^2), there is potentially sufficient free volume to accommodate hydrated ions in the film and that possibility cannot be overlooked. Experiments to vary the Nylon surface coverage and studying interactions with different sized ion pairs and multivalent ions are currently in progress in order to gain additional insight into the mechanism of saltwater-polymer interactions in RO systems. However, these preliminary results provide a unique insight into the complex fundamental interfacial interactions of RO systems and further demonstrate the sensitivity of Raman spectroscopy to subtle changes in organic thin film conformational order.

61
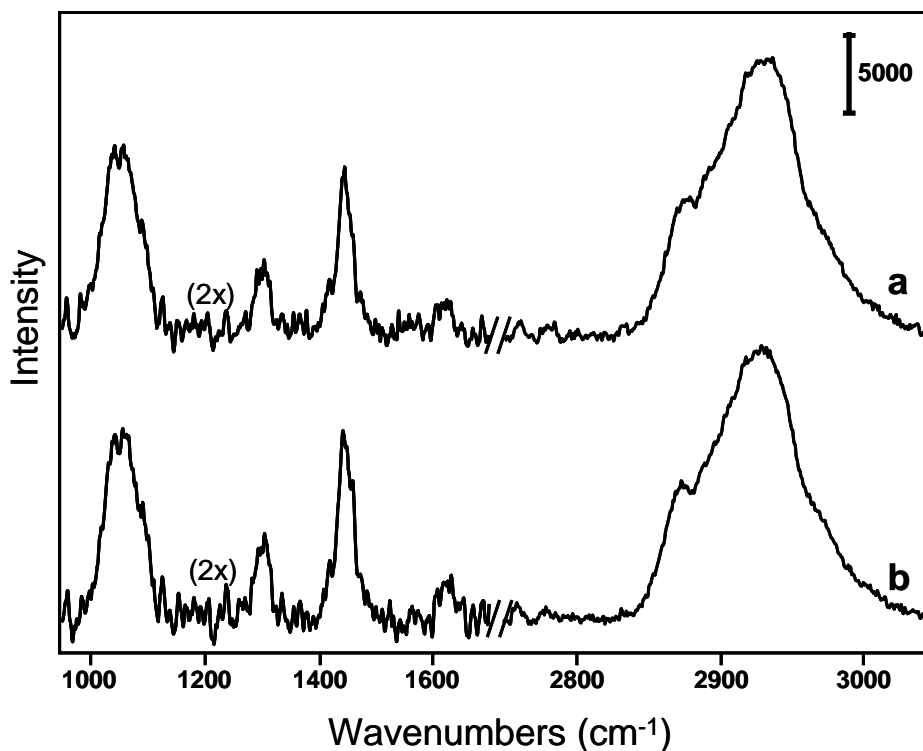
Figure 8. Raman spectra of Nylon$_{3.0}$ in aqueous (a) 10^{-4} M and (b) 1 M NaCl. Acquisition times are 5 min for all spectra.

Conclusions

The structure of model Nylon 6,6 thin films is studied by Raman spectroscopy in an effort to elucidate the mechanisms that govern separations in RO systems. Raman spectral data are used to create molecular pictures of the surface-bond Nylon 6,6 films. The structure in bulk and surface-tethered Nylon 6,6 are both dominated by chain-chain hydrogen-bonding interactions, but the degrees of freedom available to accommodate hydrogen-bonding are restricted in the surface case. For bulk α– and β–phase Nylon 6,6, aliphatic all-trans chains are off-set in order to align amide groups of neighboring chains. In the surface-tethered case, Nylon chains adopt a bent and kinked structure in order to maximize interactions with neighboring chains (Figure 3). Gauche methylene and amide conformers along the length of the chain facilitate alignment of adjacent amide groups and hydrogen-bonding for a high degree of chain coupling. Increasing temperature, as observed in the Raman spectral data, disrupts intermolecular hydrogen-bonding and weakens chain coupling interactions. This new minimum energy conformation for Nylon$_{3.0}$ is established at higher temperature. A molecular picture of a possible chain conformation of Nylon$_{3.0}$ at 90°C is shown in Figure 9, where there are fewer amide hydrogen-bonds and gauche defects, but the amide groups maintaining a gauche conformation and aliphatic chains spread apart as the free volume of the system increases.
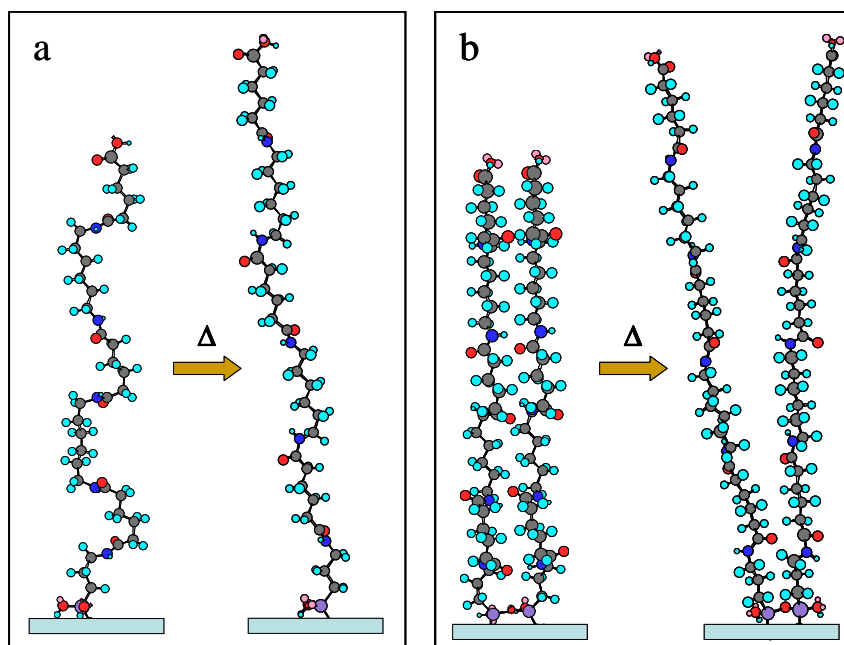
Figure 9. A molecular picture of Nylon$_{3.0}$ at 23 and 90°C for (a) a single Nylon3.0 chain and (b) a 90° rotated view of adjacent Nylon$_{3.0}$ chains. Models are energy minimized using the MM2 (Molecular Modeling 2) calculation. Structures are colored by atom: carbon atoms are pink, oxygen atoms are red, nitrogen atoms are blue, and hydrogen atoms are pale blue.

These Raman data also suggest that hydration of these thin films begins at the distal end of the aliphatic chains and complete film hydration causes similar conformational changes to the chains as increasing temperature. In addition, these conformational changes for hydrate Nylon thin films does not appear to have any dependence on salt concentration from 10^{-4} to 1 M NaCl. This is evidence that either salt is excluded from these model thin films, as in RO membrane systems, or the that there is enough free volume in these films to accommodate hydrated ions over a wide range of concentrations without inducing conformational changes to the polymer chains.

References

1. Hawkridge, A. M.; Gardella, J. A.; Toselli, M. Macromolecules 2002, 35, 6533.

2. Kim, H. I.; Kushmerick, J. G.; Houston, J. E.; Bunker, B. C. Langmuir 2003, 19, 9271.

3. Yan, H.; Lee, P.; Armstrong, N. R.; Graham, A.; Evmenendo, G. A.; Dutta, P.; Marks, T. J. J. Am. Chem. Soc. 2005, 127, 3172.

4. Malinsky, J. E.; Veinot, J. G. C.; Jabbour, G. E.; Shaheen, S. E.; Anderson, J. D.; Lee, P.; Richter, A. G.; Burin, A. L.; Ratner, M. A.; Marks, T. J.; Armstrong, N. R.; Kippelen, B.; Dutta, P.; Peyghambarian, N. Chem. Mater. 2002, 14, 3054.

5. Peng, W.; Escobar, I. C.; White, D. B. J. Membrane Sci. 2004, 238, 33.

6. Riedl, K.; Girard, B.; Lencki, R. W. J. Membrane Sci. 1998, 139, 155.

7. Childress, A. E.; Elimelech, M. J. Membrane Sci. 1996, 119, 253.

8. Knoell, T.; Safarik, J.; Cormack, T.; Riley, R.; Lin, S. W.; Ridgway, H. J. Membrane Sci. 1999, 157, 117.

9. Fuller, C. S.; Baker, W. O.; Pape, N .R. J. Am. Chem. Soc. 1940, 62, 3275.

10. Brill, R. *J. Prakt. Chem.* **1942**, *161*, 49.

11. Bunn, C. W.; Garner, E. V. *Proc. Royal Soc.* **1947**, *189*, 39.

12. Starkweather, H. W.; Whitney, J. F.; Johnson, D. R. *J. Polym. Sci.* **1963**, *1*, 715.

13. Starkweather, H. W.; Jones, G. A. *J. Polym. Sci.* **1981**, *19*, 467.

14. Jones, N. A.; Cooper, S. J.; Atkins, E. D. T.; Hill, M. J.; Franko, L. *J. Polym. Sci.* **1997**, 675.

15. Miyake, A. *J. Polym. Sci.* **1960**, *44*, 223.

16. Song, K.; Rabolt, J. F. *Macromolecules* **2001**, *34*, 1650.

17. Stephens, J .S.; Chase, D. B.; Rabolt, J. F. *Macromolecules* **2004**, *37*, 877.

18. Orendorff, C. J.; Alam, T. M.; Frankamp, B. L.; Clawson, J.; Holland, G. P.; Huber, D. L.; Bunker, B. C. *Langmuir* submitted

19. MacPhail, R. A.; Snyder, R. G.; Strauss, H. L. *J. Chem. Phys.* **1982**, *77*, 1118.

20. Orendorff, C. J**.**, Ducey, M. W., and Pemberton, J. E. *J. Phys. Chem. A*. **2002**, 106, 6991.

21. Gaber, B. P.; Peticolas, W. L. *Biochim. Biophys. Acta* **1977**, *465*, 260.

22. Larsson, K.; Rand, R. P. *Biochim. Biophys. Acta* **1973**, *326*, 245.

23. Thompson, W. R.; Pemberton, J. E. *Anal. Chem.* **1994**, *66*, 3362.

24. Ho, M.; Cai, M.; Pemberton, J. E. *Anal. Chem.* **1997**, *69*, 2613.

25. Ducey, M. W.; Orendorff, C. J.; Sander, L. C.; Pemberton, J. E. *Anal. Chem.* **2002**, 74, 5576.

26. Ducey, M. W.; Orendorff, C. J.; Sander, L. C.; Pemberton, J. E. *Anal. Chem.*. **2002**, 74, 5585.

27. Orendorff, C. J.; Pemberton, J. E. *Anal. Chem.* **2005**, 77, 6069.

28. Stuart, B. H. *Polym. Bull.* **1994**, *33*, 681.

29. Maddams, W. F.; Royaud, I. A. M. *Spectrochim. Acta* **1991**, *47A*, 1327.

30. Ding, Y.; Rabolt, J. F.; Chen, Y.; Olson, K. L.; Baker, G. L. *Macromolecules* **2002**, *35*, 3914.

31. Miyazawa, T. *J. Mol. Spectrosc.* **1960**, *4*, 155-167.

32. Zimba, C. G.; Rabolt, J. F.; English, A. D. *Macromolecules* **1989**, *22*, 2867.

33. Sander, L. C.; Wise, S. A. *Anal. Chem.* **1984**, *56*, 504.

34. Snyder, R. G. *J. Phys. Chem.* **1989**, *93*, 7520.

35. Orendorff, C. J.; Ducey, M. W.; Pemberton, J. E.; Sander, L. C. *Anal. Chem.* **2003**, *75*, 3360.

36. Pemberton, J. E.; Ho, M.; Orendorff, C. J.; Ducey, M. W. *J. Chromatogr. A* **2001**, *913*, 943.

37. Lora, J.; Soriano, E. *Desalination* **1987**, *64*, 375.

38. Khan, W. Z.; Hamad, E. Z. *Desalination* **1996**, *105*, 191.

39. Rao, A. P.; Desai, N. V.; Rangarajan, R. *J. Membrane Sci.* **1997**, *124*, 263.

40. Khedr, M. G. *Desalination* **2003**, *153*, 295.

Lubrication Theory of Drag on a Scanning Probe in Structured Water, Near a Hydrophilic Surface

Abstract

The drag is evaluated, in lubrication theory, on a parabolic-cylindrical tip moving parallel to a flat sample, in water, close enough that its and the sample's presumed, nm-thick structured-water, "interphase" coatings overlap. Assuming coatings of width, w, and of viscosity, η much larger than bulk water's, the friction force is predicted to equal $-2\pi\eta cR\ \Phi(D/2w)$, where R is the tip's radius of curvature, c is its speed, D is the tip-sample separation, and Φ is a universal function whose value only differs noticeably from $\ln(2w/D)$ for $D < w$.

Introduction

Measurements of the resistance to water drainage, when a hydrophilically functionalized Au probe tip closely approaches a similarly prepared flat sample, have been interpreted to imply that highly viscous "interphase" layers, roughly 2 nm thick, coat the surfaces of both.[1,2] This interpretation was, however, based on several assumptions not subjected to independent verification:

1) Reference 1's remarkably smooth (i.e., non-oscillatory) force vs. separation curves[3] mean that interphase water can be treated as an isotropic continuum, despite being only a few molecular layers thick, and bound to a hydrophilic surface.
2) Surface roughness of the tip and the sample can be ignored.
3) The boundary between the interphase water and the bulk liquid can be treated as spatially sharp, and flat.
3) The details of the OH-terminated tri(ethylene glycol) undecylthiol [or "EG3OH"] hydrophilic SAMs on the Au surfaces can be ignored, apart from their elastic compliance.[1]

Given these drastic assumptions, one might be inclined to dismiss as mere "curve-fitting" the apparently excellent account that the Navier-Stokes equations in the "lubrication approximation"[2] give of Reference 1's Interfacial Force Microscope[4] data. Reinforcing such skepticism, the value of interphase viscosity that emerged from the data fit is roughly 7×10^7 that of ordinary bulk water,[2] i.e., extremely large.

It is appealing to think that water drainage can be understood in terms of a small set of physically meaningful parameters, despite the array of possible complications. To support such a notion, it would help to show that the hydrodynamic picture is applicable not just to drainage data, but more broadly. I have therefore derived numerical results for the hydration force in the same tip-water-sample arrangement as in the IFM drainage experiment, but now assuming a tip moving parallel to the sample, instead of approaching or receding from it.[5,6]

Of primary interest, the drag forces opposing tip motion parallel and perpendicular to the sample are predicted to depend very differently on physical parameters. Approaching the sample at speed c, the tip should experience drag force, $F_\perp = -6\pi\eta cR^2/D\ (1 - D/2w)^2$ at tip-sample distance,

D, where η and w are the interphase viscosity and width, and R is the tip radius.[2] For motion along the sample, the derivation presented here predicts $F_{//} = -2\pi\eta cR \; \Phi(D/2w)$ instead, where $\Phi(D/2w)$ is the scale-free function shown in Figure 1. Thus, $F_{//}$ depends *linearly* on R and vanishes *linearly* when $D \rightarrow 2w$, while $F_\perp$ is proportional to R^2 and vanishes quadratically as D approaches $2w$. At a minimum, these dependences must be manifest experimentally, for the hydrodynamic theory to be viable.
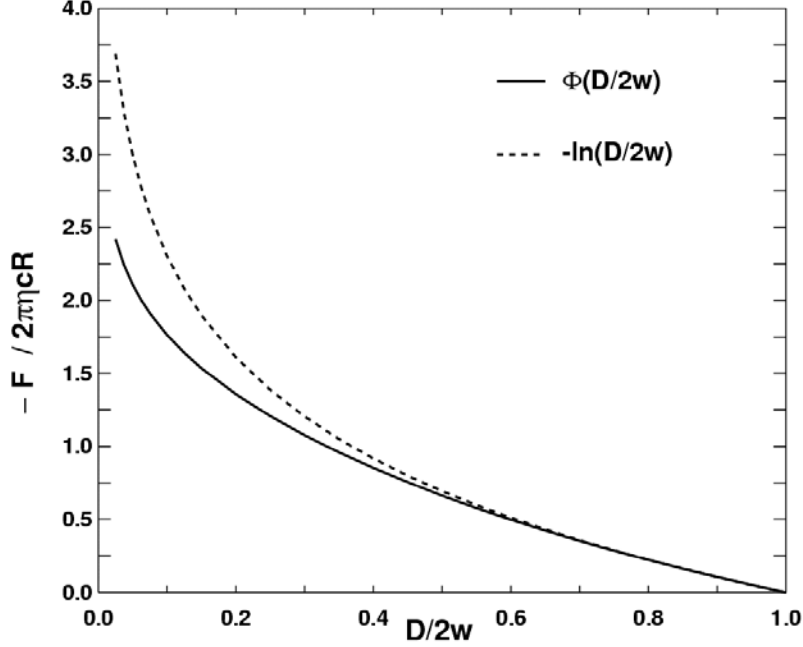
Figure 1. Drag force $F_{||}$ vs. tip-sample separation, for tip motion along the surface. The exact ratio, $-F_{||} / 2\pi\eta cR$ is well approximated by $\ln(D/2w)$ when tip and sample interphases barely overlap.

Lubrication approximation

The "modified Reynolds equation" developed by Tichy[7] to deal with lubrication when asperities on opposing, functionalized surfaces produce a spatially-varying fluid viscosity, embodies the basic approximations needed to evaluate interphase drag on a tip moving along a sample. One starts from Reynolds' "lubrication approximation," wherein:[8,9] (1) fluid velocities are small enough that, in the Navier-Stokes equations, terms quadratic in velocities can be dropped, (2) the fluid velocity normal to the sample (henceforth, the z direction) is small compared to the velocity parallel to it, (3) the variation of the velocity parallel to the plane surface is weak compared to that along z, and (4) the pressure gradient along z is negligible.

In addition, the radius of curvature of the tip surface, R, is assumed large compared to the distance, D, between it and the planar sample (see Figure 2) and the viscosity is presumed to be a function only of the distance from either surface. Also, the fluid flow is assumed to be steady-state, i.e., all velocities are constant in time.
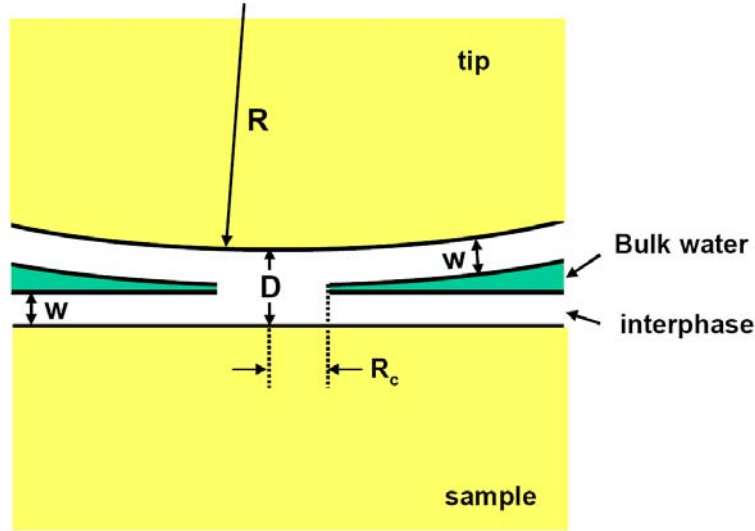
Figure 2. A tip of curvature radius R whose apex lies a distance D above a sample. By assumption, the intervening space contains a highly viscous, structured-water "interphase" of width, w, coating each surface, and bulk water elsewhere. Viscous drag is generated within a radius $R_c = [2R(2w\text{-}D)]^{1/2}$ of the tip axis, where the fluid is highly viscous all the way from tip to sample.

It is worth appreciating that the basic ideas of lubrication theory, which underlie Tichy's and the present model, have a long history—indeed, they are the stuff of introductory textbooks.[10] What is new is the spatial dependence of the viscosity at the nm scale, representing physical situations not considered earlier.[11]

Hydrodynamic Friction Formula

For comparison with the drainage force derived in earlier work,[2] I assume a tip and sample of the same material, each coated, in water, with a highly viscous interphase layer of width w and viscosity η. For simplicity, I confine attention to the limit of zero viscosity in the bulk water outside the interphase coatings.

As in the drainage problem, I seek solutions to the Navier-Stokes equations that satisfy "stick" boundary conditions at the sample and tip. Thus, fluid velocity components $v_x = v_y = v_z = 0$ at $z = 0$, the sample surface.

The tip is assumed to be a parabolic cylinder, of curvature radius, R, moving in the x-direction at constant speed c, with its apex at height D above the surface (cf. Figure 1). Given the assumption of zero bulk water viscosity, there is no drag unless $D < 2w$.

At the tip surface, defined by,

$$z \;=\; h(x - ct, y) \;=\; D \;+\; [(x - ct)^2 \;+\; y^2]\,/\,2R \tag{1}$$

the stick boundary condition requires $v_x = c$, $v_y = 0$, and, assuming that $\partial h / \partial x \ll 1$ over the x-range of interest, $v_z = \partial h/\partial t + c\, \partial h/\partial x$. The conditions on v_x and v_y ensure that the fluid moves at the tip's velocity at the tip-water interface. The condition on v_z means the fluid speed normal to the tip vanishes there.

The momentum equation for fluid flow, whether the curved tip moves parallel or normal to the planar surface, is,[9]

$$\frac{\partial}{\partial z}\left(\eta(z)\frac{\partial}{\partial z}\right)v_i = \frac{\partial P}{\partial r_i} \tag{2}$$

where $\eta(z)$ is the spatially varying viscosity, v_i is velocity component in the $i(= x$ or $y)$ direction, and $P(x,y)$ is the pressure. Integrating Equation (2) and enforcing the $z = 0$ boundary conditions, one obtains,

$$v_i(z) = \int_0^z dz'(z'-C_i)/\eta(z')\frac{\partial P}{\partial r_i} \tag{3}$$

where tip-surface boundary conditions determine the integration constants, C_i. Defining the auxiliary functions,[7]

$$f^{(n)}(z) \equiv \int_0^z dz'z'^n / \eta(z') \tag{4}$$

Equation (3) can be rewritten as

$$v_i(z) = [f^{(1)}(z) - C_i f^{(0)}(z)]\frac{\partial P}{\partial r_i} \tag{5}$$

Thus, the boundary condition, $v_y(h) = 0$, trivially requires,

$$C_y = f^{(1)}(h)/f^{(0)}(h) \tag{6}$$

or,

$$v_y(z) = [f^{(1)}(z) - f^{(1)}(h)\, f^{(0)}(z)/f^{(0)}(h)]\frac{\partial P}{\partial y} \tag{7}$$

The result for $v_x(z)$,

$$v_x(z) = c\, f^{(0)}(z)/f^{(0)}(h) + [f^{(1)}(z) - f^{(1)}(h)\, f^{(0)}(z)/f^{(0)}(h)]\frac{\partial P}{\partial x} \tag{8}$$

has an extra term because the tip motion is in the x-direction.

To take advantage of the boundary conditions on v_z, namely that it vanishes at $z = 0$ and $z = h$, one now integrates the continuity equation,

$$\frac{\partial v_z}{\partial z} = -\frac{\partial v_x}{\partial x} - \frac{\partial v_y}{\partial y} \tag{9}$$

obtaining,

$$\int_0^h dz \left[\frac{\partial v_x}{\partial x} + \frac{\partial v_y}{\partial y} \right] = 0 \tag{10}$$

In evaluating the derivatives in the square bracket, one needs to remember that h, which defines the tip surface, is the function of x and y,

$$h(x, y) = D + (x^2 + y^2)/2R \tag{11}$$

Consider the y-direction term of Equation (10) first. It can be evaluated using the identity,

$$\int_0^h dz \frac{\partial v_y}{\partial y} \equiv \frac{\partial}{\partial y} \int_0^h dz v_y - \frac{\partial h}{\partial y} v_y(z = h) \tag{12}$$

The last term of Equation (12) vanishes because of the stick boundary condition $v_y(h) = 0$. The first term on the right-hand side of Equation (12) can be evaluated by substituting from Equation (7). With the definition,

$$g(x, y) \equiv \int_0^h dz[f^{(1)}(z) - f^{(1)}(h) f^{(0)}(z)/f^{(0)}(h)] \tag{13}$$

one finds,

$$\int_0^h dz \frac{\partial v_y}{\partial y} = \frac{\partial}{\partial y} \left(g \frac{\partial P}{\partial y} \right) \tag{14}$$

The x term is once again slightly more complicated, because the tip motion is in the x-direction. Analogously to Equation (12).

$$\int_0^h dz \frac{\partial v_x}{\partial x} \equiv \frac{\partial}{\partial x} \int_0^h dz v_x - \frac{\partial h}{\partial x} v_x(z = h) \tag{15}$$

71

But now, $v_x(h) = c$, not zero, and $\partial h / \partial x = x/R$. Substituting these results and Equations (8) and (13) into Equation (15), one learns that,

$$\int_0^h dz\, \frac{\partial v_x}{\partial x} = -c\,\frac{\partial F}{\partial x} + \frac{\partial}{\partial x}\left(g\,\frac{\partial P}{\partial x}\right) \tag{16}$$

where $F(x,y)$ is defined by,

$$F(x,\, y) \equiv h - \int_0^h dz\, \frac{f^{(0)}(z)}{f^{(0)}(h)} \tag{17}$$

A partial differential equation for the pressure now follows, substituting Equations (14) and (16) into the integrated continuity Equation (10). That yields,

$$\vec{\nabla}_\parallel \cdot \left(g\vec{\nabla}_\parallel P\right) = c\,\frac{\partial F}{\partial x} \tag{18}$$

Use of Symmetry

To simplify Equation (18), I now introduce the assumption that the tip and sample surfaces are identical. Implicitly, that means the viscosity z is symmetrical about $z = h/2$, and thus,

$$2f^{(1)}(h) - hf^{(0)}(h) \equiv \int_0^h dz'(2z' - h)\frac{1}{\eta(z')} = 0 \tag{19}$$

Equation (19) allows $F(x,y)$ of Equation (17) to be evaluated explicitly, and independently of the z-dependence of $\eta(z)$. To see this, note the identity,

$$\int_0^h dz f^{(0)}(z) \equiv \int_0^h dz'(h - z')\frac{1}{\eta(z')} \equiv hf^{(0)}(h) - f^{(1)}(h) \tag{20}$$

which follows from Equation (4), after an interchange of integration variables. Combining Equations (19) and (20),

$$\int_0^h dz f^{(0)}(z) = \frac{h}{2}\, f^{(0)}(h) \tag{21}$$

Thus,

$$F(x,\, y) = h\,/\,2 \tag{22}$$

So, taking note of Equation (11) for h, the pressure equation simplifies to,

$$\vec{\nabla}_{\parallel} \cdot \left(2g\vec{\nabla}_{\parallel}P\right) = cx / R \tag{23}$$

where, by the assumption that $h = h(x^2 + y^2)$ and Equation (13), g is also just a function of x^2+y^2.

Solution of Equation (23)

An *ansatz* formal solution to the inhomogeneous Equation (23), consistent with the requirement of finite pressure at $x = y = 0$, is to write $P(x,y) = xQ(r)$, where $r \equiv (x^2 + y^2)^{1/2}$. Substituting this factorization into Equation (23) and evaluating derivatives explicitly, one arrives at an ordinary, inhomogeneous differential equation for $Q(r)$,

$$g\,\frac{d^2Q}{dr^2} + \left(\frac{3g}{r} + \frac{dg}{dr}\right)\frac{dQ}{dr} + \frac{1}{r}\frac{dg}{dr}Q = c / 2R \tag{24}$$

To proceed, it is necessary to specify the z-dependence of the viscosity, from which the form of $g(r)$ follows.

For the sake of comparison to the drainage problem of Reference 2, I consider the same model as there, in which the viscosity within a distance w of the sample and tip surfaces is spatially constant and much larger than the viscosity of bulk water, and is negligible otherwise. This means the friction force resisting the tip's motion parallel to the sample surface is entirely generated in the cylindrical region,

$$r^2 \le R_c^2 \equiv 2R(2w - D) \tag{25}$$

wherein the fluid lies within w of *both* tip and sample surfaces (cf. Figure 2). Because the model implies that $g(r > R_c)$ is essentially infinite, it follows that $Q(r > R_c) = 0$.

The assumption of constant viscosity η for $r < R_c$ yields the explicit result,

$$f^{(n)}(z) = \frac{z^n}{(n + 1)}\frac{1}{\eta} \tag{26}$$

from which it follows that

$$g(r) = -\frac{h(r)^3}{12\eta} \tag{27}$$

Substituting Equation (27) into Equation (24) produces an explicit differential equation for the fluid pressure under the tip, namely,

$$\frac{d^2Q}{dr^2} + 3\left[\frac{1}{r} + \frac{r}{h(r)R}\right]\frac{dQ}{dr} + \frac{3}{h(r)R}Q = -\frac{6\eta c}{h(r)^3 R} \tag{28}$$

Equation (28) can be rendered scale free by defining,

73

$$\rho \equiv \frac{r}{\sqrt{2RD}} \tag{29}$$

and,

$$Q(r) \equiv \frac{12c\eta}{D^2} S(\rho) \tag{30}$$

Thus, one needs to solve,

$$(1 + \rho^2)\frac{d^2S}{d\rho^2} + \frac{3}{\rho}(1 + 3\rho^2)\frac{dS}{d\rho} + 6S = -\frac{1}{(1 + \rho^2)^2} \tag{31}$$

to evaluate the fluid pressure and the frictional force resisting tip motion.

Near the origin, $\rho = 0$, Equation (31) reduces to,

$$\frac{d^2S}{d\rho^2} + \frac{3}{\rho}\frac{dS}{d\rho} + 6S = -1 \tag{32}$$

Substituting the trial solution, $S = const. \times \rho^P$, into Equation (32) implies that p equals either -2 or 0. The choice, $p = -2$ is impermissible, because the pressure must be finite at the origin. Thus, S can be expanded in the form $a + b\rho^2 + c\rho^4 + ...$, near $\rho=0$.

At $\rho = \rho_c \equiv (2w / D - 1)^{1/2}$, the excess pressure exerted by the tip vanishes. This is the second boundary condition needed to solve Equation (31). Note that Equation (31) itself is free of *any* physical parameter. Thus the boundary condition at ρ_c is the *only* way that physics affects the form of $S(\rho)$.

Equation (31) can be solved in several ways. For $\rho_c < 1$, both sides can be expanded in powers of ρ^2, yielding a trivially soluble two-term, inhomogeneous recursion relation. One can also discretize ρ and integrate outward from $S(0) = const.$ and $dS/d\rho = 0$ at $\rho = 0$, adding solutions of the homogeneous and inhomogeneous equations to obtain a function that correctly vanishes at a given ρ_c. In the present work, I used Mathematica[12] to accomplish this. The resulting $\rho S(\rho)$, which embodies the radial dependence of the tip-induced pressure, is shown in Figure 3.
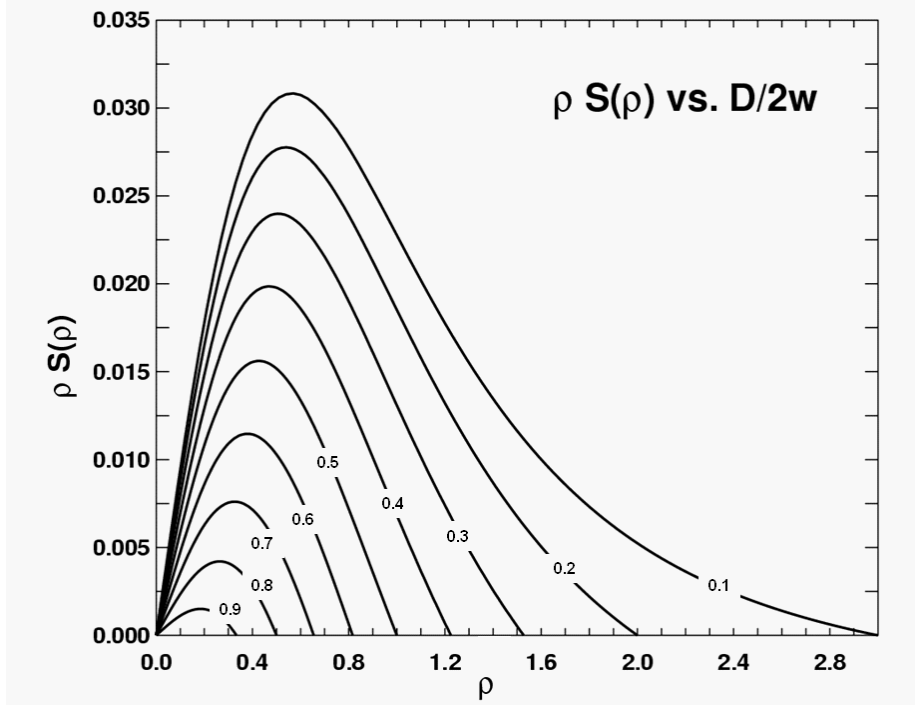
Figure 3. The radial variation of pressure, $\rho S(\rho)$, versus scaled radial coordinate ρ and labeled values of $D/2w$. Note that the scaled cutoff radius, $\rho_c = (2w/D - 1)^{1/2}$, beyond which the tip and sample interphases do not overlap grows from 1/3 to 3 as the tip is pushed in from $D/2w = 0.9$ to 0.1. Because the tip-induced pressure is proportional to $\rho S(\rho)\cos\phi$, where azimuth $\phi = 0$ corresponds to the direction of tip motion, the pressure is negative behind the tip and positive in front of it.

Evaluation of the Force on the Moving Tip

The force resisting the motion of the tip is the integral of the shear stress at the tip surface,

$$F_{\parallel} = -\eta \int_0^{R_c} r\,dr \int_0^{2\pi} d\phi \, \left.\frac{dv_x}{dz}\right|_{z=h} \tag{33}$$

Using Equations (8) and (26), one obtains the integrand as,

$$\left.\frac{dv_x}{dz}\right|_{z=h} = \frac{h(r)}{2\eta}\frac{dP}{dx} + \frac{c}{h(r)} \tag{34}$$

or, given $P(x,y) \equiv xQ(r)$, and Equations (11), (29) and (30),

$$\left.\frac{dv_x}{dz}\right|_{z=h} = \frac{6c(1+\rho^2)}{D}\left[S(\rho) + \rho\frac{dS}{d\rho}\cos^2\phi\right] + \frac{c}{D(1+\rho^2)} \tag{35}$$

75

Substituting Equation (35) into Equation (33), performing the azimuthal integral, and integrating on ρ by parts, one obtains the simple result,

$$F_{\parallel} = -2\pi\eta cR\Phi(D / 2w) \tag{36}$$

where the universal function, $\Phi(y)$, is defined by,

$$\Phi(y) \equiv -12 \int_0^{\sqrt{1/y-1}} \rho^3 d\rho S(\rho) - \ln y \quad 0 < y < 1 \tag{37}$$

The integrand, of Equation (37), $\rho^3 S(\rho)$, is plotted in Figure 4. $\Phi(y)$ is shown in Figure 1.
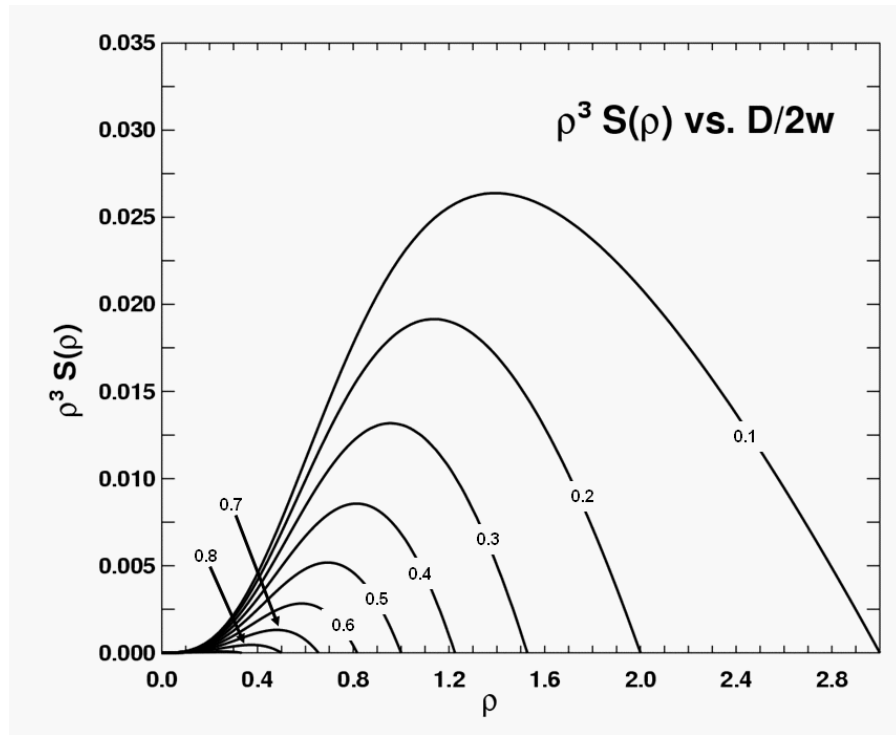
Figure 4. The integrand of Equation (37), $\rho^3 S(\rho)$, versus scaled radial coordinate ρ and labeled values of $D/2w$. The factor ρ^3 greatly diminishes the magnitude of the integral when $D/2w$ is close to 1, i.e., when the tip and sample interphases barely overlap.

Discussion

Friction Force Dependence on Tip Parameters
Comparing to the viscous drag when the tip *approaches* the surface,[2]

$$F_{\perp} = -6\pi\eta \frac{cR^2}{D}\left(1 - \frac{D}{2w}\right)^2 \tag{38}$$

$F_\parallel$ behaves quite differently. It scales *linearly* with R instead of quadratically. It vanishes as $1-D/2w$ (cf., Figure 1), and not $(1-D/2w)^2$, when $D \approx 2w$. It increases much more slowly as $D \rightarrow 0$. The source of these differences is that $F_\perp$ and $F_\parallel$ are governed by different components of the fluid stress tensor.

In tip motion parallel to the surface, because $P(x,y) = xQ(r)$, the pressure integral over the tip surface vanishes by symmetry and plays no role in generating viscous drag. In physical terms, the effect of the excess pressure in front of the tip is exactly compensated by suction behind it. The shear rate, dv_x/dz at $z = h$, is what makes $F_\parallel$ non-zero. Driven by the motion of the tip at speed, c, the shear rate is symmetric under $x \rightarrow -x$, and (see, Equation (35)) independent of the tip radius, R. Thus, the R-dependence of $F_\parallel$ reflects only the area of the region of overlapping interphases over which dv_x/dz at $z = h$ is integrated, namely, $\pi R_c^2 \equiv 2\pi R(2w - D)$. $F_\parallel$ is therefore proportional to one power of $R(2w - D)$.

Just the opposite obtains in the drainage experiment. There, as the tip approaches the sample, squeezing out interphase fluid radially, the velocity field and its shear rate are antisymmetric under $\vec{r} \rightarrow -\vec{r}$, while the pressure is symmetric. Thus, it is the excess pressure on the approaching tip that integrates to $F_\perp$. Because the amount of fluid drained per decrement of D is proportional to R_c^2, the same is true of the back pressure. Accordingly, the excess pressure on the tip integrated over the effective tip area is proportional to R_c^4 or to $R^2(2w-D)^2$.

It is worth appreciating that the different parametric dependences in the formulas for $F_\perp$ and $F_\parallel$ can be quantitatively *very* significant. For example, at a tip-sample separation of 3 nm, for a representative tip radius of $R = 500$ nm and an interphase width $w = 2.5$ nm, the force resisting approach to the surface will be 157 times greater than the drag opposing motion along the surface, assuming the same tip speed in both cases. Alternatively, to observe comparable resistances to tip motion parallel to, and approaching the sample, the tip speed will have to be 157 times greater in the parallel case.

Reassuringly, recent measurements of drag on a hydrophilically-functionalized Au tip moving over a similarly functionalized Au sample confirm this scaling. They also obey (cf. Figure 1) the approximate linear dependence predicted for $F_\parallel$ vs. D, when $0.5 < D/2w < 1$.[13]

Do Viscous Interphases Exist?
As noted at the outset, an array of unproved assumptions raises doubts[14] on the applicability of lubrication hydrodynamics to interphase effects. The results of the present study,

$$F_\parallel = -2\pi\eta cR\Phi(D / 2w) \tag{36}$$

and of the earlier Reference 2,

$$F_\perp = -6\pi\eta \frac{cR^2}{D}\left(1 - \frac{D}{2w}\right)^2 \tag{38}$$

77

for tip motion along and toward a sample, represent necessary conditions for hydrodynamics to be acceptable. Specifically, measurements of $F_\parallel$ and $F_\perp$, must yield the same interphase viscosity, η, the correct rise in friction as D drops below $2w$, and the correct dependence on tip radius.

But satisfying those requirements may still not prove that a large viscosity emerging from a fit to force data is a manifestation of friction in a structured aqueous interphase. Consider, for example, Ponomarev and Meyerovich's demonstration that the problem of flow over a "slightly" rough surface[15] is isomorphic to another, where the surface is flat and the viscosity somewhat enhanced, within a distance from the average surface comparable to the mean spacing between bumps.[16,17] To assess the possible consequence of this isomorphism, that enhanced drag may in part reflect surface roughness rather than water-structure formation, force-distance data need to be supplemented with independent surface roughness measurements, and the theory of Reference 16 extended beyond slight roughness.

Whether a viscosity enhancement of order 10^6–10^8 can be explained other than by an appeal to water-structure formation near a hydrophilic surface is a question of considerable interest—the idea that roughness is an important, if not the only source of viscosity enhancement is appealing, because that might simultaneously account for the smooth force-distance profiles seen in experiments where the near-surface viscosity is large. It is on extremely smooth mica surfaces that near-contact, force-distance profiles are oscillatory.[3,14]

References

1. Kim, H. I.; Kushmerick, J. G.; Houston, J. E.; Bunker, B. C., Langmuir 2003, 19, 9271.

2. Feibelman, P. J., Langmuir 2004, 20, 1239.

3. Contrasting, e.g., with Pashley; R. M.; Israelachvili, J. N., J. Coll. Interf. Sci. 1984, 101, 511

4. Joyce, S. A.; Houston, J. E., Rev. Sci. Instrum. 1991, 62, 710.

5. For an early analysis of flow around a sphere approaching a surface in a viscous fluid, see, Brenner, H., Chem. Eng. Sci. 1961, 16, 242.

6. And, for the sphere moving parallel to a surface, see Goldman, A. J.; Cox, R. G.; Brenner, H., Chem. Eng. Sci. 1967, 22, 637.

7. Tichy, J. A., Tribology Transactions 1995, 38, 577.

8. Reynolds, O. Philos. Trans. R. Soc., London 1886, 177, 157.

9. Chan, D. Y. C.; Horn, R.G. J. Chem. Phys. 1985, 83, 5311, Appendix A.

10. See, e.g., Batchelor, G. K., *An Introduction to Fluid Mechanics* (Cambridge University Press, Cambridge, **1967**), pp 219-222.

11. Another such situation involves dramatically enhanced viscosity for *non-polar* liquids, when nano-confinement drives their solidification. Klein, J.; Kumacheva, E., *J. Chem. Phys.* **1998**, 108, 6996, in their Appendix A, propose to interpret the drag forces they measure in this case via a viscosity that varies with distance from the tip axis according to the corresponding distance between the tip and sample surfaces, i.e., the *local* degree of nano-confinement. Analyzing and solving that model is beyond the scope of the present work, however.

12. Wolfram, S., et al., *Mathematica5.1*, Copyright **1998-2004** Wolfram Research, Inc.

13. Major, R. C.; Houston, J. E.; McGrath, M. J.; Siepmann, J. I.; Zhu, X.-Y., unpublished.

14. Israelachvili, J.; Wennerström, H., *Nature* **1996**, *379*, 219.

15. "Slightly" rough means there is a small parameter in the theory, namely the mean roughness amplitude compared to the average distance between bumps.

16. Ponomarev, I. V.; Meyerovich, A.E., *Phys. Rev. E*, **2003**, *67*, 026302.

17. See also, Lauga, E.; Brenner, M. P.; Stone, H. A., *Handbook of Experimental Fluid Dynamics*, Eds. Foss, J.; Tropea, C.; Yarin, A. (Springer, New York, **2005**), Chap. 15, Sec. 5.1.

Does Exceptional Viscous Drag Impede Flow Through a Nano-Sieve's Pores?

Abstract

To address the concern that a material functionalized to reject dissolved ions may give rise to a highly viscous aqueous interphase within nanometers of its surface, we conducted and interpreted Interfacial Force Microscope measurements of the dissipative forces that resist motion of a tip parallel to a sample, in water. The results are consistent with earlier measurements where the tip approached the sample. They confirm that near hydrophilically functionalized surfaces, interphase viscosities more than 10^6 that of bulk water can be expected.

Introduction

The quality of a desalination membrane is measured by the purity and flux of the water that emerges downstream. Thus, in designing a synthetic desalination nano-sieve, an obvious question is how to functionalize its surfaces to reject ions to as large a distance as possible. If functionalization imposes a low ionic density within a distance w of a sieve's surfaces, then in the simplest model its pores can be as large as 2w in diameter without permitting many ions to pass (see Figure 1). The flux of purified water then scales as w^2, and there is no downside to making w as big as one can.

Appealing as this approach to better membranes may be, it is predicated on the assumption that functionalizing a surface has no countervailing impact on the viscosity of nearby water. The concern addressed herein is that it might, i.e., that within a few nm of an ion-rejecting surface, water will form an "interphase," whose molecular structure gives rise to high viscosity. If this happened, downstream water would be pure. But, because of impeded transport, there would not be much of it. It would be possible to make a sieve with large holes, and not impair the downstream water. But flow of water through it would be "as slow as molasses."
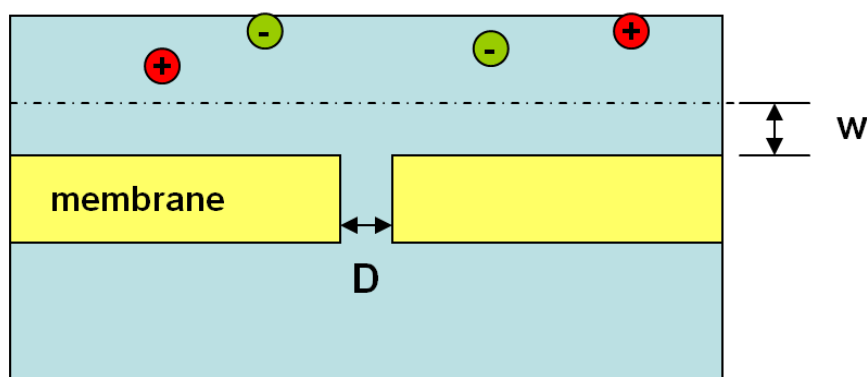
Figure 1. Schematic of a pore in a nano-sieve. If ions are rejected to a distance greater than w of the membrane surface, then pores of diameter D < 2w will only pass pure water.

Behind this worry lie Interfacial Force Microscope (IFM)[1] measurements of the interphase viscosity at various functionalized surfaces.[2-4] The IFM is a scanning probe instrument designed so that the delivery of charge to a pair of capacitor pads balances the force between a tip and a sample (see Figure 2). The exquisite control this gives of the tip-sample separation allows one to measure the force that resists *drainage* of liquid from between a tip and a sample as the tip-sample separation is reduced at a fixed speed. It also permits a study of the resistance, in liquid, to motion of a tip *along* a sample.
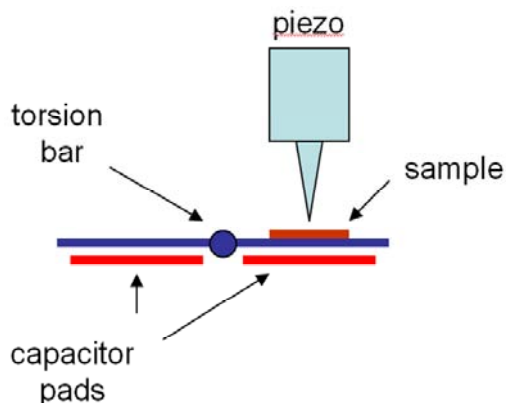
Figure 2. Schematic of an Interfacial Force Microscope (see Reference 1). Delivery of charge to the capacitor pads balances the force acting between tip and sample.

In a first IFM-based drainage experiment, Kim, et al. coated a gold tip and sample with a self-assembled monolayer (SAM) comprised of long chain molecules, whose –OH head groups functionalized the coatings hydrophilic.[2] The remarkable result was that although the force resisting drainage was virtually not measurable for tip-sample separations greater than 5 nm, below this separation the force increased rapidly, and, characteristic of viscous drag, was greater for higher approach speed (see Figure 3).
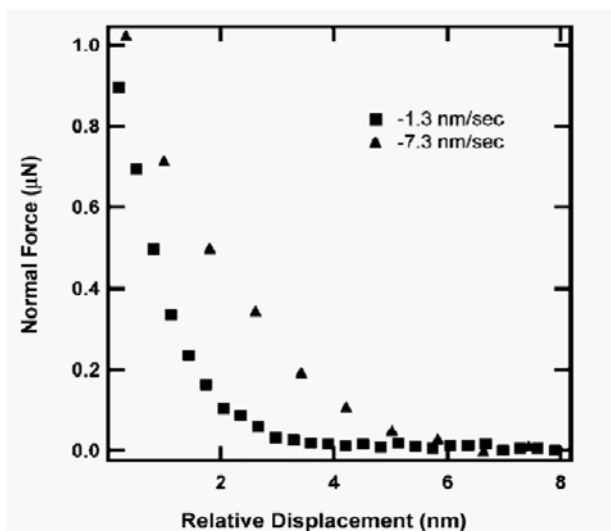
Figure 3. From Reference 2, the force resisting the approach of tip and sample, as a function of their separation and the approach speed.

The Kim, et al. data were analyzed using continuum, hydrodynamic lubrication theory, within a model in which tip and sample surfaces are each coated with an interphase layer of thickness, w, and viscosity, η (see Figure 4).[2,3] The bulk water beyond distance w from either surface is assumed to have zero viscosity. The sample surface, i.e., the locus of the ends of the SAM molecules, is taken to lie in the plane $z = 0$. The tip surface is a cylindrical, paraboloid. Thus, at a radial distance r from its central axis, the tip surface is at $z = D + r^2/2R$, where D, the minimum distance from its apex to the sample, is assumed to be much smaller than R, its radius of curvature.
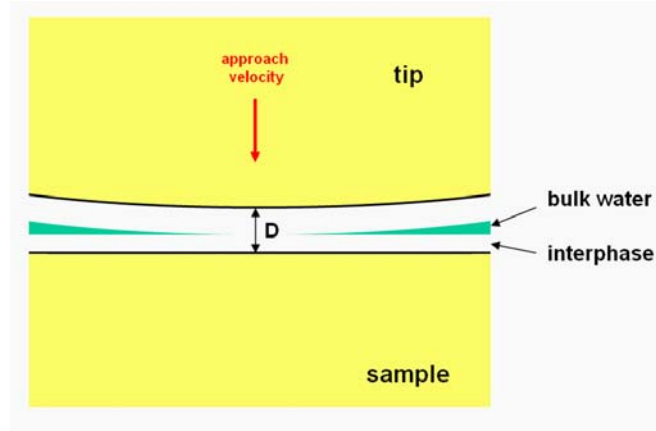
Figure 4. Schematic of drainage experiment. The tip surface lies at $z = D + r^2/2R$, where r is the radial distance from the central axis. The sample surface is at $z = 0$.

Solution of the Navier-Stokes equations for this model, assuming a slow enough tip-sample approach speed, c, (= a few nm/sec) that terms quadratic in fluid velocity can be ignored, yields the formula for the force, $F_\perp$, resisting tip-sample approach,[3]

$$F_\perp \approx -6\pi\, \eta\, c\, (1 - D/2w)^2\, R^2\, /D \tag{1}$$

in which c and R are known, and D can be determined relative to a c-independent origin. Fitting Kim, et al.'s rather limited data set, the interphase viscosity was estimated to be some 7×10^7 that of bulk water.[2,3]

The question is what to make of this remarkable result. At face value, it implies that functionalization of membrane surfaces to improve desalination efficiency is a more complicated matter than looking for ways to reject ions to larger distances. A more judicious approach is to step back and criticize the assumptions underlying the fit. They are that: 1) interphase water can be treated as an isotropic continuum, despite being only a few molecular layers thick, and bound to a hydrophilic surface, 2) surface roughness of the tip and the sample can be ignored, 3) the boundary between the interphase water and the bulk liquid can be treated as spatially sharp, and flat, and 4) the details of the OH-terminated tri(ethylene glycol) undecylthiol [or "EG3OH"] hydrophilic SAMs on the Au surfaces can be ignored, apart from a zero[th] order effort to account for their elastic compliance.[2]

Beyond the perhaps unjustified use of these approximations, there is no current microscopic explanation for the large viscosity. Neutron scattering experiments imply that the interphase density is virtually identical to that of bulk water.[5] X-ray scattering shows no evidence for formation of more than one or two ordered water-molecule layers at oxide surfaces.[6] The idea that confinement between tip and sample causes the water to crystallize into an "ice" layer[7] is belied by an interphase viscosity that, though large, is some 7 orders of magnitude smaller than the viscosity of ice just below the freezing point.[8] Thus, one may imagine that interphase water is characterized by an enhanced formation of transient clusters. But, though there is no evidence against that hypothesis, nothing directly supports it either.

Friction Experiments

Faced with these good reasons for doubt, we undertook to extend the IFM data set to measurements of the force resisting tip drag *along* sample surfaces.[4] This has immediate advantages: 1) In contrast to the drainage experiment, the effects of any "body forces" i.e., forces at a distance between tip and sample, like van der Waals, are eliminated from consideration, because the tip-sample distance is fixed. 2) The same applies to the concern that elastic compliance of the SAM layers played a role in producing what looks like a huge interphase viscosity. In addition, 3) the drag experiment provides an internal consistency check. Does the effective viscosity in this case equal what is found in a drainage measurement, using the same tip and sample preparations?

Thus, IFM drag measurements (see Figures 5 and 6) have been conducted, and not just for EG3OH-coated Au tip and sample, but also, in an effort to eliminate the effects of SAM elasticity entirely, for a W tip on a Si sample, both hydroxylated by dipping in H_2O_2. To enable fits to the new data, we once again applied hydrodynamic lubrication theory.[9] The model used was identical to that for the drainage experiment, apart from changing the tip's velocity from normal to parallel to the sample surface.
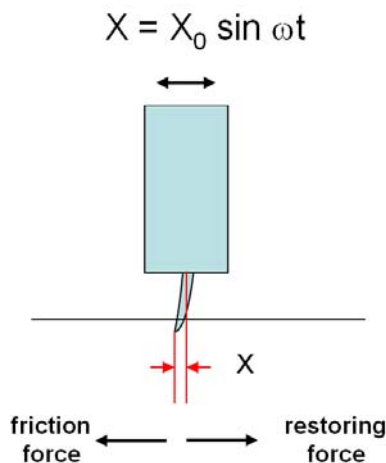
Figure 5. Schematic of drag experiment. As the piezo on which the tip is mounted is caused to oscillate, the tip is bent by frictional resistance (in the present case, by viscosity). Balancing the friction against the tip's elastic restoring force yields a forced oscillator equation. From its solution, one derives the dissipative force, i.e., the measured force 90° out of phase with the piezo's oscillation.
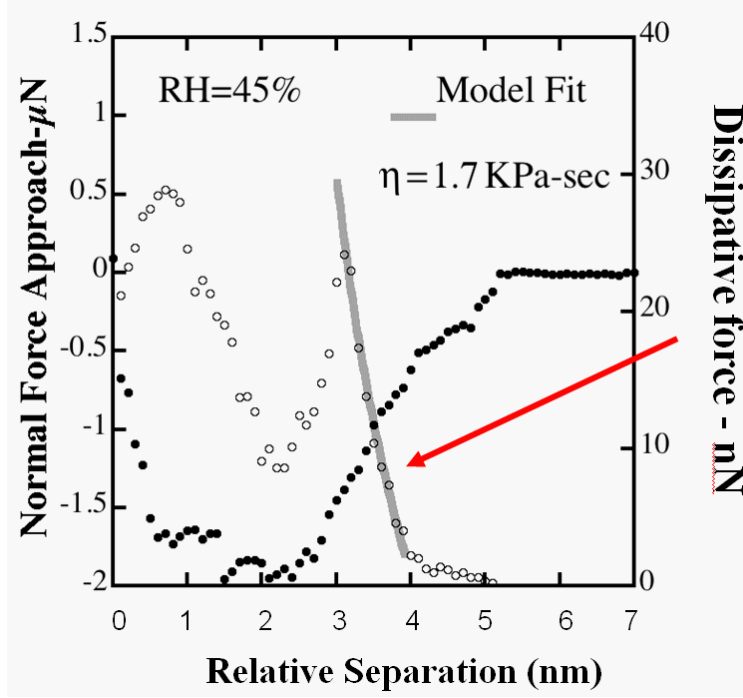
Figure 6. After Reference 4. Results of a drag experiment involving a W tip and a Si sample, both hydroxylated by dipping in H_2O_2. As the tip approaches the sample in a chamber maintained at 45% relative humidity, a meniscus forms when the tip-sample separation is 5 nm, as evidenced by the appearance of an attractive force (black dots). At this separation, a frictional resistance (open circles) is first observed, but is small. At 4 nm separation, the frictional force begins a dramatic increase, described extremely well by the Navier-Stokes solution (grey line) discussed in the main text. The fit allows a value of the viscosity to be extracted, which is more than 10^6 larger than that of bulk water. At a tip-sample separation somewhat above 3 nm, the hydrodynamic fit is no longer valid. The significance of this behavior remains to be understood, both physically, and regarding its implications for filtration.

Hydrodynamic Theory and Comparison to Experiment

The asymmetry inherent in this change complicates the solution of the Navier-Stokes equations. Nevertheless, the typical scaling behavior of hydrodynamic theory makes it possible to present the solution simply. In particular, the force, $F_{//}$, resisting tip motion along the sample, is given by,

$$F_{//} = -2\pi\,\eta\,cR\,\,\Phi(D/2w) \tag{2}$$

where the smoothly varying function Φ is well approximated by $-\ln(D/2w$, if $D/w > 1$.[9] Thus, one has an analytic expression for the drag force, provided the tip-sample distance is greater than the width of a single interphase, namely,

$$F_{//} \approx 2\pi\,\eta\,cR\,\,ln(D/2w) \tag{3}$$

When the tip and sample interphases barely overlap, i.e., when $2w/D$ is just a bit larger than 1, the logarithm of Equation (3) can be expanded, yielding the asymptotic expression,

$$F_{//} \approx - 2\pi \eta \, cR \, (\, 2w/D - 1) \tag{4}$$

This result is of interest in comparison with the drainage result of Equation (1). Given the assumption that $R \gg D$, and in the experiments, typically, R was of order a micron, while D was a few nm, $F_\perp$ is expected to be much larger than $F_{//}$ assuming equal tip speeds. Alternatively, the drag experiment has to be run with the tip moving roughly 100 times faster than in the drainage mode, to yield an equally large frictional resistance. Satisfyingly, this turns out to be true in the experiments.[1,4] Indeed, no signal is detected in a drag experiment if the tip is moving appreciably slower than a µm/s.

Fits of Equation (3) to drag force measurements are shown in Figure 6. As in the earlier drainage study, the agreement of data and hydrodynamic prediction is excellent, although in this case the agreement only lasts as long as the tip is not "too close" to the sample. Restricting attention to the regime in which the fit is good, the viscosity extracted from the data once again is more than 10^6 greater than that of bulk water. The agreement with the drainage result is imperfect, but likely as close as should be expected, considering the limited measurements of Reference 1.

Comparison with data for other tip and sample materials combinations (not shown) yield equally good fits, and comparably large interphase viscosities. The conclusion thus seems inescapably that viscosity is drastically enhanced within nanometers of hydrophilic surfaces.

Future Directions

As noted, when the tip-sample separation reaches what looks to be a "critical value," the hydrodynamic model appears to break down. Future efforts are aimed at interpreting this surprising result. Does it mean that there is a critical strain rate above which interphase viscosity decreases? Does it signal the regime in which continuum theory no longer applies? And are there implications for using functionalized surfaces to build efficient desalination membranes? These are the questions we hope to answer.

References

1. S.A. Joyce and J.E. Houston, Rev. Sci. Instrum. 62, 710 (1991).

2. H.I. Kim, J.G. Kushmerick, J.E. Houston and B.C. Bunker, Langmuir 19, 271 (2003).

3. P.J. Feibelman, Langmuir 20, 1239 (2004).

4. R.C. Major, J.E. Houston, M.J. McGrath, J.I. Siepmann, and X.-Y. Zhu, Phys. Rev. Lett. (in press), and unpublished.

5. D. Schwendel, et al., Langmuir, 19 2284 (2003).

6. L. Cheng, et al., Phys. Rev. Lett. 87, 156103 (2001).

7. See, e.g., M. Antognozzi, A.D.L. Humphris, and M.J. Miles, App. Phys. Lett. 78, 300 (2001).

8. R.A. Freitas Jr., Nanomedicine, Volume I: Basic Capabilities, (Landes Bioscience, Georgetown, TX, 1999).

9. P.J. Feibelman, Langmuir 22, 2136 (2006).

Stress Correction for Slab Asymmetry in Supercell Calculations

Abstract

In ab initio, supercell optimizations of slab total energy, a dipole layer is commonly introduced in the periodically-repeated vacuum to cancel unphysical fields attributable to differing work functions of upper and lower slab surfaces. This artifice changes the formulae needed to compute slab total energy and the forces on atoms. Here, for a supercell of height, Z_{UC}, the correction to the slab stress tensor is shown to equal $-\delta_{ij}(\Delta\Phi)^2/8\pi e^2 Z_{UC}$, where $\Delta\Phi$ is the work-function difference, e is the electron charge, and i and j represent the x-y coordinates in the plane of the surfaces.

Introduction

To reduce the computational cost of optimizing surface structure in Density Functional Theory (DFT) implementations,[1] one commonly relaxes atomic positions near the top of a few-layer slab, while fixing bottom-layer atoms in sites characteristic of the bulk crystal in question. In periodic-supercell methods, however, this approach can make it necessary to correct for unphysical electric fields generated between each slab and its neighboring periodic image. These fields are an artifact of the different work functions on the two sides of the slab and their strength increases with work-function difference, $\Delta\Phi$.

Several papers addressed this problem in the 1990s, ultimately producing formulas for the DFT total energy and for forces on atoms, in which effects of the unphysical fields are removed;[2-6] these formulas are incorporated into modern DFT codes.[7] In the present note, I derive and estimate the correction needed to compute an asymmetric slab's surface stress tensor.

The reassuring result is that the correction is small, because, to lowest order, an electric field along a slab's normal does not couple to intra-surface-plane atomic interactions. The needed stress correction is accordingly the strain derivative, $-\delta_{ij}(\Delta\Phi)^2 / 8\pi Ha_B Z_{UC}$, of the unphysical field's electrostatic energy, where H is the Hartree, a_B is the bohr, and Z_{UC} is the height of the slab-containing cell. Even with $\Delta\Phi$ as large as 2 eV, if $Z_{UC} > 20$ Å, as is typical, then $(\Delta\Phi)^2/8\pi Ha_B Z_{UC} < 6 \times 10^{-4}$ eV/Å^2, well below the numerical noise level of most stress calculations. The asymmetric-slab stress correction can therefore be neglected.

Derivations

Asymmetric-Slab Correction to the Total Energy
Following Bengtsson, (see Reference 4, Equation 7), a dipole layer introduced in the middle of the vacuum region separating each slab from its adjacent periodic image will cancel the unphysical electric field if it produces the potential,

$$V_{dip}(z) = 4\pi\mu\left(\frac{z}{Z_{UC}} - \frac{1}{2}\right) \qquad 0 < z < Z_{UC} \tag{1}$$

where μ is the slab's dipole moment per unit area,

$$\mu \equiv \int z'dz'\overline{\rho}(z') \tag{2}$$

In Equation (2), the slab's planar average charge density is,

$$\overline{\rho}(z') \equiv \frac{1}{A_{UC}} \int_{A_{UC}} d^2r' \left[\rho^I(\vec{r}') + \rho^e(\vec{r}')\right] \tag{3}$$

wherein the ionic term, ρ^I, is a positive quantity, and the electronic ρ^e is negative. A_{UC} is the area of the surface unit cell.

Corresponding to the added potential of Equation (1), Bengtsson showed (see Reference 4, Equations 12 and 13) that the DFT total energy per unit cell must be supplemented by,

$$\Delta E = \frac{1}{2} \int_{\Omega_{UC}} d^3r V_{dip}(z)\left[\rho^I(\vec{r}) + \rho^e(\vec{r})\right] \tag{4}$$

The "−1/2" term of Equation (1) integrates to zero in Equation (4), by virtue of charge neutrality. Equation (4) thus reduces to,

$$\Delta E = 2\pi\mu^2 A_{UC} / Z_{UC} \tag{5}$$

According to the Hellmann-Feynman theorem,[8] the desired, added contribution to the slab stress is the explicit strain derivative of this ΔE.[9]

Asymmetric-Slab Correction to the Stress
To evaluate this derivative, I write explicit expressions for the ionic and electronic charge densities. In particular, the ionic density is,

$$\rho^I(\vec{r}) \equiv e\sum_j Q_j\delta(\vec{r} - \vec{R}_j) \tag{6}$$

where the jth ion resides at position $\mathbf{R_j}$ and has charge eQ_j. The electronic charge density is given by

$$\rho^e(\vec{r}) = -2e \int_{\Omega_{SBZ}} \frac{d^2k_{\parallel}}{\Omega_{SBZ}} \sum_n f_{k_{\parallel},n}\left|\psi_{k_{\parallel},n}(\vec{r})\right|^2 \tag{7}$$

where the $k_\parallel$-integral averages over the surface brillouin zone, n is a band index, $f_{k_\parallel,n}$ is the Fermi function, and the factor 2 represents spin summation. Assuming that the periodic images of the slab are generated by translating along its normal (by convention the z-direction), the Kohn-Sham wave functions,[10] $\Psi_{k_\parallel,n}(\vec{r})$, can be expanded as,

$$\psi_{k_\parallel,n}(\vec{r}) = \frac{1}{\sqrt{A_{UC}}} \sum_{\vec{G}_\parallel} e^{i(\vec{k}_\parallel + \vec{G}_\parallel)\cdot\vec{r}} u_{\vec{k}_\parallel + \vec{G}_\parallel,n}(z) \tag{8}$$

Thus, substituting from Equations (3) and (6-8) into Equation (2), one finds that,

$$\mu \equiv \frac{e}{A_{UC}}\left[\sum_j Q_j Z_j - 2\int \frac{d^2 k_\parallel}{\Omega_{SBZ}} \sum_n f_{k_\parallel,n} \int zdz \left| u_{\vec{k}_\parallel + \vec{G}_\parallel,n}(z) \right|^2 \right] \tag{9}$$

In Equation (9), the $1/A_{UC}$ preceding the square bracket comes from averaging the ionic and electronic densities over the planar unit cell. The square of the normalization factor $(A_{UC})^{-1/2}$ in Equation (8) has canceled against the area of the surface unit cell that results from the $d^2 r$ integration of Equation (3).

The key feature of Equation (9) is that the explicit strain derivative of the square bracket's contents is zero. The ionic term is self-evidently independent of the parallel lattice repeat distances. The surface brillouin zone average is also inherently strain independent. In the electronic term, the $u_{k_\parallel + G_\parallel,n}(z)$ do depend on strain, but in plane-wave methods only implicitly,[11] i.e., through the Kohn-Sham equation. This means their strain derivatives collectively yield a vanishing contribution to the stress tensor, as in the proof of the Hellmann-Feynman theorem.[8]

The asymmetric film energy correction of Equation (5) can therefore be written as,

$$\Delta E = [2\pi(\mu A_{UC})^2 / Z_{UC}]^2 / A_{UC} \tag{10}$$

where the term in square brackets has no explicit strain derivative. Thus, the contribution of ΔE to the Hellmann-Feynman stress is derived uniquely from the final factor, $1/A_{UC}$. Noting that the unit cell area scales as $A_{UC} \rightarrow \det(1 + \varepsilon)A_{UC}$, under the mapping, $R_i \rightarrow \Sigma_j(\delta_{ij} + \varepsilon_{ij})R_j$, one obtains,

$$\frac{dA_{UC}^{-1}}{d\varepsilon_{ij}} = -\delta_{ij} A_{UC}^{-1} \tag{11}$$

where δ_{ij} is the Kronecker delta. On a per unit area basis, therefore, the contribution to the correction to the stress formula associated with slab asymmetry is,

$$\Delta S_{ij} = -\delta_{ij} 2\pi\mu^2 / Z_{UC} \tag{12}$$

Estimating the Stress Correction

For a sense of how large this contribution may become, it is helpful to rewrite it in terms of the work function difference between the two slab surfaces, rather than the slab dipole moment. The relation between these quantities is simply,

$$\Delta\Phi = -4\pi e\,\mu \tag{13}$$

according to Lang and Kohn.[12] Substituting this relationship into Equation (12), and noting that $e^2 = Ha_B$, where H is the Hartree and a_B the bohr, the new term in the stress formula becomes,

$$\Delta S_{ij} = -\delta_{ij}(\Delta\Phi)^2 / 8\pi Ha_B Z_{UC} \tag{14}$$

As noted at the beginning of this report, with $\Delta\Phi$ unlikely ever to exceed a couple of eV, and supercell periodic repeat distances typically exceeding ~20Å, this term can generally be expected to be negligible. Thus, the result of the present work is the knowledge that the asymmetric-slab, surface-stress correction is generally of little consequence, and can safely be ignored.

References

1. For a review emphasizing accuracy issues, see A. E. Mattsson, P. A. Schultz, M. P. Desjarlais, T. R. Mattsson, and K. Leung, Modelling and Simulation in Mat. Sci. and Eng. 13, R1 (2005).

2. G. Makov and M.C.Payne, Phys. Rev. B 51, 4014 (1995).

3. J. Neugebauer and M. Scheffler, Phys. Rev. B 46, 16067 (1992).

4. L. Bengtsson, Phys. Rev. B59, 12301 (1999).

5. P. A. Schultz, Phys. Rev. B60, 1551 (1999).

6. The word "ultimately," here, refers to a factor 2 error in the energy correction of Reference 3, as explained in Reference 4.

7. See, e.g., G. Kresse, VASP Guide, http://cms.mpi.univie.ac.at/vasp/vasp/node148.html, Oct. 2004.

8. H. Hellmann, Einführung in Die Quantenchimie (Deuticke, Leipzig, 1937); R. P. Feynman, Phys. Rev. 56, 340 (1939).

9. O. H. Nielsen and R. M. Martin, Phys. Rev. Lett. 50, 697(1983); Phys. Rev. B32, 3780 (1985).

10. W. Kohn and L. J. Sham, Phys. Rev.**140**, A1133 (1964).

11. In local-basis methods, the Kohn-Sham wave functions are expanded in atom-centered orbitals instead of plane waves, the energy thereby acquires an explicit dependence on atom

positions, and the stress formula must be modified. For details, see P. J. Feibelman, Phys. Rev. **B44**, 3916 (1991).

12. N. D. Lang and W. Kohn, Phys. Rev. **B3**, 1215 (1971).

Substitutional NaCl Hydration in Ice

Abstract

Na^+ and Cl^- can replace water molecules in ice Ih, with minimal lattice strain and without disrupting the crystal's H-bond network. First principles calculations show that substitutional solvation is endothermic by as little as 0.49 eV per ion pair. Interstitial ion solvation is less favorable by >1.5 eV.

Introduction

In cold places, freezing is an efficient way to produce potable from salty water. A qualitative explanation is that breaking H-bonds to hydrate Na^+ and Cl^- is too costly at low T, and ice therefore rejects salt. In liquid water, with many H-bonds broken thermally, rotation and displacement of H_2O dipoles is facile, and salt dissolves.

A first-principles survey of water molecule arrangements around Na^+ and Cl^- in ice now points to a more specific explanation. It reveals a strong energetic preference for the ions to reside in substitutional sites, where, as H-bond topology is found to allow, each is hydrated by four, tetrahedrally situated, H_2O neighbors, and local lattice strain is slight. Remarkably, this means that substitutional hydration is consistent with a virtually perfect H-bonding network. The energy cost of breaking H-bonds does not inhibit an ideal solvation structure; what it does do is limit each ion's first hydration shell to four H_2Os. In water, a fifth H_2O approaches a dissolved Na^+ almost as closely, according to first principles simulations.[1] Thus, the present results suggest asking if water dissolves NaCl primarily because Na^+ and Cl^- ions attract >4 nearby waters of hydration.

In an era of cheap computing, the standard way to analyze a system with many degrees of freedom is to perform a molecular dynamics (MD) simulation, hoping to derive insight *a posteriori* from metrics such as pair-distribution functions. This was the approach in recent simulations of Na^+ and Cl^- in ice and water, aimed at accounting for thundercloud electrification.[2] I have operated "in reverse," however, *starting* from Pauling's celebrated insight that the energy of ice is almost entirely determined by the satisfaction of "ice rules" (two H atoms on each O, one H between every O-atom pair),[3] and searching for the structure consistent with these rules that hydrates ions best. Thus, my "surveying tool" has been the notion[4] that denumerable, charged point defects are what hydrate Na^+ and Cl^- in ice, either pairs of OH and H_3O ions, or pairs of rotational, "Bjerrum defects."[5]

A corollary of the ice rules is that there is no penalty for focusing on a *particular* model ice crystal—details of proton order or disorder produce only minor energetic corrections. It is therefore appropriate to ask how a certain periodic model with a modestly large unit cell, 192 H_2O molecules, optimally accommodates one Na^+ and, well separated from it, one Cl^- impurity ion (in what amounts to a dilute, 0.29M solution). The results will provide approximate asymptotic structures and energies for hydrated, and thus screened, Na^+ and Cl^- ions in ice at large ion separations.[6]

Binding of Na^+ and Cl^- in a rigid ice crystal is so weak that subtracting the 7.9 eV needed to form Na^+ and Cl^- from rocksalt leaves an extremely negative 0 K heat of NaCl solution, ~6.9 eV.[7] The reason is not just lattice rigidity; in a perfectly H-bonded network, no lattice sites are surrounded by negatively charged O atoms, which would attract a Na^+, or by positive H atoms, to satisfy a Cl^-. How can charged sites form without greatly disturbing the remainder of the ice crystal? One way is by proton transfer, as shown in Figure 1a. Better, because disproportionation incurs an energy cost, is by forming a rotational (or "Bjerrum") defect[3,4] pair, as in Figure 1b.
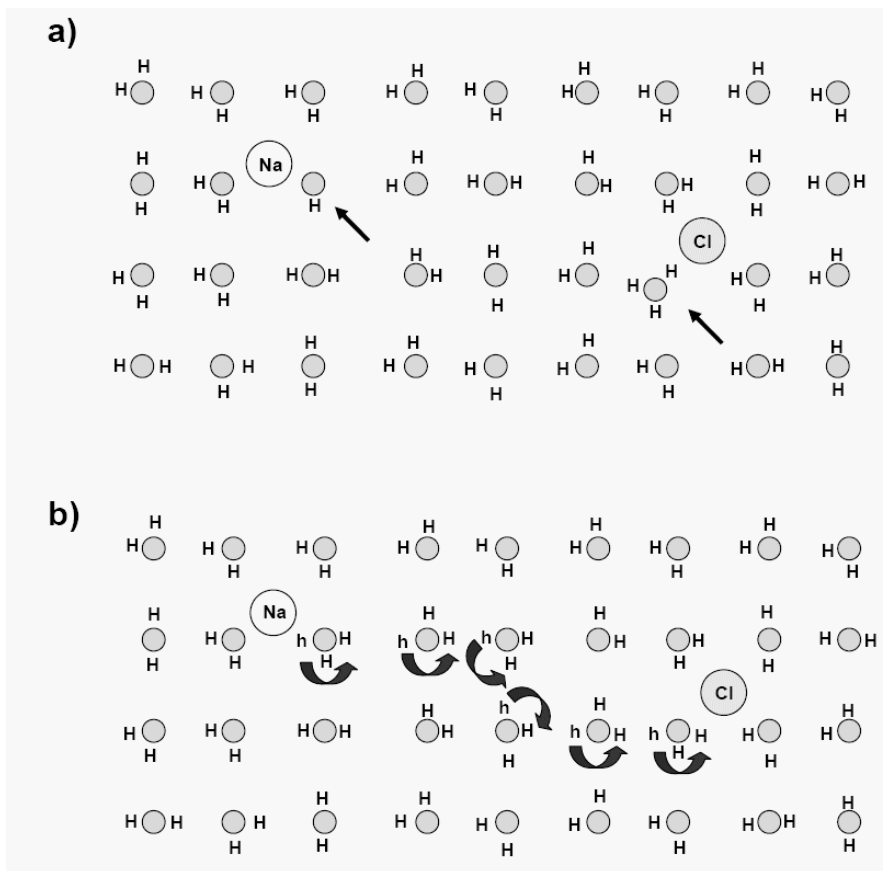
Figure 1. With shaded circles representing O atoms, and the letter **h** or **H** representing an H atom, a "square-ice" model (Reference 8) of a Na^+ and Cl^- pair, hydrated a) by a proton transfer to form the OH and H_3O ions indicated by arrows, or b) by a Bjerrum defect pair created by rotating lower case **h**'s into black **H**'s following the arrows. Note that the number of intact H-bonds is the same in both panels.

Another good question is whether interstitial ions also impose unneeded energy cost by straining the host ice lattice. Figure 2 implies that they do. In Figure 2a, each interstitial ion is hydrated by a pair of Bjerrum defects; two negatively charged, L-type defects lie adjacent to the Na^+ and two positive, D-type defects are next to the Cl^-. By virtue of 1.0 and 1.8 Å ionic radii, both ions push neighboring water molecules away, at a cost in elastic energy. In addition, the intact H-bonds adjacent to the ions prevent water molecule rotations that might make hydration more effective.
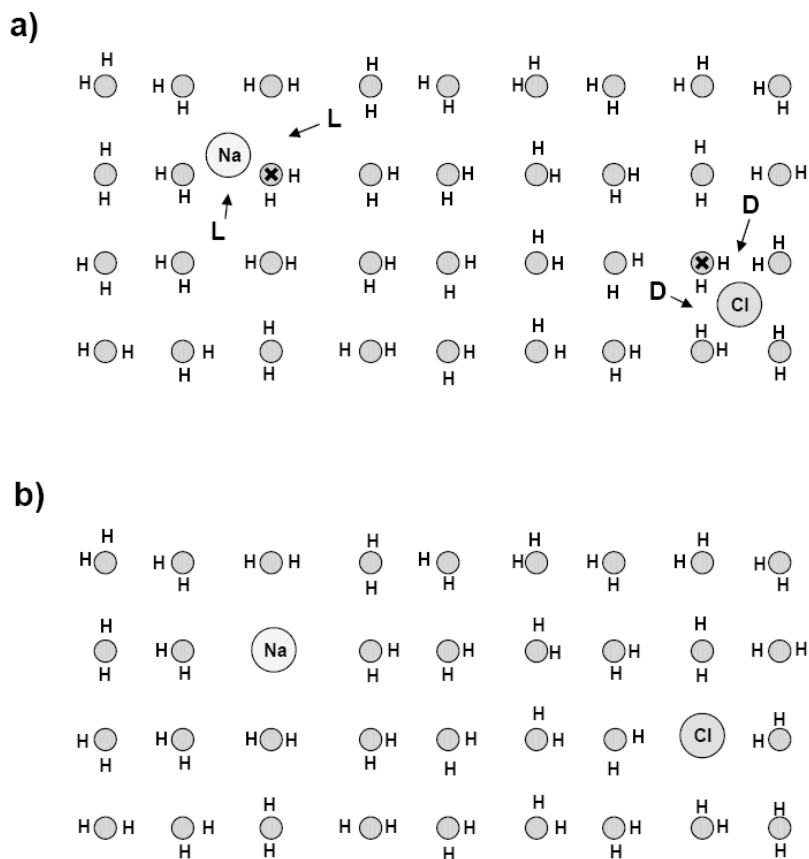
Figure 2. a) Na and Cl *interstitial* ions hydrated by two Bjerrum pairs, arrows pointing to L- and D-type defects, and b) Na and Cl *substitutionals*, each hydrated by four nearest neighbor H_2Os. Showing that formation of two Bjerrum defect pairs is the precursor to the ideal, substitutional structure, removing H_2Os labeled with an **x**, and moving the Na and Cl into their sites, converts panel a) to b).

Compare now to Figure 2b, where the ions *replace* H_2Os. The substitutional Na^+ is surrounded by four negative O atoms. Similarly, positive Hs on four H_2O molecules ideally hydrate the Cl^-. Comparing impurity ionic radii to the O–O separation of 2.76 Å in pure ice, a $Na^+(Cl^-)$ should pull(push) its H_2O neighbors inward(outward) by about 0.4 Å. Beyond that, with all H-bonds intact, lattice strain should be small.

This picture based on 2D schematics is borne out by first principles energy calculations for realistic, 3D ice crystals, which imply that substitutional solvation can be endothermic by as little as 0.49 eV per ion pair. In dramatic contrast, interstitial ion solvation is less favorable by >1.5 eV. On a thermal scale, this is an enormous difference. With 0.49 eV endothermicity, NaCl doping of ice is possible to ppb; with 2.0 eV endothermicity, it is not, not even remotely.

Computational Details

Eliminating potential artifacts attributable to a poor choice of semi-empirical force-fields,[1] solvation structures and energies were obtained here using VASP[9,10] in the PW91 Generalized Gradient Approximation (GGA),[11] with Projector Augmented Wave (PAW) electron-core

interactions.[12,13] The hardest VASP PAW potentials available for H, O and Na were used, optimized for a 700 eV plane-wave cutoff. Pressure was computed using the Nielsen-Martin[14] method, and, for acceptable accuracy, a 1000 eV cutoff. Cell volumes were chosen to reduce the pressure below 0.3 kB in magnitude. No attempt was made to optimize cell shape beyond the ideal hcp c/a =1.633 (experimental value = 1.628, at -20°C).[4]

To model dilute Na and Cl in ice Ih, I started from a unit cell comprised of four hexagonal layers of 24 H_2O molecules, constructed to have no dipole or quadrupole moment, and to satisfy a suite of quasi-randomness criteria.[15] I stacked two such cells, introducing a Na nucleus into one (represented by the four leftmost water molecule layers of Figure 3) and, >13 Å from the Na, a Cl into the other. In all calculations of Na + Cl in ice, the Brillouin Zone (BZ) was sampled at the single point, Γ.
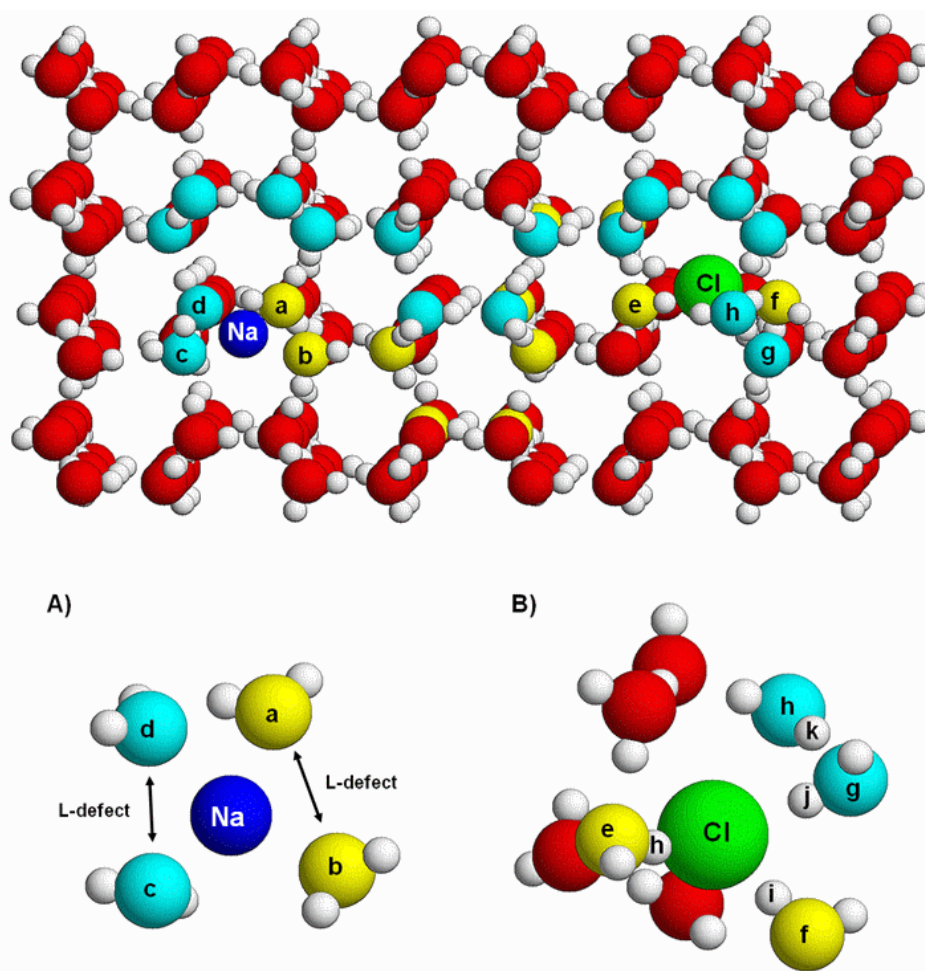
Figure 3. Upper panel: A 192 H_2O-molecule, ice supercell, optimized with interstitial Na and Cl impurities. Non-intersecting chains of H_2Os whose O atoms are cyan and yellow connect two L-type Bjerrum defects hydrating the Na to two D-type defects adjacent to the Cl. Remaining O atoms are red; Hs are white. Labels a–h on O atoms correspond to those in the blow-ups of first Na and Cl hydration shells in panels A) and B).

To study hydration energetics, I relaxed cell geometries containing pairs of Bjerrum defects generated "by hand" (as in Figure 1b), or containing an H_3O and an OH. Figure 3 shows an optimized structure with two pairs of D- and L-type Bjerrum defects hydrating interstitial impurity ions.

Surveying a hand-selected sample of hydration structures risks missing an important one. This is a particular worry in PW91 calculations for H_2O molecules, because PW91 barriers to H-bond breaking are somewhat too high.[16] After relaxing each hypothetical structure to a relative minimum, I therefore ran a short series of MD steps, amounting to a time evolution over 48 fs, at 350 K to allow the system to find a lower energy basin. It often turned out to be some tens of meV deeper. Repeating such a search typically yielded additional improvement of < 10 meV.

A thermodynamic energy zero, here the pure-ice sublimation energy plus the cohesion of rocksalt, is needed to estimate a solution energy. I optimized rocksalt using an $8 \times 8 \times 8$ BZ sample and the same PAW potentials and plane wave cutoff as for solution in ice. The result was a cohesive energy of 6.843 eV, relative to neutral Na and Cl atoms, and a lattice parameter of 5.67 Å, differing by 5% and 0.5% from the experimental 6.52 eV and 5.64 Å. Errors at this level are expected from an approximate, GGA functional. Optimizing the double Hayward-Reimers cell,[16] containing 192 water molecules, yielded an ice Ih lattice energy of 0.678 eV at a volume per H_2O of 30.27 $Å^3$, compared to low T experimental values of 0.611 eV and 32.1 $Å^3$. As usual, one hopes that error cancellation renders energy comparisons meaningful, even if absolute errors are large compared to kT.

Numerical results

The structure survey encompassed: a) three cases of hydration by a single pair of D- and L-type Bjerrum defects, b) one involving transfer of a proton to form an OH adjacent to the Na and an H_3O near the Cl, c) three examples of two pairs of hydrating Bjerrum defects, d) one with three pairs of Bjerrum defects, e) replacement of an H_2O molecule by the Cl, and, lastly, f) in addition, replacement of second H_2O by the Na. Solvation energies, E_{solv}, were obtained according to,

$$E_{solv} = N E_{coh}(\text{pure ice}) + E_{coh}(\text{NaCl}) - E(\text{Na} + \text{Cl in ice}) \tag{1}$$

where N is the number of H_2Os in the ice cell containing the Na and Cl ions, $E(\text{Na} + \text{Cl in ice})$ is its energy, and $E_{coh}(\text{pure ice})$ is 1/192 times the energy of the 192-molecule, pure ice cell.

The remarkably varied results in Table 1 bear important lessons. First, proton transfer is a costly way to hydrate ions. Moving a proton from an H_2O adjacent to the Na to one near the Cl, yielded an endothermic, -2.63 eV hydration energy, whereas the best of three cases of hydration by a Bjerrum defect pair ("D + L"), yielded -2.43 eV.

Table 1. Best GGA/PW91 solvation energies (all endothermic) computed starting with the listed defect types adjacent to the impurity Na and Cl ions in interstitial (I) or substitutional (S) sites. The ions are separated by at least $|\mathbf{R}_{Na} - \mathbf{R}_{Cl}|_{min}$, in a unit cell of dimensionless repeat vectors, ($\sqrt{3}$, 6, 0), (-3$\sqrt{3}$, 0, 0), (0, 0, 11.3137) and volume Ω_{cell}.

Defects	#H$_2$Os	Na site	Cl site	Ω_{cell}/192	$|\mathbf{R}_{Na} - \mathbf{R}_{Cl}|_{min}$	E_{solv}
H$_3$O + OH	192	I	I	30.52 Å^3	13.21 Å	-2.63 eV
D + L	192	I	I	30.52 Å^3	14.23 Å	-2.43 eV
2D +2L	192	I	I	30.60 Å^3	14.25 Å	-1.99 eV
3D+3L	192	I	I	30.68 Å^3	14.17 Å	-2.66 eV
2D +2L	191	I	S	30.42 Å^3	13.63 Å	-1.18 eV
2D +2L	190	S	S	30.25 Å^3	14.39 Å	-0.49 eV

In the latter, the Na's nearest neighbors were two O atoms 2.25 to 2.29 Å away; two H$_2$Os also hydrated the Cl, such that its nearest neighbors were two H atoms at distances 1.89 and 1.97 Å. In the proton-transfer example, the Na was hydrated by an OH ion and an H$_2$O, whose O atoms were 2.38 Å and 2.32 Å from it, and the Cl by two H$_2$Os and an H$_3$O, with nearest H atoms at distances of 1.99, 2.08 and 1.81 Å. Thus, even though the first shell hydration number of the Cl was greater in the proton transfer case, the energy needed to form OH and H$_3$O ions made this hydration mode 0.2 eV more endothermic, and uncompetitive at low T.

It is not obvious, *a priori*, what number of broken H-bond defects is optimal. If there are too few, then electrostatic attraction between the impurity ions and the defects is unnecessarily low; if too many, their mutual repulsion reduces the heat of solvation. First principles results settled this issue; *two* Bjerrum-defect pairs yielded the lowest energy solvation structure with interstitial Na + Cl ions. The geometry of the optimal arrangement, endothermic by 1.99 eV, is displayed in Figure 3. Four nearest H$_2$Os hydrate the Na$^+$, with O atoms, a, b, c and d at distances 2.38, 2.37, 2.38 and 2.33 Å. The Cl is hydrated by a pair of conjoined D-type defects, such that only *three* OH bonds (ei, fj, and gk, in panel 3b) point an H atom at the Cl.

The *surprising* result of the present survey is that optimal hydration of substitutionals is far better than of interstitials. Substituting the Cl ion for an H$_2$O improves the total energy by as much as 0.81 eV per Na + Cl. Substituting the Cl *and* the Na for H$_2$Os leads to an additional improvement of 0.69 eV. The reasons are that for each Na or Cl, the four first-neighbor H$_2$Os, forming a trigonal pyramid, are as widely separated as possible, minimizing their mutual repulsion. In addition (see Figure 4), the ice lattice is minimally strained. Consistent with their ionic radii, the Na$^+$ ions lie 2.40 Å from their four equidistant, nearest O-atom neighbors, and the Cl$^-$ ions 3.02 Å from theirs, compared to O–O separations of 2.70 Å in pure, PW91 ice. Thus,

the Na^+ pulls its neighboring waters 0.30 Å towards itself, and the Cl^- pushes its hydrating molecules 0.32 Å away. Otherwise, lattice strain is slight.
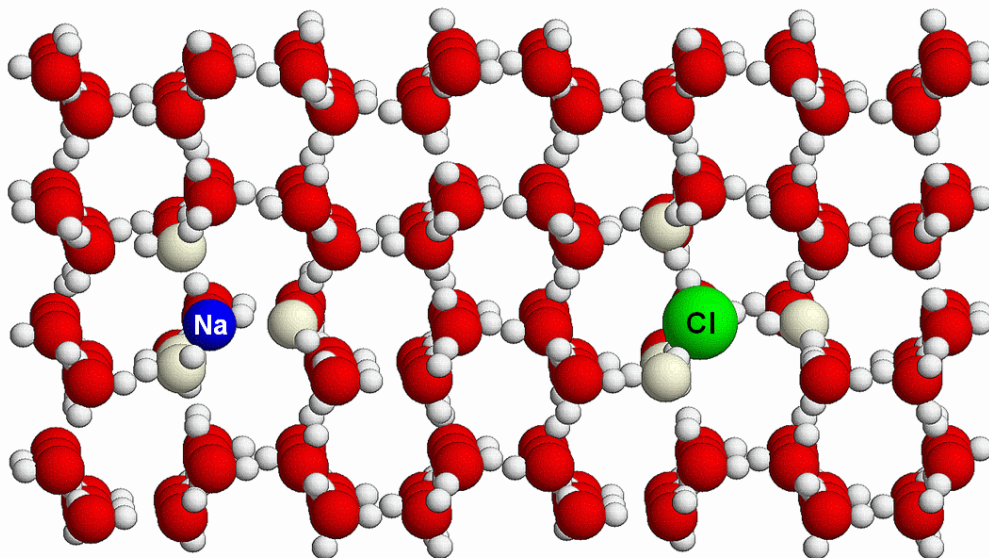
Figure 4. An optimized ice supercell, comprising interstitial Na and Cl impurities and 190 H_2Os. The O atoms of the nearest H_2Os to each ion are colored light yellow instead of red. The figure shows a lattice barely disturbed by the ions.

Discussion

Comparison of Figure 4 with snapshots (see Figure 5) from Reference 2's MD 150 K simulation[17] shows how important it is to make use of all *a priori* physical insight before embarking on energy optimization. Reference 2 separately considered the hydration of Na^+ and of Cl^-, in each case, in a 768 water-molecule cell neutralized by a uniform background charge. Figure 5 makes plain that separate treatment of the ions and fixing the number of water molecules to fill the unit cell *each* drove the calculated solvation energies down by at least several tenths of an eV.

Topology dictates (cf. Figure 1b) that forming a D-type defect to hydrate a Cl^- also creates an L-type Bjerrum defect. In a cell containing both Na^+ and Cl^- ions, the L-type defect hydrates the Na^+, lowering the system energy. But if there is no Na^+ in the cell, the L-type defect finds no low energy site,[18] and thus represents not a benefit, but a several tenths eV formation energy *cost*.[19] Figure 5a underlines the reality of this argument. This snapshot of Reference 2's simulation of Cl^- hydration reveals a free L-type Bjerrum defect. For Na^+, Figure 5b similarly shows a free D-type defect.

Consequences of having too many H_2O molecules in the unit cell are also implied by Figure 5. Note the blue arrows pointing to H_2Os displaced into interstitial sites. According to first principles calculations,[20] forming a water interstitial in ice incurs a minimum cost of ~0.7 eV. In Figure 4, there are no water interstitials or free Bjerrum defects. That is why the Na + Cl solvation heat is only -0.49 eV, overall.

101
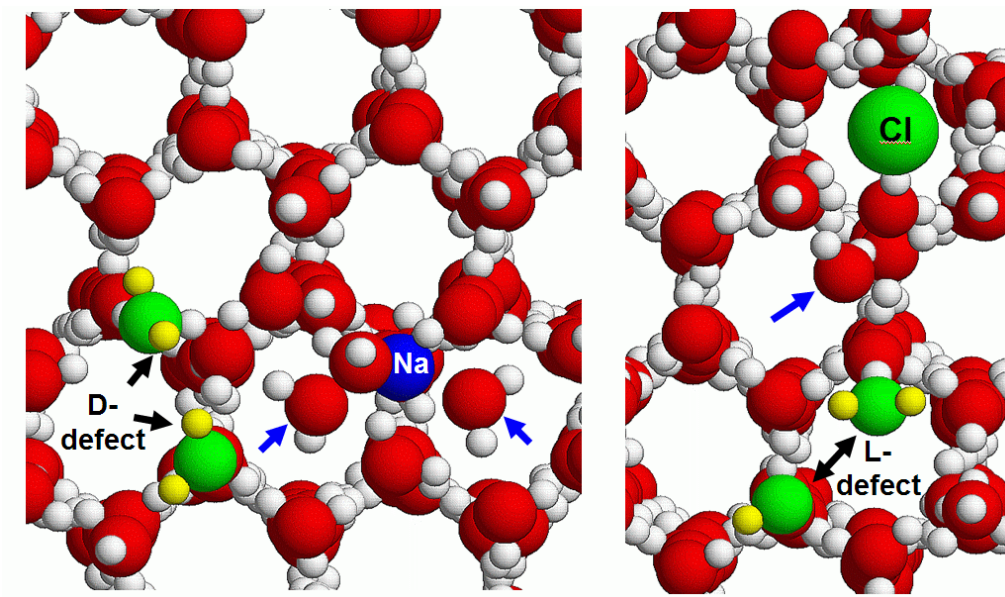
Figure 5. Snapshots from Reference 2's simulations of Na+ and of Cl⁻ ion hydration in ice, highlighting free Bjerrum defects generated. Blue arrows point to H2Os pushed out of lattice sites.

Conclusion

In summary, drawing insight from the Pauling ice rules and H-bond network topology *before* embarking on an energy optimization has led to discovery of a low energy Na + Cl solvation structure. Comparing theory to data is not a current possibility, because NaCl is so insoluble in ice. But, there *are* ice-soluble salts, e.g., NH_4F, which offer a chance for an experimental test.

References

1. S. Varma and S. B. Rempe, Biophys. Chem. 124, 192 (2006).

2. E. J. Smith, T. Bryk. A. D. J. Haymet, J. Chem. Phys. 123, 034706 (2005).

3. L. Pauling, J. Am. Chem. Soc. 57, 2680 (1935).

4. V. F. Petrenko, R. W. Whitworth, Physics of Ice (Oxford University Press, Oxford, 1999), sections 5.4 and 6.8.

5. N. Bjerrum, Kong. Dansk. Vid. Sels.Mat.-fys. Medd. 27, 1 (1951).

6. Because NaCl solvation in ice is endothermic, this periodic ion arrangement is metastable. That does not make it physically interesting; however, to ask how the 192 atom supercell's energy decreases and its ion hydration structures change with decreasing Na–Cl separation. In thermodynamic equilibrium, the 192 molecule cell has no meaning. The Na and Cl ions, having shed their hydration shells, reside in a phase-separated, rocksalt inclusion in otherwise pure ice.

7. E. J. Smith, A. D. J. Haymet Mol. Sim. 30, 827 (2004).

8. J. F. Nagle, J. Math. Phys. 7, 1484 (1966).

9. G. Kresse and J. Hafner, Phys. Rev. B 47, 558 (1993); Phys. Rev. B 49, 14251 (1994).

10. G. Kresse and J. Furthmüller, Comput. Mat. Sci. **6**, 15 (1996); Phys. Rev. **B 54**, 11169 (1996).

11. J.P. Perdew, in *Electronic Structure of Solids '91*, ed. by P. Ziesche and H. Eschrig (Akademie Verlag, Berlin, 1991); J.P. Perdew, et al., Phys. Rev. **B 46**, 6671 (1992).

12. P.E. Blöchl, Phys. Rev. **B 50**, 17953 (1994).

13. G. Kresse and D. Joubert, Phys. Rev. **B 59**, 1758 (1999).

14. O. H. Nielsen, R. M. Martin , Phys. Rev. **B 32** , 3780 (1985).

15. J. A. Hayward and J. R. Reimers, J. Chem. Phys. **106**, 1518 (1997).

16. D. Asthagiri, L. R. Pratt, J. D. Kress, Phys. Rev. **E 68,** 41505 (2003).

17. Comparing the simulation results to structures computed from first principles at 0 K assumes that the latter would not change appreciably in 1st principles simulations at 150 K. With *T* times the entropy of ice no more than 0.04 eV, at 150 K, [see, G. P. Johari, J. Chem. Phys. **112**, 10957, (2000), Figure 2] and the energy advantage of substitutional hydration amounting to ~1.5 eV, this seems an excellent assumption.

18. P. J. Feibelman, J. Chem. Phys., **126**, 237101 (2007).

19. M. de Koning, et al., Phys. Rev. Lett. **96**, 075501 (2006).

20. M. de Koning, et al., Phys. Rev. Lett. **97**, 155501 (2006).

Comment on "Free Energy of Solvation of Simple Ions: Molecular-Dynamics Study of Solvation of Cl⁻ and Na⁺ in the Ice/Water Interface"

Abstract

Salt uptake by ice requires ions to bind strongly near broken H-bonds. Because these favorable binding sites form in oppositely charged pairs, a salt's heat of solution in ice does not converge at low concentration to the sum of ionic heats of solution taken separately. Individual ion solution heats are diminished by the formation energies of free H-bonding defects, amounting to several tenths of an eV each.

Introduction

As it freezes, water rejects most impurity ions to its surface.[1] Thus, little theoretical work has been done to understand the energetics of salt in ice. Recently, though, Smith, Bryk and Haymet[2] conducted classical molecular dynamics simulations of Na^+ and Cl^- solvation in water, in ice and at a water-ice interface, postulating that a microscopic understanding of ion solvation might yield clues to the Workman-Reynolds effect,[3] a "massive charge separation … during the freezing of dilute aqueous solutions" of many different salts, of interest for its possible role in thundercloud electrification.

The simulations of Reference 2 were done separately for Na^+ and for Cl^- ions in periodically-repeated unit cells containing 768 H_2O molecules, with the tacit assumption that solvation energies so obtained would provide a basis for understanding ion thermodynamics in dilute salt solutions. H-bond network topology, however, undermines this assumption. At stake is a corollary of the dominance of H-bond conservation in ice thermodynamics,[4,5] namely that the best ion-hydration structures minimize H-bond breaking while maximizing attraction between water-molecule dipoles and impurity ions.

For an ice simulation cell containing just one of a salt's component ion species, this corollary conflicts with the topological necessity that any H-bond defect formed to hydrate an ion is formed together with a complementary defect. With both cation and anion present, the complementary defect binds to the complementary ion. But, in a cell containing only one ion type, the complementary defect has no energetically favorable place to go. Thus, the sum of separately calculated anion and cation solvation energies does not converge to the salt's heat of solution, no matter how low the concentration. The irreducible difference is the sum of the free, complementary defects' formation energies.

A recent ab initio study estimated a minimum energy of ~1.15 eV to form a pair of infinitely separated topological defects in ice.[6] Thus, on a thermal scale, simply summing cation and anion results underestimates the heat of salt solvation in ice to a very large degree.

Discussion

Smith and Haymet earlier showed[7] that interstitial Na^+ and Cl^- ions bind weakly to a rigid ice lattice, so weakly that, given the 7.9 eV needed to form Na^+ and Cl^- from rocksalt, the 0 K heat of NaCl solution is very endothermic, 6.9 eV. One reason for the weak binding is that Reference 7's ice lattice was purposely held rigid. The other is that in a perfectly H-bonded network, impurity ions are not hydrated; there are no sites surrounded by O atoms, to attract a Na^+, nor sites surrounded by positive H atoms, to satisfy the electrostatic demands of a Cl^-.

The incisive molecular-level question is how such sites may form while minimally disturbing the remainder of the ice crystal. One answer, illustrated in the "square ice"[8] schematic of Figure 1a, is by dissociating a water molecule. Another, illustrated in Figure 1b, is by forming "Bjerrum defect" pairs.[9] In both schematics, all H-bonds are intact except next to the ions, where electrostatic gain compensates the formation energy cost of H-bond breaking.
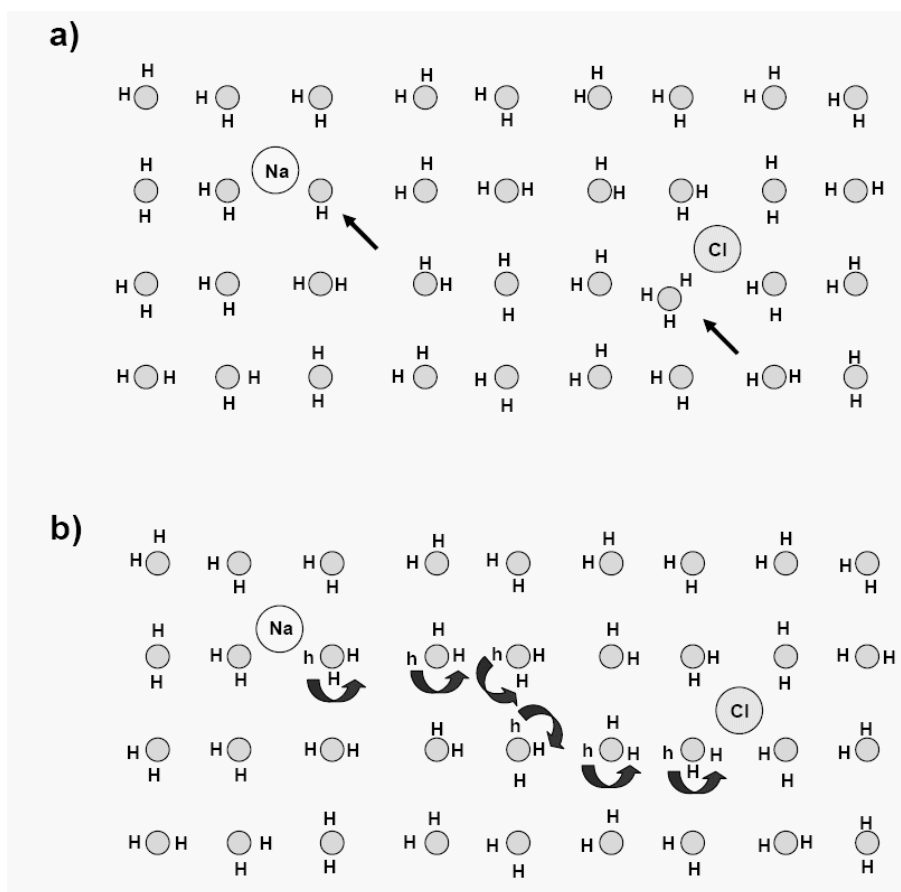
Figure 1. With small, shaded circles representing O atoms, and the letter **h** or **H** representing an H atom, a) a "square ice" model (Reference 7) of an Na^+ and Cl^- pair, hydrated by dissociating a water molecule to form the OH^- and H_3O^+ ions indicated by arrows, and b) hydrated by a Bjerrum defect pair created by rotating lower case **h**s into black **H**s following the arrows.

Figure 1 makes the argument of this note plain. Remove the Na^+ ion from either panel, and the result is a unit cell containing two neighboring O atoms with no positive Na or H ion to screen

their repulsion. Remove the Cl⁻, and one is left with a cell wherein an O-O pair has two H atoms between them, again with no counter-ion to screen their repulsion. Add the solvation energies computed for the cells containing the anion and the cation separately, and one obtains the solvation energy of the ion pair reduced by the formation energies of the pair of complementary topological defects.

To show that this argument is not just hypothetical, I searched atom coordinates from Reference 2's 150 K simulations,[10] for O atoms among whose four nearest neighbor Os, one is particularly distant compared to the ~2.75 Å expected in pure ice. This exercise yielded an O-atom pair separated by 3.41 Å, centered ~9.1 Å from the Cl⁻ in the cell containing that ion (Figure 2a.). The minimum distance between one O of this pair and an H atom bonded to the other is 2.83 Å, much larger than the 1.7 Å typical of an H-bond. The labeled atoms in Figure 2a, accordingly, mark the core of a free L-type Bjerrum defect. Similarly, in the Na⁺-containing simulation cell, an O-O pair separated by 3.42 Å is centered about 6.7 Å from the ion (Figure 2b), and two H atoms belonging to the two Os lie only 2.26 Å from each other. Thus, the labeled atoms in this case are the core of a D-type Bjerrum defect.
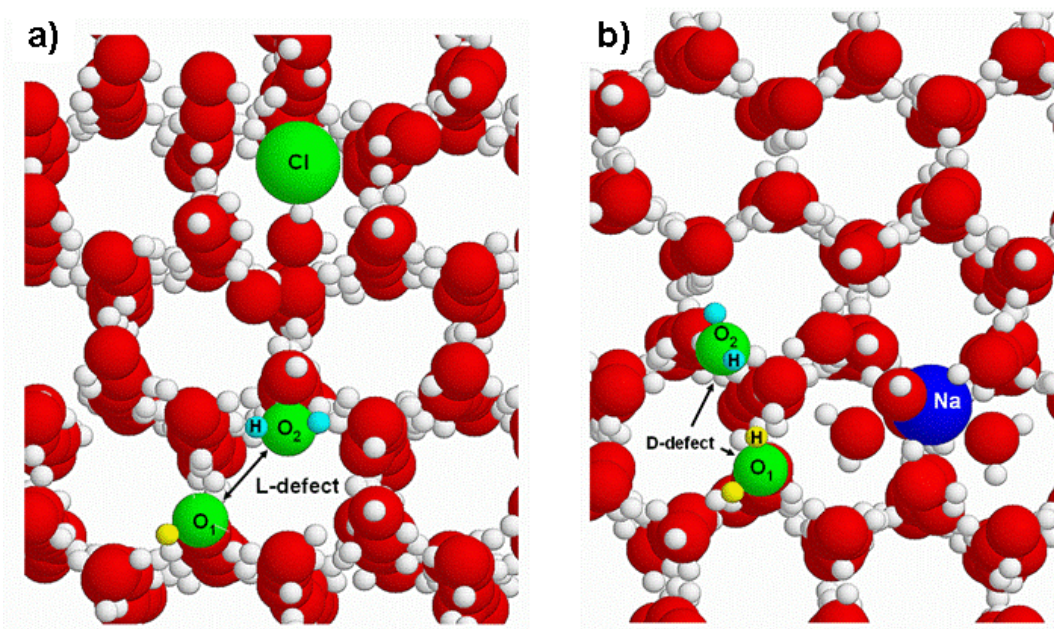
Figure 2. Free Bjerrum defects spawned by hydrating C̃l and Na⁺ ions, in Ref. 2's simulations. a) an L-type defect, at whose core oxygen atoms O₁ and O₂ lie 10.2 Å and 8.1 from the Cl⁻ while the H atom, labeled **H**, (cyan-colored, online) to the left of O₂, lies 2.83 Å from O₁, and b) a free D-type defect, with O₁ and O₂ residing 6.3 and 7.1 Å from the Na⁺ ion, and the labeled H-atoms (cyan- and yellow-colored, online) separated by only 2.26 Å.

Free defects in Smith, et al.'s simulation cells suggest an interpretation of their remark[2] that "insertion of either a Na⁺ or Cl⁻ ion in the smaller (i.e., 96 H₂O molecule) systems caused significant melting, even at 150 K. As a result, the larger ice system (containing 768 H2Os) was used." It is that confinement of free defects was the source of susceptibility to melting. This

would be more significant in 96-molecule cells, whose sites the defects would visit, and disrupt, eight times as often.

Conclusion

A repeat of Reference 2's study with both ions in the simulation cell would provide a solvation energy free of corrections from free-defect formation, and allow an evaluation of the hydration-screened interaction of Na^+ and Cl^- versus separation. One might also learn if the melting noted in small simulation cells is alleviated when all topological defects can be pinned by ions.

References

1. V. F. Petrenko, R. W. Whitworth, Physics of Ice (Oxford University Press, 1999).

2. E. J. Smith, T. Bryk, A. D. J. Haymet, J. Chem. Phys. 123, 034706(2005).

3. E. J. Workman, S. E. Reynolds, Phys. Rev. 78, 254(1950).

4. L. Pauling, J. Am. Chem. Soc. 57, 2680(1935).

5. J. D. Bernal, R. H. Fowler, J. Chem. Phys. 1, 515(1933).

6. M. de Koning, et al., Phys. Rev. Lett. 96, 075501(2006).

7. E. J. Smith, A. D. J. Haymet Mol. Sim. 30, 827(2004).

8. J. F. Nagle, J. Math. Phys. 7, 1484(1966).

9. N. Bjerrum, Kong. Dansk. Vid. Sels. Mat.-fys. Medd. 27, 1(1951).

10. E. J. Smith, private communication.

Salt Permeation and Exclusion in Hydroxylated and Functionalized Silica Pores

Abstract

We use combined *ab initio* molecular dynamics (AIMD), grand canonical Monte Carlo, and molecular dynamics techniques to study the effect of pore surface chemistry and confinement on the permeation of salt into silica nanopore arrays filled with water. AIMD shows that 11.6 Å diameter hydroxylated silica pores are relatively stable in water, whereas amine groups on functionalized pore surfaces abstract silanol protons, turning into NH_3^+. Free energy calculations using an *ab initio* parametrized force field show that the hydroxylated pores strongly attract Na^+ and repel Cl^- ions. Pores lined with NH_3^+ have the reverse surface charge polarity. Finally, studies of ions in carbon nanotubes suggest that hydration of Cl^- is more strongly frustrated by pure confinement effects than Na^+.

Introduction

The permeation and exclusion of salt in nanoconfined aqueous media is central to both selective ion transport and purification or desalination of sea and brackish water. The recent synthesis of highly ordered, nanoporous, functionalized silica thin films [1,2], transport experiments in slitlike nanofluidic channels [3,4], and theoretical study of single wall carbon nanotube (SWNT) membranes[5] underscore the timeliness of using water-filled nanoporous materials to study the effect of pore surface chemistry and confinement on salt hydration.

Confinement has long been known to reduce the hydration free energy or Born self energy (ΔG_{hyd}) of electrolytes in aqueous channels [6,7]. A recent quasichemical theory[8] shows that the inner and outer hydration shell contributions to ΔG_{hyd} in bulk water are comparable. This suggests that nanopores with diameter less than 12 Å can potentially frustrate the outer shell hydration (by ~10 kcal/mol), effectively excluding salts from the pores. Currently nanoporous silica membranes have pore diameters down to 2 nm [1]; functionalizing the pore interior and/or applying atomic layer deposition have the potential to achieve subnanometer pores [2]. In such solid state pores, surface chemistry and charge distributions will also be critically important in controlling ion permeation. While ion transport in thin trans-cell membrane biological channel settings (~20 Ångstrom in length) has been the subject of extensive theoretical studies [7,9-11], porous silica materials have submicron thickness [1,2]. SWNTs, proposed as a new, salt-excluding, reverse osmosis membrane material [5], also have large aspect ratios. In this work, we model these systems as infinitely long pore arrays, and focus on the material aspects, and on computing the potential of mean force (PMF) inside the water-filled channels.

Simulation Methods

First we consider the surface chemistry of model amorphous silica pores (Figure 1). We focus on *p*H at zero charge conditions throughout this work; thus the silica framework is overall charge neutral. While atomistic modeling of water and electrolyte inside wide silica pores have been performed [12], molecular force fields that accurately capture all aspects of silica-water-ion

interactions, polarizability or dielectric properties, and deprotonation of surface silanol (-SiOH) groups [13] do not yet exist. Therefore, we design a model system that permits a combined quantum and molecular dynamics (MD) treatment. Figure 1 depicts the L_x x L_y x L_z = 17.1 x 17.4 x 15:3 Å unit cell of this pore array, periodically replicated in all directions. (1) We first generate an amorphous silica solid of appropriate mass density [14]. (2) Next, a ~11.6 Å diameter cylindrical void is created, and all undercoordinated Si atoms are terminated with -OH. The unit cell contains 70 Si, 158 O, and 38 H atoms. This diameter would imply 6.8 silanol groups per nm^2 if the pore is featureless. However, the pore surface is corrugated and a ~3 Å diameter passage exists between adjacent unit cells; thus actual silanol density should be closer to the experimental value ($5/nm^2$) [15]. (3) The pore geometry is optimized using the VASP density functional theory (DFT) code [16] with the PW91 exchange correlation functional [17]. (4) Freezing all silica atoms except the surface silanol protons, we use the grand canonical Monte Carlo (GCMC) technique to determine the water content [18]. We apply the SPC/E water model [19] and silica force fields with partial charges fitted to the *ab initio* electrostatic potential of a $Si_{14}O_{21}H_{30}$ cluster [20], and 12/6 Lennard-Jones (LJ) terms fitted to DFT/PW91 calculations of water adsorption on crystalline silica surfaces [21]. On average, 41 H_2O molecules reside in the unit cell.
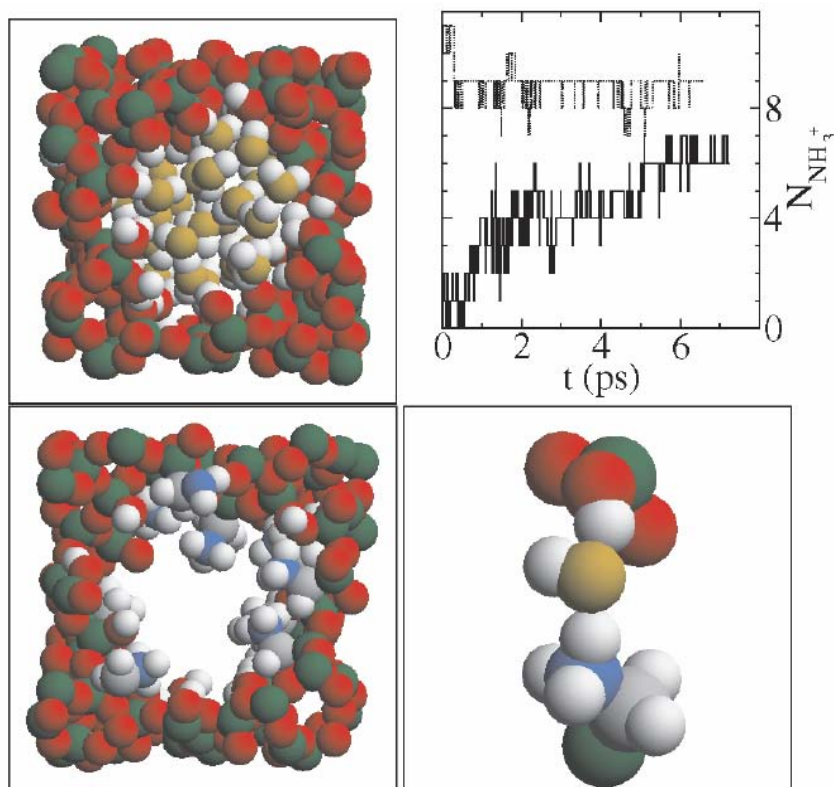
Figure 1. Counterclockwise from upper left: water-filled silica pore unit cell; silica pore functionalized with -$CH_2NH_3^+$ (water removed for clarity); expanded view of a -CH_2HN_2 group in the process of abstracting a proton from H_2O; total number of -NH_3^+ groups as a function of time in two AIMD trajectories, starting with 0 and 11 -NH_3^+, respectively. The first three panels are AIMD snapshots, and periodic boundary conditions apply in all three directions. Green spheres: Si; red/yellow: O; blue: N; white: H; gray: C.

Strained silica rings are known to react with H_2O to form silanol groups with low energy barriers [22], in picosecond time scales at $T = 300$ K [23]. To examine the stability of our model hydroxylated pore in water, we conduct *unconstrained ab initio* molecular dynamics (AIMD) at an elevated temperature of 375 K using the DFT code/method mentioned above. A 0.5 fs time step and molecular mechanics preequilibrated starting configurations are used. No chemical reaction or H_2O incorporation into the silica framework occurs within ~4.5 ps, showing that our model pore array is relatively stable at this pH.

Functionalized pores behave qualitatively differently. Experimentally, a fraction of the pore surface OH groups have been successfully replaced with $-(CH_2)_3NH_2$ groups[2]. Thus, in a second model, we randomly replace 11 of the 38 surface -SiOH in our unit cell with $-SiCH_2NH_2$. Because silanol groups are acidic and amines are basic, proton transfer may occur. However, $-NH_3^+$ is usually stabilized with hydrogen bonding to 3 H_2O molecules [24], and there are only 35 H_2O in the pore. To determine the $-NH_3^+$ content, we apply AIMD. We examine two initial conditions—one with all $-NH_2$ terminations, the other with all $-NH_3^+$, with the 11 -SiOH closest to the ammonium groups deprotonated to preserve charge neutrality (Figure 1). We graft a CHARMM22 [25] and DFT/PW91-fitted description of the amine/ammonium groups to our silica force fields, and use them to preequilibrate the initial configurations.

Results and Discussion

Figure 1 depicts the evolution of the number of $-NH_3^+$ (N_{NH3+}). The AIMD trajectory starting with all $-NH_3^+$ rapidly equilibrates to $N_{NH3+} \sim 8{:}8$. In the one starting with $N_{NH3+} = 0$, although equilibration of the titratable protons has not been achieved in 7 ps, most $-NH_2$ have turned into $-NH_3^+$, either by abstracting a proton directly from a nearby SiOH or by indirect transfer via a bridging H_2O (Figure 1). The fast proton hopping rate is reminiscent of that between adjoining $-NH_2/-COOH$ groups in glycine [24]. Thus, AIMD shows that a majority of the amine groups exist in water-filled pores as $-NH_3^+$, stabilized by hydrogen bonds to framework silica oxygens as well as water. Hereafter we assume they are all $-NH_3^+$. NH_3^+ protrude into the pore center while the compensating SiO^- reside closer to the pore surface. As will be shown, this yields a charge distribution, and a PMF [$W(x, y, z)$] for ions, dramatically different from hydroxlyated pores.

Next, we use the aforementioned silica force fields to sample $W(x, y, z)$ for Cl^- and Na^+. (AIMD is too costly for this purpose.) We use LJ-based ion force fields [26], with σ_{Na+} adjusted to 2.4 Å, so that in bulk water Cl^- and Na^+ exhibits ΔG_{hyd} of -90.9 and -88$:$8 kcal$/$mol, respectively. We apply umbrella sampling to obtain $\overline{W}(z)$, the PMF averaged over x, y, by adding a harmonic bias along z but otherwise allowing the ions to move freely. $\overline{W}(z)$ is shifted to match thermodynamic integration (TI) results for $W(x, y, z)$ along the pore axis, $x = L_x/2$, $y = L_y/2$, in sampling windows where the pore center is found to be most favored. Electrostatic contributions to TI are computed by applying a 2-point integration formula to the ionic charge [27]. The packing contribution to TI from inserting uncharged LJ spheres in water is about 1 kcal$/$mol, and further should largely cancel between bulk and confined water; thus it will be neglected. 15-90 ns and 0.2-1 ns MD trajectories are used for each umbrella sampling window/TI calculation.

Figure 2(a) highlights the dramatic effect of confining ions inside narrow, water-filled, hydroxylated pores. Cl⁻ (Na⁺) is strongly destabilized (stabilized). The large, almost equal but opposite effect on Cl⁻/Na⁺ suggests that the repulsion/attraction is due to electrostatic interactions with the polar pore surface [28]. Figure 2(c) shows that functionalization with 11 NH_3^+ groups (and compensating SiO^-) indeed reverses this polarity, except for a Na^+ trap site.
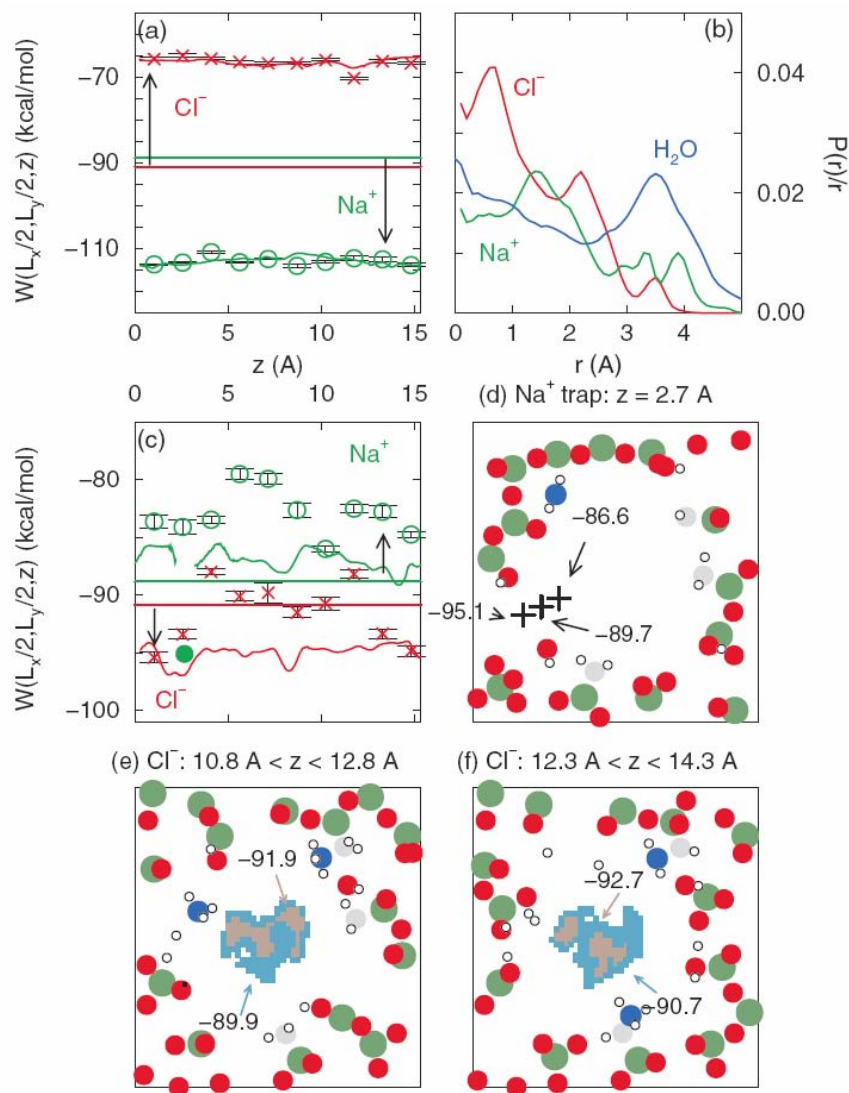
Figure 2. (a), (b) refer to hydroxylated pore arrays, (c)-(f) to -$CH_2NH_3^+$ lined sytems. (a), (c) Crosses/open circles: potential of mean force for Cl⁻/Na⁺ frozen along the pore axis. Solid curves: umbrella sampling $W(z)$ for *unconstrained* Cl⁻ (red) and Na⁺ (green). Horizontal lines: ΔG_{hyd} for Cl⁻/Na⁺ in bluk water. Panel (c), filled circle: Na⁺ trap site at the pore surface. (b) Radial distribution of Cl⁻ (red), Na⁺ (green), and H_2O (blue) in hydroxylated pores. (c) Na⁺ at and near trap site (pluses) at $z = 2.7$ Å; (e), (f) Regions where Cl⁻ free energy is at or below the listed values are shown in color. Atom key: see Figure 1; water removed for clarity.

The PMF depicted in Figure 2 is computed by placing one ion in the unit cell (Figure 1). Our objective is the dilute limit, i.e., for a single ion in an $n \to \infty$ pore array, with a simulation cell (''supercell'') made up of n^3 unit cells replicated n times periodically in all directions. Table 1

shows that $W(L_x/2, L_y/2, z)$ for $n = 1$ is already converged to 2 kcal/mol—but only after we have added the Ewald self-energy, which is large (-27.3 kcal/mol) for $n = 1$ and is appropriate because the water present in the pore array effectively screens the ion-ion image interaction. Extrapolating to $n = 3$, the axis of the hydroxylated pore repels (attracts) Cl^- (Na^+) by an average of -25:8 (-22:0) kcal/mol relative to bulk liquid water.

Table 1. $W(L_x/2, L_y/2, 13.3 \text{ Å})$/kcal/mol in hydroxylated pore supercells, computed via thermodynamic integration.

Ion/cell	$n = 1$	$n = 2$	$n = 3$
Cl^-	-66.3 ± 0.3	-62.9 ± 0.7	-64.5 ± 0.8
Na^+	-112.3 ± 0.5	-111.5 ± 0.6	-110.1 ± 0.8

These results are slightly force field dependent. Applying TI to the partial charges and LJ parameters of another silica force field [12] yields $W(L_x/2, L_y/2, z)$ for Cl^-/Na^+ that differ by ~4 kcal/mol. The results also depend on pore surface structure and silanol coverage.

In hydroxylated pores, the variations in $\overline{W}(z)$ and in $W(L_x/2, L_y/2, z)$ computed via TI at 10 equally spaced positions along the pore axis agree to within 2 kcal/mol [Figure 2(a)], indicating that the latter is a good measure of ion permeability in such pores. This is consistent with the fact that the radial density of ions divided by r (the distance from the pore axis, and volume element in polar coordinates), $P(r)/r$, is relatively r independent, and there are no trap sites. The H_2O oxygen $P(r)/r$ in hydroxylated pores [Figure 2(b)] trails off at $r = 4:25$ Å yielding our estimate of an 11.6 Å pore diameter after accounting for the size of H_2O. The two peaks in $P(r)/r$ suggest that this pore can accommodate one water molecule at the center and a water shell around it. Overall, Cl^- is found to prefer the pore center [Figure 2(b)]. Its $P(r)/r$ also exhibits features at the ''trough'' of the H_2O radial distribution. Na^+ has a higher concentration at the -OH line pore surface.

In the NH_3^+ lined model silica pores, $W(L_x/2, L_y/2, z)$ is less useful. The free energy contours in Figures 2(e) and 2(f) show that Cl^- exhibits more tendency to sample the pore surface near NH_3^+ groups. Hence, in some umbrella windows, a radial $0.5r^2$ kcal/mol/Å^2 potential is applied, and its effect is removed by reweighting, to facilitate sampling. Na^+ can also reside off center to avoid protruding NH_3^+ (not shown). With the pore interior now generally unfavorable, Na^+ is found to be strongly trapped at the aforementioned passageway in the pore wall, which is devoid of NH_3^+ groups [Figures 2(c) and 2(d)]. One-dimensional umbrella sampling does not readily converge near this Na^+ trap, but TI reveals that it is deep and localized [Figure 2(d)]. $W(x,y,z)$ rapidly relaxes to pore centerlike values as r decreases, yielding a large free energy barrier against escape. Thus, this trap should always be occupied by an immobile Na^+, which does not readily take part in ion *transport* but should be considered part of the functionalized silica framework. It will repel other Na^+, making the pore even more unfavorable towards Na^+. Thus we expect that the pore polarity reversal of silica pores suggested by the Na^+ $\overline{W}(z)$ [Figure 2(c)] is qualitatively unchanged by this rare, deep trap. Indeed, polarity reversal via NH_3^+ functionalization has recently been demonstrated in 40 nm wide nanofluidic channels [4]. Figure 2(c) demonstrates this general behavior, but also points out that incomplete NH_3^+ coverage may lead to isolated cases of Na^+ trapping.

The results discussed so far convolve confinement and pore surface polarity effects. To isolate the pure confinement contribution [6], we also consider water-filled (18, 18) SWNT placed in a 18 x 18 Å^2 square lattice. This nanotube has an 11.4 Å pore diameter, similar to our silica pore, but carries no charges. We apply force fields that reproduce the experimental graphite-water contact angle [29]. GCMC calculations show that this SWNT exhibits a water density similar to that in our silica pores: 46 H_2O molecules per 17.04 Å tube length.

Figure 3(a) shows that n = 1 supercells converge TI-predicted $W(L_x/2, L_y/2, z)$ to within 2.5 kcal/mol, similar to silica pores [28]. SWNT pores of this size thus show little confinement penalty for Na^+, in agreement with Reference [30], but Cl^- is surprisingly unfavorable by 12.6 kcal/mol relative to bulk water. This ''pure'' confinement effect is smaller than, and nonadditive to, the electrostatic contribution in hydroxylated silica pores. The $P(r)/r$ depicted in Figure 3(b) shows that layering is more pronounced for H_2O in SWNT than in silica pores, where there is substantial surface inhomogeneity. Na^+ is lodged between two shells of water, while Cl^- prefers the pore center [31]. Preferential transport of Na^+ over Cl^- has been reported for model transmembrane channels [31,32]; the asymmetry between Cl^- and Na^+ likely arises from outer water shell contributions, and is related to ion size, charge, and the hydrogen bond network of first hydration shell water. It may be missed by a purely dielectric continuum treatment of water [6,7,33].
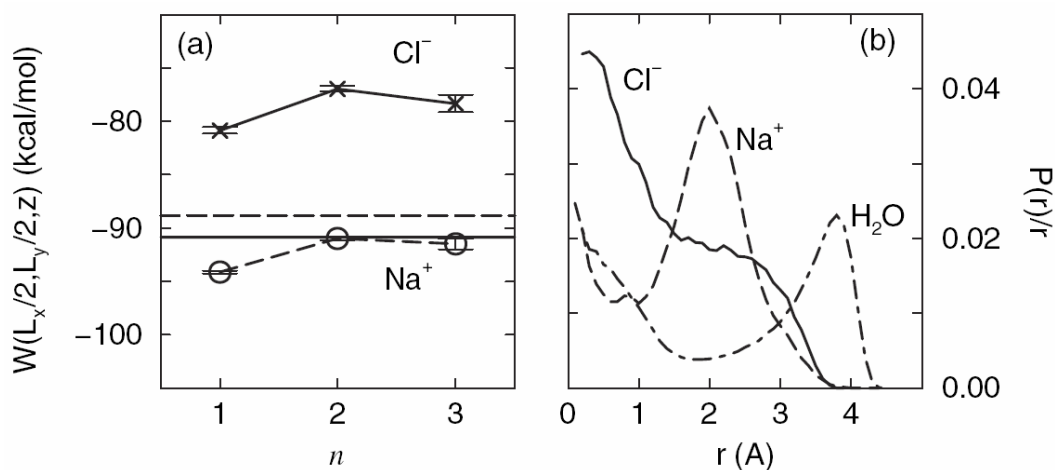
Figure 3. (a) z-independent PMF of ions along the pore axis of a SWNT array as supercell size n varies. Solid lines/crosses: Cl^-; dashed lines/circles: Na^+. (b) Radial distribution for Cl^- (solid line), Na^+ (dashed line), and H_2O (dot-dashed line).

Conclusion

In conclusion, we have shown that 11.6 Å diameter silica nanoporous membranes dramatically alter ion permeability. Hydroxylated silica pores repel (attract) Cl^- (Na^+) by ~28(22) kcal/mol. Amine groups on functionalized silica pores turn into $-NH_3^+$ by abstracting protons from silanol groups. This reverses the pore polarity, and molecular force fields now predict that the pore center slightly attracts Cl^- and repels Na^+. However, Na^+ can become trapped at surface sites. Pure confinement effects are asymmetric for these ions. Based on these results, a viable way to

exclude both ions may be to use alternating hydroxylated and amine-functionalized silica pore segments. In that case, ion trapping, pH and multiple ion effects, and contact ion pair formation may occur, and may strongly affect ion transport.

References

1. D. A. Doshi et al., Science 290, 107 (2000).

2. N.-G. Liu, R. A. Assink, B. Smarsly, and C. J. Brinker, Chem. Commun. (Cambridge) 10, 1146 (2003).

3. D. Stein, M. Kruithof, and C. Dekker, Phys. Rev. Lett. 93, 035901 (2004).

4. R. Fan et al., Phys. Rev. Lett. 95, 086607 (2005).

5. A. Kalra, S. Garde, and G. Hummer, Proc. Natl. Acad. Sci. U.S.A. 100, 10 175 (2003).

6. A. Parsegian, Nature (London) 221, 844 (1969); P. C. Jordan, Biophys. J. 39, 157 (1982).

7. O. Beckstein, K.-H. Tai, and M. S. P. Sansom, J. Am. Chem. Soc. 126, 14 694 (2004), and references therein.

8. L. R. Pratt and S. B. Rempe, in Simulation and Theory of Electrostatic Interactions in Solution, edited by L. R. Pratt and G. Hummer (ALP, New York, 1999), p. 172.

9. S. Holmann, S. Nielsen, and P. Agre, Aquaporins (Academic, New York, 2001).

10. B. Roux, T. Allen, S. Berneche, and W. Im, Q. Rev. Biophys. **37**, 15 (2004).

11. C. Dellago, M. M. Naor, and G. Hummer, Phys. Rev. Lett. **90**, 105902 (2003).

12. A. Kohlmeyer, C. Hartnig, and E. Spohr, J. Mol. Liq. **78**, 233 (1998), and references therein.

13. J. R. Rustad *et al.*, J. Colloid Interface Sci. **198**, 119 (1998).

14. D. A. Litton and S. H. Garofalini, J. Appl. Phys. **89**, 6013 (2001); C. D. Lorenz *et al.*, Tribol. Lett. **19**, 93 (2005).

15. L. T. Zhuravlev, Colloids Surf. A **173**, 1 (2000).

16. G. Kresse and J. Furthmu¨ller, Phys. Rev. B **54**, 11 169 (1996); Comput. Mater. Sci. **6**, 15 (1996).

17. J. P. Perdew and Y. Wang, Phys. Rev. B **45**, 13 244 (1992).

18. For the MD/MC codes used, see: S. J. Plimpton, J. Comput. Phys. **117**, 1 (1995); M. G. Martin and A. P. Thompson, Fluid Phase Equilib. **217**, 105 (2004).

19. H. J. C. Berendsen, J. R. Gridera, and T. P. Straatsma, J. Phys. Chem. **91**, 6269 (1987).

20. M. Tsige *et al.*, J. Chem. Phys. **118**, 5132 (2003).

21. $\sigma_{si} = 0.1$ kcal/mol; $\sigma_o = 0.155$ kcal/mol; $\sigma_{si} = 4$ A; $\sigma_o = 3.1656$ A; $q_o = -0.60e$ ($-0.74e$) for bulk (silanol) oxygens; $q_H = 0.43e$. Each q_{si} is adjusted to yield local charge neutrality. Optimal O-H bond length and Si-O-H angle are 0.968 A and 120.0°, with harmonic force constants of 596 kcal/mol/A^2 and 22.1 kcal/mol/rad^2.

22. R. M. van Ginhoven, H. Jo´nsson, B.-G. Park, and L. R. Corrales, J. Phys. Chem. B **109**, 10 936 (2005).

23. S. H. Garofalini, J. Non-Cryst. Solids **120**, 1 (1990).

24. K. Leung and S. B. Rempe, J. Chem. Phys. **122**, 184506 (2005).

25. A. D. MacKerell *et al.*, J. Phys. Chem. B **102**, 3586 (1998).

26. S. Rajamani, T. Ghosh, and S. Garde, J. Chem. Phys. **120**, 4457 (2004).

27. D. Asthagari, L. R. Pratt, and H. S. Ashbaugh, J. Chem. Phys. **119**, 2702 (2003).

28. We use Ewald sums with tin-foil boundary conditions. We do not reference our PMF to the silica membrane surface, which can have different functionalization and charge distributions than that inside the pore. Thus our PMF excludes extrinsic potential effects [A. Redblack and J. Grindlay, J. Phys. Chem. Solids **36**, 73 (1975)]. The silica pores can be thought of as infinite cylinders with dipolar pore walls.

29. T. Werder *et al.*, J. Phys. Chem. B **107**, 1345 (2003).

30. C. Peter and G. Hummer, Biophys. J. **89**, 2222 (2005).

31. Polarizable force fields predict higher Cl^- concentrations at interfaces [E. C. Brown *et al.*, J. Phys. Chem. B **109**, 7934 (2005)].

32. P. S. Crozier *et al.*, Biophys. J. **81**, 3077 (2001). Here the pore is smaller than the Cl^- first hydration shell.

33. M. Carrillo-Tripp, H. Saint-Martin, and I. Ortega-Blake, Phys. Rev. Lett. **93**, 168104 (2004).

Coordination Numbers of Alkali Metal Ions in Aqueous Solutions

Abstract

The level of complexity with which any biological ion interaction mechanism can be investigated, whether it is a binding mechanism in proteins or a permeation mechanism in ion channels, is invariably limited by the state-of-the-art of our understanding of the characteristic properties of ion solvation. Currently, our understanding of the energetic properties of ion solvation in aqueous phase is considered adequate enough to have helped us obtain satisfactory descriptions of the role of energetics in several biological ion interaction processes. In contrast, the lack of consensus among all the experimental structural hydration data determined more than 10 years ago, particularly regarding ion hydration numbers, has limited us to nothing better than speculation regarding the roles of local spatial environments in these mechanisms. Here we revisit experimental and theoretical work applied to probe hydration numbers of three alkali metal ions, Li^+, Na^+ and K^+, and analyze them to clarify the current state-of-the-art of our understanding of their structural hydration properties. We find that with substantial improvements over the past 10 years in areas of experimental techniques, data analysis strategies, and theoretical and computational approaches for interrogating ion hydration structures, there is now growing consensus regarding the hydration numbers of these ions. We see that under physiological conditions, *ab initio* methods suggest that all three ions prefer strong coordination with exactly 4 water molecules, a result we find consistent with some older experimental measurements. *Ab initio* molecular dynamics (AIMD) simulations invariably identify additional "loosely" coordinated water molecules at the far slopes of the principle maxima of the radial distribution profiles for Na^+ and K^+ ions. We suggest that these statistical admixtures of additional oxygen atoms have resulted in the most recent experimentally determined hydration numbers of Na^+ ions to be 5 and K^+ ions to be 6.

Introduction

The characterization of ion solvation properties in aqueous phases has been an area of active research and interest for close to a century. Research in this area began as early as the 1930s since it was of particular interest to chemists who pursued investigations of chemical reactions in aqueous media. Their investigations required a detailed understanding of the nature of ion solvation in terms of both energetics as well as the formation of solvent microstructures around ions. To achieve this, comprehensive studies were carried out in water that included measurements of ion-water interaction energies, aqueous phase ion solvation energies, partial molar volumes of ions, average hydration numbers of ions, and ion-water distances. These studies now take on even greater significance as current biological research targets a molecular level understanding of ion solvation in biological environments, where interest lies in the mechanisms controlling ion binding to biomolecules and selective ion permeation through narrow channel proteins. A precise molecular level understanding of these biological processes holds tremendous potential for yielding spatial and electrical design parameters for next-generation biomimetic devices that control ion movements between aqueous and biological environments (for example, see Reference [1]). These devices can in turn provide improved

solutions to such diverse problems as water desalination and implantable electrical power generation.

Since water is the reference environment in biology, a precise molecular knowledge of ion hydration properties is a necessary prerequisite for developing mechanistic conclusions about biological control of ion movements. Although not strictly separable, many investigations have addressed ion hydration energetics apart from the geometries of their hydrated structures. In the past few decades, the energetic properties of ion hydration have been considered sufficiently understood so as to not hamper our abilities to describe the role of energetics in several physical and biological phenomena. They have also been appropriately parameterized into classical force fields and are now used on a regular basis to investigate diverse scientific and engineering problems. At the same time, however, a distinct lack of consensus [2] characterizes the structural properties of hydrated ions, especially their hydration numbers determined more than 10 years ago by experimental methods. Even the hydration properties of the simple alkali metal ions, though repeatedly investigated using multiple theoretical and experimental techniques, yet appear to reflect ambiguities in terms of hydration structure. This dissension limits our abilities to assign concrete and unambiguous roles for the structural effects of local environments on ion phenomena, a critical issue in understanding the molecular mechanisms driving ion binding and selective permeation in biological systems.

Here we summarize the older literature and consider current investigations of the hydration properties of three simple alkali metal ions: Li^+, Na^+, and K^+. With improvements in methods for probing liquid state structure, we find that the earlier confusion is giving way to a growing consensus, which may surprise some investigators, regarding the hydration numbers of these ions.

Experimental Hydration Numbers

Table 1 lists hydration numbers determined experimentally for the first three alkali metal ions more than 10 years ago. Hydration numbers reflect the average number of water molecules occupying the nearest coordination volume around an ion. Prior to 1996, we see from Table 1 that the experimental hydration numbers of Li^+ ions vary between the values of 3 and 6. The hydration numbers of Li^+ were considered to be dependent on salt concentrations during this period [3,4], with higher salt concentrations resulting in lower hydration numbers. Since these dependencies were measured well beyond salt concentrations of 1M in all cases, they are not directly relevant to investigations of biological systems. Over the same time frame, scattered hydration numbers appear for Na^+ ions as well, with values all the way from 4 through 8. Note that the hydration number of Na^+ evaluated from neutron diffraction data stands out as exceptionally different from those determined using any other experimental technique. Hydration numbers for K^+ ions similarly span the range between 4 and 8, with the neutron diffraction data once again reproducing an exceptionally different value.

Table 1. Hydration numbers of ions estimated from experiments carried out prior to the year 1996.

M^+	n_{M^+O}	Method	Year [Ref.]
Li^+	4	Neutron Diffraction	1973 [61]
	4	X-ray	1973 [62]
	4	X-ray	1975 [63]
	4	Raman Spectroscopy	1978 [64]
	4	Neutron Diffraction	1979 [65]
	4	X-ray	1980 [66]
	3-6[a]	Neutron Diffraction	1980 [3]
	6	X-ray	1981 [67]
	5	X-ray	1983 [68]
	4	X-ray	1983 [69]
	4	X-ray	1984 [70]
	6	X-ray	1987 [71]
	5	Neutron Diffraction	1991 [72]
	3-6[a]	Neutron Diffraction	1996 [4]
Na^+	4	X-ray	1975 [73]
	4	Raman Spectroscopy	1978 [64]
	6	X-ray	1980 [74]
	8	Neutron Diffraction	1980 [75]
	4	X-ray	1980 [66]
	5	X-ray	1989 [76]
K^+	6	X-ray	1957 [77]
	4	X-ray	1958 [78]
	5	X-ray	1969 [79]
	6	X-ray	1980 [66]
	8	Neutron Diffraction	1980 [75]

[a]Dependence of hydration numbers on salt concentrations: concentrations close to 1 M correspond to hydration numbers of 6, and higher concentrations correspond to lower hydration numbers.

Both neutron and x-ray diffraction techniques determine [5] differential scattering cross-sections that are proportional to weighted sums of partial structure factors in polyatomic systems, like salt solutions. These partial structure factors can in theory be determined with high accuracy, and can yield accurate partial pair-distribution functions ($g_{M-O}(r)$). Following the traditional statistical definition of hydration number, these partial pair-distribution functions (or radial distribution functions) can then be integrated up to their first absolute minima, which should define the nearest volume of coordinating solvent molecules, to obtain hydration numbers (n_{M-O}) of ions. This entire process, however, requires very high spectral resolutions to define the critical first peaks and minima in radial distribution functions and thus to obtain accurate hydration numbers. Other challenges that further compound structural inferences arise in

obtaining absolute normalizations of measured intensities and treating momentum truncations during data analysis. These difficulties make diffraction measurements on liquids particularly challenging, and data analysis efforts generally complicated, requiring a variety of delicate corrections and careful interpretations to infer ion coordination numbers. Presumably these are the challenges that resulted in exceptional ambiguities seen in hydration data numbers estimated in the past [6].

In the last 10 years or so, several developments have significantly advanced these methods both in terms of data gathering and data analysis (see Reference [6] for the most recent review). Table 2 summarizes the consequent experimental results obtained most recently for the hydration numbers of the small alkali metal ions: 4 for Li^+, 5 for Na^+, and 6 for K^+ ions. Note that the hydration number of 4 for Li^+ ion derives from using older neutron diffraction data [4], from which a hydration number of 6 had been inferred, and reanalyzing it using a more sophisticated data analysis technique [7]. In general, we note that advancements in neutron diffraction techniques and data analysis methods lead to coordination numbers considerably lower than those determined earlier using the same experimental methodology. Considering these hydration numbers to be the best experimental estimates to date, analysis of coordination numbers determined by diffraction reveals a unique pattern in ion hydration numbers. There appears to be a distinct structural feature associated with each hydrated ion wherein each unit move down the periodic table increases the hydration number by the same amount.

Table 2. Hydration numbers of ions estimated from most recent experiments.

M^+	n_{M^+O}	Method	Year [Ref.]
Li^+	4	Neutron Diffraction[a]	2006 [7]
Na^+	5	Neutron Diffraction	2006 [42]
K^+	6	Neutron Diffraction	2001 [80]
	6	Neutron Diffraction	2006 [81]

[a]Pair-wise radial distribution functions re-evaluated using more sophisticated analysis methods [7] from older [4] neutron diffraction data.

While experimental diffraction studies often rely on molecular models for support in data interpretation, computational and theoretical approaches can be used independently of experiments to probe the structural features of hydrated ions.

Theoretical Approaches to Probe Hydration Structures

Molecular Dynamics Employing Parameterized Force Field Models
It is a common misconception that a molecular dynamics calculation employing a parameterized (empirical) force field can be utilized to *predict* the structural properties of ion solvation. Use of such methods to probe the effect of parameters and functions in order to *understand* the nature of ion solvation is, however, an entirely different matter. In the traditional method of constructing

force fields, which is by no means a straightforward task, the solvation properties deemed necessary for a certain investigation are plugged in via optimization of parameters belonging to a set of mathematical expressions chosen specifically to describe those solvation properties. Therefore, such force fields can at best be considered a reflection of our current understanding of the nature of particle interactions, although at the same time they are constrained by limitations in computing power. This implies that, in principle, such parameterized force fields should only be utilized to probe those properties of ion solvation for which they were originally parameterized, and should *not* be used for the purpose of predicting other solvation properties of ions.

For the sake of argument, we consider here two of the most commonly used ion force fields in theoretical biology, one that has been incorporated [8] into the CHARMM27 [9] package of force fields and the other that has been incorporated [10] into the OPLS-AA [11] package of force fields. In both these force fields, the overall strategy employed to generate ion parameters consisted of two separate steps. In the first step, the parameters describing water molecule interactions were optimized to reproduce certain experimental bulk water properties, and then in the next step these preset water parameters were used to optimize the 6-12 Lennard-Jones parameters of the ions. Obvious assumptions made in the construction of the ion force fields were that the 6-12 Lennard-Jones functional form and the previously optimized functions and parameters describing the water molecules could capture the new interaction of water molecules with ions. In adherence to tradition (instead of 'In fact'), in both cases the 6-12 Lennard-Jones parameters of Na^+ and K^+ ions were hand picked to reproduce a subset of ion hydration properties, the experimental values of hydration free energies and ionic radii, without any special care administered to reproduce other properties like hydration numbers.

Table 3 lists the hydration numbers of Na^+ and K^+ ions obtained [12] as a result of using these force fields. We clearly see that the simulated hydration numbers are higher than those estimated by the most recent experiments. Moreover, the computed K^+ ion hydration numbers of 7 were in fact never estimated by any of the previous experiments. Furthermore, due to the non-linear nature of Lennard-Jones interactions, the two experimental observables used as targets for parameterization could just as well have been reproduced by an alternate set of parameters, which implies that reproducing two experimental hydration properties does not guarantee that all other hydration properties would be simultaneously and automatically reproduced. Therefore these force fields are appropriately applied to simulate the energetic properties of ion solvation, but not to predict structural properties like radial distributions of ligand molecules around ions. When such limitations of using these force fields are overlooked, inconsistent results can arise. For example, a force field used to simulate the energetic solvation properties of a certain ion may in fact simultaneously simulate the structural properties of an entirely different ion. Thus interpretations regarding the structural properties of ion solvation derived from simulations employing such force fields should be dealt with carefully as they can be misleading. In the cases of Na^+ or K^+ ions, this is true even if that force field predicts a coordination number that is off by a single unit since the most recent experimental data show that each of these ions has characteristically distinct hydration numbers that differ by exactly one unit.

Table 3. Hydration numbers of ions computed [12] using two of the most commonly used empirical (parameterized) force fields in theoretical biology. Both these ion force fields describe ion water interactions using simple 6-12 Lennard-Jones functions, and do not explicitly account for atomic polarizabilities or multi-body effects on ion-water interactions.

M^+	CHARMM27 [8]	OPLS-AA [10]
Na^+	6	6,7
K^+	7	7

The two force fields considered above employ pair-additive potentials to describe interactions between ions and water molecules, which means the interaction between an ion and any given water molecule is assumed to be independent of all other atoms in the system. Several investigations [13-26], some of which were carried out as early as the 1970s, have identified certain non pair-additive interactions that are critical to describing atomic-level details of ion solvation. These include the classical dipole polarizabilities of water molecules and the influence of other water molecules on the interaction between a given ion-water pair (many-body interactions). Inclusion of such effects can be expected to enhance the predictive capabilities of empirical force fields. Even with access to large computing resources, however, this is not a straightforward task since the degree of required theoretical accuracy must be balanced with computational efficiency. Inclusion of such effects generates complicated target potential surfaces that require the use of more sophisticated approaches for optimization purposes, and higher dimensionalities in mathematical functions that increase computational expense tremendously. This area of research is being actively pursued across several laboratories, and there is still much work needed to arrive at a single justifiable approach toward constructing such force fields [27-32].

Nonetheless, several noteworthy attempts have been made toward construction of such enhanced force fields that incorporate these additional interactions. Table 4 lists the hydration numbers of ions computed as a result of using these enhanced force fields. We see that in the case of Li^+ ions, the computed hydration numbers exactly match those estimated by recent experiments. For Na^+ and K^+ ions, however, the computed hydration numbers are still almost always higher than those obtained from the most recent experiments. This clearly exemplifies our earlier argument that work is still required to accurately capture the details of ion solvation when using empirical force fields. In such a scenario, the role of making predictive statements regarding structural details of ion solvation mechanisms is better left to either experiments or higher levels of theory that do not explicitly rely on parameterization of particle interactions. In the following section, we review the work done so far using *ab initio* methods to determine hydration numbers of the first three alkali metal ions.

Table 4. Hydration numbers of ions computed using force fields that explicitly account for atomic polarizabilities (P) and/or multi-body effects on ion-water interactions (M).

M^+	n_{M^+O}	Method	Year [Ref.]
Li^+	4	Molecular Dynamics with P + M	2004 [24]
	4	Molecular Dynamics with M	2004 [24]
	4	Molecular Dynamics with P	2006 [82]
Na^+	6	Optimization with P + M	1985 [17]
	5,6	Monte Carlo with P + M	2003 [83]
	6	Molecular Dynamics P	2003 [12]
	7	Molecular Dynamics P + M	2004 [24]
	6	Molecular Dynamics with M	2004 [24]
	6	Molecular Dynamics with P	2006 [82]
K^+	4+2	Optimization with P + M	1985 [17]
	7,8	Monte Carlo P + M	2003 [83]
	7	Molecular Dynamics P	2003 [12]
	7	Molecular Dynamics P	2006 [82]

Ab Initio Methods

Ab initio (quantum) calculations do not rely on parameterization to the extent or variety present in empirical force fields [33]. The nature of parameterizations present in the functionals used in density functional methods to describe correlated electron interactions are invariably also present in empirical force fields since results of quantum calculations are typically used as benchmarks for parameterizing empirical force fields. Including the variety of functionals available for describing atomic systems, we identify two other issues that can potentially affect the reliability of *ab initio* investigations on ion solvation: sampling and system size. In *ab initio* approaches that involve generation of dynamical trajectories, as in *ab initio* molecular dynamics (AIMD) simulations, the associated computational expenses currently prohibit effective sampling in systems containing a large number of atoms. Currently, AIMD simulations have access to a few tens of picoseconds of time-scales and most investigations are also limited to system sizes containing a few hundreds of atoms. We present below results from liquid state *ab initio* studies carried out to investigate hydration structures of the three ions, discussing alongside the effect that each of the three issues can have on the reliability of these investigations. The results on hydration numbers of the three ions have been summarized in Table 5.

Table 5. Hydration numbers of ions estimated using *ab initio* approaches. The functionals represent different implementations of gradient-corrected density functional theory except for "HF", which stands for Hartree-Fock theory. Numbers joined by a "+" refer to subpopulations found in the first peak of the ion-oxygen pair distribution functions: an innermost population of tightly coordinating water molecules and a more distant population of "loosely" coordinating water molecules, respectively. Parentheses around hydration numbers refer to the preferred number of tightly coordinating water molecules.

M^+	n_{M^+O}	Method		Year [Ref.]
		Approach	Functional	
Li^+	4	AIMD	BLYP	2001 [84]
	4	AIMD	PW91	2000 [45]
	(4)	Quasi-chemical	B3LYP	2000 [44,45]
	4	QM/MM	HF	2002 [85]
	4	QM/MM	B3LYP	2002 [85]
Na^+	6	QM/MM	HF	1998 [34]
	5	AIMD	PBE	2000 [40]
	5	AIMD	PW91	2001 [41]
	(4)	Quasi-chemical	B3LYP	2001 [41]
	4+1	AIMD	PW91	This work
K^+	8	QM/MM	HF	1998 [34]
	5.5 – 7.5	AIMD	BLYP	1999 [36]
	4+2	AIMD	PW91	2004 [38]
	(4)	Quasi-chemical	B3LYP	2004 [38]
	4+2	AIMD	PW91	This work

In 1998, Tongraar *et al.* [34] reported a liquid state *ab initio* investigation of the hydrated structures of Na^+ and K^+ ions. In their approach, they combined quantum mechanical and molecular mechanical (QM/MM) methods, in which the ions along with their first solvation shells were treated quantum mechanically and the remaining portion of the solution was treated using empirical force fields. This approach enabled them to circumvent both issues of sampling and system size. Their calculations produced a hydration number of 8 for K^+ ions and a hydration number of 6 for Na^+ ions. These results, however, differ substantially from results of the most recent experiments and also from any of the AIMD simulations reported in subsequent years. This is presumably because the quantum mechanical portions of their calculations were carried out at the Hartree-Fock (HF) level of theory, which neglects electron correlation effects. In contrast, electron correlation interactions are taken into account in the density functional approaches used in subsequent studies. Neglect of electron correlations result in weaker water-water interactions (see for example Reference [35]), which leads to a smaller water dipole and thereby an underestimation of water-water repulsion. In such calculations this effect is presumably manifested as an increase in hydration numbers, although higher hydration numbers may also be an artifact of the nature of coupling between the quantum and molecular mechanical regions.

In 1999, Ramaniah *et al.* [36] reported the first fully *ab initio* molecular dynamics simulation investigation on K^+ ion hydration. They applied density functional theory (DFT) using the BLYP generalized gradient approximation to the electron density functional to describe the valence electrons, which accounts for electron correlations, and generated a ~2ps long dynamics trajectory of the ion solvated by 59 water molecules. In this case interactions between all the atoms of the system were treated quantum mechanically. As part of this study, the authors also presented separate empirical force field calculations, which ascertained that their system size did not introduce artifacts in the structural analysis of K^+ ion hydration, as also established in other studies [37]. An analysis of their trajectory, however, led to a "rugged" looking radial distribution profile of water molecules around the K^+ ion, suggesting lack of equilibration. As the authors acknowledged, the first minimum of their radial distribution profile was not well-defined, which led them to arrive at a range of hydration numbers for K^+ ions that depended on the radial cutoff distance used for defining the inner coordination volume. The resulting hydration numbers ranged from 5.5 to 7.5 water molecules. In their analysis, the authors also found a subset of four water molecules to be most tightly bound to the K^+ ion.

In 2004, Rempe *et al.* [38] used a different density functional (PW91), which also accounts for electron correlations, and generated a longer time-scale (10ps for analysis and 10ps for equilibration) AIMD trajectory of a K^+ ion solvated by 32 water molecules. This longer simulation produced a smoother radial distribution profile of water molecules around the central K^+ ion, which by the traditional definition of coordination number resulted in a hydration number of 6, consistent with the most recent experimental data described in this issue [81]. Their radial distribution profile at the same time also presented a distinct shoulder on the far slope of the principal maximum ($r_{K\text{-}O} \sim 3$ Å), also visible in the radial distribution profile of K^+ ions obtained from an earlier AIMD simulation [39]. The analysis of their trajectory led to the finding that the first coordination shell was actually composed of two distinct subpopulations of water molecules. One subset, containing 4 water molecules, was found to occupy a region closest to the ion ($r_{K\text{-}O} < 3.4$ Å) and the other subset, with only 2 water molecules, was situated at a slightly larger distance. In other words, we see that in the case of K^+ ions, the principal occupancy in the inner coordination shell is actually 4, but at the same time there also is a statistical admixture of two other outlying oxygen atoms that blur the primary minimum of the radial distribution profile. An integration of the radial distribution profile up to this primary minimum yields a hydration number of 4, but when integrated to include the "loosely" coordinated water molecules, the hydration number is 6. Current work using a larger simulation box containing 64 water molecules produces the same results, as illustrated in Figure 1. We indicate this characteristic inner shell occupancy of K^+ ions as 4+2 in Table 5.
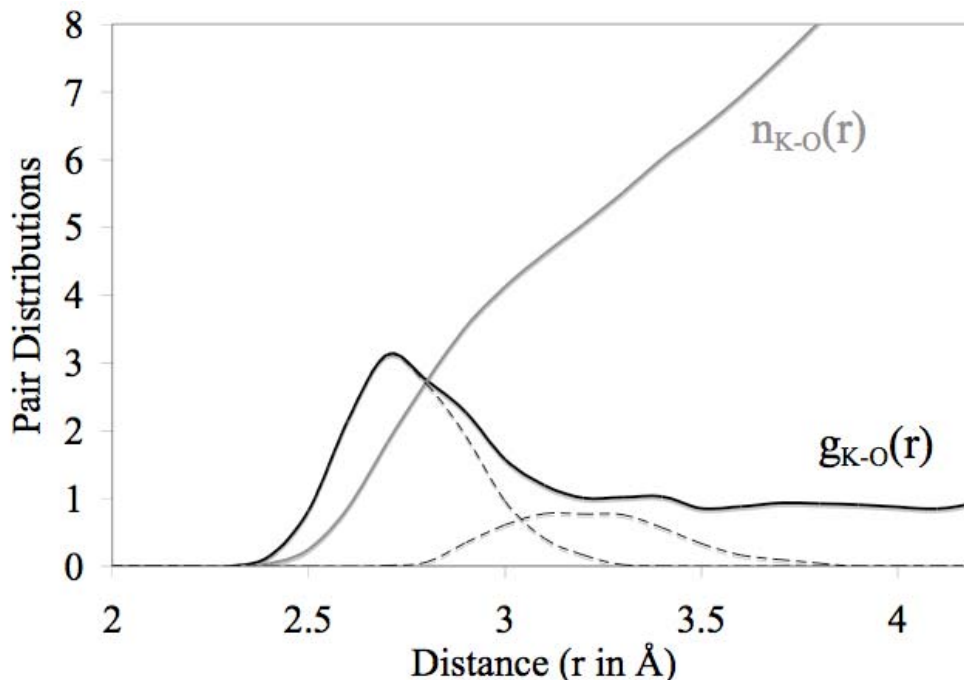
Figure 1. Distributions of water oxygen atoms around K^+ ion estimated from a 10 ps long equilibrated AIMD trajectory using a methodology similar to the one presented earlier [38], but with some improvements. In the new simulation, twice as many water molecules are present than in the earlier work, the 3P core electrons of K^+ are now included explicitly, and the core-valence electron interactions are now described using the improved projector augmented-wave method. $g_{K-O}(r)$ indicates the density of oxygen atoms at a given radial distance from the central K^+ ion. The dashed curve closer to the central K^+ ion indicates the contribution of the nearest four water molecules to this density distribution, while the dashed curve further away from the central K^+ ion indicates the contribution from the fifth and sixth nearest water molecules. The composite radial distribution function $g_{K-O}(r)$ reflects these two subpopulations as distinct shoulders on the far slope of its principle maximum. $n_{K-O}(r)$ indicates the average number of oxygen atoms within a certain distance from the central K^+ ion.

In 2000, White *et al.* [40] applied DFT using another generalized gradient approximation to the electron density functional, the Perdew-Burke-Ernzerhof (PBE) functional, to generate a 2.5 ps long AIMD trajectory of a Na^+ ion in water. The integration of the radial distribution profile determined from this data resulted in a Na^+ hydration number of 5. In 2001, Rempe and Pratt reported [41] data from a longer (6 ps) AIMD simulation of a Na^+ ion in water using a different density functional (PW91) and arrived at the same result. The most recent neutron diffraction experiments [42], described in this issue, are consistent with this finding. The radial distribution profile reported by Rempe and Pratt [41] also indicated the presence of a tiny shoulder on the far slope of the principal maximum, but in contrast to the case of K^+ ion, the AIMD data was not analyzed any further due to the relatively smaller length of the trajectory.

To rectify the lack of detailed information about possible substructure in the first peak of the Na^+ ion radial distribution profile, we generated a longer (13ps) trajectory of a Na^+ ion with 64 water molecules using a methodology similar to the one presented earlier [41], but with some improvements. In the new simulation, twice as many water molecules are present than in the earlier work, the 2P core electrons of Na^+ are now included explicitly, and the core-valence

electron interactions are now described using the improved projector augmented-wave method. The radial distribution profile of water oxygens around Na$^+$ ion is illustrated in Figure 2 and does not differ perceptibly from the earlier results. As in the case of K$^+$ ions, we find features at the far slope of the principle maximum rather than a smooth curve. Decomposition of the principle curve shows that the first coordination shell in this case is also composed of two subpopulations of water molecules. One subset occupies a region closest to the ion, and is composed of 4 oxygen atoms, while the other subset is situated at a slightly larger distance, and is composed of one "loosely" coordinated oxygen atom. We indicate this characteristic inner shell water occupancy of Na$^+$ ions as 4+1 in Table 5.
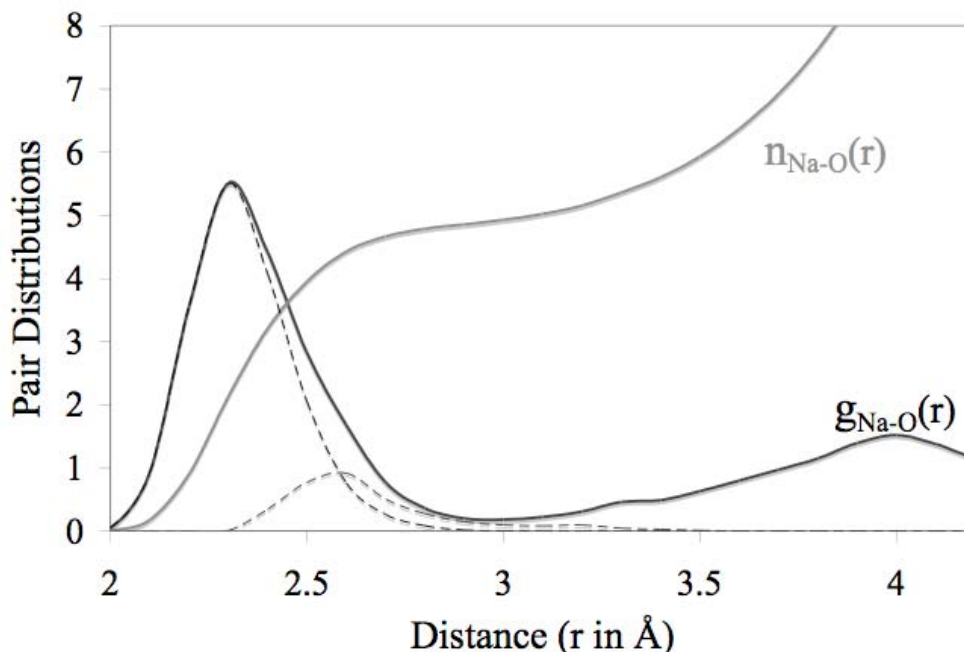
Figure 2. Distributions of water oxygen atoms around Na$^+$ ion estimated from a 13 ps long equilibrated AIMD trajectory. $g_{Na\text{-}O}(r)$ indicates the density of oxygen atoms at a given radial distance from the central Na$^+$ ion. The dashed curve closer to the central Na$^+$ ion indicates the contribution of the nearest four water molecules to this density distribution, while the dashed curve further away from the central Na$^+$ ion indicates the contribution from the fifth nearest water molecule. The composite radial distribution function $g_{Na\text{-}O}(r)$ reflects these two subpopulations as a distinct shoulder on the far slope of its principle maximum. $n_{Na\text{-}O}(r)$ indicates the average number of oxygen atoms within a certain distance from the central Na$^+$ ion.

In the case of Li$^+$ ions, all AIMD simulations produce radial distribution profiles that have clearly defined inner coordination shells. In all studies, integration of these curves up to their respective first minima result in a Li$^+$ hydration number of 4. Taken together, AIMD simulations consistently predict that, in aqueous phase, all three ions prefer to strongly coordinate with exactly 4 water molecules. Additional "loosely" coordinated water molecules raise the number of water molecules within the first minimum of the pairwise radial distribution curves of Na$^+$ ions to 5 and K$^+$ ions to 6.

In the past few years, *ab initio* computations have also been utilized in connection with formal molecular association equilibrium theories developed by Pratt and coworkers to probe ion

hydration numbers [38,41,43-51]. Such formal theories that describe molecular association equilibria have a very long history of development, and have been utilized on a regular basis to describe the physics of several other phenomena (see for example References [52-58]). The most unique feature of the statistical mechanical formulation [38,41,43-51] constructed specifically to describe particle solvation in condensed phases is that it allows for a decoupling of the solute's 3-dimensional interaction hyper-surface into two separate domains without consideration of the specific form of the interaction potential. Consider the following ion solvation reaction,

$$A^+_{gas} + n[X]_M \xrightarrow[]{K_n} [A^+X_n]_M \tag{1}$$
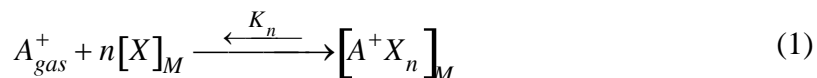
which takes place in a certain environment M, where n independent ligands (X) from this environment react with monovalent cation A^+ to form a coordination complex A^+X_n. Here K_n represents the equilibrium constant of this reaction. Starting from the potential distribution theorem [59,60], the standard form of the chemical potential of this ion (μ_A) can be separated out into ideal and non-ideal contributions, and in a way such that the non-ideal contributions can be expressed in terms of the equilibrium constants (K_n) of these clustering reactions [43,44,58], i.e.,

$$\beta\mu_A = \ln\left[\frac{\rho_A V}{q_A}\right] - \ln\left[\left\langle e^{-\beta\Delta U}\prod_j\left(1 + f_{Aj}\right)\right\rangle_0\right] - \ln\left[\sum_{n\geq 0}K_n\left(\rho_X\right)^n\right] \tag{2}$$

Here ΔU represents the interaction energy between the n-fold ion ligand cluster and the rest of the system, ρ_A is the density of the ion, and q_A is its single molecule partition function, while ρ_X is the density of solvent molecules. f_{Aj} is the Mayer f-(cluster)-function describing the interaction between the solute and the solvent molecule. It is 0 when solvent j is outside the cluster, and takes a value of -1 if that solvent molecule is inside the cluster, which serves to exclude additional solvent molecules from the cluster.

It is easy to see that such a decoupling of the net chemical potential of the ion allows for the treatment of a subsection of its spatial environment on a different footing from the rest of its environment. Furthermore, such a formulation also provides for a quasi-chemical type of physical setting in which the chemical potential can be directly probed as a function of the number and arrangement of ligands around that ion, thereby directly linking structural information to the thermodynamic properties of ion solvation. The computational implementation of this formulation has typically been carried out by treating the most significant nearest neighbor interactions of an ion quantum mechanically, and the remaining interactions using either implicit or explicit solvent models [38,41,43-47,49,51]. This circumvents critical issues that include parameterization of nearest neighbor interactions, accounting for traditional system size limitations, and determination of coupling parameters such as those present in hybrid QM/MM dynamics settings.

Such treatments applied to the phenomenon of ion hydration have yielded a tetrahedral arrangement of 4 water molecules as the preferred hydration number of all three cations considered here [38,41,44,45,47], consistent with AIMD simulation results. Interestingly,

inorganic chemists also cite tetrahedral coordination for these ions in water [87]. Note that although the formal theory that has yielded these hydration numbers is exact, its implementation can still benefit from a better treatment of the thermal motions of clusters via incorporation of anharmonic modes of vibrations, and an incorporation of additional energetic terms due to dispersion and packing. Such improvements in implementation, however, are not expected to alter the predicted hydration numbers of these ions [44,47].

Conclusion

This review and analysis of experimental and theoretical work carried out in the last decade shows that the lack of consensus previously characterizing structural properties of hydrated ions has given way to a remarkably consistent picture of water coordination structure for the first three alkali metal ions: Li^+, Na^+, and K^+. Theoretical studies based on *ab initio* methods and experimental work using diffraction and spectroscopic methods converge on this surprising conclusion: exactly four (4) water molecules directly coordinate each of these ions. Additional water molecules occupy more distant but overlapping regions of space in larger ions, thus obscuring the distribution profiles of the innermost coordinating water molecules and raising the hydration numbers determined by traditional analysis of the ion-oxygen pair distribution curves. As a result of these superimposed populations of water molecules, a unique pattern in hydration number emerges. For each unit move down the periodic table, the inner population of four coordinating water molecules is joined by one additional "loosely" coordinating water molecule to give hydration numbers of 4, 5, and 6 for the first three alkali metal ions.

References

1. H. Bayley and L. Jayasinghe, Functional engineered channels and pores (Review), Mol. Membr. Biol. 21 (2004) 209-20.

2. H. Ohtaki and T. Radnai, Structure and Dynamics of Hydrated Ions, Chem. Rev. 93 (1993) 1157-1204.

3. J. R. Newsome, G. W. Neilson and J. E. Enderby, Lithium ions in aqueous solution, J Phys. C: Solid State Phys. 13 (1980) L923-L926.

4. I. Howell and G. W. Neilson, Li+ hydration in concentrated aqueous solution, J Phys: Condensed Matter 8 (1996) 4455-4463.

5. G. L. Squires, Introduction to the Theory of Thermal Neutron Scattering (Dover Publications, 1997).

6. H. E. Fischer, A. C. Barnes and P. S. Salmon, Neutron and x-ray diffraction studies of liquids and glasses, Rep. Prog. Phys. 69 (2006) 233-299.

7. L. R. Pratt, D. Asthagiri and S. B. Rempe, Personal Communication (2006).

8. D. Beglov and B. Roux, Finite representation of an infinite bulk system: Solvent boundary potential for computer simulations, J Chem. Phys. 100 (1994) 9050-9063.

9. A.D. MacKerell Jr., D. Bashford, M. Bellott, R. L. Dunbrack Jr., J. D. Evanseck, M. J. Field, S. Fischer, J. Gao, H. Guo, S. Ha, D. Joseph-McCarthy, L. Kuchnir, K. Kuczera, F. T. K. Lau, C. Mattos, S. Michnick, T. Ngo, D. T. Nguyen, B. Prodhom, I. Reiher, W.E., B. Roux, M. Schlenkrich, J. C. Smith, R. Stote, J. Straub, M. Watanabe, J. Wiorkiewicz-Kuczera, D. Yin and M. Karplus, All-atom empirical potential for molecular modeling and dynamics studies of proteins, J Phys. Chem. B 102 (1998) 3586-3616.

10. J. Aqvist, Ion-Water Interaction Potentials Derived from Free Energy Perturbation Simulations, J Phys. Chem. 94 (1990) 8021-8024.

11. W. L. Jorgensen, D. S. Maxwell and J. Tirado-Rives, Development and Testing of the OPLS All-Atom Force Field on Conformational Energetics and Properties of Organic Liquids, J Amer. Chem. Soc. 118 (1996) 11225-11236.

12. A. Grossfield, P. Ren and J. W. Ponder, Ion solvation thermodynamics from simulation with a polarizable force field, J Amer. Chem. Soc. 125 (2003) 15671-82.

13. P. A. Kollman and I. D. Kuntz, Cation hydration, J Amer. Chem. Soc. 94 (1972) 9236-9237.

14. P. Barnes, J. L. Finney, J. D. Nicholas and J. E. Quinn, Cooperative effects in simulated water, Nature 282 (1979) 459-464.

15. E. Clementi, H. Kistenmacher, W. Kolos and S. Romano, Non-additivity in water-ion-water interactions, Theor. Chim. Acta 55 (1980) 257-266.

16. I. Ortega-Blake, O. Novaro, A. Les and S. Rybak, A molecular orbital study of the hydration of ions. The role of nonadditive effects in the hydration shells around Mg^{2+} and Ca^{2+}, J Chem. Phys. 76 (1982) 5405-5413.

17. T. P. Lybrand and P. Kollman, Water–water and water–ion potential functions including terms for many body effects, J Chem. Phys. 83 (1985) 2923-2933.

18. P. Cieplak, T. P. Lybrand and P. A. Kollman, Calculation of free energy changes in ion–water clusters using nonadditive potentials and the Monte Carlo method, J Chem. Phys. 86 (1987) 6393-6403.

19. M. M. Probst, A study of the additivity of interactions in cation-water systems, Chem. Phys. Letts. 137 (1989) 229-232.

20. L. A. Curtiss, J. W. Halley and J. Hautman, Many-body effects in ion-water interactions: Fe^{3+} in water, Chem. Phys. 133 (1989) 89-94.

21. J. Caldwell, L. X. Dang and P. A. Kollman, Implementation of Nonadditive Intermolecular Potentials by Use of Molecular Dynamics: Development of a Water-Water Potential and Water-Ion Cluster Interactions J Amer. Chem. Soc. 112 (1990) 9144-9147.

22. L. Perera and M. L. Berkowitz, Many-body effects in molecular dynamics simulations of $Na^+(H_2O)_n$ and $Cl^-(H_2O)_n$ clusters, J Chem. Phys. 95 (1991) 1954-1963.

23. M. A. Carignano, G. Karlstrom and P. Linse, Polarizable Ions in Polarizable Water: A Molecular Dynamics Study, J Phys. Chem. B 101 (1997) 1142-1147.

24. D. Spangberg and K. Hermansson, Many-body potentials for aqueous Li^+, Na^+, Mg^{2+}, and Al^{3+}: Comparison of effective three-body potentials and polarizable models, J Chem. Phys. 120 (2004) 4829-4843.

25. G. Ahn-Ercan, H. Krienke and W. Kunz, Role of polarizability in molecular interactions in ion solvation, Curr. Opin. Colloid & Interface Scie. 9 (2004) 92-96.

26. B. M. Rode, C. F. Schwenk, T. S. Hofer and B. R. Randolf, Coordination and ligand exchange dynamics of solvated metalions, Coord. Chem. Rev. 249 (2005) 2993-3006.

27. T. A. Halgren and W. Damm, Polarizable force fields, Curr. Opin. Struc. Biol. 11 (2001) 236-242.

28. B. Guillot, A reappraisal of what we have learnt during three decades of computer simulations on water, J Mol. Liq. 101 (2002) 219-260.

29. J. W. Ponder and D. A. Case, Force fields for protein simulations, Adv. Prot. Chem. 66 (2003) 27-85.

30. M. Masia, M. M. Probst and R. Rey, On the performance of molecular polarization methods close to a point charge, Comp. Phys. Comm. 169 (2005) 331-334.

31. H. Yu and W. F. v. Gunsteren, Accounting for polarization in molecular simulation, Comp. Phys. Comm. 172 (2005) 69-85.

32. K. A. Dill, T. M. Truskett, V. Vlachy and B. Hribar-Lee, Modeling water, the hydrophobic effect, and ion solvation, Ann. Rev. Biophys. Biomol. Struc. 34 (2005) 173-199.
33. M. Sprik, *Ab initio* molecular dynamics simulation of liquids and solutions, J Phys. C: Condens. Matter 12 (2000) A161-A163.

34. A. Tongraar, K. R. Liedl and B. M. Rode, Born-Oppenheimer ab Initio QM/MM Dynamics Simulations of Na^+ and K^+ in Water: From Structure Making to Structure Breaking Effects, J Phys. Chem. A 102 (1998) 10340-10347.

35. T. Todorova, A. P. Seitsonen, J. Hutter, I.-F. W. Kuo and C. J. Mundy, Molecular Dynamics Simulation of Liquid Water: Hybrid Density Functionals, J Phys. Chem. B 110 (2006) 3685-3691.

36. L. Ramaniah, M. Bernasconi and M. Parrinello, *Ab initio* molecular-dynamics simulation of K^+ solvation in water, J Chem. Phys. 111 (1999) 1587-1591.

37. K. Leung and S. B. Rempe, *Ab initio* molecular dynamics study of glycine intramolecular proton transfer in water, J Chem. Phys. 122 (2005) 184506-12.

38. S. B. Rempe, D. Asthagiri and L. R. Pratt, Inner shell definition and absolute hydration free energy of K^+(aq) on the basis of quasi-chemical theory and *ab initio* molecular dynamics, Phys. Chem. Chem. Phys. 6 (2004) 1966-1969.

39. B. Chen, I. Ivanov, J. M. Park, M. Parrinello and M. L. Klein, Solvation Structure and Mobility Mechanism of OH^-: A Car-Parrinello Molecular Dynamics Investigation of Alkaline Solutions, J Phys. Chem. B 106 (2002) 12006-12016.

40. J. A. White, E. Schwegler, G. Galli and F. Gygi, The solvation of Na^+ in water: First-principles simulations, J Chem. Phys. 113 (2000) 4668-4673.

41. S. B. Rempe and L. R. Pratt, The hydration number of Na^+ in liquid water, Fluid Phase Equilibria 183 (2001) 121-132.

42. S. Ansell, A. C. Barnes, P. E. Mason, G. W. Neilson and S. Ramos, X-ray and neutron scattering studies of the hydration structure of alkali ions in concentrated aqueous solutions, Biophys. Chem. 124 (2006) 171-179.

43. R. L. Martin, P. J. Hay and L. R. Pratt, Hydrolysis of Ferric Ion in Water and Conformational Equilibrium, J Phys. Chem. A 102 (1998) 3565-3573.

44. L. R. Pratt and S. B. Rempe, in: Quasi-Chemical Theory and Implicit Solvent Models for Simulations, eds. L. R. Pratt, & G. Hummer, Simulation and Theory of Electrostatic Interactions in Solution, vol. 492 (AIP Conference Proceedings, 1999) p. 172-201.

45. S. B. Rempe, L. R. Pratt, G. Hummer, J. D. Kress, R. L. Martin and A. Redondo, The Hydration of Li^+ in Liquid Water, J Amer. Chem. Soc. 122 (2000) 966-967.

46. H. S. Ashbaugh, D. Asthagiri, L. R. Pratt and S. B. Rempe, Hydration of krypton and consideration of clathrate models of hydrophobic effects from the perspective of quasi-chemical theory, Biophys. Chem. 105 (2003) 323-338.

47. D. Asthagiri, L. R. Pratt and H. S. Ashbaugh, Absolute hydration free energies of ions, ion–water clusters, and quasichemical theory, J Chem. Phys. 119 (2003) 2702-2708.

48. D. Asthagiri and L. R. Pratt, Quasi-chemical study of Be^{2+}(aq) speciation, Chem. Phys. Letts. 371 (2003) 613-619.

49. D. Asthagiri, L. R. Pratt, M. E. Paulaitis and S. B. Rempe, Hydration structure and free energy of biomolecularly specific aqueous dications, including Zn^{2+} and first transition row metals, J Amer. Chem. Soc. 126 (2004) 1285-1289.

50. D. Asthagiri, L. R. Pratt, J. D. Kress and M. A. Gomez, Hydration and mobility of HO^-(aq), Proc. Natl. Acad. Sci. U S A 101 (2004) 7229-7233.

51. D. Asthagiri, L. R. Pratt and J. D. Kress, Ab initio molecular dynamics and quasichemical study of H^+(aq), Proc. Natl. Acad. Sci. U S A 102 (2005) 6704-6708.

52. H. A. Bethe, Statistical Theory of Superlattices, Proc. Royal Soc. Lond. Series A, Math. and Phys. 150 (1935) 552-575.

53. J. Frenkel, A General Theory of Heterophase Fluctuations and Pretransition Phenomenon, J Chem. Phys. 7 (1939) 538-547.

54. W. Band, Dissociation Treatment of Condensing Systems II, J Chem. Phys. 7 (1939) 927-931.

55. R. Kikuchi, A Theory of Cooperative Phenomena, Phys. Rev. 81 (1951) 988-1003.

56. F. H. Stillinger Jr., Rigorous Basis of the Frenkel-Band Theory of Association Equilibrium, J Chem. Phys. 38 (1963) 1486-1494.

57. S. G. Brush and R. Kikuchi, Lattice Models for Cooperative Phenomena I. Survey and Comparison of Approximate Methods, Technical Report UCRL-14287, University of California, Lawrence Radiation Laboratory, Livermore, California. (1965).

58. L. R. Pratt and R. A. LaViolette, Quasi-chemical Theories of Associated Liquids, Mol. Phys. 95 (1998) 909-915.

59. B. Widom, Some Topics in the Theory of Fluids, J Chem. Phys. 39 (1963) 2808-2813.

60. B. Widom, Potential-Distribution Theory and the Statistical Mechanics of Fluids, J Phys. Chem. 86 (1982) 869-872.

61. A. H. Narten, F. Vaslow and H. A. Levy, Diffraction pattern and structure of aqueous lithium chloride solutions, J Chem. Phys. 58 (1973) 5017-5023.

62. G. Licheri, G. Piccaluga and G. Pinna, X-ray diffraction studies of alkali halide solutions, J Appl. Crystallogr. 6 (1973) 392-395.

63. G. Licheri, G. Piccaluga and G. Pinna, X-ray diffraction study of LiBr aqueous solutions, Chem. Phys. Letts. 35 (1975) 119-123.

64. K. H. Michaelian and M. Moskovits, Tetrahedral hydration of ions in solution, Nature 273 (1978) 135-136.

65. N. Ohtomo and K. Arakawa, Neutron Diffraction Study of Aqueous Ionic Solutions. I. Aqueous Solutions of Lithium Chloride and Caesium Chloride, Bull. Chem. Soc. Jpn. 52 (1979) 2755-2759.

66. G. Palinkas, T. Radnai and H. Hajdu, Z. Naturforsch Teil A 35 (1980) 107-114.

67. T. Radnai, G. Palinkas, G. I. Szasz and K. Heinzinger, Z. Naturforsch Teil A 36 (1981) 1076.

68. I. Okada, Y. Kitsuno, H. G. Lee and H. Ohtaki, Stud. Phys. Theor. Chem. 27 (1983) 81.

69. G. Paschina, G. Piccaluga and G. Pinna, X-ray investigation of Co-Cl bonding in a concentrated aqueous solution of $CoCl_2$ and LiCl, Chem. Phys. Letts. 98 (1983) 157-161.

70. A. Musinu, G. Paschina, G. Piccaluga and M. Magini, X-ray diffraction study of $CoCl_2$–LiCl aqueous solutions, J Chem. Phys. 80 (1984) 2772-2776.

71. Y. Tamura, T. Yamaguchi, I. Okada and H. Ohtaki, Z. Naturforsch, Teil A 42 (1987) 367.

72. T. Cartailler, W. Kunz, P. Turq and M. C. Bellisent-Funel, Lithium bromide in acetonitrile and water: a neutron scattering study, J Phys: Condens. Matter 3 (1991).

73. M. Maeda and H. Ohtaki, Bull. Chem. Soc. Jpn. 48 (1975) 3755.

74. G. Caminiti, G. Licheri, G. Piccaluga and G. Pinna, Interactions and structure in aqueous $NaNO_3$ solutions, J Chem. Phys. 72 (1980) 4522-4528.

75. N. Ohtomo and K. Arakawa, Bull. Chem. Soc. Jpn. 53 (1980) 1789.

76. N. T. Skipper and G. W. Neilson, X-ray and neutron diffraction studies on concentrated aqueous solutions of sodium nitrate and silver nitrate, J Phys. C: Solid State Phys. 1 (1989) 4141-4154.

77. C. L. van P. van Eck, H. Mendel and W. Boog, X-ray diffraction of aqueous electrolyte solutions, Discuss. Faraday Soc. 24 (1957) 200-205.

78. G. W. Brady, Structure in Ionic Solutions. II, J Chem. Phys. 28 (1958) 464-469.

79. D. S. Terekhova, A. I. Ryss and I. V. Radchenko, J Struct. Chem. 10 (1969) 107.

80. G. W. Neilson, P. E. Mason, S. Ramos and S. D., Neutron and X-ray scattering studies of hydration in aqueous solutions, Philos. Trans. R. Soc. London Ser. A 359 (2001) 1575-1591.

81. A. K. Soper and K. Weckstrom, Ion solvation and water structure in potassium halide aqueous solutions, Biophys. Chem. 124 (2006) 180-191.

82. G. Lamoureux and B. Roux, Absolute Hydration Free Energy Scale for Alkali and Halide Ions Established from Simulations with a Polarizable Force Field, J Phys.Chem. B 110 (2006) 3308 -3322.

83. M. Carrillo-Tripp, H. Saint-Martin and I. Ortega-Blake, A comparative study of the hydration of Na^+ and K^+ with refined polarizable model potentials, J Chem. Phys. 118 (2003) 7062-7073.

84. A. P. Lyubartsev, K. Laasonen and A. Laaksonen, Hydration of Li^+ ion. An ab initio molecular dynamics simulation, J Chem. Phys. 114 (2001) 3120-3126.

85. H. H. Loeffler and B. M. Rode, The hydration structure of the lithuium ion, J Chem. Phys. 117 (2002) 110-117.

87. F. A. Cotton, G. Wilkinson, C. A. Murillo and M. Bachmann, Advanced Inorganic Chemistry, 6th Edition (Wiley, New York, 1999).

Tuning Ion Coordination Architectures to Enable Selective Partitioning

Abstract

K$^+$ ions seemingly permeate K-channels rapidly because channel binding sites mimic coordination of K$^+$ ions in water. Highly selective ion discrimination should occur when binding sites form rigid cavities that match K$^+$, but not the smaller Na$^+$, ion size; or when binding sites are composed of specific chemical groups. Although conceptually attractive, these views cannot account for critical observations: 1) K$^+$ hydration structures differ markedly from channel binding sites; 2) channel thermal fluctuations can obscure sub-Ångström differences in ion sizes; and 3) chemically identical binding sites can exhibit diverse ion selectivities. Our quantum mechanical studies lead to a novel paradigm that reconciles these observations. We find that K-channels utilize a "phase-activated" mechanism where the local environment around the binding sites is tuned to sustain high coordination numbers (>6) around K$^+$ ions, which otherwise are rarely observed in liquid water. When combined with the field strength of carbonyl ligands, such high coordinations create the electrical scenario necessary for rapid and selective K$^+$ partitioning. Specific perturbations to the local binding site environment with respect to strongly selective K-channels result in altered K$^+$/Na$^+$ selectivities.

Introduction

Potassium (K-)channels catalyze fast K$^+$ ion transport across cellular membranes while simultaneously discriminating against Na$^+$ ion permeation by more than a factor of 1000 (1). Structural studies (2-5) show bare K$^+$ ions occupying binding sites in the narrowest channel regions in a state of high coordination by all eight surrounding oxygen ligands from the channel walls (Figure 1).
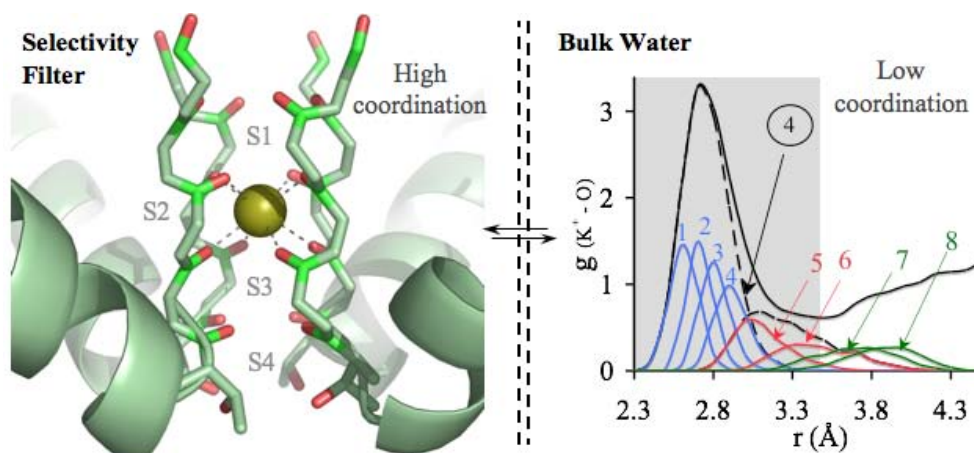
Figure 1. K$^+$ ion coordination in selectivity filters of K-channels is markedly different from that in bulk water. KcsA, for example, offers 3 binding sites for K$^+$ ions (2), S1, S2 & S3, where it coordinates with the ion using 8 of its backbone carbonyl oxygen atoms (highlighted in red) at an average distance of 2.8 Å. In contrast, in a 40 ps long AIMD (PW91) simulation of K$^+$ ion in bulk water (generated by extending the previously reported (8) 14 ps long trajectory), only 4 water molecules are seen most tightly bound to the

K$^+$ ion at an average distance of 2.8 Å. These 4 water molecules correspond to the maximum number that contribute to the principle maxima of the radial distribution function ($g(r)$); the 5th and the 6th nearest waters statistically do not contribute to the peak of the principle maxima; while the 7th and the 8th nearest waters are seldom seen within the canonical inner coordination shell (grey area) of the ion.

Equilibrium thermodynamics dictates that the partition coefficient of an ion between liquid water and the channel depends on the difference between the solvation free energies provided by these two environments. Transfer of an ion from water to the channel is favorable when its solvation free energy in the channel is lower than its value in the aqueous phase (*aq*),

$$\Delta\Delta G_{I^+} = \Delta G_{I^+}(channel) - \Delta G_{I^+}(aq) < 0 \tag{1}$$

where $\Delta G_{I+}(M)$ is the free energy change of the ion I^+ in solvation phase M relative to the gas phase. Selective partitioning of a K$^+$ ion into the channel is favorable when the free energy change for partitioning from water to the channel, $\Delta\Delta G_{I+}$, is lower for a K$^+$ relative to a Na$^+$ ion,

$$\Delta\Delta\Delta G(channel) = \Delta\Delta G_{K^+} - \Delta\Delta G_{Na^+} < 0 \tag{2}$$

In the common view of this mechanism, which emerged from a series of seminal investigations (1), fast, selective K$^+$ ion transport in K-channels arises by two categories of "fit." To assure rapid transport, the channel forms an environment like water for K$^+$ ions, producing a fit in terms of both local hydration structure and hydration energy. To assure discrimination between ions, the channel maintains rigid binding sites with cavity sizes that precisely fit K$^+$, but not the slightly smaller Na$^+$ ions (size difference ~0.4 Å), thus energetically destabilizing Na$^+$ ions in the channel relative to water. Although attractive due to their conceptual simplicity and remarkably insightful in their time, today these explanations appear insufficient in light of new experimental and theoretical advances and thus undermine initiatives to engineer biomimetic channels and design new drug therapies.

The long-standing hypothesis (2,6,7) that K$^+$ ions permeate K-channels rapidly because the binding sites mimic the coordination of K$^+$ ions in water can be attributed in part to an earlier lack of consensus regarding ion hydration structures. A compelling body (8) of evidence now exists showing both experimentally and theoretically that smaller numbers (<8) and different arrangements of ligands coordinate K$^+$ ions in liquid water, and, more specifically, that eight water molecules seldom simultaneously coordinate a K$^+$ ion (Figure 1). Consequently, a new mechanism is needed to explain how K-channel binding sites match K$^+$ hydration energies despite using higher numbers of coordinating ligands than found near K$^+$ in liquid water.

The mechanistic view that strong ion discrimination results from a rigid cavity size that exactly fits the permeant K$^+$ ion in K-channels has been challenged recently (9), where the authors argue that ion channel binding sites thermally fluctuate at Ångström length scales, which obscures sub-Ångström size differences between Na$^+$ and K$^+$ ions. Using classical force fields and molecular simulation strategies, these authors instead emphasize that chemistry, specifically the intrinsic electrostatic properties of the fluctuating carbonyl ligands in the channel, controls ion selectivity, a mechanism in line with an older ligand field strength model of ion selectivity (10,11).

Although this modified idea of ion discrimination is attractive because it allows for thermal fluctuations in the channel, it still leaves several critical observations unexplained: (a) the computed selectivity (9) is not uniform across the chemically identical binding sites S1, S2 and S3 in the wild-type KcsA channel; (b) recent structural studies (12) reveal that binding sites in NaK channels are composed of the same eight carbonyl ligands present in highly selective K-channels, and yet this identical ligand chemistry only weakly discriminates between Na^+ and K^+ ions; and (c) perturbations of the proximal binding site environment with respect to strongly selective K-channels, which specifically introduce nearby hydrogen-bond (H-bond) donor groups, lead to diminished ionic selectivity as experimentally observed in the context of mutated G-protein regulated inwardly rectifying potassium (GIRK) channels (13,14), and as can be inferred from a comprehensive sequence alignment of weakly selective wild-type K-channels (15).

To resolve these issues, we apply quantum chemical methods within the framework of a statistical molecular association theory and interrogate numerous ion-binding reactions. We vary ion coordination architectures and ligand chemistries in different physical solvation environments until we arrive at a specific physiologically justified combination that reproduces both structural and thermodynamic data for selective ion partitioning into the binding sites of K-channels. Our selection and rejection criteria for different ion-binding scenarios are guided by our objective to answer three questions about K-channel mechanism. First, how and why should ion coordination numbers be different in liquid water and in K-channels, and for that matter, why should eight ligands coordinate with K^+ ions and not any other "magic" number? Second, how do K^+ ions permeate the channel at high diffusion rates when the energetic probability that a K^+ ion forms eightfold complexes in water is negligible? And third, how do these new ideas about structural transitions in ion coordination simultaneously account for the fact that chemically identical binding sites give rise to strikingly different degrees of K^+/Na^+ selectivity?

Our studies lead us to a novel channel-centric paradigm for the mechanism of K^+/Na^+ selectivity that reconciles the critical observations neglected previously. We find that the environment surrounding the channel binding site and the binding-site coordination structure are two key components for selective ion partitioning. For K-channels, the binding-site environment is distinctly not a liquid environment and is tuned specifically to allow for local structural shifts in ion coordination architectures that ultimately enable it to differentiate energetically between Na^+ and K^+ ions. Perturbations of the binding-site environment with respect to strongly selective K-channels, which specifically introduce nearby hydrogen-bond (H-bond) donor groups, can help distort ion binding-site coordination structures and consequently lead to altered ion selectivity. We refer to this behavior as a "phase-activated" mechanism of selective ion partitioning. While the overall mechanism of ion permeation (as opposed to partitioning) may involve kinetic effects and will require treatment of interactions between individual ion binding sites, it is important to note that interactions between binding sites can only be understood after the selective partitioning mechanisms of individual binding sites are fully elucidated.

Methods

To understand selective ion partitioning in K-channels, we investigate the thermodynamics of coordination reactions that occur in water and in the binding sites of K-channels,

$$I^+_{gas} + n[X]_M \xrightleftharpoons{\quad \Delta G_{I^+ \to I^+(X)_n}(M) \quad} [I^+X_n]_M \qquad (3)$$
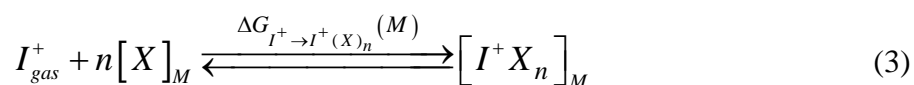
for K^+ and Na^+ ions (I^+) as a function of the number (n) and variety (X) of the coordinating ligands, concurrently with changes in the environment (M) external to a coordination complex (I^+X_n). Such calculations are statistically permissible under a quasi-chemical organization of solution theory (16-19) as its mathematical construct formulates an ion's excess chemical potential as a sum of the independent free energies ΔG (or equilibrium constants) for reactions involving different numbers of ligands. To assess the free energies, the region around an ion is divided into inner- and outer-shell domains. We define the inner-shell domain as the region containing the tighter subset of ligands directly coordinated to the ion, as opposed to more distant ligands distributed broadly within, or occupying regions beyond, the first peak of measured radial distribution functions. Since local interactions are most significant in differentiating the behavior of various ions coordinating with the same ligands, we treat the inner-shell interactions quantum mechanically using density functional theory (DFT) with the B3LYP functional. Less significant interactions with the environment outside the inner coordination shell are treated using an implicit solvent model. On multiple occasions ((8,19) see references therein) this methodology has reproduced simultaneously both the structural and the energetic properties of ion hydration.

Results

The point of departure for the current work derives from recent results (20) on ions interacting with water ligands in high and low dielectric environments. The first set of coordination reactions of interest were computed (20) in liquid water, the reference phase for the partitioning of ions into K-channels. Despite their size difference, both K^+ and Na^+ ions prefer thermodynamically to coordinate directly with exactly four water hydroxyl ligands, as also statistically observed in separate AIMD simulations (8,21-24) (see also Figure 1). More importantly, the thermodynamic probability for these ions to coordinate simultaneously with eight hydroxyl oxygens in liquid water is negligible. Yet crystallographic data (2-5) shows that K-channels utilize eightfold carbonyl-ligand geometries to partition K^+ ions for fast transport, which implies that factors present in K-channels alter the structural and/or energetic properties of the ions relative to water. Viewing the problem from a different perspective, we might ask what is so special about liquid water that limits formation of higher-order ion coordination complexes.

To test whether the chemical properties of carbonyl oxygen ligands in a liquid environment result in this coordination anomaly, we determine the coordination structures and solvation free energies of both ions in liquid formamide (NH_2CHO). Surprisingly, neither structural nor energetic properties of either ion changes appreciably in liquid phases even though stronger electrostatic field strengths (dipole moments) characterize the formamide carbonyl ligands compared to water hydroxyl ligands.

Tests on the effect of the environment lead to the first clues of a new K-channel mechanism. We created an environment that contrasts with the high dielectric liquid phases described above by setting the dielectric constant of the environment to its lowest value of unity ($\varepsilon = 1$). Revisiting

ion coordination reactions with water ligands, we discovered that coordination preferences are not fixed intrinsic properties of an ion (20). In environments characterized by a range of low dielectric constant values ($\varepsilon < 3$), both ions in fact prefer higher coordination numbers: K^+ ions now favor eight water ligands, and Na^+ ions six. The underlying physical mechanism that drives up ion coordination preferences, as described in detail elsewhere (20), is the decreased electrostatic penalty associated with extracting ligands from their low dielectric solvation phases. Conversely, in high dielectric aqueous phase, ion coordination complex formation requires overcoming these electrostatic penalties (~8 kcal/mol for each water molecule), which increase linearly with coordination number and eventually result in substantially lowering the thermodynamic probability for formation of higher-order coordination complexes. Therefore, in the case of K-channels, if the electrostatic penalty associated with extracting carbonyl-oxygen ligands were reduced by some mechanism, then the thermodynamic probability for 8-fold complex formation could be increased to values that do not obstruct K^+ ion partitioning.

Even though a low macroscopic dielectric value is an unlikely descriptor of an ion channel protein, an alternative mechanism for reducing electrostatic interactions between binding-site ligands and their environment presents itself upon recognition of the local nature of polar ligand (dipole) solvation in dielectric phases (20,25). Polar ligands receive the majority of their electrostatic stabilization from direct favorable interactions. As a consequence, the electrostatic penalty associated with extracting ligands can be substantially reduced without actually invoking the concept of dielectric constant, but by simply eliminating direct favorable interactions of the ligands. In the case of a K-channel binding site, the specific conditions that would yield reduced electrostatic penalties for extracting carbonyl oxygen ligands for ion complex formation, regardless of its dielectric characteristics, consist of a proximal environment that is devoid of only those polar chemical groups that can directly and favorably interact with the carbonyl oxygens. Such chemical groups in this case consist of H-bond donors. Note that in the x-ray structures of 4 strongly selective K-channels (KcsA, MthK, KvAP and KirBac1.1), there are no relevant side chain H-bond donor groups within a direct coordination distance of 6 Å from the carbonyl oxygens, and all proximal backbone H-bond donors are occupied in maintaining the integrity of the protein's three-dimensional fold. These conditions appear to create a local environment electrostatically equivalent to the low dielectric phase found earlier that led to increased probability for formation of eightfold K^+ ion hydration states. We term the particular conditions that drive up ion coordination preferences a "quasi-liquid" environment (20). Interestingly, we observe the same behavior of increased coordination preferences when Na^+ and K^+ ion reaction free energies are computed instead in quasi-liquid formamide, suggesting that the chemistry of the ligands utilized by K-channels to partition K^+ ions does not alter this phenomenon.

At this point, our studies suggest how the local electrostatic properties of the phase surrounding a K-channel binding site can sustain K^+ ions bound in states of high 8-fold coordination that contrast to the low coordination schemes preferred in liquid phase, a result that is independent of the coordinating-ligand chemistries. In alignment with previous theories, one might anticipate that K^+ ions readily partition into and permeate K-channel binding sites because the eightfold binding site coordination scheme matches the preferred number of water or formamide molecules that bind to K^+ ions in the same quasi-liquid phase. Further calculations of ion partitioning into representative binding sites, however, indicate otherwise.

Figure 2 illustrates the structures of eightfold complexes of K^+ ions with water and formamide ligands optimized by quantum chemical methods. In both cases the eight molecules are arranged in two separate four-molecule ring-like structures around the K^+ ions. This skewed cubic architecture resembles the crystallographically resolved binding site structures in the selectivity filter of K-channels (and also the NaK channel), but with one exception: The coordinating molecules in these two eightfold complexes are H-bonded to each other. In fact, we also find a certain degree of inter-ligand H-bonding present in the five-, six-, and sevenfold complexes. In the context of K-channels therefore, the reaction free energies obtained using these coordination complexes are physiologically irrelevant. Consequently we recompute the free energies of the five-, six-, seven- and eightfold K^+ ion formamide complexes, ensuring this time that the formamide molecules avoid H-bond interactions. The quantum chemical optimized structure of the alternate non-hydrogen-bonded eightfold formamide complex of K^+ ion is also illustrated in Figure 2. This new structure is similar to K-channel binding sites as it has the same skewed cubic geometry and a similar K^+–oxygen distance of 2.9 Å. We now find, however, that the free energy required to partition a K^+ ion from bulk water into this new 8-fold formamide geometry in a quasi-liquid phase is substantially unfavorable ($\Delta\Delta G > 14$ kcal/mol), which was not the case when inter-ligand hydrogen bonding was permitted. Figure 3 illustrates these free energy values as part of a phase diagram.
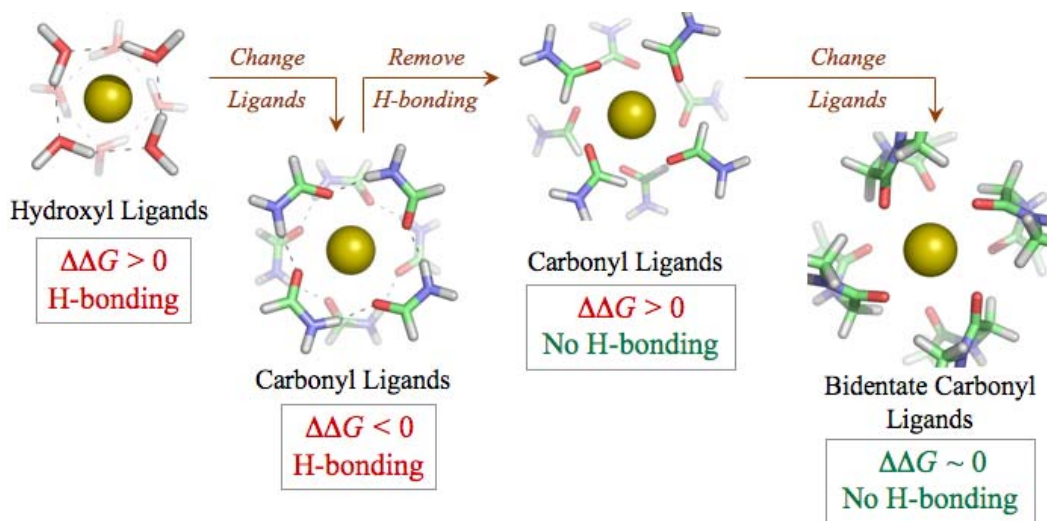
Figure 2. The different 8-fold coordinated complexes of K^+ ions considered in this investigation. $\Delta\Delta G$ refers to the free energy of partitioning a K^+ ion from liquid water (reference environment) into the respective 8-fold coordinated chemistries embedded in a quasi-liquid phase. The inter-ligand hydrogen bonds are depicted using dashed lines connecting the hydrogen (white) and oxygen atoms (red). The chemistry and architecture that favors K^+ ion partitioning precisely matches the binding sites S1-S3 found in the selectivity filters of K-channels.
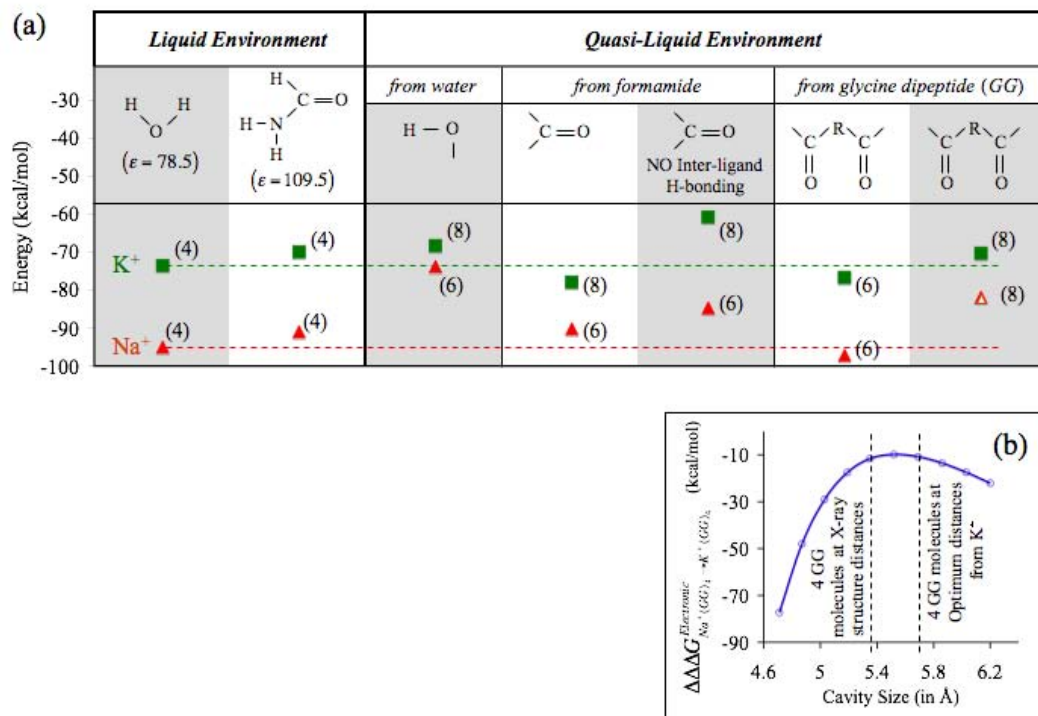
Figure 3. (a) Phase diagram illustrating the structural and thermo-chemical effects of transferring Na^+ and K^+ ions from one combination of chemistry, architecture and phase into another. The absolute free energies of solvating ions in these combinations can be inferred from the scale on the y-axes of the plot, and the coordination numbers corresponding to these free energies are indicated in brackets. The hydration free energies of Na^+ and K^+ ions (n=4) are also indicated as dashed lines, colored red and green, respectively. The open symbol enclosed in a dashed box denotes the only case where ligands are held rigid. This particular case represents the minimum of the cavity size-dependent K^+/Na^+ selectivity (~10 kcal/mol) conferred by the chemistry of 8 carbonyl ligands from 4 glycine dipeptide molecules arranged in a skewed cubic architecture, as estimated using the data in plot (b). From plot (b), we see that irrespective of cavity size, measured as the distance between furthest oxygen atoms, the K^+/Na^+ ion selectivity conferred by this 8-fold coordination is maintained. Since these values correspond to the lowest energy positions of the Na^+ ions in the cavities, a choice of any other position for the ion will also result in K^+/Na^+ selectivity.

Another approach toward creating a representative K-channel binding site that avoids nonphysical inter-ligand hydrogen bonding in ion complex formation is to choose a different chemical ligand. We select bidentate ligands in the form of glycine dipeptide ($CH_3CONHCH_2CONHCH_3$) molecules since the carbonyl oxygens in these molecules also provide a good chemical representation of the coordinating oxygen atoms present in the binding sites of K-channels. Furthermore, use of bidentate ligands improves the representation of K-channel binding sites over monodentate ligands as they capture the native bidentate character of ion-ligand association in K-channels, where each monomer of a tetrameric K-channel supplies two ligands to a binding site. Quantum chemical optimizations carried out using these bidentate ligands result in no inter-ligand hydrogen bonding. In fact, the optimized structure of the eightfold coordinated K^+ ion complex, as illustrated in Figure 2, matches the structures of binding sites in the selectivity filters of K-channels, with a K^+-oxygen distance of 3 Å and a root mean square deviation (RMSD) of only 0.4 Å with respect to the S2 binding site of KcsA (2).

143

The free energy change ΔG associated with the formation of this eightfold bidentate K^+ ion complex, plotted in the phase diagram of Figure 3, indicates that it is energetically more stable than the eightfold complex formed from non-hydrogen-bonded formamides. An analysis of free energy contributions shows that this extra stabilization of the eightfold bidentate complex is due in part to the slightly different chemistries of the ligands as well as to the reduced loss in entropy associated with aggregation of ligands with reduced mobility due to intra-molecular bonding.

To probe the significance of the K-channel eightfold coordinated binding sites with respect to other binding site coordination possibilities, we compare the free energies for ion partitioning into eightfold and sixfold coordinated states formed by our bidentate ligands. The free energy $\Delta\Delta G$ required to partition a K^+ ion from aqueous phase into the tetrameric eightfold bidentate complex described above is negligible. In the other set of calculations, the free energies $\Delta\Delta G$ for partitioning either Na^+ or K^+ ions from aqueous phases into their respective trimeric sixfold geometries are also negligible (see Figure 3), which implies that in a scenario where K-channels could provide three bidentate ligands for coordination instead of four, both ions would partition into the binding site although without any apparent K^+/Na^+ selectivity. The thermodynamic condition essential for rapid K^+ ion transport is therefore met with both sixfold and eightfold coordinated states, however, ion selectivity is lacking in the sixfold trimeric coordination scheme. Furthermore, K^+ ions slightly prefer coordination by three rather than four bidentate ligands, demonstrating that K^+ ions do not readily partition into K-channels to match preferred numbers of coordinating ligands.

Due to the long-range nature of electrostatic interactions, an exact estimation of the solvation energy of a K^+ ion inside an entire K-channel requires further incorporation of its interactions with the remaining portion of the channel-membrane system. Nevertheless, in such a calculation we expect the solvation energy of a K^+ ion to be more exothermic than the value reported here. Thermodynamic stabilization resulting from a higher dielectric constant of the protein ($\varepsilon > 1$) is expected to be larger than destabilization resulting from multi-ion repulsion in the selectivity filter, eventually resulting in a more exothermic reaction free energy value.

To understand ion selectivity in 8-fold tetrameric binding sites, we calculate the interaction of a Na^+ ion with 4 bidentate ligands, the same number and variety of ligands that allow K^+ ions to partition from aqueous phase. Attempts to optimize 4 bidentate ligands around a Na^+ ion using quantum chemical methods (DFT/B3LYP), such that all of the 8 carbonyl oxygens directly coordinate the ion, fail. Instead an overall 5-fold coordinated structure results, with 3 oxygens pushed outside the ion's inner coordination shell. This structure can also be described as a distorted K-channel binding site structure having an RMSD of 1.8 Å with respect to the x-ray coordinates (2) of the S2 binding site of KcsA. A similar distortion of the S1 binding site of KcsA, which resulted in an overall sixfold coordinated geometry, has also been reported in a separate quantum chemical optimization study (26). Reaction free energies computed using these distorted structures present an interesting scenario. In the event that the selectivity filter were flexible enough to allow such local distortions in the number of coordinating ligands, not only would Na^+ ions partition into the binding sites from aqueous phase, but the filter would also exhibit a reversed Na^+/K^+ selectivity. The fivefold distorted structure results in a potent reversed selectivity ($\Delta\Delta G$) of ~15 kcal/mol, while an alternate distortion corresponding to a sixfold

coordination (reported elsewhere (26)) leads to a milder, yet still reversed Na^+/K^+ selectivity of ~3 kcal/mol.

Next, we investigate selectivity for the possibility that the eightfold coordinated geometry formed from four glycine dipeptide ligands cannot distort other than in a manner that maintains direct coordination of the Na^+ ion with all eight carbonyl oxygen atoms, yielding either a reduction or an expansion in binding site cavity size. Electronic energy differences computed for transferring a Na^+ ion relative to a K^+ ion ($\Delta\Delta\Delta G^{electronic}$) into an eightfold bidentate complex, with coordinates that were optimized in the presence of a K^+ ion, result in a K^+/Na^+ selectivity of -10.7 kcal/mol. Contrary to expectations that a smaller cavity size by itself would destroy selectivity by energetically stabilizing the smaller Na^+ ion, we find that the same set of electronic energy calculations repeated after stepwise radial expansions and contractions of this eightfold geometry around the Na^+ ion still preserve K^+/Na^+ selectivity, as illustrated in Figure 3b. Assuming that thermal contributions to the relative free energies approximately cancel, we find that electrostatic interactions, the dominant component of the electronic energy, arising from eight carbonyl oxygens are by themselves sufficient to achieve K^+/Na^+ selectivity. Moreover, thermal motions need not be identical for the two ions nor set to zero to result in ion selectivity. As computed on numerous occasions using parameterized force-fields (27,28), filter selectivity appears tolerant of thermal atomic fluctuations (< 1 Å), fluctuations that are in any case essential for ion translocation to take place across the narrow regions of the filter. Electrostatic interactions from this 8-fold coordination result in K^+/Na^+ selectivity because of ligand-ligand repulsion, as elaborated in a separate molecular dynamics based study (9). Results from our quantum chemical calculations illustrated in Figure 3b confirm the inferences derived from these empirical force field calculations, where atomic polarization effects were neglected.

Discussion and Conclusions

In summary, we find that direct coordination by eight carbonyl oxygens in the form of four bidentate ligands yields selective partitioning of K^+ ions from an aqueous phase. Eight ligands overcoordinate both ions. In the event of structural distortions that can reduce coordination numbers to five or six during Na^+ ion partitioning, ion selectivity is either nonexistent or reversed. Structural rigidity is therefore necessary for selective K^+ ion partitioning, but *not* to maintain specific cavity sizes, as considered conventionally, but instead to maintain specific direct coordination numbers. In fact, we find a narrow window of flexibility within which the selectivity filter achieves selective K^+ ion partitioning: On the one hand, if the filter were frozen solid, K^+ ions could never physically partition from one binding site to another, whereas on the other hand, if it were entirely flexible like a liquid, no K^+/Na^+ selectivity could occur. Furthermore, it is the quasi-liquid nature of the local binding-site environment that in the first place makes the direct coordination of a K^+ ion with higher numbers of ligands (>6) a statistical possibility, as they are otherwise rarely observed in aqueous phase. Along with the strengths of the ligating oxygens, these two determinants, phase and coordination number, together generate the electrical scenario necessary for selective K^+ ion partitioning in K-channels. To distinguish this mechanism from conventional views, we term this a "phase-activated" mechanism of selective ion partitioning.

Experiments to test this mechanism consist of creating mutations in K-channels that can facilitate reductions in binding-site coordination numbers. One way to achieve this is to disturb the quasi-liquid nature of the binding-site environment by introducing proximal H-bond donor groups. Clearly this will introduce electrostatic penalties for extracting ligands from the environment for ion coordination, which will reduce the free energy for K^+ ion partitioning. Nevertheless, the results from optimizing four bidentate ligands about a Na^+ ion suggest a route for balancing these energetic penalties with energetic rewards to retain favorable K^+ ion partitioning.

Consider a scenario where one H-bond donor group is introduced per monomer of a tetrameric K-channel. As computed earlier, the free energy to partition a Na^+ ion from liquid water to a fivefold distorted structure formed from four bidentate ligands is favorable by -9.5 kcal/mol. In the event that such a distortion occurred in the selectivity filter during Na^+ partitioning, only one ligand from one monomer would need to be extracted from the environment for ion coordination, while three carbonyl oxygen ligands on the remaining monomers could remain bonded to their respective H-bond donor groups. This implies that even when penalized electrostatically for ligand extraction, a Na^+ ion will partition into the distorted selectivity filter. For example, in an extreme case of ligand extraction involving removal of one formamide molecule from liquid formamide ($\varepsilon = 109.5$), the electrostatic penalty was computed to be 10.8 kcal/mol. Under these conditions, a K^+ ion will also partition into the selectivity filter because, as a separate calculation shows, the free energy for transferring a K^+ ion from liquid water into a distorted fivefold coordination (similar to the one obtained for a Na^+ ion) in a quasi-liquid phase is favorable by -10.1 kcal/mol. Clearly, introduction of one H-bond donor per monomer will not only permit K^+ partitioning, but will now result in a substantially diminished K^+/Na^+ selectivity.

Physiological characterizations of such mutations in K-channels exist, but their mechanisms could not be explained using any of the previous theories of ion selectivity. For a recent example, a mutation in a strongly selective GIRK channel that introduced a H-bond donor group in the form of a Trp side-chain in the proximity of its selectivity filter resulted in a substantial reduction in its K^+/Na^+ selectivity (13,14). Another example comes from a comprehensive sequence alignment study of K-channels (15), which show that weakly selective K-channels, such as HYP or pacemaker channels, carry H-bond donors in the form of arginine residues proximal to their selectivity filters, and that these side-chain groups are completely absent from all strongly selective K-channels.

Another way to facilitate reductions in binding site coordination numbers is to create ample structural freedom for binding site distortion along with introduction of H-bond donors. The crystal structure of the weakly selective NaK channel exemplifies this, as it shows that its ion binding sites are interspersed with water-filled cavities (12). Data from recent MD simulations (29) of the NaK channel also lend support to these original ideas (30, 31). Relative proximities to bulk water perhaps also explains why the computed selectivity (9) is not uniform across the chemically identical binding sites in wild-type KcsA. The S2 site is the least exposed to water in comparison with sites S1 and S3, making it the most selective site in KcsA.

Together, these investigations introduce the interplay and individual thermo-chemical effects of two determinants of ion partitioning: phase and coordination number. As demonstrated, they play critical roles in selective ion-partitioning mechanisms in K-channels, suggesting their

potential implications for other chemical and biological settings as well. We anticipate that future investigations that explicitly account for their effects will also prove beneficial towards developing a better understanding of the nature of ion solvation.

References

1. Hille, B. 2001. Ionic channels of excitable membranes. Sinauer Associates, Sunderland, MA.

2. Zhou, Y., J. H. Morais-Cabral, A. Kaufman, and R. MacKinnon. 2001. Chemistry of ion coordination and hydration revealed by a K+ channel-Fab complex at 2.0 Å resolution. Nature. 414:43-48.

3. Jiang, Y., A. Lee, J. Chen, M. Cadene, B. T. Chait, and R. MacKinnon. 2002. Crystal structure and mechanism of a calcium-gated potassium channel. Nature. 417:515-522.

4. Jiang, Y., A. Lee, J. Chen, V. Ruta, M. Cadene, B. T. Chait, and R. MacKinnon. 2003. X-ray structure of a voltage-dependent K+ channel. Nature. 423:33-41.

5. Kuo, A., J. M. Gulbis, J. F. Antcliff, T. Rahman, E. D. Lowe, J. Zimmer, J. Cuthbertson, F. M. Ashcroft, T. Ezaki, and D. A. Doyle. 2003. Crystal structure of the potassium channel KirBac1.1 in the closed state. Science. 300:1922-1926.

6. Bezanilla, F. and C. M. Armstrong. 1972. Negative Conductance Caused by Entry of Sodium and Cesium Ions into the Potassium Channels of Squid Axons. J Gen. Physiol. 60:588-608.

7. Miller, C. 2001. See potassium run. Nature 414:23-24.

8. Varma, S. and S. B. Rempe. 2006. Coordination numbers of alkali metal ions in aqueous solutions. Biophys. Chem. 124:192-199.

9. Noskov, S. Y., S. Berneche, and B. Roux. 2004. Control of ion selectivity in potassium channels by electrostatic and dynamic properties of carbonyl ligands. Nature. 431:830-834.

10. Eisenman, G. 1961. Symposium on Membrane Transport and Metabolism. A. Kleinzeller and A. Kotyk, editors. NY: Academic Press. 163 p.

11. Aqvist, J., O. Alvarez, and G. Eisenman. 1992. Ion-Selective Properties of a Small Ionophore in Methanol Studied by Free Energy Perturbation Simulations. J Phys. Chem. 96:10019-10025.

12. Shi, N., S. Ye, A. Alam, L. Chen, and Y. Jiang. 2006. Atomic structure of a Na^+- and K^+-conducting channel. Nature. 440:570-574.

13. Bichet, D., Y.-F. Lin, C. A. Ibarra, C. S. Huang, B. A. Yi, Y. N. Jan, and L. Y. Jan. 2004. Evolving potassium channels by means of yeast selection reveals structural elements important for selectivity. Proc. Natl. Acad. Sci. USA. 101:4441-4446.

14. Bichet, D., M. Grabe, Y. N. Jan, and L. Y. Jan. 2006. Electrostatic interactions in the channel cavity as an important determinant of potassium channel selectivity. Proc. Natl. Acad. Sci. USA. 103:14355-14360.

15. Shealy, R. T., A. D. Murphy, R. Ramarathnam, E. Jakobsson, and S. Subramaniam. 2003. Sequence-function analysis of the K^+-selective family of ion channels using a comprehensive alignment and the KcsA channel structure. Biophys. J. 84:2929-2942.

16. Widom, B. 1982. Potential-Distribution Theory and the Statistical Mechanics of Fluids. J Phys. Chem. 86:869-872.

17. Pratt, L. R. and R. A. LaViolette. 1998. Quasi-chemical Theories of Associated Liquids. Mol. Phys. 95:909-915.

18. Pratt, L. R. and S. B. Rempe. Quasi-Chemical Theory and Implicit Solvent Models for Simulations. In: L. R. Pratt and G. Hummer, editors; 1999. p 172-201.

19. Beck, T. L., M. E. Paulaitis, and L. R. Pratt. 2006. The Potential Distribution Theorem and Models of Molecular Solutions. New York: Cambridge University Press. 244 p.

20. Varma, S. and S. B. Rempe. 2008. Solvation phase properties increase coordination preferences of ions. Submitted.

21. Rempe, S. B. and L. R. Pratt. 2001. The hydration number of Na^+ in liquid water. Fluid Phase Equilibria. 183:121-132.

22. Rempe, S. B., D. Asthagiri, and L. R. Pratt. 2004. Inner shell definition and absolute hydration free energy of K^+(aq) on the basis of quasi-chemical theory and ab initio molecular dynamics. Phys. Chem. Chem. Phys. 6:1966-1969.

23. Ramaniah, L., M. Bernasconi, and M. Parrinello. 1999. Ab initio molecular-dynamics simulation of K^+ solvation in water. J Chem. Phys. 111:1587-1591.

24. White, J. A., E. Schwegler, G. Galli, and F. Gygi. 2000. The solvation of Na^+ in water: First-principles simulations. J Chem. Phys. 113:4668-4673.

25. Simonson, T. 2003. Electrostatics and dynamics of proteins. Rep. Prog. Phys. 66:737-787.

26. Ban, F., P. Kusalik, and D. F. Weaver. 2004. Density functional theory investigations on the chemical basis of the selectivity filter in the K^+ channel protein. J Amer. Chem. Soc. 126:4711-4716.

27. Luzhkov, V. B. and J. Aqvist. 2005. Ions and blockers in potassium channels: insights from free energy simulations. Biochim. *et* Biophys. Acta - Proteins & Proteomics. 1747:109-120.

28. Asthagiri, D., L. R. Pratt, and M. E. Paulaitis. 2006. Role of fluctuations in a snug-fit mechanism of KcsA channel selectivity. J. Chem. Phys. 125:24701-24706.

29. Noskov, S.R., and B. Roux. 2007. Importance of hydration and dynamics on the selectivity of the KcSA and NaK channels. J. Gen. Physiol. 129:135-143.

30. Varma, S., and S. B. Rempe. 2006. Selective permeation of ions across the selectivity filter of KcSA: A perspective from the coordination chemistry of ions. Biophpys. J. 90:1961. (abstract)

31. Varma, S. and S. B. Rempe. 2006. Technical Report No. SAND2006-0711J, Sandia National Laboratories, Albuquerque, NM. http://arxiv.org/pdf/physics/0608180.

Viscous Water Meniscus under Nanoconfinement

Abstract

Water molecules confined between interfaces with nanoscopic separation are of critical importance in many fields. Examples include, among others, hydration forces in biology and colloid science,[1] stiction in microelectromechanical systems,[2] swelling of layered clays,[3] and capillary forces in scanning probe microscopy and nanolithography.[4-6] Here we use interfacial force microscopy (IFM)[7] to measure normal and lateral forces between two surfaces nanometers apart, with water confined between them. For two hydrophilic –COOH terminated surfaces, both friction and attractive normal forces peak at ~0.6 nm separation, owing to the water meniscus; this meniscus has an estimated viscosity nearly seven orders of magnitude greater than that of bulk water. Grand canonical Monte Carlo simulations confirm the presence of a nanoscopic meniscus and indicate an enhancement of the tetrahedral water structure in the meniscus as source for the enhanced friction force.

Introduction

"Structured" water near surfaces has long been thought to explain a wide range of physical, chemical, biological, and geological processes. Experimental evidence has mainly come from vibrational spectroscopies,[8-11] atomic force microscopy (AFM),[12] and X-ray diffraction.[13] Despite the broad interest, little is known about the details of water confined between two surfaces with nanoscopic separation, where macroscopic theories for capillary condensation are expected to break down.[4,6] In principle, AFM may be used to probe the nanoscopic water meniscus, but quantitative measurements are difficult because sensor instability results in the well-known "jump-to-contact" in the attractive region.[14] Similar difficulties are encountered in experiments based on the surface force apparatus (SFA),[15] which accordingly has been used to probe confined molecules in the repulsive region. SFA studies by Granick and coworkers showed very high effective viscosity of liquid films confined between mica surfaces;[16] in particular, this group showed that an ionic water solution compressed by two mica surfaces exhibits azimuthal angle dependent shear viscosity up to three orders of magnitude higher than that of bulk water.[17] On the other hand, Klein and co-workers reported the fluidic nature of pure water confined between mica surfaces at < 3.5 nm interfacial separation, with bulk water like viscosity.[18]

Methods

Here we probe the mechanical properties of the water meniscus between two chemically distinct surfaces using interfacial force microscopy (IFM, shown schematically in Figure 1)[7,19] whose self-balancing, force-feedback sensor eliminates the mechanical instability problem and allows quantitative measurements of normal and lateral (shear) forces throughout the entire range of interfacial separation. We use a single-crystal Au(111) substrate and an electrochemically etched parabolic Au tip with relatively large radius ($R = 500$ nm) as shown by scanning electron microscope (SEM) image in Figure 1. Each Au surface is made hydrophilic or hydrophobic by the chemisorption of a COOH or CH_3 terminated alkanethiol self-assembled monolayer (SAM).

We use mercaptoundecanoic acid, $HS-(CH_2)_{10}-COOH$, and hexadecanethiol, $HS-(CH_2)_{15}-CH_3$, for the results presented here. The water contact angle on the hydrophilic –COOH terminated surface is $\leq 9°$ while that on the hydrophobic –CH_3 surface is $\sim 115°$. We measure the normal force (F_N) and friction force (F_μ) as a function of relative interfacial separation at $20°C$ and one atm with controlled relative humidity (RH) $\leq 45\%$. Friction is measured by oscillating the tip laterally at 100 Hz and ~ 1 nm amplitude, and recording the resulting force signal synchronously. We are not able to carry out measurements for RH > 45% due to sensor instability. A recent study by environmental SEM of an AFM tip on a solid surface showed that, for RH > 60%, the size of the meniscus increases dramatically and approaches that of the tip.[20]
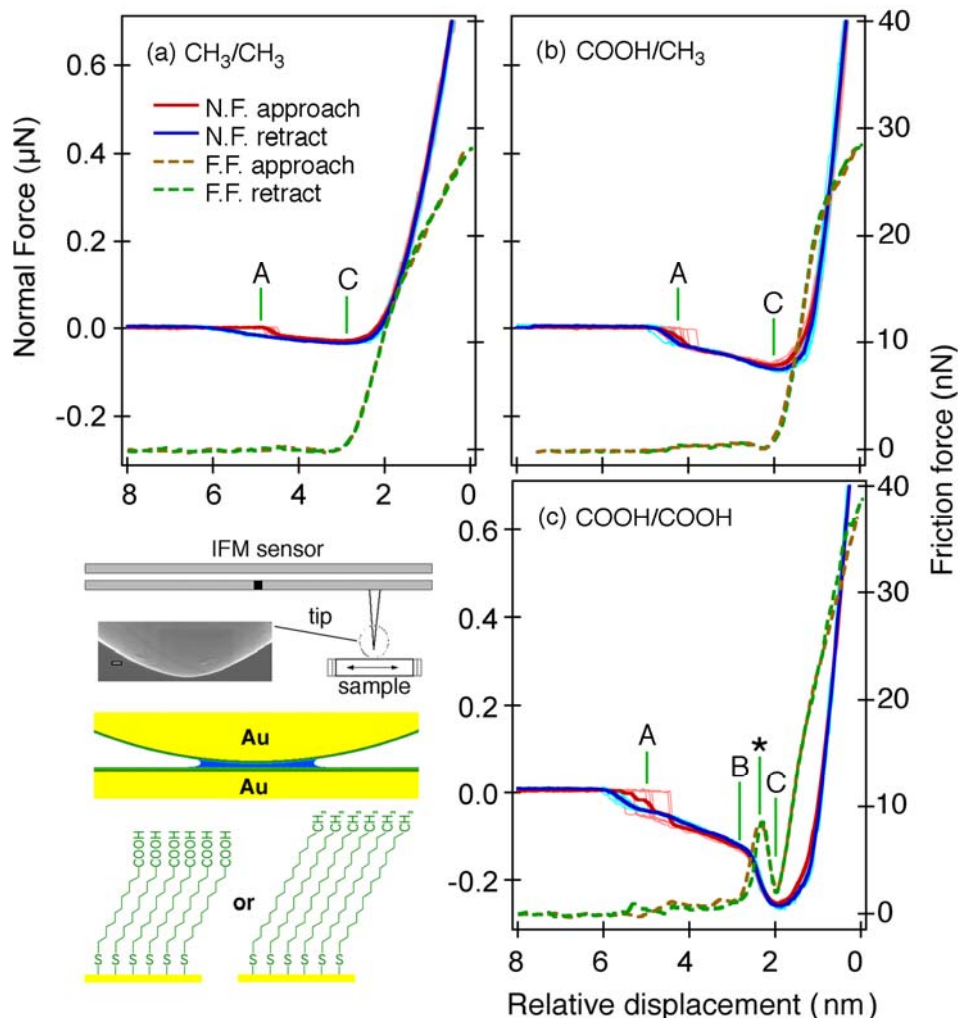
Figure 1. Schematic illustration: experimental system. The scanning electron microscope image in the middle shows the parabolic Au tip with radius of curvature of 500 nm (scale bar on the picture is 100 nm). Panels (a-c): Normal force (F_N, solid curves and left axis) and friction force (F_μ, dashed curves and right axis) profiles as a function of relative displacement between the tip and the sample for the following interface combinations: (a) CH_3 tip on CH_3 surface; (b) COOH tip on CH_3 surface; and (c) COOH tip on COOH surface. In each of the above panels, the thin pink and blue curves are individual F_N profiles during approach and retract, respectively; the thick red (approach) and blue (retract) curves are averaged data. Only averaged data are shown for F_μ profiles (dashed brown for approach and dashed green for retract). All measurement were carried out at RH = 40-45% and at room temperature.

Results and Discussion

Figure 1 shows normal- and friction-force profiles at RH = 40-45% for: (a) –CH$_3$ tip on –CH$_3$ surface; (b) –COOH tip on –CH$_3$ surface; (c) –COOH tip on –COOH surface. Close agreement of forces on approach and retraction shows that hysteresis is small. Note that there are 12 independent measurements as well as the averaged data for each force profile. The excellent agreement from measurement to measurement shows that the experiment is highly reproducible. The zero point of relative displacement (RD) refers to the F_N value (1 μN) at which the tip begins its retraction. Also shown are the averaged friction data indicated by the heavy dashed lines.

When both surfaces are hydrophobic, panel (a), the force profiles are virtually independent of RH (data not shown). Note that there is a small but measurable jump in attractive force, as well as a slow increase to a shallow well just before contact indicated by point C. The source of this behaviour is not known. A possible reason is a structural instability owing to a small concentration of adventitious adsorbates. After contact between the two films (C, at RD ~ 2.5 nm) the normal force begins its rise to the repulsive region and the friction force increases rapidly above zero. The repulsive region of the F_N profile can be analyzed within the Johnson-Kendall-Roberts (JKR) model,[15] which describes deformable interfaces with the presence of an attractive potential. The JKR fit gives a composite modulus of 13 GPa. For comparison, fits to the COOH/CH$_3$ and COOH/COOH combinations give composite moduli of 29 GPa and 33 GPa, respectively. The composite modulus increases in the order CH$_3$/CH$_3$ < COOH/CH$_3$ < COOH/COOH, owing to different total molecular lengths of the SAM combinations.[19] The differences in the composite modulus are responsible for the different relative RD scales for the three panels.

Compared to CH$_3$/CH$_3$, the maximum attractive force for COOH/CH$_3$ increases about three fold, panel (b). We attribute the increased adhesion to the addition of a dipole–induced dipole component to the van der Waals (vdW) interaction due to the polar nature of the COOH surface (~2 Debye per COOH group), as well as capillary condensation of water on the COOH surface. The later serves to decrease the effective distance for the vdW interaction between the two surfaces. As the two surfaces approach, there is an attractive jump in F_N around point A (RD ~ 4.2 nm). The scatter in this point is consistent with nucleation and capillary condensation; this is supported by simulation below. As the tip continues its approach, F_N begins a slow decrease up to approximately the point C (RD ~ 2.0 nm), where F_N enters the repulsive region and F_μ rises rapidly. This point, again, corresponds to contact between the two films.

When both surfaces are hydrophilic, panel (c), the magnitudes of the initial jump in F_N and the attractive force in the slow growth region (from point A to B) are higher than those seen for the COOH/CH$_3$ combination. This is consistent with the nucleation and growth of water meniscus at the hydrophilic interface. A quantitative understanding of the jump-in and the slow growth of attractive normal force requires realistic simulation at a scale not possible with current theoretical methods.[4,6] Here we focus on the most provocative aspect of experimental observation for confinement within ~1 nm of interfacial separation. The unique aspect of the COOH/COOH data is the rapid increase in attractive force beginning near point B (to a

maximum value an order of magnitude larger than that in CH_3/CH_3). At virtually the same distance, the friction force begins a rapid rise. This is very different from the CH_3/CH_3 and $COOH/CH_3$ combinations, where the friction force only rises sharply at film contact (point C). This behaviour strongly suggests capillary condensation to form a water meniscus, which is responsible for both F_N and F_μ. Note that the F_N continues to rise until film/film contact (point C) whereas F_μ peaks (*) and then decreases to near baseline at point C, before rising again after film contact. This is because the meniscus is squeezed or swept away from the nanogap as the interfacial separation decreases beyond a critical point (*).

If the dramatic rise in friction is due to the water meniscus, its viscosity must be significantly larger than that of bulk water, since a submerged tip shows negligible friction force under the same conditions. To get an idea of how large this increase would have to be, we make the following crude calculation. The cross sectional area (A_m) of the water meniscus can be estimated from the peak attractive normal force and the Kelvin radius (r_K) of the meniscus given by:[15]

$$r_K = \frac{\gamma_{H_2O} V_M}{RT \log(p/p_s)} \tag{1}$$

where γ_{H2O}, V_M, R, T, and p/p_s are the surface tension, the molar volume of the water meniscus, the gas constant; the absolute temperature, and the relative humidity, respectively. Using the values of bulk water at 20°C, we have r_K = -1.6 nm at 45% RH. The Laplace pressure[15] of the water meniscus is $P_L = \gamma_{H2O}/r_K$ and the capillary force is $F_C = A_m P_L$. When the attractive normal force reaches a minimum (F_N = -0.26 μN), the maximum size of the meniscus is A_m ~ 5600 nm^2. Note that γ_{H2O} of the nanoscopic meniscus is not known and the calculation uses the value for liquid water. For comparison, the surface tension of ice can be as high as twice that of liquid water.[21]

Under the simple assumption that the velocity profile under shear is linear and given A_m, the peak friction force value of F_μ* = 8.6 nN, and an experimental shear velocity of v_s = 180 nm/s, we can calculate the effective viscosity (η_{eff}) of the water meniscus as:

$$\eta_{eff} = \frac{\text{shear stress}}{\text{shear rate}} = \frac{(F_\mu*/A_m)}{(v_s/d*)} = 5.1 \times 10^3 \, \text{Pa} \cdot \text{s} \tag{2}$$

where $d*$ (~ 0.6 nm) is the interfacial distance at which the friction force peaks. The effective viscosity of the water meniscus between two COOH surfaces is nearly seven orders of magnitude higher than the viscosity of bulk water (η_{bulk} = 8.6x10^{-4} Pa·s at room temperature). The value of η_{eff} for the water meniscus is similar to that reported for a quasi-liquid layer on the ice surface[22] or to that estimated for structured water near an oligo(ethylene glycol) surface.[23]

Capillary condensation and water-meniscus formation depend on RH. Figure 2 shows a set of F_N and F_μ profiles for the COOH/COOH interface at RH = 10-45%. The characteristic fingerprint of the viscous water meniscus is observed for all RH values. At RH = 10%, the presence of viscous water shows up as a shoulder (*) in F_μ profile before interfacial contact. With increasing

154

RH, this feature grows and develops into a distinct peak. The calculated maximum cross sectional areas of the meniscus are 2000, 3600, and 5600 nm^2 for RH = 10%, 26%, and 45%, respectively. Growth of the meniscus is also shown by the outward shift of the point of meniscus nucleation (*A*) or capillary condensation (*B*) with increasing RH.
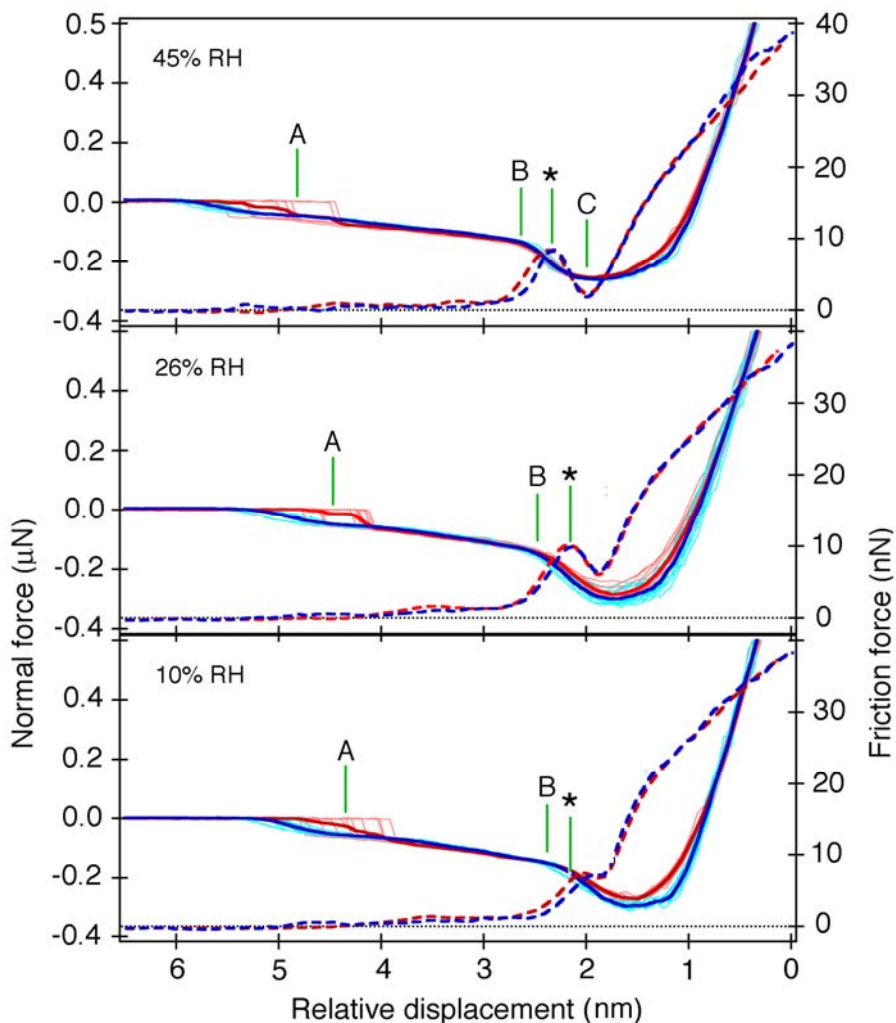
Figure 2. Normal force (F_N, solid curves and left axis) and friction force (F_μ, dashed curves and right axis) profiles as a function of relative displacement between the tip and the sample for COOH tip on COOH surface at the indicated RH values (0-45%). In each panel, the thin pink and blue curves are individual F_N profiles during approach and retract, respectively; the thick red (approach) and blue (retract) curves are averaged data. Only averaged data are shown for F_μ profiles (dashed red for approach and dashed blue for retract). All measurements were carried out at room temperature.

Our grand canonical Monte Carlo simulations provide microscopic-level information on the water meniscus confined in nanoscopic gaps. The methodology employed closely follows an earlier simulation study of the mechanical relaxation of methyl-terminated SAMs.[24] Three different systems formed by combination of Au-S-$(CH_2)_{15}$-COOH or Au-S-$(CH_2)_{15}$-CH_3 SAMs were investigated at a temperature of 300 K and RH = 10%. Figure 3 shows snapshots taken from COOH/COOH and COOH/CH_3 simulations during approach. Results for CH_3/CH_3 are not shown because there are only a few water molecules present at all interfacial separations

155

investigated. The number shown on each image corresponds to the Au-Au distance (D_{Au-Au}). For comparison with the experimental data, the two SAM films account for ~4.1 nm of the total separation. For COOH/COOH at $D_{Au-Au} > 5.2$ nm, the simulation shows mostly surface water molecules on each hydrophilic surface. At $D_{Au-Au} \leq 5.2$ nm, hydrogen bonded water bridges connecting the two COOH surfaces start to appear. Further decrease in interfacial separation leads to a rapid rise in the number of interfacial water molecules; this is essentially capillary condensation and corresponds to the rapid increase in attractive force and friction force in experiments. A snapshot at $D_{Au-Au} = 4.8$ nm (or interfacial separation of ~0.7 nm) clearly shows that the meniscus corresponds to an extensively hydrogen-bonded network connecting the two surfaces. When D_{Au-Au} decreases below 4.6 nm, the water molecules are squeezed out. For the COOH/CH$_3$ combination, the snapshots in Figure 3 show fewer water molecules, but the formation of water clusters extending into the gap is still observed for 4.5 nm $< D_{Au-Au} <$ 5.0 nm.
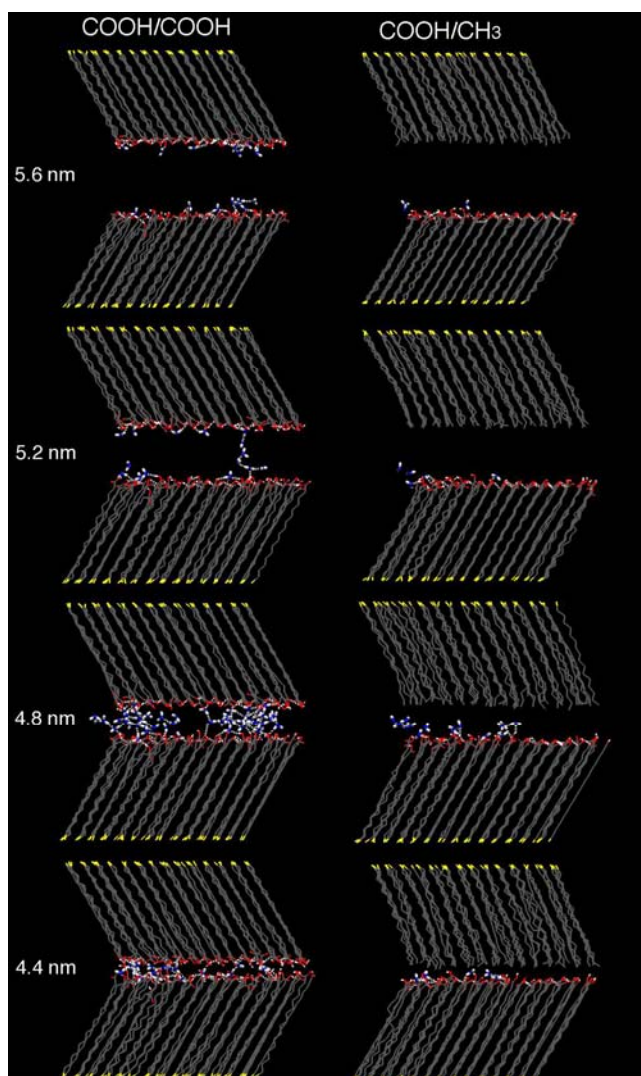
Figure 3. Snapshots of the COOH/COOH (left) or CH$_3$/COOH (right) interfaces during approach at the indicated Au-Au distances taken from grand canonical Monte Carlo simulations. The Au atoms are yellow and oxygen atoms in water or COOH groups are blue or red, respectively. The dashed white lines represent hydrogen bonds.

Panel (a) in Figure 4 plots the number of H_2O (N_{H2O}) within the simulation cell as a function of D_{Au-Au}. For the COOH/COOH combination, the water population peaks at $D_{Au-Au} = 4.7$ or 5.1 nm (approach or retract) or an interfacial separation of 0.6 or 1.0 nm. This distance is in excellent agreement with the experimental positions of peak friction force. On the other hand, simulation yields an onset of capillary condensation at an interfacial separation of ~1.0-1.8 nm (approach-retract), while experimentally observed jump-in occurs at ~2.3 nm for RH = 10% (point A in bottom panel of Figure 2). This level of discrepancy is not unexpected, given the much smaller size of the simulation cell. For the COOH/CH₃ combination, a smaller peak in water population is seen during approach; the peak is less obvious in retraction. The slow rise in water population as interfacial separation decreases from ~3 nm to 0.6-0.9 nm is consistent with the shallow attractive well seen in the experimental F_N profile. Note that the simulations show significant hysteresis between approach and retract, while hysteresis in experimental data is much smaller. These differences are a necessary consequence of the simulation set-up.[25]
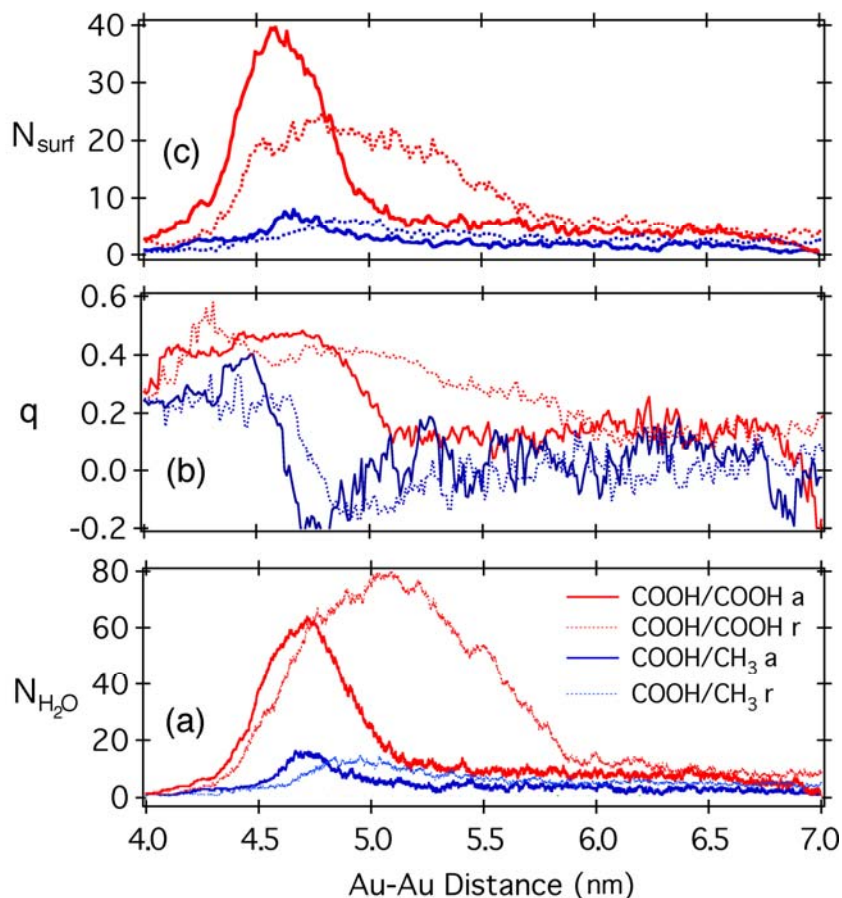
Figure 4. The number of water molecules within the simulation cell (N_{H2O}, bottom), the tetrahedral order parameter of water molecules (q, middle), and the number of water molecules bonded to each acid surface (N_{surf}, top) as a function of interfacial Au-Au distance for the COOH/COOH (red) and CH₃/COOH (blue) systems. The solid and dashed curves depict the approach and retract data, respectively. Each data set is averaged over four independent simulations. For the calculation of q, only water oxygens are taken as origin but the hydroxy- and keto- oxygens of the acid headgroup are also considered in the search for the four nearest neighbors.

Further information on the structure of the water meniscus is obtained from analysis of water molecules bonded directly to the acid surface (N_{surf}) and of the orientational order parameter (q). The former quantity is determined using the hydrogen bond criterion suggested by Wernet et al.[26] and normalized by the number of acid surfaces. The orientational order parameter introduced by Errington and Debenedetti[27] measures the degree of tetrahedral ordering with a value of unity for a perfect tetrahedral network and a value of zero for a random network. As shown in Figure 4c, at large separations, N_{surf} is the same for the COOH/COOH and the COOH/CH$_3$ systems. At short separations there is a cooperative effect for the COOH/COOH system and N_{surf} exceeds that for the COOH/CH$_3$ system by approximately a factor of two. The rise in N_{surf} is accompanied by an increase in tetrahedral order parameter (q) in Figure 4b, and q in the COOH/COOH system peaks at a significantly higher value than for the COOH/CH$_3$ combination. The interfacial distances at which q rises and N_{surf} peaks for the COOH/COOH system are in excellent agreement with the experimentally observed distance range where friction peaks. It should be noted that the increase in q by 0.3 units as found for the COOH/COOH system exceeds that observed when the density of bulk water is increased by 40%; thus, dramatic changes in diffusivity and viscosity should accompany this change in tetrahedral order.[27]

Conclusions

In conclusion, we have found direct experimental evidence for the existence of a viscous interphase of water confined at the nanoscale between a hydrophilic tip and a hydrophilic surface. The viscous layer formed as a meniscus nucleated at an interfacial separation of nanometer scale, increasing both the attractive normal force and the friction force. These conclusions are supported by state-of-the-art simulations that indicate structured water molecules with extensive hydrogen bonding connecting the two hydrophilic surfaces as the source for the high effective viscosity. The highly viscous nature of water under nanoconfinement must be taken into account when we consider interfacial processes, including mechanical contact, surface diffusion, chemical kinetics and biological interactions.

References

1. Israelachvilli, J. & Wennerström, H. Role of hydration and water structure in biological and colloidal interactions. Nature 379, 219-224 (1996).

2. Maboudian, R. Surface processes in MEMS technology. Surf. Sci. Rep. 30, 207-269 (1998).

3. Karaborni, S., Smit, B., Heidug, W., Urai, J. & van Oort, E. The swelling of clays: molecular simulations of the hydration of montmorillonite. Science 271, 1102-1104 (1996).

4. Jang, J., Schatz, G. C. & Ratner, M. A. Capillary force in atomic force microscopy. J. Chem. Phys. 120, 1157-1160 (2004).

5. Piner, R. D., Zhu, J., Xu, F., Hong, S. & Mirkin, C. A. "Dip-Pen" Nanolithography. Science 283, 661-663 (1999).

6. Jang, J., Schatz, G. C. & Ratner, M. A. Capillary force on a nanoscale tip in dip-pen nanolithography. Phys. Rev. Lett. 90, 156104 (2003).

7. (a) Houston, J. E. & Michalske, T. A. The interfacial-force microscope. Nature 356, 266-267 (1992); (b) Houston, J. E. Interfacial-force microscopy: selected applications. The Applied Scanning Probes. Bhushan, B.; Fuchs, A. H.; Hosaka, S., Eds. (Springer-Verlag, Berlin, 2004).

8. Du, Q., Freysz, E. & Shen, Y. R. Vibrational spectra of water molecules at quartz/water interfaces. Phys. Rev. Lett. 72, 238 (1994).

9. Ostroverkhov, V., Waychunas, G. A. & Shen, Y. R. New information on water interfacial structure revealed by phase-sensitive surface spectroscopy. Phys. Rev. Lett. 94, 046102 (2005).

10. Richmond, G. L. Molecular Bonding and Interactions at Aqueous Surfaces as Probed by Vibrational Sum Frequency Spectroscopy. *Chem. Rev*. **102**, 2693 (2002).

11. Asay, D. B. & Kim, S. H. Evolution of the adsorbed water layer structure on silicon oxide at room temperature. *J. Phys. Chem. B* **109**, 16760 (2005).

12. Hu, J., Xiao, D. F., Ogletree, D. F. & Salmeron, M. Imaging the condensation and evaporation of molecular thin films of water with nanometer resolution. *Science* **268**, 267 (1995).

13. Toney, M. F. et al. Voltage-dependent ordering of water molecules at an electrode–electrolyte interface. Nature **368**, 444 (1994).

14. Morita, S., Wiesendanger, R. & Meyer, E. Eds. *Noncontact Atomic Force Microscopy* (Springer, Berlin, 2002).

15. Israelachvili, J. *Intermolecular & Surface Forces*; Academic Press: New York, **1992**.

16. Hu, H.-W.; Carson, G. A.; Granick, S. Relaxation time of confined liquids under shear. *Phys. Rev. Lett.* **66**, 2758 (1991).

17. Zhu, Y. & Granick, S. Viscosity of interfacial water. *Phys. Rev. Lett.* **87**, 096104 (2001).

18. Raviv, U., Laurat, P. & Klein, J. Fluidity of water confined to subnanometre films. *Nature* **413**, 51 (2001).

19. Houston, J. E. & Kim, H. I. Mechancial properties of functionalized alkanethiol self-assembled monolayers. *Acc. Chem. Res.* **35**, 547-553 (2002).

20. Weeks, B. L.; Vaughn, M. W. & De Yoreo, J. J. Direct imaging of meniscus formation in atomic force microscopy using environmental scanning electron microscopy. *Langmuir* **21**, 8096 (2005).

21. Douillard, J. M. & Henry, M. Calculation of surface enthalpy of solids from an ab initio electronegativity based model: case of ice. *J. Coll. Interface Sci.* **263**, 554 (2003).

22. Pittenger, B. et al. Premelting at ice-solid interfaces studied via velocity-dependent indentation with force microscope tips. *Phys. Rev. B* **63**, 134102 (2001).

23. Kim, H. I., Kushmerick, J. G., Houston, J. E. & Bunker, B. C. Viscous "interphase" water adjacent to oligo(ethylene glycol)-terminated monolayers. *Langmuir* **19**, 9271 (2003).

24. Siepmann, J. I. & McDonald, I. R. Monte Carlo simulation of the mechanical relaxation of a self-assembled monolayer. *Phys. Rev. Lett.* **70**, 453 (1993).

25. Capillary condensation requires the nucleation of liquid droplets during approach while nucleation of vapour bubbles is necessary during retract. The nucleation free energy barriers for these processes are the underlying reason for hysteresis in simulation. On the other hand, each experimental measurement is carried out on a time scale of seconds, involves a much larger interfacial contact possibly with multiple nucleation sites, and provides an air-liquid interface (at the outer edge of the meniscus). All these contribute to the much smaller hysteresis in experimental data.

26. Wernet, Ph., et al. The structure of the first coordination shell in liquid water. *Science* **304**, 995 (2004).

27. Errington, J. R., & Debenedetti, P. G. Relationship between structural order and the anomalies of liquid water. *Nature* **409**, 318 (2001).

Drying Transition of Confined Water

Introduction

Long-range hydrophobic interactions operating underwater are important in the mediation of many natural and synthetic phenomena, such as protein folding, adhesion and colloid stability. Here we show that rough hydrophobic surfaces can experience attractive forces over distances more than 30 times greater than any reported previously, owing to the spontaneous evaporation of the intervening, confined water. Our finding highlights the importance of surface roughness in the interaction of extended structures in water, which has so far been largely overlooked.

The existence of 'long-range' hydrophobic interactions has been debated for more than 25 years[1-5], because their reported range of 1–100 nanometres exceeds that of van der Waals forces and cannot be explained by water restructuring. However, investigations have been limited to smooth, flat model surfaces[4], even though most surfaces are rough. Roughness strongly influences wetting—as evidenced by the high water-contact angles ($\theta \geq 160°$) and rolling of water droplets on lotus leaves[6].

Knowing that superhydrophobic surfaces occur naturally and that living systems operate mainly in water, we investigated the interaction of rough superhydrophobic surfaces beneath the water surface. Interfacial-force microscopy[7] and optical imaging were used to examine the interaction between two approaching or retracting superhydrophobic surfaces (water contact angle θ of about 170°) submerged in either air-equilibrated or de-aerated water.

We discovered a very-long-range hydrophobic interaction that was due to out-of-contact evaporation, or 'cavitation', of the intervening water at tip-to-substrate separations ranging from 0.8 µm to as much as 3.5 µm. Cavitation is a first-order phase transition characterized by a sudden, strong attractive force (Figure 1a) and by the appearance of a vapour bridge spanning the tip-to-substrate gap (Figures 1 b–e).

Pre-existing 'nanobubbles' of a size commensurate with the interaction length have been proposed as a source of long-range interactions[8]. We therefore used *in situ* confocal imaging to search for bubbles on an isolated, flat superhydrophobic surface. Neither the microscopy nor neutron reflectivity experiments[9] provide evidence for bubbles—certainly not micrometre-sized bubbles. We therefore argue that cavitation is a consequence of, and thermodynamically consistent with, the properties of confined water[10]. The critical separation, D, below which cavitation is thermodynamically favoured can be estimated from Laplace's equation as 1.4 µm; this is a lower bound and will increase if Δp, the pressure difference across the interface, is reduced by incorporation of air into the cavity.
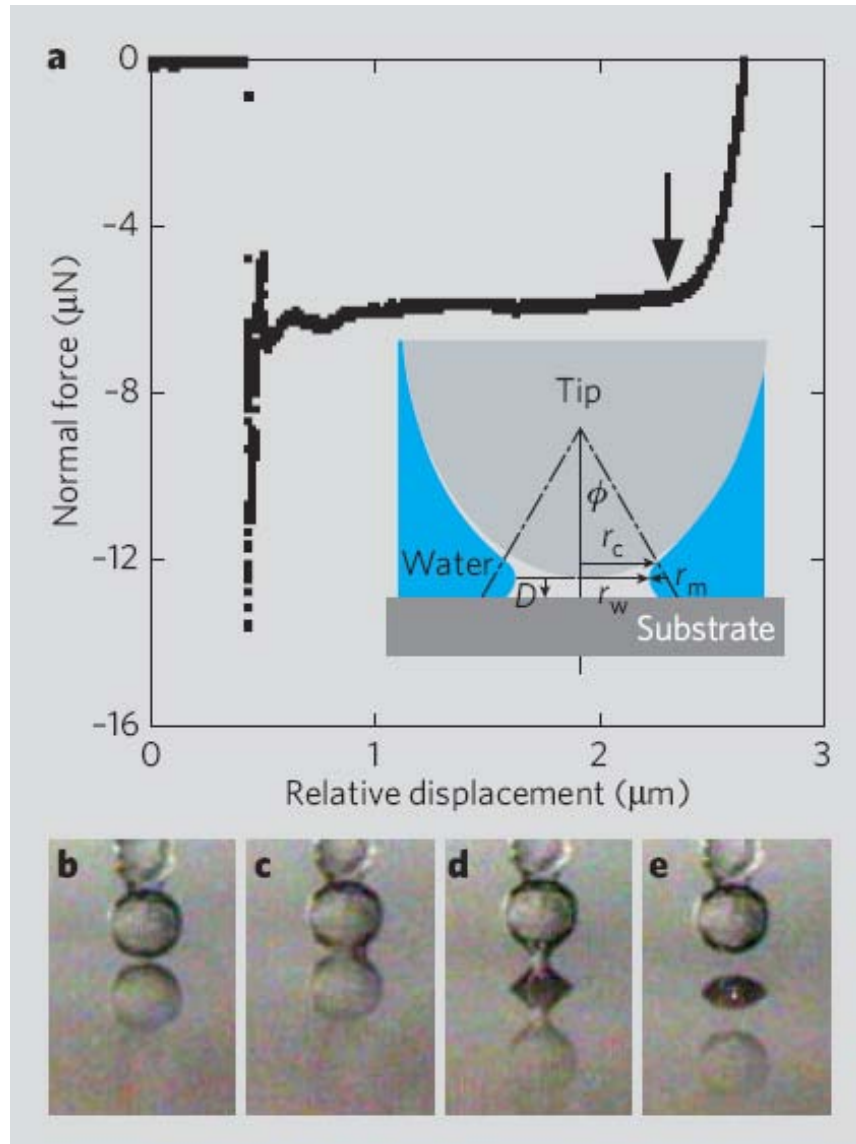
Figure 1. Cavitation between superhydrophobic surfaces. a) Plot of force versus displacement for the underwater approach of a tip towards a flat surface. The experiment starts at zero micrometres relative displacement (arbitrarily defined). The sudden development of a negative (attractive) force at about 0.4 μm relative displacement corresponds to cavitation. Contact with the surface is indicated by the inflection at about 2.2 μm (arrow). The distance between the onset of adhesion and contact (1.8 μm) is the distance over which cavitation occurs for this sample. The inset shows the cavitation geometry: $\Delta p = \gamma(1/r_w - 1/r_m)$, where Δp is the pressure difference across the interface, γ is the liquid–vapour interfacial tension, r_m is the radius of the meniscus, r_w is the radius of its waist, and r_c is the contact radius of the cavity on the tip surface. D is the critical separation below which cavitation is thermodynamically favoured. b–e), Optical images of cavitation: b) position of superhydrophobic tip and substrate just before cavitation; c) cavitation occurs about 33 ms later; d) cavity meniscus, as seen during tip retraction, one frame before its unstable collapse; e) a cavity 'bubble' is left behind on both the tip and substrate. These bubbles, attributed to air supplied from water and the porous superhydrophobic surface, are unstable and are readsorbed in about 6 seconds. In all frames, the circular image at the bottom is the reflection of the spherical 150-μm-diameter tip in the flat superhydrophobic surface.

162

Unambiguous cavitation has previously been observed only following the contact of smooth hydrophobic surfaces[3,8,11]. Although it is thermodynamically acceptable, out-of-contact cavitation has been modelled as having a large activation barrier[12], so we need to explain why we observe it and how kinetic barriers are surmounted.

Experimental Methods

Sample preparation

Superhydrophobic silica surfaces (contact angles of water $\geq 163°$, see Figure 2) were prepared on spherical IFM tips and flat single crystal Si substrates using a variation of the low temperature/pressure aerogel thin film process developed in our lab[13] where a quarter of the tetraethylorthosilicate (TEOS) was replaced with 3,3,3 trifluoropropyltrimethoxysilane, and the as-deposited films were exposed to hexamethyldisilizane vapor at 50°C. SH surfaces were deposited by dipping (tips) or spin-coating (silicon substrates).
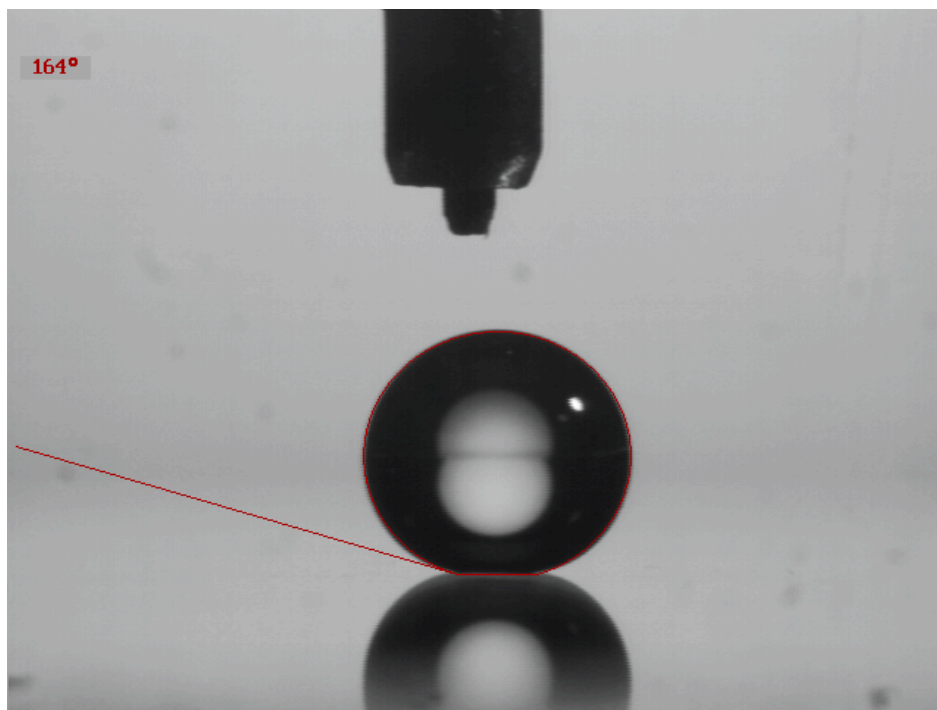
Figure 2. Water droplet on representative SH surface prepared on a smooth flat silicon substrate. Contact angle = 164°.

Interfacial force Microscopy

IFM experiments were conducted in standard low conductivity (18.2 MΩ) de-ionized (DI) water and deaerated DI water (prepared by repeated freezing/pump/thaw cycles) with similar results. Figure 3 shows a series of images where we observe out of contact cavitation occurring over a distance of 3.5-µm.

Figure 3. Movie frames showing out of contact cavitation at a distance of ~3 micron a) one frame prior to b, b) clip showing cavitation, and c) extended vapor cavity visible during withdrawal. Bottom semicircular shape is a reflection of the spherical SH tip from the underlying flat SH surface.

Confocal Fluorescence Imaging

Confocal fluorescence imaging was used to look for the presence of vapor bubbles at the SH/water interface, as so-called 'nanobubbles' have been argued to be a source of long range hydrophobic interactions the growth and coalescence of pre-existing bubbles could conceivably be an explanation of the long range out of contact cavitation we observe. To perform these experiments the SH film was was fluorescently labeled with the water insoluble green fluorescent dye, fluorescein isocyanate (Molecular Probes), and submerged in water containing the water soluble red fluorescent dye rhodamine B (Kodak). The movies shg_waterr_interface _slic1.avi (Movie 1) and shg_waterr_interface_slic2.avi (Movie 2) show a series of confocal optical sections (Z-stack) through the fluorescently labeled SH/water interface. Images were taken with a Zeiss LSM 510 using two simultaneous laser excitation sources (Ar (488 nm) and He-Ne (543)) and a 63x objective. Image scan size is: (Movie 1) 29.2-µm x 29.2-µm x .06 µm and (Movie 2) 6.6 µm x 6.6 µm x .06 µm. Starting in the SH film (green) optical sections taken at successively shallower focal planes show the progressive development of a patchwork of red regions corresponding to water and emphasizing the rough three-dimensional nature of the SH/water interface. Whereas within the green regions we see black textural features (that eventually become infiltrated with red) indicative of the nanoscale porosity of the SH surface, within the red (water) regions there is no evidence of vapor bubbles, which would appear as black (presumably circular) shapes. This argues against the coalescence of pre-existing ~300-nm 'nanobubbles' as being responsible for long range out of contact cavitation between submerged SH surfaces.

Results and Discussion

First, we used interfacial-force microscopy[7], in which interfacial forces are counterbalanced, to avoid snap-to-contact (when the rate of change of the force exceeds the spring constant and the two surfaces snap together uncontrollably, as occurs in atomic-force microscopy and in surface-force apparatus studies[5]). Second, the calculated *D* for submerged super hydrophobic surfaces is more than ten times that of smooth surfaces, which increases the probability of cavity nucleation at larger separations. Third, the submerged superhydrophobic surface presents an intrinsic liquid/vapour/solid interface, which may serve as a heterogeneous nucleation surface.

We simulated the molecular dynamics of a model fluid, which showed the necessary liquid–vapour behaviour, confined between two closely spaced surfaces containing opposing ($\theta = 180°$) superhydro phobic patches. The simulations show that cavitation occurs by the growth of capillary-like fluctuations of vapour films extending from the super hydrophobic surfaces, leading to the sudden formation and growth of a vapour bridge.

Conclusion

Our experiments reveal that cavitation can be one source of long-range hydrophobic interactions. For rough surfaces, the interaction length extends to micrometre scales. Correspondingly, interaction lengths of hundreds of nanometres, observed for smooth surfaces (for example, snap-to-contact), might also be explained by cavitation, in agreement with thermodynamic expectations.

References

1. Blake, T. D. & Kitchener J. A. J. Chem. Soc. Farad. Trans. 1 68, 1435–1442 (1972).

2. Christenson, H. K. & Claesson, P. M. Adv. Colloid Interface Sci. 91, 391–436 (2001).

3. Christenson, H. K. & Claesson, P. M. Science 239, 390–392 (1988).

4. Israelachvili, J. & Pashley, R. Nature 300, 341–342 (1982).

5. Stevens, H., Considine, R. F., Drummond, C. J., Hayes, R. A. & Attard, P. Langmuir 21, 6399–6405 (2005).

6. Lafuma, A. & Quéré, D. Nature Mater. 2, 457–460 (2003).

7. Joyce, S. A. & Houston, J. E. Rev. Sci. Instr. 62, 710–715 (1991).

8. Parker, J. L., Claesson, P. M. & Attard, P. J. Phys. Chem. 98, 8468–8480 (1994).

9. Doshi, D. et al. Langmuir 21, 7805–7811 (2005).

10. Lum, K., Chandler, D. & Weeks, J. D. *J. Phys. Chem. B* 103, 4570-4577 (1999).

11. Pashley, R. M., McGuiggan, P. M., Ninham, B.W. & Evans, F. D. *Science* 229, 1088–1089 (1985).

12. Luzar, A. *J. Phys. Chem. B* 108, 19859–19866 (2004).

13. Prakash, S. S., Brinker, C. J., Hurd, A. J., & Rao, S. M. *Nature*, 374, 439-443 (1995).

Nanometer-Thick Conformal Pore Sealing of Self-Assembled Mesoporous Silica by Plasma-Assisted Atomic Layer Deposition

Introduction

As device dimensions in semiconductor integrated circuits (ICs) continue to shrink, low dielectric constant (low-*k*) materials are needed as interlevel dielectrics (ILD) to mitigate issues caused by reduced line width and line-to-line distances such as increasing RC-delay. To satisfy the technical requirements imposed by the microelectronics roadmap (where ultra-low *k* values < 2 are specified), future generation ILD materials must incorporate porosity. However, the pores, typically on the order of angstroms to a few nanometers and connected to each other at elevated porosities, can trap moisture, gas precursors and other contaminants in subsequent processes, making practical pore-sealing techniques essential to ultra low-*k* implementation.[1-3]

To be useful for microelectronics applications, a pore-sealing coating must be conformal to the 3D topology of patterned ILD films. In addition, at the 65 nm or smaller technology node, it must be less than several nm thick so that its impact on the overall ILD *k* value is negligible.[1] These requirements exclude many thin film techniques, however one exception is atomic layer deposition (ALD), for which the coatings are inherently conformal and precisely controlled at sub-nm thicknesses. However, on a porous substrate, regular ALD not only takes place on top of the substrate, but also penetrates into the internal porosity, filling pores and drastically increasing the effective ILD *k* value.[4-6] Therefore, an approach capable of localizing ALD to the ILD surface and allowing spanning of the pores is needed.

Generally this is hard to achieve because ALD is a surface adsorption-based deposition process that takes place wherever gas precursor adsorption occurs, including throughout the complete network of connected internal porosity. Short precursor exposure times may reduce the ALD penetration depth, but with small ILD feature dimensions, even a 10 nm penetration depth means that a large percentage of the ILD porosity will be filled up.

Here we report a plasma-assisted process in which ALD is confined to the immediate surface, allowing pore sealing at minimal ILD thickness. Several groups have demonstrated the use of plasmas to enhance the extent of ALD reactions and achieve better film quality.[7-9] In our work, the purpose of the plasma is to define the location of ALD. If ALD precursors are chosen to be non-reactive unless triggered by plasma, then, ALD can be spatially defined by the supply of plasma irradiation. In this regard it is important to recognize that the Debye length and the molecule mean free path in a typical plasma greatly exceed the pore dimension of a porous low-*k* material, thus plasma cannot penetrate (and ALD cannot occur) within the internal porosity.

Experimental Methods

The experiments were carried out in a self-designed, home-built plasma-assisted ALD (PA-ALD) system. The deposition chamber was a 25mm diameter Pyrex tube, evacuated by a turbomolecular pump to a base vacuum of 5×10^{-7} Torr. An RF coil surrounded the Pyrex tube

167

for plasma generation. Samples were mounted in a remote plasma zone for reduced ion bombardment and plasma-heating effects. Oxygen and TEOS (tetraethylorthosilicate $Si(OCH_2CH_3)_4$) were used as the precursors for SiO_2. In the absence of plasma, they remain unreactive at room temperature. These precursors were admitted into the reactor alternately via pneumatic timing valves. A constant Ar flow of 15 sccm was used as the carrier gas as well as the purging gas.

The mesoporous silica thin film samples were prepared on silicon substrates by evaporation-induced self-assembly using Brij-56 as the surfactant to direct the formation of a cubic mesostructure characterized by a continuous 3D network of connected pores with diameters ~2-nm.[10] These films exhibit excellent mechanical strength and thermal stability, along with an isotropic k and low surface roughness important for etching or chemical mechanical polishing. At 50 volume % porosity, the k value can be 2.5 or less. Prior to PA-ALD, the samples were patterned by interferometric lithography and etched with a CHF_3/Ar plasma to create 400 x 400-nm trenches (Figure 1a). Then the photoresist and any residual organics were removed by oxygen-plasma treatment.
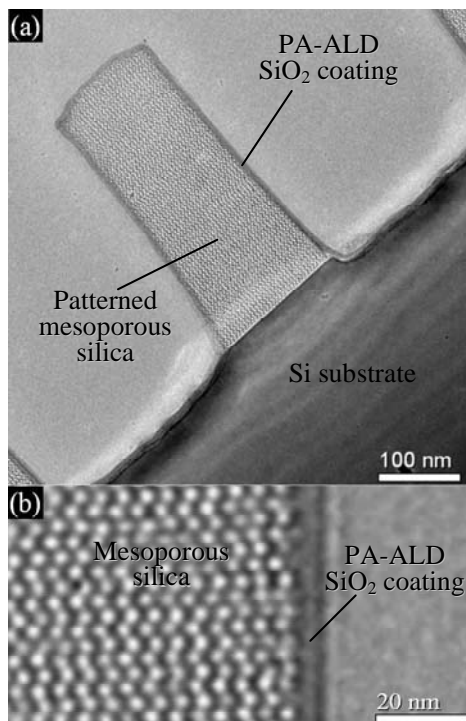
Figure 1. Cross-sectional TEM images showing: a) conformal 5nm thick pore-sealing coating of SiO_2 prepared on a patterned mesoporous low-k silica film by plasma-assisted ALD; b) enlarged image at the interface between PA-ALD layer and the mesoporous film.

Plasma-assisted ALD was performed by first introducing TEOS vapor into the reactor, followed by Ar purging to obtain monolayer (or sub-monolayer) adsorption on the sample surface. RF power was then delivered to the coil, creating an O_2 and Ar plasma to produce active radicals that convert surface-adsorbed TEOS into reactive silanols and may promote further conversion to siloxane. After that, the deposition chamber was purged again to remove the residual gaseous products. The above steps were repeated 150 times, with each step lasting 5 seconds.

Results and Discussion

Figures 1a and 1b show cross-sectional TEM images of the sample. A 5 nm thick SiO_2 coating is observed as the smooth dark rim bordering the patterned mesoporous silica feature. Clearly, the coating is conformal to the patterned morphology and uniform in thickness. No penetration of the SiO_2 into the porous matrix can be observed, and the interface between the coating and the mesoporous silica film remains sharp.

To verify the pore-sealing effectiveness of PA-ALD, the PA-ALD coated sample was put into a traditional thermal ALD reactor, where we performed TiO_2 ALD. We have shown that standard TiO_2 ALD will infiltrate surfactant-templated mesoporous silica, so this experiment was conducted to demonstrate the effectiveness of PA-ALD pore sealing. At 180 ^{o}C, the PA-ALD coated sample was treated with 100 thermal ALD cycles using $TiCl_4$ and H_2O as the precursors. Figure 2 shows the corresponding TEM images. Figure 2a is a regular cross-sectional TEM image, where we observe two ALD layers. The inner, lighter layer is the PA-ALD SiO_2 coating, and the outer, darker layer is the TiO_2 thermal ALD coating. The mesoporous low-*k* silica appears completely unaffected, suggesting that $TiCl_4$ and H_2O cannot penetrate through the PA-ALD SiO_2 coating to form TiO_2 in the underlying porous silica matrix. This is further supported by the Ti- mapping image in Figure 2b. The bright border in this image represents the location of Ti, and corresponds to the TiO_2 overlayer shown in Figure 2a. Comparing the Ti- mapping image (Figure 2b) to the original regular TEM image (Figure 2a), no detectable TiO_2 can be found beyond the PA-ALD SiO_2 coating. Therefore, the PA-ALD SiO_2 coating, although only 5 nm thick, is pinhole-free and sufficiently dense to seal the pores and protect the underlying porous low-k silica from exposure to gaseous chemicals.
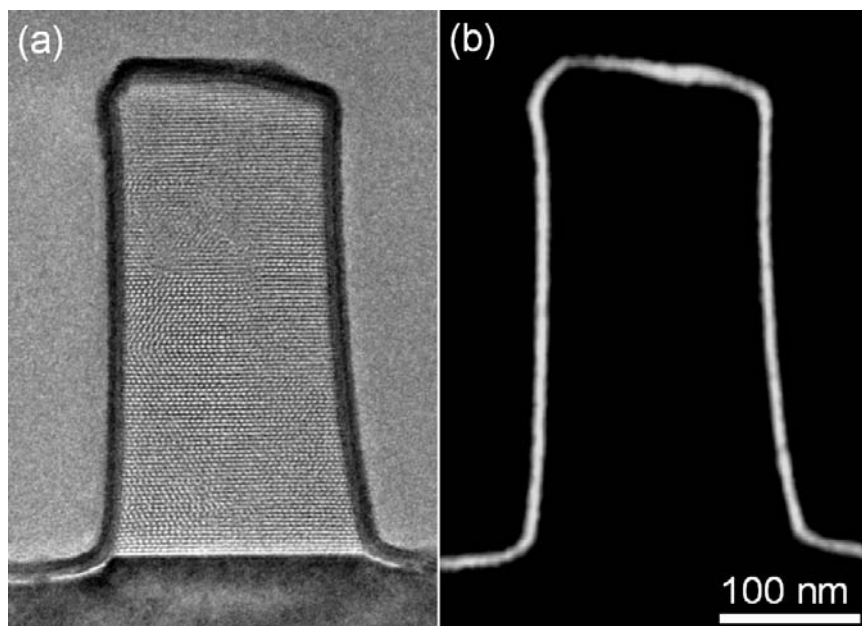
Figure 2. TEM images demonstrating the pore-sealing effectiveness by PA-ALD: a) regular cross-sectional TEM image showing the mesoporous sample treated by PA-ALD pore-sealing process and then exposed to TiO_2 ALD conditions; b) Ti- mapping image in the same area acquired with electron-energy-loss image filtering mode.

Concerning the mechanism of room temperature PA-ALD of SiO_2, we first note that the deposition rate is quite low, 0.03-nm/cycle, compared to 0.07-0.08-nm/cycle measured by George *et al.* for conventional NH_3 catalyzed SiO_2 ALD.[11] Conventional ALD uses multiple water/TEOS cycles, where water exposures serve to hydrolyze ethoxysilane bonds to form silanols, and alkoxide exposure results in condensation reactions to form siloxane bonds. As for the related solution-based 'sol-gel' reactions, hydrolysis and condensation are bimolecular nucleophilic substitution reactions catalyzed by acid or base.[12] In PA-ALD, plasma exposure takes the place of hydrolysis, activating the alkoxide surface toward TEOS adsorption. Based on studies of plasma-enhanced CVD of SiO_2 from TEOS and O_2 performed by Aydil *et al.*[13] where silanol groups were identified after exposure of TEOS to an oxygen plasma, we expect silanols to form similarly during PA-ALD. However due to the monolayer (or sub-monolayer) $\equiv$Si-OH coverage, we cannot quantify the extent of surface hydrolysis. Additionally we expect the plasma could serve a catalytic role by generating nucleophilic oxo radicals, $\equiv$Si-O· that promote siloxane bond formation. Apparently at room temperature the extent of these plasma assisted hydrolysis and condensation reactions are less than for conventional ammonia catalyzed hydrolysis and condensation reactions, explaining the low deposition rates. Consistent with a low rate of siloxane bond formation is the highly conformal and dense PA-ALD layer indicative of a reaction-limited monomer-cluster growth process—in our case confined exclusively to the plasma-activated surface.[12]

Conclusions

Here we emphasize PA-ALD as a means of sealing pores. However with the very high degree of thickness control that we demonstrate, we envision that, prior to complete pore sealing, we will progressively reduce the pore size of the mesoporous silica in a sub-Å/cycle fashion. This combined with the thin PA-ALD layer thickness could have very important implications for membrane formation, where extremely thin inorganic films with precisely controlled pore size could enable the synthesis of robust mimics of natural ion or water channels of interest for sensors and water purification.

References

1. 2004 International Technology Roadmap for Semiconductors, Interconnect, SIA.

2. Peters, L., Semiconductor International, October 2005, 49-53.

3. de Rouffignac, P; Li, ZW; Gordon, RG. Electrochemical and Solid State Letters 2004; 7, G306-G308.

4. Cameron, M.A.; Gartland, I.P.; Smith, J.A.; Diaz, S.F.; George S.M. Langmuir 2000, 16, 7435-7444.

5. Ek, S.; Iiskola, E.I.; Niinistö, L. Langmuir 2003, 19, 3461-3471.

6. Travaly, Y; Schuhmacher, J; Baklanov, MR; Giangrandi, S; Richard, O; Brijs, B; Van Hove, M; Maex, K; Abell, T; Somers, KRF, J. Appl. Phys 2005, 98, 083515.

7. Elers, KE; Winkler, J; Weeks, K; Marcus, S J. Electrochem. Soc. 2005; v.152, no.8, p.G589-G593.

8. Kim, DH; Kim, YJ; Song, YS; Lee, BT; Kim, JH; Suh, S; Gordon, R J. Electrochem. Soc. 2003, 150, C740-C744.

9. Kim, H; Detavenier, C; van der Straten, O; Rossnagel, SM; Kellock, AJ; Park, DG, J. Appl. Phys. 2005, 98, 014308.

10. Brinker, C.J.; Lu, Y.F.; Sellinger, A; Fan, H.Y. Adv. Mater 1999, 11, 579-585.

11. Ferguson, JD; Smith ER; Weimer, AW; George SM, J. Electrochem. Soc. 2004, 151, G528-G535.

12. Brinker, C.J.; Scherer G.W. Sol-Gel Science: The Physics and Chemistry of Sol-Gel Processing, Academic Press, San Diago, 1990.

13. Deshmukh S.; Aydil E., J. Vac. Sci. Technol. A, 13, 1995, 2355-2367.

Sub-10 nm Thick Microporous Membranes Made by Plasma-Defined Atomic Layer Deposition of a Bridged Silsesquioxane Precursor

Introduction

Membranes exhibiting high flux and selectivity are important for many applications, including water desalination, greenhouse gas storage and abatement, H_2 purification, and selective proton/oxygen conduction in fuel cells. Combined high flux and selectivity is achieved in natural systems by membrane-bound ion and molecular channelsswhose pore size is defined with sub-nanometer precision through protein folding and whose thickness is limited to that of the cellular membrane bilayer, only 4 nm. By comparison, synthetic membranes can seldom be fabricated with similar molecular level precision (the exceptions being carbon nanotubes and zeolites) and are often 100-1000× thicker. This is problematic because membrane flux varies reciprocally with membrane thickness. The inherent issue is that most synthetic approaches require relatively thick membranes to avoid defects or, in the case of zeolites and CNTs, the smallest-sized building blocks used for membrane fabrication are of the order 1 μm.[1,2]

Here we describe an atomic layer deposition (ALD) approach to construct ultrathin membranes with sub-angstrom control of pore size. Our approach extends the burgeoning ALD field[3-7] in several new directions. First, we perform ALD on a self-assembled nanoporous support, where the internal porosity is protected from deposition. Second, we restrict ALD to the extreme surface by plasma activation. Third, we employ a bridged bis-silsesquioxane precursor to deposit a hybrid organosilicate film, uniformly incorporating organic ligands that serve as molecular templates/porogens upon subsequent removal. Beyond membrane formation, this plasma-directed ALD approach naturally forms a low k dielectric sealing layer needed for future generations of microelectronics.

ALD is a self-limiting layer-by-layer thin film deposition technique composed normally of successive steps of adsorption and hydrolysis/activation of metal halide or metal alkoxide precursors.[3-6] To date, ALD has focused principally on the formation of dense thin film oxides, metals, or semiconductor alloys on solid substrates. Our previous research introduced plasma-assisted (PA)-ALD as a means to deposit dense oxide films on the immediate surface of a nanoporous film. In PA-ALD, exposure to a remote Ar + O_2 plasma, rather than hydrolysis, is used to activate the surface through formation of hydroxyl groups. Because both the plasma Debye length and the radical mean free path exceed greatly the pore diameter (~3 nm; see Figure 1), deposition does not occur within the interior pores.[7]
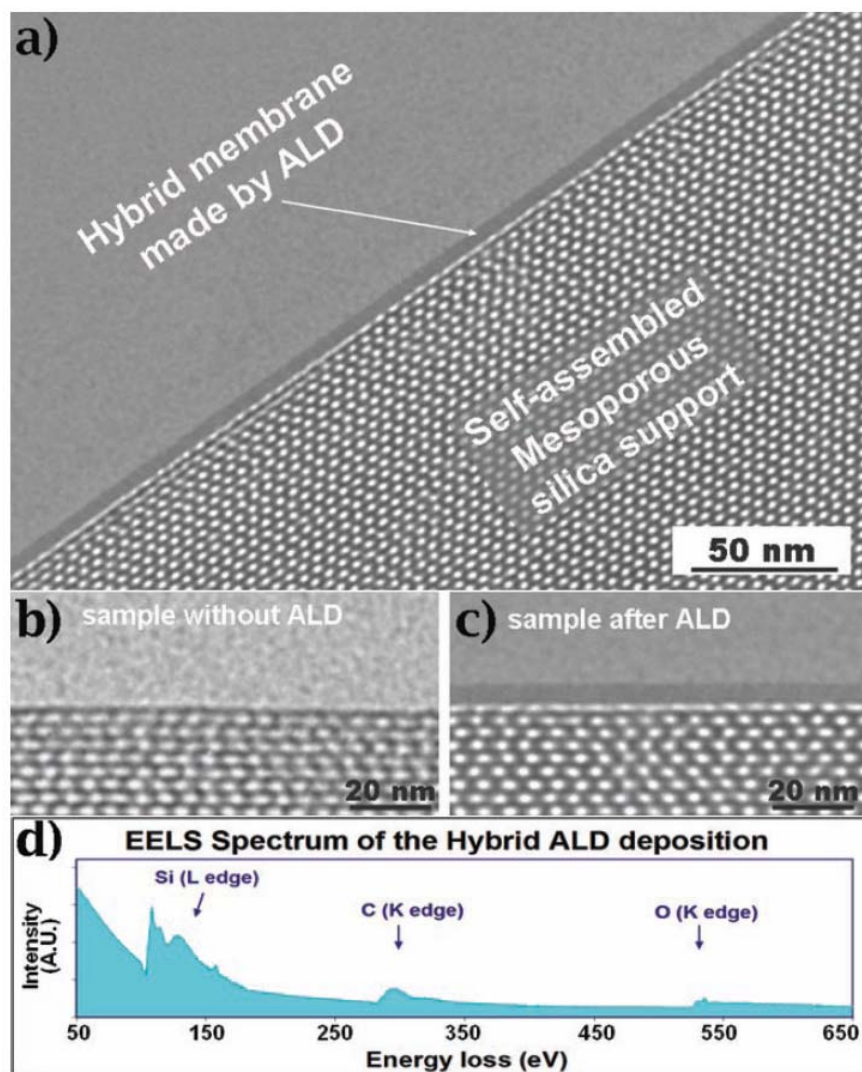
Figure 1. (a) Cross-sectional TEM image of the hybrid membrane supported on mesoporous silica; (b) original mesoporous silica support; (c) support coated with ALD membrane; (d) EELS spectrum of the membrane.

Experimental Methods

Surface-limited deposition of ultrathin layers on porous supports is important for sealing low *k* dielectrics. It is also of interest in the formation of high flux membranes. Here we achieve surfacelimited deposition and develop a high flux, high selectivity membrane by an approach combining remote plasma exposure and surface passivation with conventional ALD of an (unconventional) hybrid precursor. We start with a nanoporous silica film (Figure 1), consisting of an ordered cubic arrangement of monosized pores, formed by evaporation-induced self-assembly[8] on an underlying anodized alumina support having 20 nm pores aligned normal to the support surface. Following calcination and UV/ozone exposure,[9] the nanoporous film has fully hydroxylated 3.2 nm pores as measured by a surface acoustic wave based technique.[10] To avoid ALD on any interior porosity, which would detrimentally increase the membrane thickness, we expose this hierarchical membrane support structure to hexamethyldisilazane and then to

174

trimethylchlorosilane vapor at 180°C for 5 min. This exposure converts the surface and internal hydroxyl groups to trimethylsiloxane groups, which remain inert to hydrolysis reactions and therefore passivate the surface against ALD during subsequent steps. To activate the immediate surface of the nanoporous film to ALD, the sample is exposed to a remote Ar + O_2 plasma for 2 s. As reported previously by us, the plasma was designed so that its Debye length (several mm) and radical mean free path (several mm) are much larger than the pore size.[7] In this condition, the plasma radicals cannot penetrate the internal porosity, and only trimethylsiloxane groups residing on the immediate surface of the nanoporous film are converted to silanols $\equiv$Si-OH. These surface silanols are active to halide and alkoxide ALD precursors, $M(X)_n$ and $M(OR)_n$, respectively, undergoing condensation reactions to form $\equiv$Si-O-M$\equiv$ plus HX and HOR byproducts. Therefore, ALD takes place on the surface of the substrate, while internal, hydrophobic -$Si(CH_3)_3$ groups remain unhydrolyzed and do not undergo condensation reactions with ALD precursors.

In the case of passivated internal porosity, successive steps of adsorption and hydrolysis of $M(X)_n$ and $M(OR)_n$ precursors first reduce the size of surface nanopores and then, when the film thickness exceeds the original pore radius, progressively seal the surface. If molecular-sized pore templates, so-called porogens, could be introduced within a dense, ultrathin sealing layer, their removal would create a corresponding ultrathin microporous membrane with controlled pore size and shape.[11-13] Introduction of organic templates using organosilanes R_xSiX_{4-x} is rather straightforward and has been demonstrated previously.[5,12] However, in this case, the condensation reactions position the organic ligands R on the external surface, where they passivate it toward further ALD. Additionally, the coverage of R groups must be sufficiently low so as to avoid association of multiple R groups, which when removed would create larger and more polydisperse pores than individual R groups. To resolve these problems, we used an organically bridged silsesquioxane $(RO)_3Si$-R′-$Si(OR)_3$ as an ALD precursor. In this case, the R′ unit, which serves as the pore template, is incorporated uniformly within the developing siloxane framework, avoiding passivation of the surface and reducing template aggregation.

Here, as an example, we describe ALD of BTEE (bis(triethoxysilyl) ethane, $(C_2H_5O)_3$-Si-C_2H_4-Si-$(OC_2H_5)_3$). Following remote plasma exposure to activate the nanoporous substrate, ALD was performed in a home-built reactor according to the following steps: (1) evacuate ALD chamber to a base vacuum of 10^{-6} Torr; (2) inject BTEE vapor, causing BTEE molecules to condense with surface $\equiv$Si-OH groups; (3) purge chamber with Ar to remove all non-condensed BTEE and condensation byproducts; (4) inject water vapor to hydrolyze the ethoxysilane groups of surface chemisorbed BTEE; (5) purge chamber with Ar to remove residual water vapor and ethanol byproducts; (6) repeat steps 2-5 to obtain desired thickness.

Results and Discussion

Figure 1a shows a representative cross-sectional TEM image of the nanoporous supported ALD film prepared by 300 cycles of ALD (each cycle comprising steps 2-5 above) followed by UV/ozone exposure to remove the organic C_2 template. The film is ultrathin (~5 nm thick) and smooth and spans the ~3 nm diameter pores of the underlying support. The somewhat lower electron contrast with respect to silica derives from its sub-nanometer microporosity (see following discussion) not resolvable in this image. Comparison of the higher magnification

images in Figure 1b (support prior to ALD) and Figure 1c (support after ALD) shows that the film is confined to the immediate surface of the support with no evidence of penetration into the nanoporous sublayer. Figure 1d shows the electron energy loss spectrum (EELS) of the as-deposited ALD film. Prior to EELS, the sample was cleaned in a plasma oxidizer to remove any carbon contamination on the sample surface as well as epoxy used for cross-sectional sample preparation. The energy loss edges at 104, 286, and 540 eV are attributed to Si, C, and O, respectively. The absence of a shoulder edge at ~282 eV indicates that the carbon is mainly σ-bonded as expected from the bridging ethylene group in the BTEE precursor.[14]

To demonstrate the efficacy of this approach to form selective membranes, the organic template was removed by 30 s of UV/ozone exposure, and the permeance of the film to the series of gases He, N_2, and SF_6 was measured at room temperature using standard techniques.[11,12] Figure 2 shows the gas permeances and selectivities of the samples after differing numbers of ALD cycles. The original porous support had a He permeance of 171 $cm^3/bar \cdot cm^2 \cdot min$ and He/N_2 selectivity and He/SF_6 selectivity of 2.08 and 4.28, consistent with Knudsen diffusion. With increasing cycle numbers, the permeance decreased, and after 100 cycles, the selectivity increased logarithmically. These results are consistent with the requirement to form a defect-free, pore-spanning sealing layer of several nanometer thickness prior to template removal. Due to the thinness of the membrane, after 200 ALD cycles, the He permeance was a very remarkable 5.3 $cm^3/bar \cdot cm^2 \cdot min$, and the He/$N_2$ and He/SF_6 selectivities exceeded 10^3 and 10^4, respectively.
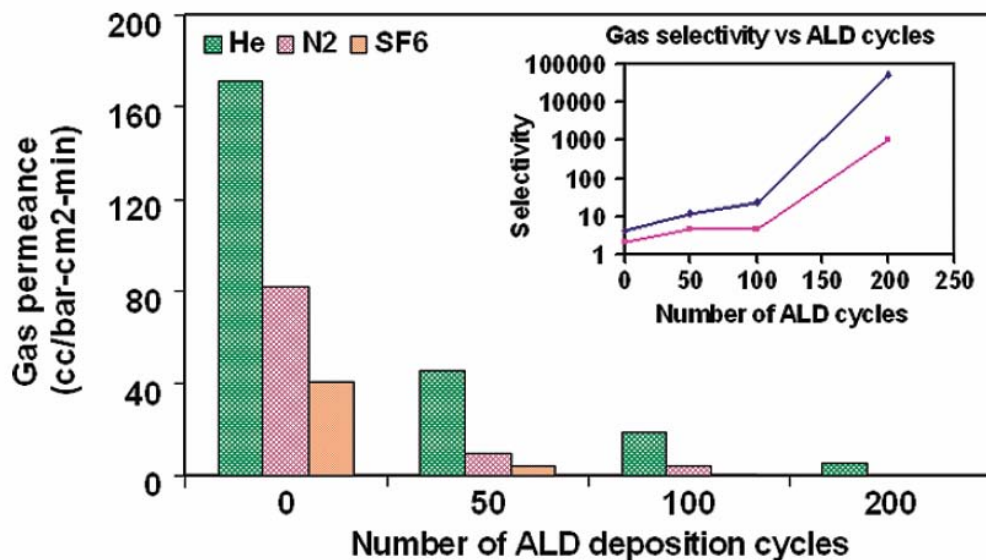
Figure 2. Gas permeances of ALD membranes to He, N_2, and SF_6 with kinetic diameters of 2.2, 3.6, and 5.5 Å, respectively.

In order to demonstrate the importance of bridging, rather than pendant, organic templates to this membrane fabrication strategy, we attempted to perform ALD using organosilane precursors, such as R′-SiX_3, R′-$Si(OR)_3$, and (R′-$SiX_2)_2O$, but we found the deposition rate to be practically zero, presumably due to surface passivation.

Conclusions

We have established a route to fabricate ultrathin hybrid organic/inorganic sealing layers on porous supports and to convert them to high flux/selectivity membranes by removal of the bridging organic template. Prior to conversion, these materials are of interest for low k sealing layers. Use of R′ ligands with other shapes and sizes should enable this route to be generalized to many different demanding separation problems. Through intermittent replacement of BTEE with $TiCl_4$ or $ZrCl_4$, we expect to be able to increase further the thermal stability, allowing operation at higher temperatures.

References

1. Lai, Z.; Bonilla, G.; Diaz, I.; Nery, J.; Sujaoti, K.; Amat, M.; Kokkoli, E.; Thompson, R.; Tsapatsis, M.; Vlachos, D. *Science* **2003**, *300*, 456-460.

2. Holt, J.; Park, H.; Wang, Y.; Stadermann, M.; Artyukhin, A.; Grigoropoulos, C.; Noy, A.; Bakajin, O. *Science* **2006**, *312*, 1034-1037.

3. Cameron, M.; Gartland, I.; Smith, J.; Diaz, S.; George, S. M. *Langmuir* **2000**, *16*, 7435-7444.

4. Lim, B. S.; Rahtu, A.; Gordon, R. G. *Nat. Mater.* **2003**, *2*, 749-754.

5. Ek, S.; Iiskola, E. I.; Niinisto¨, L. *Langmuir* **2003**, *19*, 3461-3471.

6. Chen, R.; Bent, S. F. *Ad∨. Mater.* **2006**, *18*, 1086.

7. Jiang, Y. B.; Liu, N. G.; Gerung, H.; Cecchi, J. L.; Brinker, C. J. *J. Am. Chem. Soc*. **2006**, *128*, 11018-11019.

8. Brinker, C. J.; Lu, Y. F.; Sellinger, A.; Fan, H. Y. *Ad∨. Mater* **1999**, *11*, 579-585.

9. Clark, T.; Ruiz, J.; Fan, H.; Brinker, C. J.; Swanson, B.; Parikh, A. *Chem. Mater.* **2000**, *12*, 3879-3884.

10. Hietala, S.; Hietala, V.; Brinker, C. J. *IEEE Transactions on Ultrasonics, Ferroelectrics, and Frequency Control* **2001**, *48*, 262-267.

11. Brinker, C. J.; Sehal, R.; Hietala, S.; Deshpande, R.; Smith, D.; Loy, D.; Ashley, C. S. *J. Membr. Sci*. **1994**, *94*, 85-102.

12. Raman, N.; Brinker, C. J. *J. Membr. Sci.* **1995**, *105*, 273-279.

13. Lu, Y.; Fan, H.; Doke, N.; Loy, D.; Assink, R.; LaVan, D.; Brinker, C. J. *J. Am. Chem. Soc*. **2000**, *122*, 5258-5261.

14. Schmid, H. K. *Microsc. Microanal. Microstruct.* **1995**, *6*, 99-111.

Molecular Dynamics of Ionic Transport and Electrokinetic Effects in Realistic Silica Channels

Abstract

Silica is one of the most widely used inorganic materials in experiments and applications involving aqueous solutions of biomolecules, nanoparticles, etc. In this paper, we construct a detailed atomistic model of a silica interface that captures the essential experimentally known properties of a silica interface. We then perform all atom molecular dynamics simulation of a silica nanochannel subjected to either an external pressure or an electric field and provide an atomistic description of ionic transport and both electro-osmotic flow and streaming currents for a solution of monovalent (0.4 M NaCl) as well as divalent (0.2 M and 1.0 M $CaCl_2$) salts. Our results allow a detailed investigation of -potentials, Stern layer conductance, charge inversion, ionic mobilities as well as continuum theories and Onsager relations. We conclude with a discussion on the implications of our results for silica nanopore experiments and micro and nano-fludic devices.

Introduction

Electrokinetic phenomena such as *electro-osmotic flow* (EOF), solvent flow induced by an external electric field, and *streaming current* (SC), the electric current resulting from an applied pressure gradient within a ionic solution, are classic effects in physical chemistry [1]. In recent years, electrokinetic effects have become an active area of research as they provide an elegant and precise tool to manipulate fluid motion at the nano- and micro-scales [2] and show potential for new sources of energy [3,4]. Furthermore, the development of synthetic nanopores as sensors for DNA, RNA or proteins [5], or nanoporous functionalized silica thin films [6,7] for applications such as desalination membranes [8], has prompted the need for an understanding of ionic transport and electrokinetic effects in confined geometries.

Models where both the solvent and ions are approximated as a continuum, such as the Poisson-Nernst-Planck (PNP) model [1], provide the simplest and most widely used approach to electrokinetic phenomena and ionic transport. The PNP model, however, is strictly valid in the dilute limit only, where ionic activity coefficients are close to unity. Even in dilute systems, however, additional empirical corrections are often required. For example, experimental ζ-potential determinations can only be brought in agreement with theory by assuming the existence of Stern layer currents [1,4,9,10]. Further nuances arise for divalent ionic solutions, which, for example, show *charge inversion* (CI) [11], where an interface attracts charges in excess of its own nominal charge. The origins of CI are diverse [12-14] and its description within continuum models still presents considerable challenges. In addition, effects related to the discrete nature of the solvent may play a dramatic role [15].

Amorphous silica (SiO_2) has become one of the most widely used materials in wet technologies. Even synthetic nanopores made of Si_3N_4, commonly used in many DNA translocation experiments [5,16], are usually treated on an oxygen plasma, in many cases leading to a pore covered with a thin SiO layer. Experimentally, silica interfaces have an intricate structure [17],

which has been mostly ignored in theoretical studies. The detailed modeling of the silica interface is critical for understanding electrokinetic and ion transport properties, even more so as the characteristic size shrinks to the nanometer scale, as in, for example, the physics of nanopores [5].

In this paper we first present a model of a silica interface that closely approximates its known experimental properties. We further present all-atom molecular dynamics (MD) simulations of both EOF and SC on a silica nanochannel containing either monovalent or divalent ionic solutions. Besides providing a detailed description of ion transport and electrokinetic effects in silica channels, our study allows an atomistic study of problems that are still the subject of numerous controversies, such as the role of Stern layer currents or conduction "behind" the Stern layer, ζ-potential determination or CI.

The electric current density J_{SC} resulting from a pressure gradient $-\nabla P$ (the SC) and the water flow J_{EOF} arising from an electric field $E = \nabla \varphi$ (the EOF), where φ is the externally applied electric potential, are given, in the linear regime, by

$$
\begin{aligned}
J_{SC} &= L_{21}(-\nabla P) \\
J_{EOF} &= \rho_w L_{12}(-\nabla \varphi)
\end{aligned}
$$

(1)

where ρ_w is the water density. The relation $L_{12} = L_{21}$ [1] is a particular case of the Onsager reciprocal relations [18]. We point out, however, that to our knowledge, all explicit derivations of the symmetry relations implied by Equation (1) have the PNP model as their starting point [19].

Previous studies of electrokinetic phenomena by MD have been focused on all-atom simulations at the point of zero charge (pzc) of silica, either at zero ionic strength [20-22] or at 1 M NaCl using specifically developed forcefield [23]. Other studies have focused on model surfaces in order to investigate effects related to surface roughness [24]. More coarse grained models [25], have been developed to provide a description of EOF at longer time scales.

Model of a Silica Interface

The Structure and Charge of a Silica Interface

The silica interface comprises two types of groups, silanol and siloxane groups, schematically represented in Figure 1. The siloxane groups are hydrophobic in character, while the silanol are hydrophilic [28]. The typical density of silanol groups is ~ 4.6 OH/nm^2 [17,28]. Silanol groups are classified as isolated, vicinal and geminal [28], as depicted in Figure 1. Experimentally, according to the Zhuravlev model [17], they are present in the following surface densities: 1.2 OH/nm^2, 2.80 OH/nm^2, and 0.60 OH/nm^2 for isolated, vicinal, and geminal respectively. Recent experiments suggest that a significant fraction of vicinal groups consist, in fact, of two silanols not directly hydrogen bonded to each other, but through an intermediate water molecule (see Figure 1) [29-31].
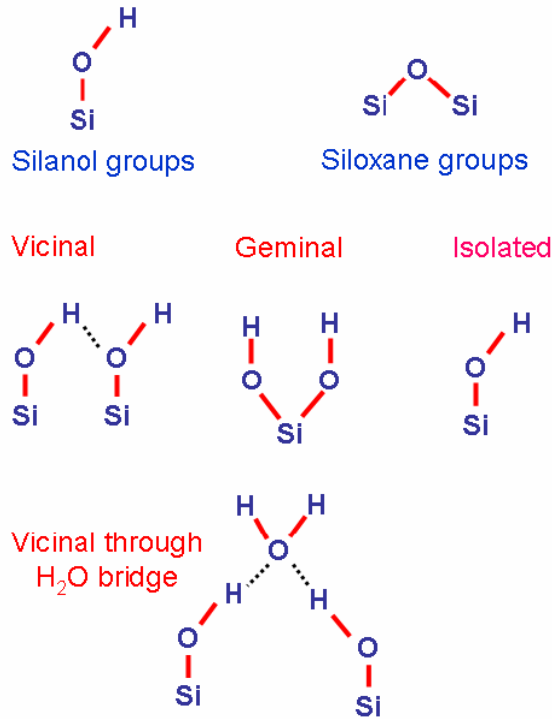
Figure 1. Types of groups that form a silica interface.

The surface charge of a silica interface strongly depends on environmental variables such as pH, ionic strength or temperature. Silica becomes electrically charged by releasing protons

$$SiOH + H_2O \rightarrow SiO^- + H_3O^+ \qquad (2)$$

In very acidic solutions pH < 3, the silanol group may become positively charged by accepting protons. In basic solutions pH > 9, silica significantly dissolves into silicate ions $HSiO_3^-$ [28]. For these reasons, all the subsequent analysis is restricted to the range 3 < pH < 9.

The simplest approach to predict the surface charge is to describe it by a triple model [1], with a single pKa and capacitance Kp. This was the approach followed by Bolt[32] and Schindler et al. [33] in the early literature. More recently, these results have been revisited by Behrens and Grier [34] who proposed $pK_a \sim 7.5$ and $K_p \sim 2.9$ F/m^2. However, these authors implicitly assume a density of silanol groups of 0.125 nm^2, a figure that is not supported by experiments.

A significantly more complex structure of the charging process of silica was revealed in the work of Ong et al. [35], who from surface second harmonic generation experiments showed that 20% of silanol groups had a $pK_a \sim 4.5$ and the remaining 80% $pK_a \sim 8.5$. It was argued that the latter corresponds to vicinal silanols, where increased proton stability arises from hydrogen bonding to neighboring oxygens, while the former corresponds to isolated silanols. A sensible model for the charging process of silica is therefore provided by isolated silanols (between 20% to 26% of the silanol groups) having a $pK_a = 4.5$ and the remaining silanols (vicinal or geminal) with a $pK_a = 8.5$. The surface charge of silica as a function of salt concentration for different models at pH =

8 is shown in Figure 2. At large ionic strength, the differences are well within experimental errors, but at low ionic strength, the triple models previously used in the literature, such as the one in Reference [34] predict a significantly larger deprotonation degree, which, most likely, explains the inability of previous triple models to describe SC flow with monovalent ions [36] in silica. Vicinal silanol groups form networks of hydrogen bonds, and the charging process becomes highly cooperative. In this regime, significantly more complex models have been developed [31].
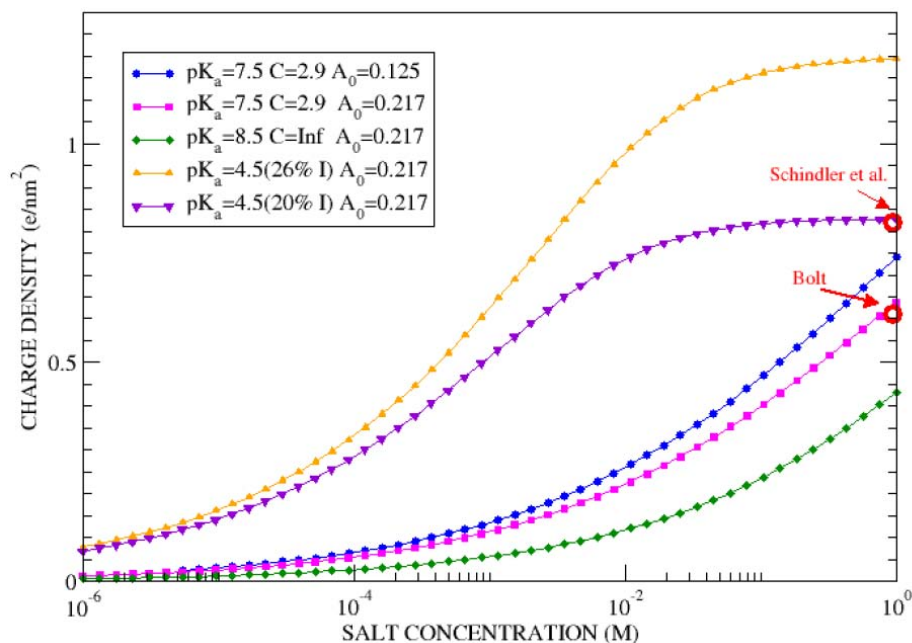
Figure 2. Predicted surface charge of silica as a function of monovalent ionic concentration at pH = 8 from the triple models [1], with the parameters described in the text. The results of Bolt are quoted from [32] and Schindler et al. from [33]. Units of capacitance (C) are F/m^2 and area per charge (A_o) are nm^2.

The charging process of silica in the presence of multivalent ions is also of interest for this paper. Experimental data on the surface charge of silica in the presence of divalent or trivalent ions is more scarce. From the early literature, we point out the work of Tadros and Lyklema [37], who analyzed Ca^{2+} salts and concluded that at high ionic strength, silica becomes significantly more charged than for monovalent ions. These results have been confirmed in [38], where a value of -1.21 e/nm^2 is quoted for 1.0 M $CaCl_2$ at pH = 8 and room temperature. Streaming current measurements suggest a surface charge for silica of the order -0.9 e/nm^2 at pH = 7.5 [11], consistent with the previous estimate. Quite interestingly, results for other divalent cations (Ba^{2+} and Sr^{2+}) at pH = 8 are on the order of -0.9 e/nm^2 [38] at pH = 8. Surface charge of silica in the presence of different trivalent ions have been studied with AFM tips [39], and yield a surface charge on the order of -2.2 e/nm^2, suggesting that all isolated and half the vicinal silanol groups are deprotonated at salt concentrations larger than 0.1 mM. The charge of silica is therefore dependent not only on ionic strength but on ionic valence also.

Model of a Charged Silica Substrate

We first construct a silica interface with the distribution of vicinal, geminal and isolated silanol groups described by the Zhuravlev model. We define two silanols as vicinal if they can form a hydrogen bond, that is, if their oxygens are within 3 Å of one another, similar to the definition used in Reference [41]. A silanol is defined as isolated if it cannot form hydrogen bonds, which we define as having its nearest neighboring silanol more than 3 Å away. This description will suffice for the goals of this paper, but greater level of detail, such as vicinal silanol groups bridged by a water molecule (see Figure 1) or clusters of vicinal groups, can be incorporated following recent experimental results [29–31].

The silica surface was generated from a bulk α-quartz silica crystalline solid, which was heated up to high temperatures (~ 2500 K) while using the BKS potential [40]. The system was then quenched to 300 K. Two free surfaces were generated along the *z*-dimension, and the substrate was annealed further at 300 K. The result of the quench is a certain number of under-coordinated silicons and oxygens. The resulting surfaces exhibit an overpopulation of isolated silanol groups, so the annealing was continued until the number of isolated silanol groups was reduced. By reducing the number of isolated silanol groups, we also reduce the overall density of silanol below the value observed experimentally.

In order to reach the experimental density of silanol groups, we randomly selected siloxane (Si-O) bonds that were within ~ 3 Å of either surface to be broken, similar to the method used in Reference [41]. We took care not to destroy any of the isolated silanols by ensuring that no bonds including the oxygens that are bonded to the silicons of the isolated silanol groups are removed. The resulting under-coordinated oxygens and silicons are terminated with -H and -OH groups respectively, which yields a fully-hydroxylated amorphous silica closely resembling the Zhuravlev model of the silica interface.

The next step is to define the charges of the atoms and the different interaction potentials: the forcefield. In this paper we used a recent CHARMM forcefield specially designed for simulating charged amorphous silica in aqueous solutions [41], which we refer to as the CHARMM water contact angle (CWCA) forcefield in order to differentiate it from the other CHARMM-based silica forcefields that have been generated for the α-quartz [42] and β-cristoballite [43] phases of silica. The charges of the different silanol groups are described by the general rule

$$q_{net} = q_{silanol} + q_{neighbor} \tag{3}$$

where q_{net} is the charge on a group of atoms containing a silanol (i.e. $q_{net} = 0$ for fully protonated silanol group(s), $q_{net} = -1$ for deprotonated silanol group), $q_{silanol}$ is the sum of the charge of each atom within silanols, and $q_{neighbor}$ is the charge contribution from the oxygen atoms bonded to the silicon(s) in silanols. The detailed charge assignment schemes, which we have supplemented with additional rules to accommodate cases not described in the original CWCA forcefield, are described in detail, with concrete examples, in supplementary materials associated with the published journal article.

The last step in the construction of the silica interface is the determination of which silanol groups are deprotonated. Obviously, the number of protons removed is dictated by experimental

conditions. Following the discussion earlier, protons are first randomly removed from isolated silanol groups, and only after all isolated silanol groups are deprotonated, vicinal groups are deprotonated. In this paper, we consider a system at pH ~ 7.5 and room temperature, so only isolated silanol groups are actually deprotonated.

Description of Simulations

We consider a silica nanochannel as described in Figure 3. The dimensions of both silica substrates are 7.49948 nm $\times$ 6.94968 nm and are separated a distance $h = 7.5$ nm. We conducted a series of simulations with three ionic solutions 1) 0.4 M NaCl, 2) 0.2 M CaCl$_2$ and 3) 1.0 M CaCl$_3$. From the discussion earlier, the surface charge of silica at pH ~ 7.5 is about $\sigma = -0.9$ e/nm^2, consistent with experimental results [4]. As already pointed out, the surface charge has a dependence on ionic valence and strength, but the effects are relatively small for the cases discussed in our simulations, so we decided to treat the surface charge as constant, thus allowing an easier comparison of the different results.
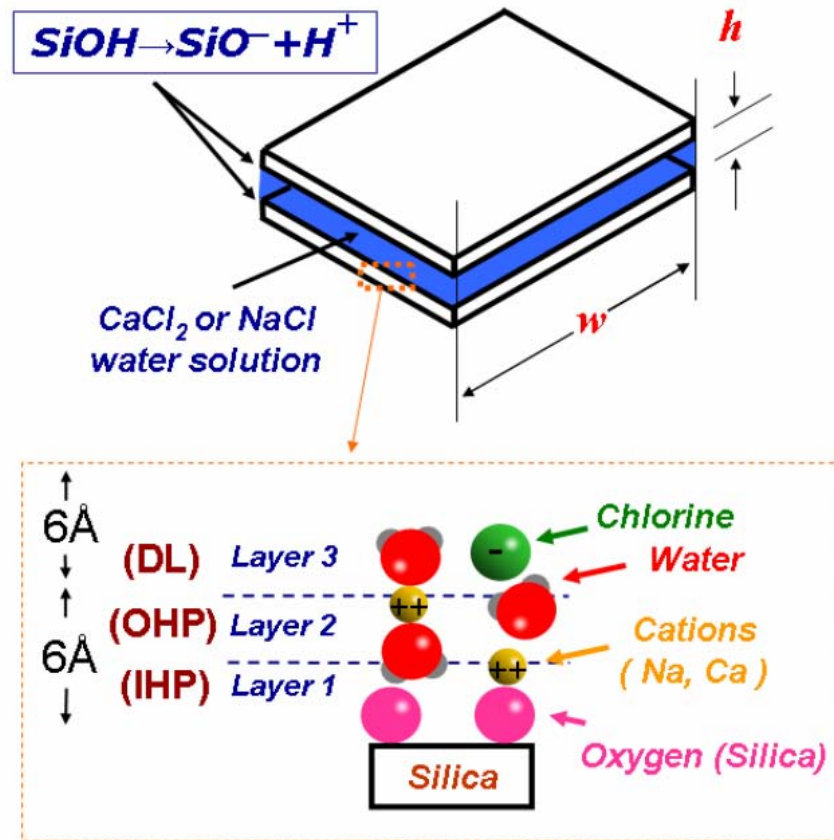
Figure 3. The silica channel consists of two interfaces separated a distance *h*. The layers next to the interface are defined as the inner Helmholtz plane (IHP) or layer 1, the outer Helmholtz plane (OHP) or layer 2 and the diffuse layer (DL).

Following our previous study [14], we define three different layers: the first layer includes all partially dehydrated ions bound to the silica oxygens, the second layer consists of hydrated counterions immediate to the silica interface and the third layer is defined as the intermediate

region before bulk values are attained. In standard physical chemistry textbooks [1], layers 1, 2 and 3 are referred to as the Inner Helmholtz plane (IHP), Outer Helmholtz plane (OHP) and the diffuse layer (DL), see Figure 3. In this paper, these layers are defined by the distance (r_{ion}) between the center of the cation and the silica oxygen. Layer 1 (IHP) includes all counterions within $r_{ion} < 3$ Å, Layer 2 (OHP) within 3 Å $< r_{ion} < 6$ Å and layer 3 (DL) within 6 Å $< r_{ion} < 12$ Å, where the diameter of the water molecule is approximated as 3 Å.

The SC simulations presented in this paper were performed by considering a "gravity" field (or flow field) [26, 27] instead of a pressure difference, as it is done in most experiments. Both a flow field and a pressure field lead to identical parabolic flows, but the former are easier to implement in MD. The small differences between a flow field or a pressure induced field are irrelevant for the questions of interest in this paper.

The EOF simulations were performed by applying an external electric field $E = 0.5$ V/nm. The SC current simulations used a "gravity" or flow field of $5 \times 10{-}5$ kcal/(Å gm) equivalent to a difference in pressure $\Delta P = 150$ atm. Certainly, these large values may be of concern to experimentalists and some theorists, but the following arguments should provide some perspective. The electric field of a water molecule near a monovalent cation is $E \sim 20$ V/nm (40 times larger), and the isothermal compressibility of water, $\kappa_w \approx 5 \cdot 10^{-5}$ atm^{-1} implies that the pressure field induces a negligible volume compression $\delta V/V \sim 10^{-2}$. While MD simulations with smaller electric and pressure field would certainly be of interest, we contend that the present simulations allow for a very reasonable all-atom description of electrokinetic phenomena, a point that will become more apparent in the discussion section. Furthermore, the values of these external fields are in line with previous MD simulations [23, 24].

All the simulations reported in this paper were performed with the LAMMPS simulation package [44]. The parameters are from CHARMM [41] and the TIP3P model for water [45] was employed. The silica substrate was not frozen, as has been done in previous simulations [23], since this could induce an undesired temperature gradient (a thermophoretic effect). Each simulation was equilibrated for 10 ns and runs with static configurations were conducted for 5 ns. All of the external field simulations lasted for 20 ns and were conducted at 300 K under NVT conditions using the Nose-Hoover thermostat [46] and a 1 fs timestep.

Results

Static Simulations
We report here the most salient results of the simulations in the absence of any applied field. These simulations can be directly compared with previous simulations conducted with the OPLS forcefield [47] and a different silica preparation method conducted by two of the authors [14]. A comparison of the OPLS results and the CWCA results for 1.0 M CaCl$_2$ in contact with silica substrates with two different surface charge densities ($\sigma = -0.9$ e/nm^2 and $\sigma = -2.0$ e/nm^2, the latter charge density can be achieved by tuning the pH) is included in the published journal article.

The population of the different layers for the 1.0 M CaCl$_2$ concentration are shown in Figure 4. The results show an excess of Ca^{2+} charge already in the IHP, thus giving raise to CI. The

residence times of Ca^{2+} are significant (~ 5.0 ns), leading to long equilibration times. For comparison, the results with the OPLS forcefield [14] are also shown. Although both forcefields give similar amounts of CI and pair distribution functions (results not shown), the population of the different layers is somewhat different. When using the OPLS forcefield, there is no CI at the IHP, it arises entirely from the OHP. Consistently, the residence times in the IHP are about 2 ns, much shorter than the residence times observed in the present simulations. A more surprising result is that the CWCA forcefield shows CI at 0.2 M $CaCl_2$ while previous results with the OPLS forcefield [14] indicated that CI disappears below 0.4 M, which is in better agreement with experimental results [11]. This seems to point out a deficiency in the CWCA forcefield, a point that will be discussed in greater detail in the following paragraphs.
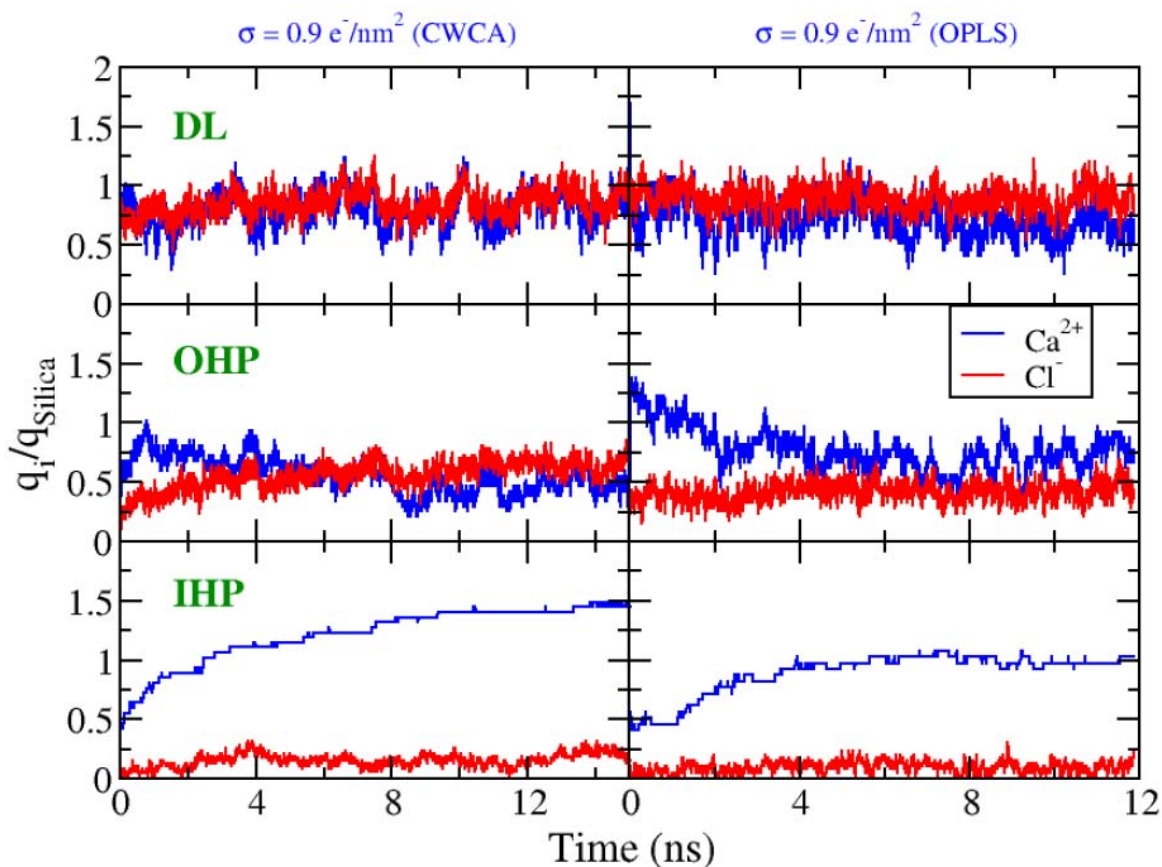
Figure 4. Evolution of the Ca^{2+} charge (blue) and the Cl^- charge (red) relative to the interfacial charge as a function of time for the different layers (see Figure 3).

Formation of Bjerrum pairs and ionic hydration numbers are important effects readily accessible by MD. In order to identify both Bjerrum pairs and hydration numbers, we used a simple distance criterion, where an atom A and an atom B are nearest neighbors (NN) if they are within a distance $r_{AB} \equiv r_A + r_B + r_{cut}$, where r_J is the crystallographic radius of atom J and $r_{cut} = 0.5$ Å is a cut-off that allows atoms to be considered a Bjerrum pair even if not in direct contact. Similar results are obtained by defining the Bjerrum pairing from the first minimum in the pair distribution functions. Results are summarized in Table 1 and Table 2.

Table 1. Number of Bjerrum pairs per cation for the static simulations of the 0.4 M NaCl, 0.2 M CaCl$_2$ and 1.0 M CaCl$_2$ systems. The numbers in the parentheses represent the error in the last digit of the stated value.

Region	0.4 M NaCl	0.2 M CaCl$_2$	1.0 M CaCl$_2$
IHP	0.05(1)	0.26(2)	0.56(2)
OHP	0.09(4)	0.50(8)	0.89(5)
DL	0.11(5)	0.55(8)	0.93(5)
Bulk	0.15(4)	0.61(8)	0.94(3)

Table 2. Number of nearest neighbor waters per ion for the 0.4 M NaCl, 0.2 M CaCl$_2$ and 1.0 M CaCl$_2$ systems in the various layers near the silica interfaces for the static simulations. The numbers in parentheses represent the error in the last digit.

System	Region	Cation	Anion
0.4 M NaCl	IHP	3.2(1)	5.4(4)
	OHP	5.5(1)	7.0(3)
	DL	5.5(1)	7.2(1)
	Bulk	5.4(1)	7.2(1)
0.2 M CaCl$_2$	IHP	5.0(1)	5.5(4)
	OHP	6.5(4)	7.4(1)
	DL	6.0(5)	7.3(1)
	Bulk	6.1(2)	7.3(1)
1.0 M CaCl$_2$	IHP	4.4(1)	5.6(3)
	OHP	4.5(2)	7.2(1)
	DL	4.4(2)	7.0(1)
	Bulk	4.4(2)	7.0(1)

The Bjerrum pairing results are summarized in Table 1. The Bjerrum pairing at the IHP is greatly reduced by the competition from the interface, as ions bound to the silanol oxygens have less accessible area to bind other ions. In the subsequent layers, Bjerrum pairing is approximately the same as in bulk. Clearly, divalent ions show larger amounts of Bjerrum pairing than monovalent ions. Rather remarkably, at 1.0 M CaCl$_2$ there are almost no free (unpaired) Ca^{2+} ions.

Table 2 summarizes the hydration numbers for the cations and anions in the various layers near the silica interface for the three different systems. In most cases, there is a noticeable surface

effect causing the hydration number for both the cation and anion to be smaller in the IHP as compared to that found in the other three layers. Rather interestingly, the hydration number of the Ca^{2+} ions in the 1.0 M $CaCl_2$ system is significantly smaller than for the 0.2 M $CaCl_2$ system, which reflects the larger degree of Bjerrum pairing.

The electrostatic potential profiles across the channel were computed using an integrated form of the Poisson equation and appropriate boundary conditions. We start with the Poisson equation in the form:

$$\frac{d^2\phi}{dz^2} = -\frac{1}{\epsilon_o} \sum_i q_i \rho_i(z) \tag{4}$$

where ϕ is the electric potential, ε_o is the vacuum permittivity constant, the summation over the index i refers to the various atom types, q_i is the charge on atoms of type i, ρ_i is the density of atoms of type i, and z is the distance in the direction perpendicular to the surface of the substrate. After integrating twice and applying boundary conditions such that the potential and its gradient are zero outside of the silica layers, we get the 1-D integrated form of the Poisson equation as:

$$\phi(z) = -\frac{1}{\epsilon_o} \sum_i q_i \int_0^z (z - u) \rho_i(u) \, du \tag{5}$$

where the integral is performed numerically using binned charge distributions from snapshots of the simulated systems. The results for the 1.0 M $CaCl_2$ cases (see Figure 5) show a relatively flat plateau corresponding to the aqueous ionic solution and a jump of the potential as the silica interface is crossed. The interface region exhibits a detailed structure that will be discussed below.
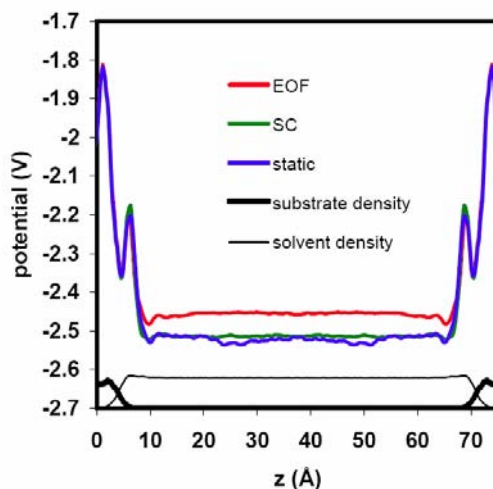
Figure 5. 1-D electrostatic potential profile as a function of the z coordinate for the 1.0 M $CaCl_2$ static (blue), SC (green) and EOF (red) cases. Solvent (thin black line) and substrate (thick black line) atomic densities are shown in arbitrary units along the bottom for spatial reference. These densities, as well as the charge densities used to produce the potential profiles, have been symmetrized across the channel midplane.

188

Also of interest is the displacement vector, defined by

$$\frac{dD(z)}{dz} = \sum_i q_i^f \rho_i(z) \tag{6}$$

where the free charges q_i^f are all system charges except the water. The "continuum" electric field within the solution is obtained from

$$E_c(z) = D(z)/(\epsilon_0 \epsilon_r) \tag{7}$$

where ε_r is the water dielectric constant ($\varepsilon_r \sim 70$ for the TIP3P model). As the silica interface is approached ε_r decreases from its value in solution, but the discussion of this effect is not necessary for the goals of this paper.

Streaming Current Simulations

The velocity profile is expected to follow the Poiseuille formula, with its characteristic parabolic profile

$$v_x^{SC}(z) = -\frac{\nabla P}{2\eta}(z - L_s)(h - L_s - z) \tag{8}$$

where L_s defines the position of the shear plane (the plane where the fluid velocity vanishes). The shear viscosity η of the TIP3P model is given by $\eta_T = 0.31$ cp, about 2.9 times smaller than the one of water at the same temperature [48]. We recall that most theoretical descriptions assume that the position of the shear plane coincides with the boundary between the OHP and the DL [1,14].

We first analyze the populations of the different layers (defined in Equation (3)). The results show a remarkable stability of the populations within the different layers (see Figure 6), thus providing clear evidence that the system has reached steady state. Compared with the static case, the actual differences are not very significant.

The velocity profiles obtained from the SC simulations are shown in Figure 7 and exhibit the expected parabolic profile. If, following previous considerations, the position of the shear plane is fixed at the boundary between the OHP and the DL ($L_s \sim 6$Å), the Poiseuille formula Equation (8) describes the flows for the 0.4 M NaCl and 0.2 M CaCl$_2$ systems without any need for fitting parameters. Although the velocity flows for the 1.0 M CaCl$_2$ system still follow the expected parabolic profile, in order to describe the flow with Equation (8) the viscosity of the system is left as a free parameter $\eta_{T,1.0M}$ yielding

$$\eta_{T,1.0M}/\eta_T \approx 1.7 \tag{9}$$

That is, at 1.0 M CaCl$_2$ the aqueous solution shows a large electroviscous effect.
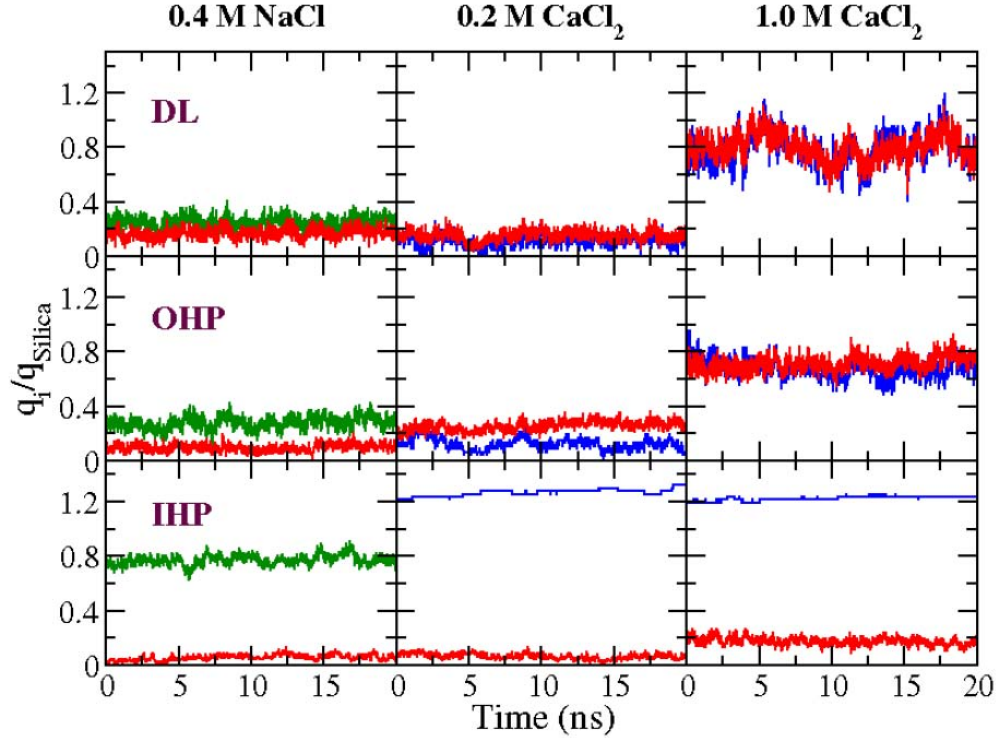
Figure 6. Evolution of the cation (Na⁺ (green) or Ca²⁺ (blue)) charge and the Cl⁻ charge (red) relative to the interfacial charge as a function of time for the different layers (defined in Figure 3) near the silica substrate for streaming current simulations.

Table 3 summarizes the main quantitative results of the simulations, namely, the net molar, mass and charge fluxes (normalized by the total channel width) for water, cations and anions. Table 4 summarizes the molar flux of the various species in each layer. The molar flux of each species was calculated by counting the number of times each molecule of a specific type spanned the length of the nanochannel in the x-dimension, and then dividing that value by the total time over which the value was obtained and the cross-sectional area of the nanochannel ($l_y \times l_z$). In the case of the values in Table 4, these flux values were binned based on the location of each molecule in the z-dimension. The SC was obtained by subtracting the net charge flux of cations from the anions.
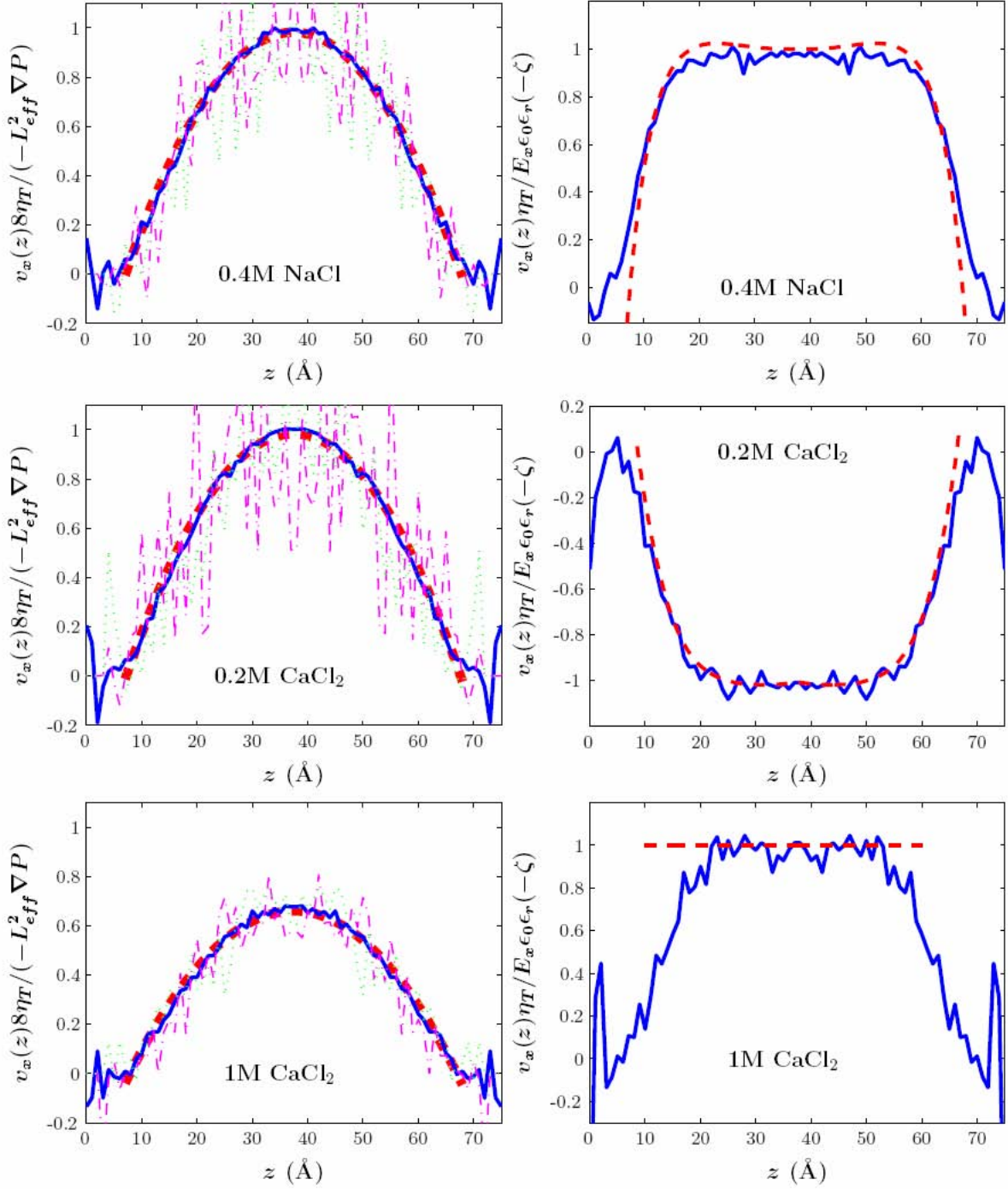
Figure 7. Velocity profiles (in normalized units) of the SC (left) and EOF (right) simulations. The blue solid lines are the water profiles, and the red dashed lines are the theoretical formulas Equation (8) (SC) and Equation (10) (EOF), with fitting parameters as discussed in the text. The green dotted line and magenta dashed-dotted line represent the cations and anions in the SC simulations. The 1.0 M CaCl$_2$ solution does not follow the continuum result Equation (10), so only the flat region is indicated.

Table 3. Net molar, mass and charge fluxes of water, cation and anion in the 0.4 M NaCl, 0.2 M CaCl$_2$ and 1.0 M CaCl$_2$ systems in the SC simulations.

System	Species	Molar flux (mol/nm^{2}ns)	Mass flux (amu/nm^{2}ns)	Charge flux (e$^-$/nm^{2}ns)
0.4 M NaCl	H$_2$O	477 ± 34	8586	0.0
	Na$^+$	3.9 ± 3.2	90	3.9
	Cl$^-$	3.5 ± 1.6	124	-3.5
0.2 M CaCl$_2$	H$_2$O	471 ± 36	8478	0.0
	Ca^{2+}	0.92 ± 0.96	37	1.8
	Cl$^-$	2.2 ± 0.87	78	-2.2
1.0 M CaCl$_2$	H$_2$O	300 ± 33	5400	0.0
	Ca^{2+}	4.9 ± 2.8	196	9.8
	Cl$^-$	10.8 ± 4.0	383	-10.8

Table 4. Net molar fluxes (mol/nm^{2}ns) of water, cation and anion in each layer of the 0.4 M NaCl, 0.2 M CaCl$_2$ and 1.0 M CaCl$_2$ systems in the SC simulations.

System	Species	IHP	OHP	DL	Bulk
0.4 M NaCl	H$_2$O	1.50	9.87	52.40	404.11
	Na$^+$	0.01	0.10	0.53	3.29
	Cl$^-$	0.01	0.05	0.35	3.23
0.2 M CaCl$_2$	H$_2$O	0.97	7.87	50.24	406.53
	Ca^{2+}	0.00	-0.01	0.10	0.92
	Cl$^-$	-0.01	0.04	0.24	2.00
1.0 M CaCl$_2$	H$_2$O	0.70	3.96	28.66	260.80
	Ca^{2+}	0.01	0.03	0.40	4.51
	Cl$^-$	0.01	0.06	0.83	8.98

Electro-Osmotic Flow Simulations

The velocity profiles of the water under EOF conditions are expected to follow the Smoluchowsky formula:

$$v_x(z) = -\frac{\varepsilon_0 \varepsilon_r}{\eta}(\eta - \phi(z) + \phi(h/2))E_x \tag{10}$$

where $\phi(z)$ is the electric potential and $\phi(h/2)$ is the value of the potential at the midplane of the channel (in most textbooks the potential is already defined such that $\phi(h/2) \equiv 0$). The Debye length is $\lambda_D > 10$ Å for all ionic concentrations discussed in this paper, so the potential reaches its midplane value at about 10 Å. The water velocity profile is therefore expected to exhibit a plug-type shape, where for $z \gg \lambda_D$, the water flow moves at a constant velocity $v_x = -\varepsilon_o \varepsilon_r E_x \zeta/\eta$. The quantity ζ is the difference in potential between the midplane (the bulk) and the interface, and is known as the ζ-potential [1].

The simulation results for the population of the different layers, shown in Figure 9, again provide clear evidence that the system has reached steady state. Similarly as with SC, the relative populations were not greatly affected by the presence of external perturbations.

The water velocity profile, shown in Figure 7, exhibits the expected plug-type flow. The electrostatic potential profile including the water explicitly is somewhat noisy, but the implicit electrostatic potential profile, defined in Equation (7) is smooth and agrees with the explicit water result in the relevant region, as shown in Figure 8. We therefore use the latter potential in the Schmoluchowsky formula, which allows us to determine the ζ potential. A detailed discussion of the ζ potential is further elaborated in the following section.
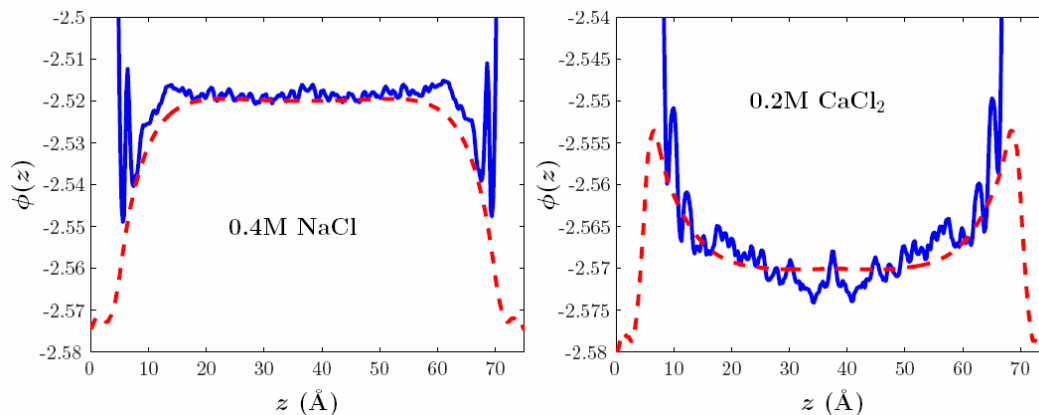
Figure 8. Comparison between the electric potential for the EOF computed with explicit water (blue solid curve) and the result with a continuum dielectric constant (red dashed curve).
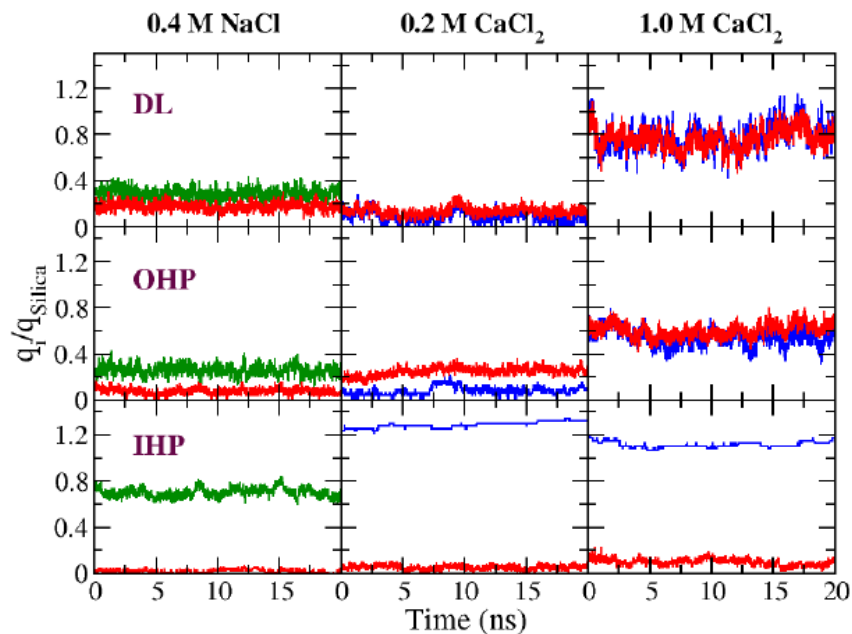
Figure 9. Evolution of the cation (Na^+ (green) or Ca^{2+} (blue)) charge and the Cl^- charge (red) relative to the interfacial charge as a function of time. The different layers are defined in Figure 3.

The ionic velocity profiles, normalized as in Figure 7, are shown in Figure 10. The results for 0.4 M NaCl and 0.2 M $CaCl_2$ show the expected behavior, where cations and anions move along in opposite directions. The 1.0 M $CaCl_2$ simulations, however, show both anions and cations moving in the same direction. It should be noted, however, that the anions move slightly slower than the water, so relative to the water, the anions are still moving in an opposite direction with respect to the cations. The direction of the anions is therefore the result of hydrodynamic drag dominating over electric migration. More surprising, however, is that the EOF is in the opposite direction as it would be expected from a negatively charged DL (see Figure 9). To rule out the possibility of simulation artifacts, we carried out a control simulation consisting of an equilibrated periodic box of water containing 1.0 M $CaCl_2$ (without any interface), and subjected it to the same external conditions as if the silica were present. The results are shown in Figure 10 (bottom right) and show the expected results: anions and cations moving in opposite directions and no induced EOF. The observed anomalous EOF at 1.0 M $CaCl_2$ is therefore a real physical effect.

Table 5 summarizes the main quantitative results of the EOF simulations, namely, the net molar, mass and charge fluxes (normalized by the total channel width) for water, cations and anions. The net molar quantities for the various species in the various layers near the silica interface are also shown in Table 6 and were computed by the same methods as described earlier.
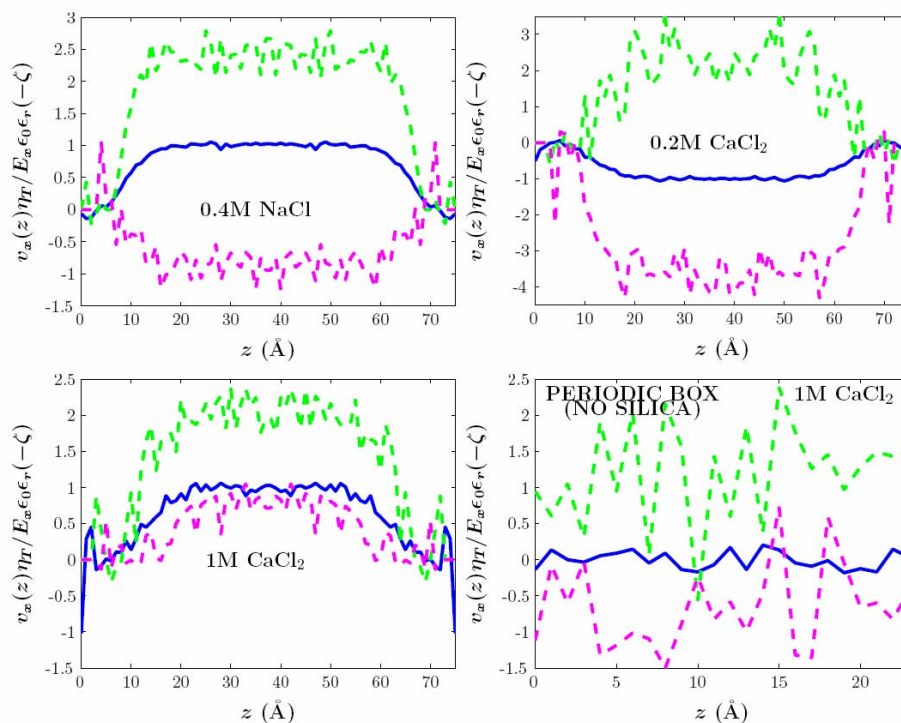
Figure 10. Velocity profiles for the water (solid blue), cations (dashed green) and anions (dashed magenta). The bottom right figure represents data collected over 5 ns from a simulation of a periodic box containing 1.0 M $CaCl_2$, without any silica interface. The data for the bulk simulation was normalized in the same fashion as the data from the nanochannel data (left bottom).

Table 5. Net molar mass and charge fluxes of water, cation and anion in the 0.4 M NaCl, 0.2 M $CaCl_2$ and 1.0 M $CaCl_2$ systems in the EOF simulations.

System	Species	Molar flux	Mass flux	Charge flux
		(mol/nm^2ns)	(amu/nm^2ns)	(e^-/nm^2ns)
0.4 M NaCl	H_2O	484.7 ± 127.6	8725	0.0
	Na^+	12.2 ± 4.9	281	12.2
	Cl^-	-3.5 ± 3.2	124	3.5
0.2 M $CaCl_2$	H_2O	-235 ± 128	-4230	0.0
	Ca^{2+}	1.22 ± 1.39	49	2.44
	Cl^-	-4.49 ± 1.96	-160	4.49
1.0 M $CaCl_2$	H_2O	172 ± 85	3096	0.0
	Ca^{2+}	6.84 ± 3.64	274	13.7
	Cl^-	4.21 ± 5.14	150	-4.21

195

Table 6. Net molar fluxes (mol/nm²ns) of water, cation and anion in each layer of the 0.4 M NaCl, 0.2 M CaCl₂ and 1.0 M CaCl₂ systems in the EOF simulations.

System	Species	IHP	OHP	DL	Bulk
0.4 M NaCl	H_2O	3.84	24.88	89.28	362.65
	Na^+	0.12	1.00	2.83	8.08
	Cl^-	-0.01	-0.10	-0.59	-2.89
0.2 M CaCl₂	H_2O	-1.61	-5.62	-35.34	-187.67
	Ca^{2+}	0.00	0.01	0.09	1.09
	Cl^-	-0.01	-0.17	-0.95	-3.79
1.0 M CaCl₂	H_2O	0.28	5.34	23.39	138.99
	Ca^{2+}	0.00	0.10	0.90	5.52
	Cl^-	-0.01	-0.04	0.18	3.47

Discussion

Ionic Mobilities
Ionic mobilities of species a are defined by

$$u^a = \frac{v_x^a}{E_x} \quad \text{units of cm}^2 \text{ V}^{-1}\text{s}^{-1} \tag{11}$$

where E_x is the external field and $v_x{}^a$ is the bulk ionic velocity. In our system, however, once the electric field is applied, the solvent is not at rest because of the EOF. The mobilities are defined in the reference frame where the solvent is at rest, hence

$$u^a = \frac{v_x^a - v_x^{EOF}}{E_x} \tag{12}$$

From the results earlier one obtains that $v_x^{EOF} \approx 20$ m/s, $v_x^{Na} \approx 50$ m/s and $v_x^{Cl} \approx -20$ m/s. Application of Equation (12), gives $u^{Na} \approx 6 \cdot 10^{-4}$ cm²/(Vs) and $u^{Cl} \approx 8 \cdot 10^{-4}$ cm²/(Vs) for the 0.4 M NaCl system. A similar calculation for the 0.2 M CaCl₂ system yields similar values for u^{Cl} and $u^{Ca} \approx 4 \cdot 10{-4}$ cm2/(Vs). At the ionic concentrations considered in our study electrophoretic and relaxation forces should provide significant contributions. Our results for mobilities compare surprisingly well with precise calculations in the dilute limit [49]. These results provide reassurance that the large values for the external fields do provide a reasonable description of ionic transport and electrokinetic effects.

The mobilities of EOF at 1.0 M CaCl$_2$ are much smaller than in the other two cases discussed. This is particularly true for the Cl$^-$ ions, whose mobility is one order of magnitude smaller. This reduction in the mobility is related to the strong Bjerrum pairing observed (see Table 1) which is suggestive of a dominance of relaxation and electrophoretic forces, reflected also in the large electroviscous effect.

Onsager Relations

The Onsager relations have been introduced in Equation (1). The electric current density JSC from the SC simulations and the water flow JEOF from the EOF simulations are computed from Tables 3 and 5, respectively. The external fields are also known to be $E_x = 0.05$ V/Å and $\nabla P = 2.1 \times 10^{15}$ Pa/m. Therefore, for the 0.4 M NaCl system we obtain

$$\frac{L_{21}}{L_{12}} = \frac{J_{SC}E_x}{J_{EOF}\nabla P} \approx 1.05 \pm 0.55 \tag{13}$$

The relative large error bars arise from the fact that the relevant currents are obtained by subtracting similar quantities. To our knowledge, all explicit derivations of Onsager relations [19] have the PNP model at its starting point, so our results clearly suggest that a similar derivation could be extended to more concentrated regimes, where ionic correlations are important. At 0.2 M CaCl$_2$ the same calculation gives

$$\frac{L_{21}}{L_{12}} = \frac{J_{SC}E_x}{J_{EOF}\nabla P} \approx 1.8 \pm 0.6 \tag{14}$$

Some deviations from unity are observed, but are not very significant.

The 1.0 M CaCl$_2$ system does present a clear violation of the Onsager relations as expressed by Equation (1), as both the SC and the EOF point in different directions. The anomaly, as it has been emphasized, lies in the direction of the EOF, which behaves as if the DL were positively charged. Furthermore, the presence of the silica interface is critical for this phenomenon, as clear from Figure (10). Here we recall that a number of effects occur at 1.0 M CaCl$_2$; almost all Ca^{2+} ions are paired (see Table 1) and approximately half of the water molecules are "dead water" (water molecules that are in the hydration sheath or directly correlated to it). Our interpretation of the anomalous EOF is that the bulk Ca^{2+} ions, which have a very compact hydration sheath, are more effective in dragging water molecules than the corresponding anions, and the no slip boundary condition set up by the interface sets the bulk water molecules in motion. A more detailed analysis of this effect will be discussed elsewhere.

ζ-Potential

The ζ-potential within SC experiments can be obtained using the approximation that the channel length is much larger than the Debye length and integrating Equation (8) [1]

$$\zeta = \frac{I_{str}\eta}{\varepsilon_0\varepsilon_r A\nabla P} \tag{15}$$

where I_{str} is calculated from Table 3, A is the effective channel area and the values of the other parameters are known. The ζ-potential is defined as the potential drop from the shear plane to the midplane. The position of the shear plane must be identified as the boundary between the DL and the OHP planes, and indeed the calculated value of the ζ-potential from Equation (15) agrees with the value of the potential difference computed in this way. The calculated values of the ζ-potential are shown in Table 7.

Table 7. Values of the ζ-potential calculated from SC and EOF simulations.

System	ζ (EOF) (mV)	ζ (SC) (mV)
0.4 M NaCl	-21	-21
0.2 M CaCl$_2$	11	17
1.0 M CaCl$_2$	-9	46

The ζ-potential is also obtained from the plug-flow velocity in the EOF, as already discussed earlier. However, it should be noted that the validity of the ζ-potential obtained hinges on the validity of the theoretical expression Equation (10), which fails for the 1.0 M CaCl$_2$ solution as discussed. Therefore, the EOF value quoted in Table 7 for the 1.0 M CaCl$_2$ does not have the physical meaning of the difference in electrostatic potential between the bulk and the shear plane.

One important point to notice, however, is that the position of the shear plane in the EOF ζ-potential is not determined as precisely as in SC flows. Also, as is clear from Figure 8, the electric potential changes very rapidly as it approaches the silica interface, so the determination of the ζ-potential is not possible without a very precise definition of where the shear plane is.

Ionic Conduction Behind the Stern Layer
The breakdown of the molar fluxes of the different ionic species within each layer (defined in Figure 3), presented in Table 5, shows a significant current within both the IHP and the OHP, which is known as "conduction behind the Stern Layer" [9, 10]. This current is negligible for divalent ionic solutions. This is expected, given the long residence times and compact hydration sheath of Ca^{2+} at silica interfaces. For NaCl however, there is a significant ionic conduction behind the Stern Layer. Clearly, its presence does not yield a significant contribution to the ζ-potential.

Conclusions

We have conducted MD simulations of electrokinetic effects, both SC and EOF, and ionic transport in silica nanochannels using all-atom molecular dynamics. We emphasized the importance of a precise description of the complex properties of silica interfaces and provided an explicit algorithm to accurately model these properties. Our results show that MD is able to

provide a description of electrokinetic effects with atomic resolution. As it is clear from the obtained parabolic and plug-type flow for SC and EOF respectively, as well as the calculated mobilities, electric potentials, etc., the large values of external electric and pressure fields at which our simulations were run do not limit the fundamental implications of our results for the significantly smaller external fields used in most experiments.

Our study of monovalent solutions, performed at 0.4 M NaCl concentration, show a textbook description of both EOF and SC. Our computed flow in SC simulations are described by the Poiseuille parabolic formula without any fitting parameters if the shear plane is made to coincide with the beginning of the DL (see Figure 3), as it has been assumed in virtually all previous theoretical descriptions [1]. The flows in EOF show the expected plug-type shape and are well described by the continuum Schmoluchowsky formula Equation (10). Our results show that electrokinetic effects can be computed if the charge distribution ρ^f (or the potential) is known in the static case. The charge distribution ρ^f (or the potential) in the static case can be easily computed from simulations or in the dilute limit, it can be approximated by a Boltzmann description, which leads to a self-consistent set of equations, the PNP model. For monovalent solutions, despite the important role of ionic correlations, the PNP model can provide a qualitative description, although for more realistic quantitative analysis the exact potential profile must be determined.

Divalent ionic solutions show a more complex behavior. Both simulations performed at 0.2 M $CaCl_2$ and 1.0 M $CaCl_2$ show charge inversion. The 0.2 M $CaCl_2$ flow in SC simulations follows the Poiseuille flow without fitting parameters. The significant amount of Bjerrum pairing, however, has an important effect on the EOF, which is likely related to the slight deviations observed in the Onsager relations. The 1.0 M $CaCl_2$ solutions show very interesting features. The SC flow follows the characteristic Poiseuille profile but the viscosity is increased by an almost factor of two, indicative of a considerable electroviscous effect. The understanding of electroviscous effects at high ionic strength and high valence is still somewhat primitive [50], so direct comparison with theories is not possible yet. At high ionic strength and high valence, we have shown that the EOF is anomalous and briefly discussed its relation to Bjerrum pairing as well as the presence of large amounts of 'dead water.'

Our studies made use of the CHARMM forcefield introduced by Cruz-Chu et al. [41], which we have referred to as the CWCA forcefield. The CWCA forcefield at 0.2 M $CaCl_2$ solution exhibits CI, which is in disagreement with experimental results [4], which report that CI should disappear below 0.4 M $CaCl_2$. The CWCA forcefield was derived from the wetting properties of silica, and it therefore significantly depends on the model used for the silica interface. It remains as a future task to investigate how the CWCA forcefield would be modified by considering the silica model interface proposed in this paper. Also relevant for an accurate model is the role of the low viscosity of the TIP3P water model. Since all transport properties depend on shear viscosity, water models that accurately model dynamic properties are of utmost relevance. MD simulations using, for example the SPC/E model [51], which has a viscosity closer to the one of real water ($\eta_{SPC/E} = 0.73\,\eta_W$) [52], should be able to unambiguously establish the possible dependence of the presented results on the actual value of the viscosity.

We discuss the implications of our results for fluidic devices and nanopore experiments. As a general rule, both ionic transport and electrokinetic effects can be modelled very accurately by a multi-scale approach, where electric potentials and charge distributions are determined from an atomistic simulation in the static case and then using the continuum results (Poiseuille flow, Schmoluchosky equation, etc.) to model transport properties. Our detailed model of the silica interface is pertinent to nanopore experiments. Experimentally, the fabrication of accurate and reliable synthetic nanopores is challenging [5], and understanding the magnitude of the ionic currents passing through the nanopore is even more difficult. The results of this paper can be used to model the detailed structure of a silica nanopore with a realistic description of silanol and siloxane groups, and thus provide an unambiguous understanding of how interfacial effects control transport properties. We hope to report more in the near future.

References

1. Lyklema, J. Fundamentals of Interface and Colloid Science; Academic Press: San Diego, 1995.

2. Stone, H. A.; Stroock, A. D.; Ajdari, A. Annu. Rev. Fluid Mech. 2004, 36, 381.

3. Yang, J.; Lu, F.; Kostiuk, L. W.; Kwok, D. Y. J. Micromech. Microeng. 2003, 13, 963.

4. van der Heyden, F. H. J.; Bonthuis, D. J.; Stein, D.; Meyer, C.; Dekker, D. Nano Lett. 2006, 6, 2232.

5. Dekker, C. Nature Nanotech. 2007, 2, 209.

6. Doshi, D. A.; Huesing N. K.; Lu, M.; Fan, H.; Lu, Y.; Simmons-Potter, K.; Potter, Jr., B. G.; Hurd, A. J.; Brinker, C. J. Science 2000, 290, 107.

7. Liu, N. G.; Assink, N. A.; Brinker, C. J. Chem. Commun. (Cambridge) 2003, 3, 370.

8. Leung, K.; Rempe, S. B.; Lorenz, C. D. Phys. Rev. Lett. 2006, 96, 095504.

9. Hidalgo-´Alvarez, R.; Mart´ın, A.; Fern´andez, A.; Bastos, D.; Mart´ınez, F.; de las Nieves, F. J. Adv. Colloidal Interface Sci. 1996, 67,1.

10. Hunter, R. *J. Adv. Colloidal Interface Sci.* 2003, 100, 153.

11. van der Heyden, F. H. J.; Stein, D.; Besteman, K.; Lemay, S. G.; Dekker, C. *Phys. Rev. Lett.* 2006, 96, 224502.

12. Lyklema, *J. Coll. and Surf. A* 2003, 291, 3.

13. Faraudo, J.; Travesset, A. *J. Chem. Phys. C* 2007, 111, 987.

14. Lorenz, C. D.; Travesset, *A. Phys. Rev. E* 2007, 75, 061202.

15. Faraudo, J.; Bresme, F. *Phys. Rev. Lett.* 2004, 92, 236102.

16. Heng, J. B.; Aksimentiev, A.; Ho, C.; Marks, P.; Grinkova, Y. V.; Sligar, S.; Schulten, K.;Timp, G. *Nano Lett.* 2005,5, 1883.

17. Zhuravlev, L. T. *Colloids Surf. A.* 2000, 173, 1.

18. Groot, S.R.; Mazur, P. *Non-Equilibrium Thermodynamics*; Dover Publications: New York, 1984.

19. Brunet, E.; Ajdari, A. *Phys. Rev. E* 2004, 69, 16306.

20. Lyklema, J.; Rovillard, S.; Coninck, J. D. *Langmuir* 1998, 14, 5659.

21. Spohr, E. *Electrochim. Acta* 2003,49, 23.

22. Qiao, R.; Aluru, N. R. *Phys. Rev. Lett.* 2004, 92, 198301.

23. Joseph, S.; Aluru, N. R. *Langmuir* 2006, 22, 9041.

24. Kim, D.; Darve, E. *Phys. Rev. E* 2006, 73, 051203.

25. Thompson, A. P. J. *Chem. Phys.* 2003, 119, 7503.

26. Travis, K. P.; Todd, B. D.; Evans, D. J. *Physica A* 1997, 240, 315.

27. Travis, K. P.; Gubbins, K. E. J. *Chem. Phys.*, 112, 1984, 2000.

28. Iler, R. K. *The Chemistry of Silica*; Wiley: New York, 1979.

29. Dong, Y.; Pappu, S. V.; Xu, Z. *Anal. Chem.* 1998, 70, 4730.

30. Shaw, A. M.; Hannon, T. E.; Li, F.; Zare, R. N. *J. Chem. Phys. B* 2003, 107, 7070.

31. Fisk, J. D.; Batten, R.; Jones, G.; O'Reilly, J. P.; Shaw, A. M. *J. Chem. Phys. B* 2005, 109, 14475.

32. Bolt, G. H. *J. Phys. Chem.* 1967, 61,1166.

33. Schindler, P. W.; F¨urst, B.; Dick, R.; Wolf, P. U. *J. Coll. Interface Sci.* 1976, 55, 469.

34. Behrens, S. H.; Grier D. G. *J. Chem. Phys.* 2001, 115, 6716.

35. Ong, O.; Zhao, X.; Eisenthal K. B. *Chem. Phys. Lett.* 1992, 191, 327.

36. van der Heyden, F. H. J.; Stein, D.; Dekker, *C. Phys. Rev. Lett.* 2005, 95, 116104.

37. Tadros, T. F.; Lyklema, J. *J. Electroanal. Chem.* 1968, 17, 267.

38. Karlsson, M.; Craven, C.; Dove, P. M.; Casey, W. H. *Aquatic Geochem.* 2001, 7, 13.

39. Besteman, K.; Zevenbergen, M. A. G.; Lemay, S. G. *Phys. Rev. E* 2005, 72, 061501.

40. Van Beest, B. W. H.; Kramer, G. J.; van Santen, R. A. *Phys. Rev. Lett.* 1990, 64, 1955.

41. Cruz-Chu, E. R.; Aksimentiev, A.; Schulten, K. *J. Phys. Chem. B* 2006 , 110 , 21497.

42. Lopes, P. E. M.; Murashov, V.; Tazi, M.; Demchuk, E.; MacKerell, Jr., A. D. *J. Phys. Chem. B* 2006, 110, 2782.

43. Nangla, S.; Washton, N. M.; Mueller, K. T.; Kubicki, J. D.; Garrison, B. J. *J. Phys. Chem. C* 2007, 111, 5169.

44. Plimpton, S. *J. Comp. Phys.* 117, 1, 01995.

45. Jorgensen, W. L.; Chandrasekhar, J.; Madura, L. T.; Impey, R. W.; Klein, M. L. *J. Chem. Phys.* 79, 926, 1983.

46. Hoover, W. G. *Phys. Rev. A* 31, 1695, 1985.

47. Jorgensen, W. J.; Maxwell, D. S.; Tirado-Rives, J. *J. Am. Chem. Soc.* 118, 11225, 1996; Jorgensen, W. J. private communication, 2003.

48. Yeah, I-C; Hummer, G. *J. Am. Chem. Soc.* 124, 23, 2002.

49. Koneshan, S.;Rasaiah, J. C.; Lynden-Bell, R. M.; Lee, S. H. *J. Phys. Chem. B* 102, 4193, 1998.

50. Chandra, A.; Bagchi, B. *J. Chem. Phys.* 113, 3226, 2000.

51. Berendsen, H. J. C.;Grigera, J. R.;Straatsma, T. P. *J. Phys. Chem.* 91, 6269, 1987.

52. Guo, G.; Zhang, Y.; Zhao, Y. *Phys. Rev. E* 67, 43101, 2003.

Role of Water in Selectivity of Niobate-Based Octahedral Molecular Sieves

Abstract

The role of occluded water in the ion exchange selectivity is examined in a class of molecular sieves named Sandia Octahedral Molecular Sieves (SOMS: $Na_2Nb_{2-x}M_xO_{6-x}(OH)_x \cdot H_2O$ (i.e., M = Ti; $0 < x < 0.4$)). SOMS exhibit a high selectivity for divalent cations only when the framework Nb(5+) are substituted by M(4+) atoms. Vibrational dynamics of the water molecules with varying charge balancing cations and M atoms are studied by inelastic neutron scattering (INS) measurements, and ^{1}H MAS NMR, and correlated to density functional theory (DFT) and molecular dynamics (MD) data. The experimental INS spectra were compared with those of ice Ih to characterize the changes induced by confinement on the occluded H_2O and the resulting hydrogen-bonding network. Data indicates that with increasing M(4+) content and divalent ion exchange, the trend of occluded water molecules is to change from extended rigid ice-like networks to restored bulk-like arrangements with increased solvation effects on the channel charge-balancing cations.

Introduction

Confinement in microporous materials is an attractive subject for a variety of both experimental and theoretical studies.[1-2] The case of nanoconfined water is of importance because understanding how the various confining matrices modify the water properties compared to those in the bulk state is of significance to control and optimization of a broad spectrum of industrial processes. In our case, we are particularly focused on the ability to understand, and, therefore, tune and predict ion exchange selectivity for water purification with zeolitic materials, especially for environmental remediation applications.

Selectivity for ion exchange in zeolites and molecular sieves is dependent on a number of factors including pore size and shape, framework composition, and surface adsorption properties.[3] In an effort to establish a comprehensive knowledge base for tuned framework design, our research is directed toward developing a structure/property relationship between zeolites and their ion exchange capabilities. In particular, we are interested in the role of the occluded water molecules. Ion selectivity and exchange have been described as resulting from a competition between the hydration free energy of a cation and the electrostatic interactions occurring in pores between crystalline framework and extra framework ions.[4] Our research is focused on a systematic study of the role of occluded water molecules in the small pored, highly selective SOMS crystalline molecular sieves.

Recently, work on occluded water in zeolites has focused on various aluminosilicates.[5-11] In particular, these studies are directed towards understanding the arrangement of water molecules inside a zeolite cage, and the interactions of that water with neighboring water molecules and the zeolite framework.[6] This includes the effects of ion exchange on the O-H stretching and H-O-H bending intramolecular vibrations and diffusional dynamics of water in zeolite A (LTA) and zeolite X with various charge balancing cations.[5] Evidence from inelastic neutron scattering

(INS) and FTIR data indicates the ability of the occluded water molecules to form structures (such as hexamers and distorted tetrahedral networks) through hydrogen bonding inside the zeolite pore, and that this is structurally similar to bulk water. Much of the state of the water molecules was determined by the concentration of cations located in the zeolite cage.

We have applied these techniques to our Sandia Octahedral Molecular Sieves (SOMS; $Na_2Nb_{2-x}M_xO_{6-x}(OH)_x \cdot H_2O$ (ie., M= Ti; $0 < x < 0.4$)), a new class of molecular sieves that show exceptionally high selectivity for divalent cations, in particular Sr^{2+}. These phases have been synthesized using hydrothermal methods,[12] and possess a framework structure composed of layers of edge-sharing $[NaO_6]$ octahedra interleaved with double chains of edge-sharing, disordered, and distorted $[NbO_6]/[MO_6]$ (see Figure 1a). The third structural unit, a square planar sodium, resides in the channels. This structure is unusual in the sense that Na^+, which is typically an extra framework cation, also participates in the framework. We have shown that when M = Ti and $x = 0.4$, we obtain a maximum ion exchange capacity for Sr^{2+} for this framework configuration.[12] Because SOMS phases exhibit favorable distribution coefficients (K_d) for ions such as Sr^{2+}, these materials may find utility in the separation of aqueous radioactive nuclear wastes and groundwater containing species such $^{90}Sr^{2+}$. Moreover, upon heating, the Sr-exchanged SOMS phases dehydrate and convert to thermally stable and chemically durable perovskites.[12] Thus, these perovskites may serve as permanent ceramic host structures for ^{90}Sr in radioactive waste management. More recently, we reported the synthesis, structure, and thermodynamic properties of the prototypic phase, $Na_2Nb_2O_6 \cdot H_2O$, containing only Nb (without Ti) in this system.[12] This end-member composition can be considered as a lueshite perovskite, $NaNbO_3$, with half a water molecule per formula unit. We have also greatly expanded the phase space of SOMS to include a wide variety of occluded cations and stoichiometrically doped framework octahedral atoms.[13] The charge balancing cations include: Li, Na, Sr, Mg, Ca, Y; the octahedral framework elements (M) include: Nb, Ti, Zr, Mo, Ge, Te.

a)
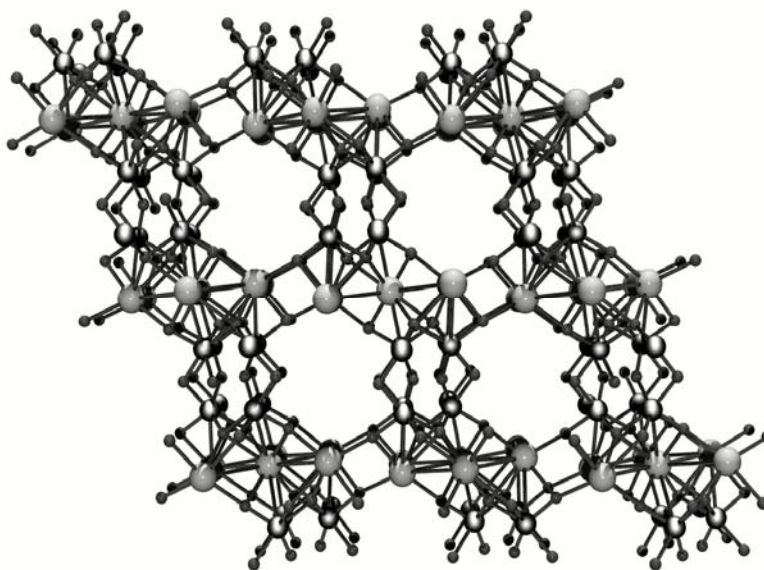
b)
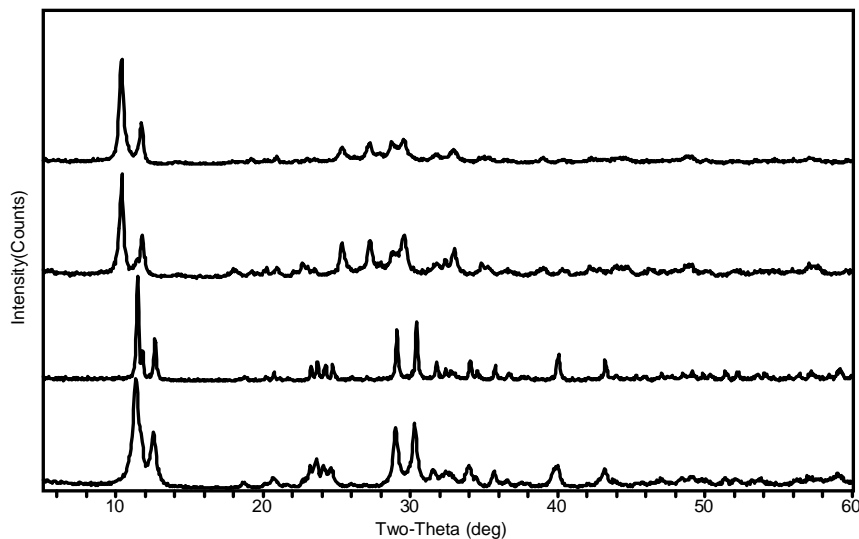
Figure 1. a) SOMS framework, $Na_2Nb_{2-x}M^{IV}_xO_{6-x}(OH)_x \cdot H_2O$; small balls = O, medium balls = Nb/Ti, large balls = Na, occluded waters and Na(1) are not shown, for clarity, but are located in the pores; b) Powder XRD data for the as-synthesized and Sr-exchanged samples; peak shifts due to changes in unit cell size from ion exchanged cation size.[12b]

We report on the state of water in the end member SOMS ($Na_2Nb_2O_6 \cdot H_2O$) and the 20%-Ti SOMS ($Na_2Nb_{1.6}M_{0.4}O_{5.6}(OH)_{0.4} \cdot H_2O$), ranging in characteristics from bulk to ice-like ("ice-like" refers to a pore-constrained water having some long-range order and limited hydrogen-bonding). Both phases were synthesized with monovalent Na^+ and ion exchanged with divalent Sr^{2+}. The state of the confined water was determined by inelastic neutron scattering and ^1H magic angle spinning (MAS) NMR experiments. Furthermore, we have correlated the experimental data with molecular simulation efforts including first principles density functional theory (DFT) with *ab initio* molecular dynamics, and large-scale molecular dynamics modeling. An overall picture of the equilibrium dynamics is obtained through the comparative analysis and correlation of theoretical power spectra with observed spectroscopic evidence from material and crystallographic characterization, MAS NMR, inelastic neutron scattering and modelling/simulation techniques. The combined efforts allow us to postulate on the role of confined water on ion exchange capacity of a molecular sieve framework.

Experimental Methods

The SOMS samples were all prepared according to methods published earlier.[13] Deuteration of samples was performed by repeated refluxing in D_2O (3 x 24 hrs). Ion exchange of the samples with Sr was performed by refluxing the as-synthesized SOMS sample with 10wt.% $Sr(NO_3)_2$ at 90°C for 12 hours. Elemental analysis was performed by ICP – OES (optical emissions spectroscopy) at Galbraith Laboratories, Inc., for all the products, and showed complete exchange of the sodium for strontium.

Ion exchange capacity, represented as the distribution coefficient, K_d, was calculated by the following relationship:

$$K_d \ (mL/g) = ([Sr_{ix}]/g_{ix})/([Sr_{sln}]/mL \ soln) \qquad (1)$$

where K_d is the distribution coefficient, ix is ion exchanger, $[Sr_{ix}]$ is the concentration of Sr adsorbed by the ion exchanger, g_{ix} is the weight of the SOMS ion exchanger, $[Sr_{sln}]$ is the concentration of the Sr remaining in solution after contacting SOMS, and mL soln is milliliters of solution.

Powder X-ray diffraction (XRD) patterns were recorded at room temperature using a Siemens Kristalloflex D 500 diffractometer (Cu K_α radiation, Kevex detector, 40 kV, 30 mA; $2\theta = 5 - 60°$, $0.05°$ step size and 3 second count time), and used for crystalline phase identification. The phases were identified by comparison with the data reported in the JCPDS database and our previous publications.[12-14]

Variable temperature time-of-flight (TOF) neutron data was collected at the neutron powder diffraction (NPDF) beamline at the Manuel Lujan, Jr. Neutron Scattering Center of Los Alamos National Laboratory (LANSCE). Prepared powder samples were sealed in a vanadium vessel (1 cm diameter) and rotated throughout data collection. Data at each temperature (270 K, 150 K and 15 K) was simultaneously collected on four detector banks which were centered at ±90° and ±151° 2θ.

Inelastic neutron scattering (INS) data were collected at the filter difference spectrometer (FDS) at the LANSCE facility. This instrument is used for vibrational spectroscopy through incoherent inelastic neutron scattering. The instrument is designed for high count rates by use of a large solid-angle (3 steradians) detector. Several grams of sample were loaded in cylindrical aluminum cans (20 mm diameter, 100 mm height) in a helium glove box. Helium gas was used to ensure good thermal contact with the powder during subsequent cooling of the sample and sample holder to 10 K. The samples were then cooled to 10 K in a closed-cycle refrigerator and data collection was started.

The ^{1}H MAS NMR experiments were performed on a Bruker Avance instrument at an observe frequency of 600.14 MHz. The MAS NMR experiments were performed on ~10 mg of sample using a 2.5 mm rotor with spinning speeds between 20 and 30 kHz. The chemical shifts, line widths and relative amounts were all obtained from analysis of the 30 kHz spinning speed spectra. The two-dimensional (2D) double quantum (DQ) side band experiments and analysis of distributions have been detailed elsewhere.[15-18] Chemical shifts were referenced to a secondary sample of adamantane ($\delta = +1.63$ ppm wrt TMS $\delta = 0.0$ ppm).

Short (3 ps) density functional theory (DFT)-based *ab initio* molecular dynamics (AIMD) trajectories, followed by geometric optimizations, were performed to explore the potential energy landscape of fully-hydrated end-member SOMS, and SOMS with ~20% Ti-substitution (both with and without Sr^{2+} exchanging for Na^+). These simulations involved a single formula unit fixed at the experimental lattice constants[12a]. DFT and AIMD calculations applied the Perdew-Burke-Ernzerhof (PBE) functional[19] and projected augmented wave[20] pseudopotentials

implemented into the VASP code,[21,22] 1x2x1 Monkhorst-Pack Brillouin zone sampling, and a 400 eV wavefunction cutoff. The VASP Born Oppenheimer AIMD simulations enforced a 10^{-6} eV convergence criterion at each of the 0.5 fs time step, and applied a thermostat that maintained an elevated simulation temperature, $T = 900$ K or 600 K, to ensure that the relatively short trajectories led to significant sampling of water configurations.

Large-scale molecular dynamics simulations were performed on the end member SOMS ($Na_2Nb_2O_3 \cdot H_2O$) and 20% Ti-substituted SOMS ($Na_2Nb_{1.6}Ti_{0.4}O_{5.6}(OH)_{0.4} \cdot H_2O$) (and their corresponding Sr-exchanged phase) using the Cerius^2 software package (Accelrys Inc., San Diego) and an energy force field based on the flexible simple point charge (SPC) water model[23,24] with compatible Lennard-Jones parameters for the Na and Sr channel cations[25]. Partial charges of Na = 0.467, Nb = 3.000, Ti = 2.325, O = -1.200, O(hydroxyl) = -0.950, and H(hydroxyl) = 0.425 were assigned to the framework atoms, while charges for the channel cations (Na^+ and Sr^{2+}) were equivalent to their formal charges. Development of Nb-O interatomic parameters proved unsuccessful and limited our simulations to systems where the framework atoms were constrained to the observed structure[12] while allowing full flexibility and translation for the water (and hydroxyls) and channel cations. Intermolecular interactions consisted of electrostatics and the short-range Lennard-Jones terms from the literature, while the intramolecular interactions included bond stretch and angle bend terms based on the SPC water model. Lorentz-Berthelot mixing rules[26] were used to combine the Lennard-Jones parameters for the various framework-channel interactions. Simulations used supercell models having $P1$ symmetry and comprised of 2 x 4 x 4 unit cells of the SOMS observed structure[12]. A series of molecular dynamics simulations were completed for an initial equilibration period of 100 ps, using a 1 fs time step, followed by a longer 500 ps simulation period. Atomic positions and velocities were saved every 2 ps for analysis. Additional trajectories for a subsequent 40 ps simulation were used for the velocity autocorrelation function (VACF)[27] and power spectra calculations. All simulations were conducted in the NVT ensemble with $T = 300$ K, and used an Ewald summation to ensure proper convergence of the electrostatic energies. The thermostat relaxation time was 0.1 ps, and the Verlet velocity algorithm was used to ensure accurate integration of the equations of motion. No differences were observed in the peak positions and peak shapes for the power spectra derived using various starting configurations from the equilibrated trajectories. Uncertainties in the molecular dynamics results are ultimately dependent upon the accuracy of the empirical force field parameters; for this study, the results are consistent and in general agreement with those derived from the DFT approach.

Results and Discussion

The ion exchange capacity for the SOMS end member $Na_2Nb_2O_6 \cdot H_2O$ indicated low selectivity for Sr^{2+}, $K_d \approx 3800$, while the $Na_2Nb_{1.6}Ti_{0.4}O_{5.6}(OH)_{0.4} \cdot H_2O$ indicated high selectivity for Sr^{2+} ions, $K_d \approx 26000$. Complete ion exchange occurred for both samples, resulting in final stoichiometries of $SrNb_2O_6 \cdot H_2O$ and $SrNb_{1.6}Ti_{0.4}O_{5.6}(OH)_{0.4} \cdot H_2O$. XRD analysis indicated no degradation or change in the SOMS frameworks (see Figure 1b).

Neutron Diffraction
The first attempt to understand the characteristics of the occluded water in the SOMS included analysis of variable low temperature neutron diffraction studies, with a focus on the oxygen atom

of the occluded water molecule (O_w). The Rietveld method[28] was used to analyze the neutron TOF data using the General Structure Analysis System (GSAS) software suite developed by Larson and Von Dreele.[29] Initial unit cells and atomic positions were taken from our previous SOMS structure solution and refined as follows: Scale factors and six background terms were refined until converged, after which, specimen displacement and lattice parameters were added and optimized. An additional six background terms were added to each refinement, and peak profiles were fit to pseudo-Voigt[29] functions. Upon convergence of the above parameters, atomic coordinates and isotropic temperature factors for all atoms were refined to yield combined R_{wp} values of 2.14, 2.11, and 2.27 for 15 K, 150 K and 270 K, respectively (Table 1).

Table 1. Structural parameters for SOMS materials.

Temperature	15 K	150 K	270 K
a (Å)	16.8814(3)	16.8562(9)	16.8294(7)
b (Å)	5.0196(7)	5.0261(1)	5.0293(4)
c (Å)	16.3731(2)	16.3849(2)	16.3758(6)
β (°)	114.059(9)	114.044(4)	114.044(2)
V (Å^3)	1269.89(7)	1271.81(3)	1275.79(8)
R_{wp} (%)	2.14	2.11	2.27
R_p (%)	1.03	1.60	1.81
χ^2	2.197	2.752	2.281
[a] Nb1-O_f (Å)	2.0484(4)	2.0422(5)	2.0366(1)
Nb2-O_f (Å)	2.0124(9)	2.0072(7)	2.0131(3)
Na1-O_f (Å)	2.4671(6)	2.4694(1)	2.4601(2)
Na1-O_w (Å)	2.4163(1)	2.4188(4)	2.4217(1)
Na2-O_f (Å)	2.4888(3)	2.4843(1)	2.5029(2)
Na3-O_f (Å)	2.3623(1)	2.3711(5)	2.3753(3)
Na3-O_w (Å)	2.1250(6)	2.1258(4)	2.1289(9)
Na3-O_f (Å)	2.3717(7)	2.3784(2)	2.3734(3)
O1w	0.04972	0.07029	0.09001

[a] O_f, O_w indicate framework and water oxygens respectively.

The SOMS crystallize in a monoclinic cell with space group $C2/c$ (No. 15). The unit cell is independent of the temperature, exchanged cations, or concentration of framework dopant.[12] The parameters of the unit cell at 15 K, 150 K and 270 K show a nearly linear expansion of the b-axis and contraction of the a-parameter resulting in a net increase in unit cell volume as room temperature is approached. Unlike the a- and b-parameters, the c-parameter does not follow a

linear behavior with temperature, and exhibits a local maximum at 150 K. The thermal behavior of this material is most readily understood through comparison of the local environment surrounding sodium ions within the pores (Na3) at 15 K, 150 K, and 270 K. Na3 is four coordinate, in square-planar configuration, by two symmetry equivalent framework oxygen atoms (O_f) and two water oxygen atoms (O_w). The channel sodium-framework oxygen (Na3-O_f) interaction is parallel to the c-parameter and has a significant contribution to its length. This Na-O bond length shows the same non-linear behavior which is exhibited be the c-parameter as room temperature is approached. Analysis of the refinement data shows that there is almost no displacement of the water positions at low temperatures and that the occluded water in the end member SOMS is not thermally labile in the range studied. Therefore, the incorporation of hydroxyl moieties through M^{4+} doping within the SOMS materials must significantly enhance the pore environment electronic structure. As we show in concurrent studies, the hydroxylated pore favors larger charged ions such as Sr^{2+} and Ba^{2+} over the smaller more highly charged ions such as Na^+ and Cs^+.[30]

Inelastic Neutron Diffraction

Due to the lack of additional information on the characteristics of the Ow from low temperature neutron diffraction data (above), inelastic neutron scattering (INS) analysis were performed to study the hydrogen-bonding of the water molecule. This technique is ideally suited to investigate the librational and rotational modes (wagging, rocking, and twisting) of water molecules in confined environments and is extremely sensitive to localized hydrogen bonding. Conceptually, the behavior of nanoconfined water molecules is the direct result of complex equilibria among four distinct types of interactions: (1) H_2O-H_2O; (2) H_2O-Ion; (3) H_2O-Framework; and (4) Ion-Framework. The collective effect of these interactions (hydrogen bonds, ion-dipole, and electrostatics) produce localized restrictions which alter the behavior of the nanoconfined water. Spectroscopically, these behavioral modifications are manifested by changes in the librational/rotational (300-1100 cm^{-1}) modes and to a lesser extent the intramolecular bending (~1600 cm^{-1}), and stretching (3300-3700 cm^{-1}) modes.[5] Water has a librational band in the 450-900 cm^{-1} region, which is normally composed of three frequencies (wagging, rocking, and twisting) in the inelastic neutron scattering spectrum. For a water molecule in a general force field, there will be three librations, one for each axis of rotation, but these will be observed only if there is a restoring force present for each libration. There is the "rock", the motion in the plane of the water molecule; the "twist", which is a rotation about the C_2 diad; and the "wag", the rotation about the H-H axis, with increasing frequency. Changes to the degree of hydrogen bonding between the occluded water molecules and between the water and cation or framework will be exhibited in this region. Liquid water, or, more appropriately for neutron spectroscopy, ice Ih, is used as a reference for the INS studies.[31] This data was reproduced in our studies at LANSCE (see Figure 2).
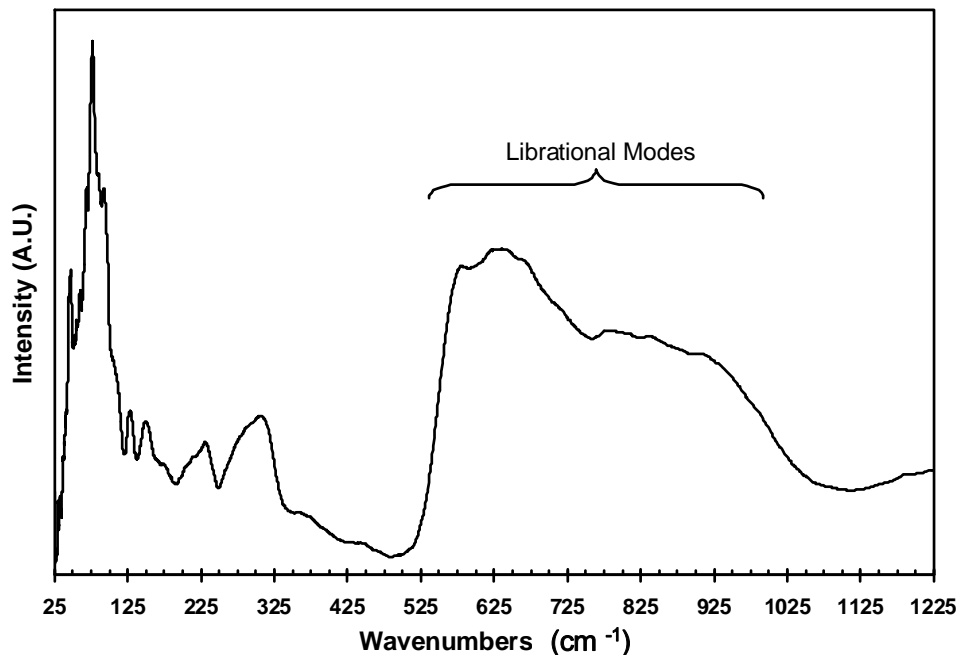
Figure 2. INS spectrum of water collected at 10K.

As-Made Samples

The INS data for the end member and 20%Ti SOMS is shown in Figure 3. Both sets of data include hydrogen bond stretching and occluded water rotational/librational modes. However, there are two distinctly different librational patterns for the librational modes of the occluded water (one per unit cell, located in the pores). In the end member case, the individual librational modes are not distinguishable. Instead the characteristic finger print of the librational edge of ice (Ih) is evident at ≈ 550 cm^{-1}. Contrary to that data, the 20%Ti SOMS data have very well defined librational peaks, visible at ≈ 533, 654, and 785 cm^{-1}. When a deuterated sample of the 20%Ti SOMS is studied, there are noticeable changes (a decrease) to the relative intensity of the librational peaks; however peak position has not changed. The decrease in relative intensity is very informative. First, it indicates only one type of proton environment has been exchanged in the deuteration process, and that is the proton associated with the occluded water molecules that are able to exhibit the librational transitions. Second, the invariance of the other bands (e.g., the hydrogen bonding modes of the metal-water bands in the 150 cm^{-1} region) further confirms only the occluded solvating waters are involved.
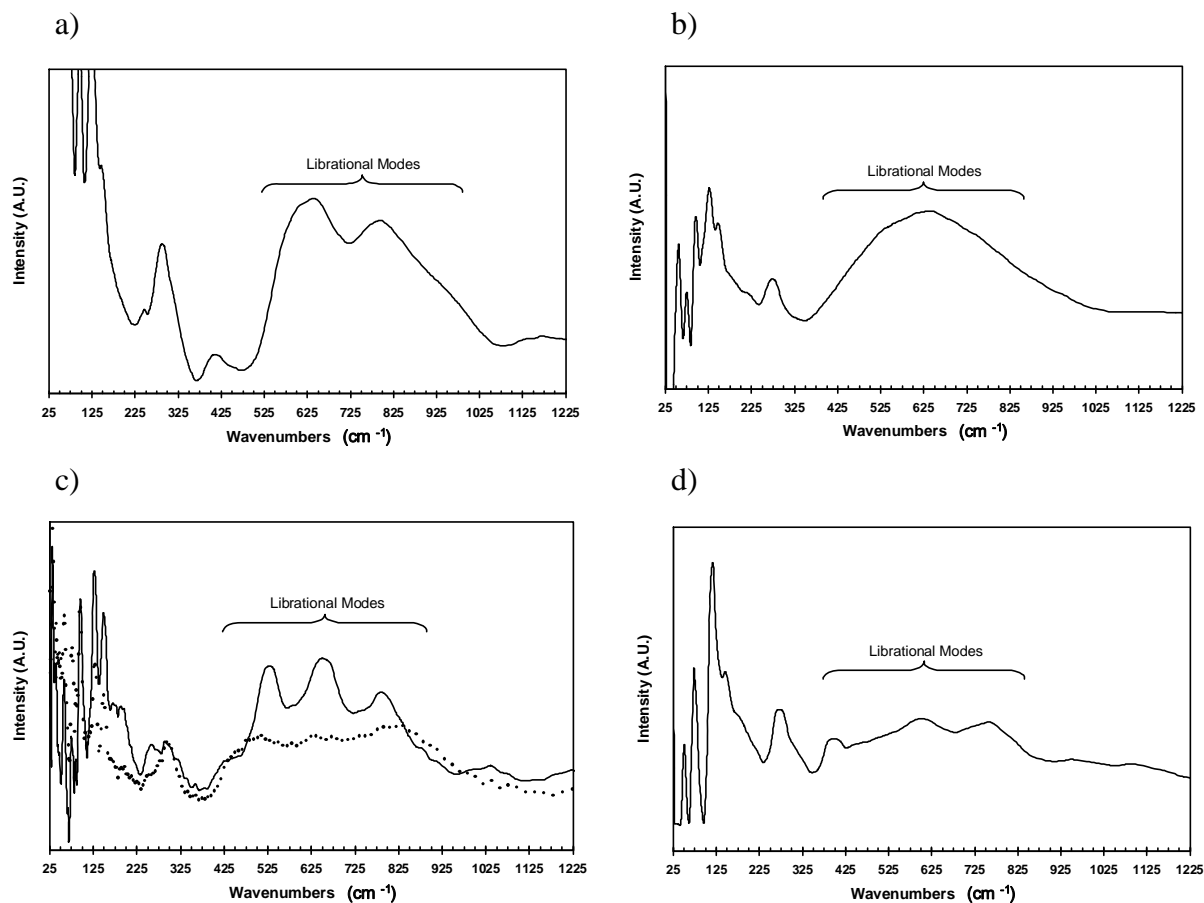
Figure 3. INS data collected at 10K for: a) SOMS end member, ice-like peak at ≈550 cm^{-1}; b) Sr-exchanged SOMS end member, librational modes at ≈ 450 cm^{-1}; c) 20%Ti SOMS, librational modes of water at 533, 654 and 785 cm^{-1} (decreased intensity data dotted line is ^{2}H sample); d) Sr-exchanged 20%Ti SOMS, librational modes at 503, 604 and 759 cm^{-1}.

Sr-Exchanged Samples

The INS data for the fully exchanged Sr-end member ($SrNb_2O_6 \cdot H_2O$) and the Sr-exchanged 20%Ti SOMS ($SrNb_{1.6}Ti_{0.4}O_{5.6}OH_{0.4} \cdot H_2O$) have been collected and are compared to their non-exchanged versions. In the Sr-exchanged end member data, the once sharp distinct Ih peak has been lost and a very broad, featureless hump is now evident (centered at ≈ 450 cm^{-1}). Also a shift to ≈ 300 cm^{-1} in the Metal-water modes is also observed. In contrast, the Sr-exchanged 20%Ti SOMS has only minor changes to the data. There is a noticeable shift to lower frequencies in the librational modes to ≈ 503, 604 and 759 cm^{-1}, and a significant broadening of the peaks. The slight shift to lower frequencies may be due to the larger sized cations (Sr^{2+} as compared to the Na^+ cations) and the presence of framework hydroxides (-O_fH) both inhibiting hydrogen bonding among water molecules in the pores.[29]

In the case of the Sr exchanged end member SOMS, we see distinctly different INS spectra. In the as-made end member, the pores contain one Na and one water per unit cell. There is little spatial interference with the water molecules forming hydrogen bonds with each other along the one-dimensional channel of the SOMS. Contrasting that is the Sr exchanged end member, with

50% of the unit cells having one water and one dangling hydroxide (attached to the framework),[12b] and the other 50% having one water, one dangling hydroxide, and one strontium ion. It is possible to view the occluded water in this phase as having segregated into two distinct networks of water molecules: one network has a charge balancing Sr^{2+} present, while the other network has no cation present. Each network has water that is hydrogen bonded, but there may not be hydrogen bonding interactions between the two networks. The librational modes for each network tend to merge into a very broad, very intense continuum and the librational edge shifts to lower frequencies if one of the networks is more loosely held together than the other.

Another possible explanation is the loss of long-range order in the network(s) of hydrogen-bonded water molecules. Short-range ordering of the water molecules is preserved (e.g., around a particular cation), but there is no long-range order throughout the structure. The resulting network of bonds of various length, strength, and orientation causes a broadening of the librational levels and a loosening of the librational motion (hence the shift of the librational edge to lower frequencies). The shift of the librational edge to a lower frequency is typically due to weakening of the O-H··O bending force constant.[32]

It is possible that the above situations (two networks of hydrogen bonds or loss of long-range order) can occur simultaneously. This is the case in high density amorphous ice, the structure of which can be thought of as two interpenetrating, but non-interacting hydrogen bonded water networks. Each has significant density of structural ions, molecules, and pore bonded hydroxyls that cause a loss of any kind of long-range order in the translational and rotational ordering of the water molecules. MAS NMR studies have been employed to help clarify the explanation of this hydrogen bonding networks in the Sr-exchanged phases (see below).

^{1}H MAS NMR

To further probe the local environment of these water molecules and the water dynamics on the micro- to millisecond time scale, ^{1}H MAS NMR techniques were utilized. The ^{1}H MAS NMR spectrum of end member $Na_2Nb_2O_6 \cdot H_2O$ (see Figure 4a) revealed three overlapping proton species with the major (90% relative concentration) resonance at $\delta = +5.0$ ppm, (full width at half maximum line width, FWHM = 892 Hz) due to an immobile water environment, a second ^{1}H resonance (9%) at $\delta = +4.3$ ppm (FWHM = 378 Hz) due to a mobile water environment, along with the minor (~ 1%) NbOH species at $\delta = +1.0$ ppm (FWHM = 300 Hz). These ^{1}H assignments are based on previous studies of niobate materials,[16,17] double quantum filtered (DQF) experiments,[18] along with the residual dipolar interaction strength measured using the 2D DQ correlation experiments described below. For the 20% Ti-SOMS $Na_2Nb_{1.6}Ti_{0.4}O_{5.6} \cdot H_2O$ material only a single resonance at $\delta = + 4.7$ ppm (FWHM = 450 Hz) was observed in the ^{1}H MAS NMR spectrum.
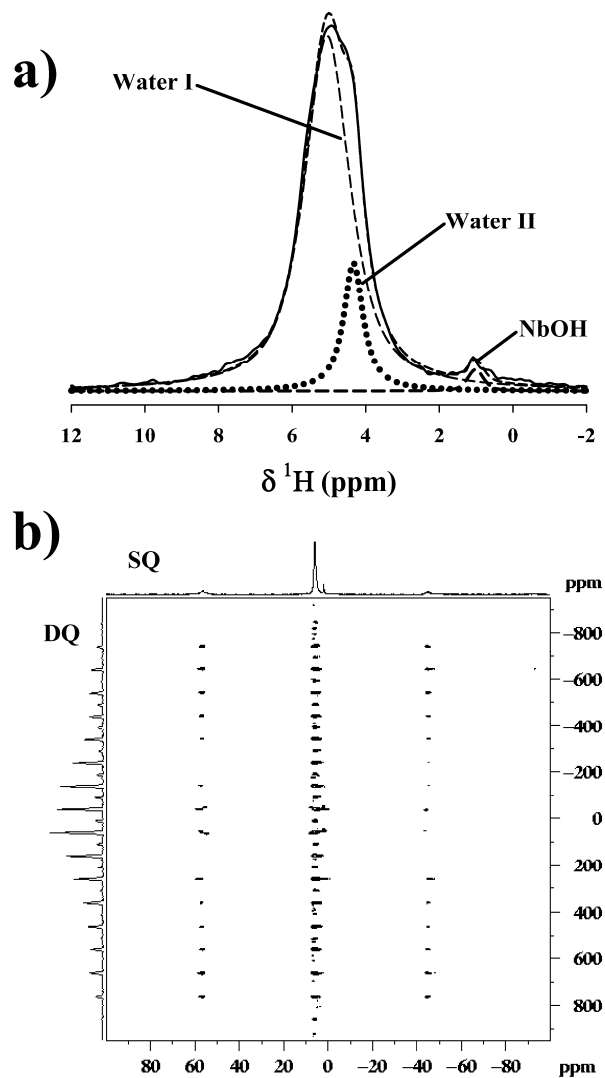
Figure 4. The (a) ^{1}H MAS NMR of the end member $Na_2Nb_2O_6 \cdot H_2O$ material revealing three overlapping proton species, including the dominant rigid water species (Water I), a mobile water species (Water II) and the NbOH hydroxyl. The (b) 2D DQ 1H MAS NMR correlation experiment where the multiple DQ spinning sidebands (left projection) can be used to determine the effective dipolar coupling of the immobile water species.

The extent of spinning sidebands (SSB) in the ^{1}H MAS NMR spectra of these different materials provides a qualitative measurement of the effective homonuclear ^{1}H-^{1}H dipole coupling present for these different water species. In a rigid (totally immobile) water molecule the ^{1}H-^{1}H dipolar coupling ($D^{ij}_{rigid} / 2\pi$) is on the order of 33.4 kHz, producing numerous SSB in the ^{1}H MAS NMR spectra.[15-18] If there are water dynamics that are rapid compared to this ^{1}H-^{1}H dipolar coupling coupling ($<< 30$ µs) then an averaging of the dipolar coupling will occur, reducing the number and intensity of the SSB observed. Comparison of the ^{1}H MAS NMR spectra for these two Na-containing samples indicates that the majority of the waters ($\delta = +5.0$ ppm) in the $Na_2Nb_2O_6 \cdot H_2O$ end member are relatively immobile, while the water species in the 20%Ti SOMS are mobile enough to produce significant averaging of the ^{1}H-^{1}H dipolar coupling and reduction of the SSB.

Two-dimensional (2D) double-quantum (DQ) ^{1}H MAS NMR correlation experiments were also performed to directly measure the mobility of the occluded water molecules in the end member $Na_2Nb_2O_6 \cdot H_2O$ material (Figure 4b). By analyzing the SSB patterns in the DQ dimension (left projection in 4b) from these 2D NMR experiments an accurate measurement of the residual [1]H-^{1}H dipolar coupling and related distribution of dipolar coupling strengths for waters can be measured.[15,17] The effective dipolar coupling found for the rigid water species in the end member material was 28 ± 0.5 kHz, with a distribution of $\sigma \approx 4$ (± 1) kHz. This corresponds to a water order parameter of $S_{H2O} = D^{ij}_{eff} / D^{ij}_{rigid} = 28$ kHz / 33.4 kHz = 0.84. This DQ measurement shows that this water environment is relatively immobile within the material even at or above RT. By comparison, the 20% Ti SOMS compound has almost all waters filtered out during the DQ experiments, consistent with a residual dipolar coupling < 3 kHz, indicating that for this compound all the water environments have a higher degree of mobility.

The same type of ^{1}H MAS NMR experiments can also be performed on the Sr-exchanged materials. The NMR of the $SrNb_2O_6 \cdot H_2O$ compound reveals (Figure 5a) two broad resonances at $\delta = +6.1$ ppm (~55%, FWHM = 1300 Hz) and at $\delta = +8.3$ ppm (~45%, FWHM = 2020 Hz), plus a small NbOH resonance at $\delta = 2.2$ ppm (~5%, FWHM = 390 Hz). This ^{1}H MAS NMR spectra is very different from the non-exchanged $Na_2Nb_2O_6 \cdot H_2O$ sample. In general there is an increase in the observed ^{1}H NMR chemical shifts following the Sr exchange suggesting subtle changes in the local partial charge of the frame work environment. Also of interest is the appearance of a water environment with an increased chemical shift ($\delta = +8.3$ ppm)[17] following Sr exchange that results from either a change in the available surface charge of the cage structure, a reduction in the rapid exchange between acid and bulk type H_2O environments or a change in the local water confinement. Figure 5b shows the full expansion of the ^{1}H 1D MAS NMR spectrum revealing numerous SSB for this resonance even at 30 kHz spinning speeds. Note that only SSB for the Water I species are observed (inset Figure 5b) consistent with these water environments being relatively immobile. Figure 5c shows the overlap between the 1D DQF ^{1}H MAS NMR spectra and the direct ^{1}H MAS NMR spectra. Inspection of this figure shows that the Water I resonance ($\delta = +8.3$ ppm) has the largest dipolar coupling (thus surviving the DQ filter), also consistent with an immobile water species. In contrast, the $\delta = +6.1$ ppm water species does not show SSB, nor does it survive the DQ filtering (Figure 5c), and is therefore is described as mobile on the NMR time scale. The 2D DQ ^{1}H MAS NMR sideband analysis for the Water I resonance ($\delta = +8.3$ ppm) gives $D^{ij}_{eff} \sim 25 \pm 0.5$ kHz , $\sigma = 7$ (± 1) kHz. ($S_{H2O} = 0.75$), and is slightly smaller than that observed for the non-exchanged material implying very similar water dynamics, but has an increased distribution of dipolar couplings (motion types). Similarly, the ^{1}H MAS NMR spectrum for the $SrNb_{1.6}Ti_{0.4}O_{5.6}OH_{0.4} \cdot H_2O$ compound revealed two broad resonances at $\delta = +8.4$ ppm (~ 28%, FWHM = 2130 Hz) and $\delta = + 6.2$ ppm (~70%, FWHM = 1975 Hz). Again, based on the intensity of the SSB in the ^{1}H MAS NMR spectrum, along with the results of the DQF experiments, the $\delta = + 8.4$ ppm water environment have the lowest degree of mobility, D^{ij}_{eff} ~ 28 ± 1 kHz, $\sigma = 8$ (± 1) kHz. ($S_{H2O} = 0.84$), while the $\delta = +6.2$ ppm resonance has a high degree of mobility.
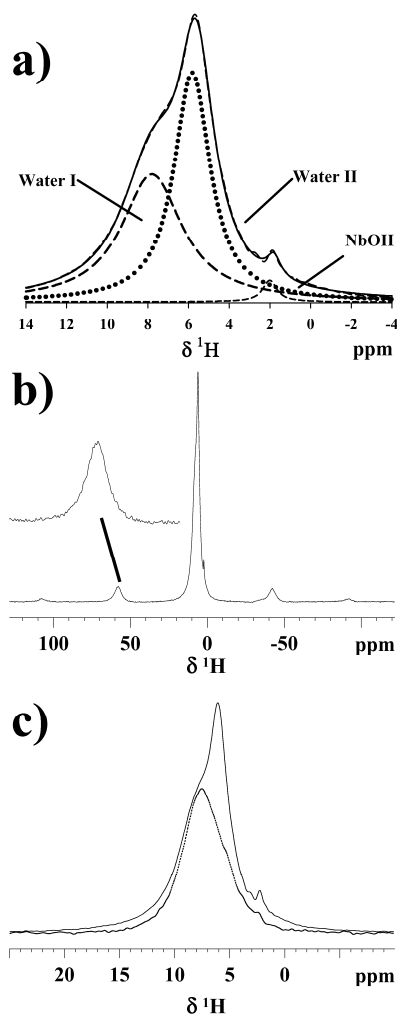
Figure 5. The (a) isotropic chemical shift region of the ^{1}H MAS NMR for the end member $SrNb_2O_6 \cdot H_2O$ material revealing three overlapping proton species, including the possible immobile water species (Water I), a mobile water species (Water II) and the NbOH hydroxyl. The (b) full ^{1}H MAS NMR spectrum showing the presence of significant sidebands for only the Water I resonance (insert) even at a 30 kHz spinning speed. The (c) DQ-filtered (lower) and direct polarization ^{1}H MAS NMR spectra clearly showing that only the Water I resonances is present following the DQ filtering, while the Water II species is suppressed.

Comparisons between the two Sr-exchanged phases reveal that the concentration of mobile water (δ ~6 ppm) increases with the addition of Ti. This correlates well with the INS data. Comparison between the Sr and the as-synthesized Na phases shows that the Sr exchange resulted in a portion of the occluded non-mobile water becoming mobile in the $NaNb_2O_6 \cdot H_2O$ end group. In the 20% Ti material, the Sr-exchange materials results in a fraction of the water species remaining immobile in comparison to the non-exchanged 20% Ti SOMS. The $NaNb_2O_6 \cdot H_2O$ end member has the most free volume in the pore allowing the occluded water to form H-bonding networks and a higher concentration of ice-like water formations. As the number of pore ions decreases due to divalent cation exchange, and/or the addition of dangling pore –OH increases due to framework substitution (ie., Ti doping in framework), the occluded water H-bonding network is interrupted and ice-like water is not formed.

A brief comment on the types of water motions that can lead to the averaging of the ^{1}H-^{1}H dipolar coupling is warranted. As previously discussed,[17] isotropic motions that would be expected for bulk water solutions completely average the ^{1}H-^{1}H dipolar coupling giving rise to $S_{H2O} \sim 0$. This type of dipolar coupling averaging is observed for the water environments we have designated as "mobile" species. Another proposed motion is the continuous spinning of the water molecule around the molecular C_{2v} symmetry axis, which will give a water dipolar order parameter of $S_{H2O} \sim 0.5$. The observation of dipolar order parameters for the "immobile" water environments between 0.74 and 0.84 precludes this type of rapid spinning motion. On the other hand, discrete 180° jumps around the molecular C_{2v} symmetry axis will not average the ^{1}H-^{1}H dipolar coupling because this motion produces coincident dipolar tensors, and is therefore not detectable using the ^{1}H-^{1}H DQ NMR experiments.[17] The experimental S_{H2O} values slightly reduced from unity suggest that librational-type water motions are present (in addition to the possibility of discrete 180° flips) giving rise to partial averaging of the ^{1}H-^{1}H dipolar coupling.

Density Functional Theory
We performed DFT calculations for the undoped end member SOMS in a unit cell containing 16 Nb, 16 Na, and 48 O atoms. Analogous simulations were performed for two 18.75 % Ti-substituted unit cells, with stoichiometries $Na_{16}Nb_{13}Ti_3O_{45}(OH)_3$ and $Na_{12}Sr_4Nb_{13}Ti_3O_{45}(OH)_3$, respectively. Since it was found that varying the Ti concentration has little effect on the lattice constants[12b], all calculations were performed at the experimental lattice constants derived for 20% Ti SOMS[12a]. All simulation cells contain 8 H_2O molecules. By performing AIMD simulations and then applying geometric optimization, we sought to investigate the changes in the potential energy landscape for water induced by the Ti- and Sr-substitution. Despite the relatively small cell size and short trajectories mandated by DFT calculations, the accuracy of DFT methods, particularly when applied to Ti substitution, makes this a worthwhile approach that enables qualitatively comparisons with experiments and classical force field MD simulations (see below).

First we considered the end member SOMS. To initiate geometric optimization, the SOMS framework atoms and the oxygen sites of 8 water molecules were placed at the X-ray determined positions[12], while the water protons were oriented to form hydrogen bonds to framework oxygen atoms. The optimal structure is depicted in Figure 6a. In this ordered structure, two water molecules coordinate to each Na atom located at the center of the SOMS channels or pores. Each H_2O is also coordinated to another framework Na, in addition to forming two hydrogen bonds with framework oxygen atoms. To further demonstrate that this water configuration is robust and independent of the initial configuration, we conducted a 3 ps AIMD simulation starting from the structure in Figure 6a, with the trajectory maintained at T=900 K to accelerate water motion and sampling of their energy landscape. When the final configuration in this trajectory was re-optimized, the same stable structure (Figure 6a) with identical total energy was recovered. While not definitive, this strongly suggests that the water structure predicted from DFT calculations is a stable global minimum.
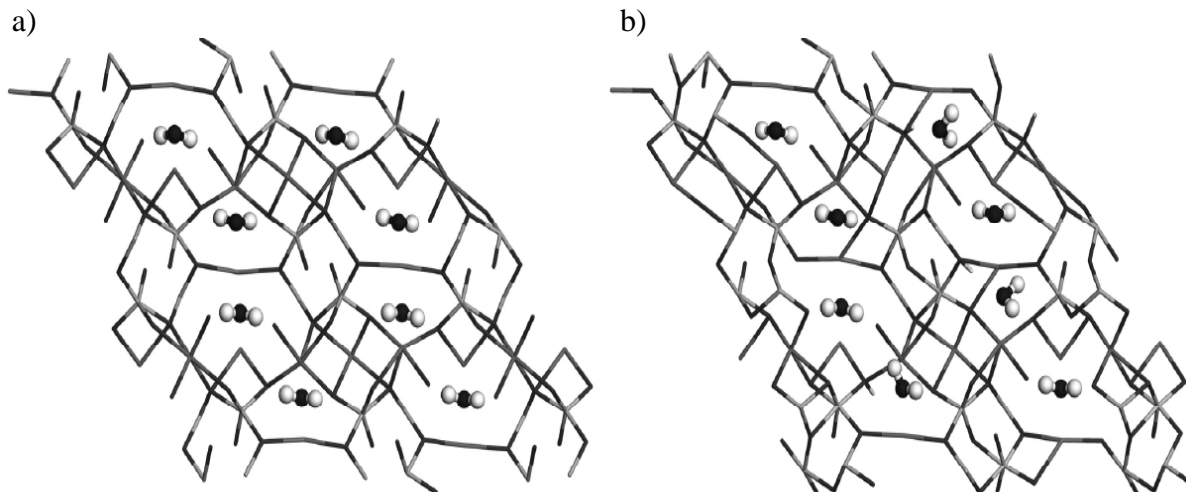
Figure 6. DFT optimized SOMS unit cell. The framework atoms are shown in wireframe and the water are depicted as ball-and-stick models. (a) 0% Ti; (b) 18.75% Ti.

We also considered SOMS structures where we randomly replaced 3 of the Nb atoms with Ti, and one of the O coordinated to each Ti with OH to preserve charge neutrality, this is a mimic for the 20%Ti-SOMS. In one structure, Sr^{2+} substituted for the Na^+ in two of the four channels in the SOMS unit cell; to maintain charge neutrality and in accordance with experiments, the remaining Na^+ in the other two SOMS channels were also removed. No Sr^{2+} was included in the other Ti-substituted structure.

For Sr-free, Ti-substituted system, performing geometry optimization from the X-ray positions led to water configurations that are less well-ordered than the end member SOMS. Some water molecules become preferentially coordinated to the hydroxyl groups in the framework instead of than the pore-center Na (see Figure 6b). We also conducted AIMD at T=900 K starting from this configuration, and re-optimized the geometry from snapshots taken 1.5 and 3.0 ps into this trajectory. The resulting water configurations are again disordered, but are considerably different from those in Figure 6b. Despite this, these two configurations quenched from high temperature are only 0.16 and 0.26 eV per formula unit higher in energy than the one directly optimized from X-ray structures. These heat-and-quench numerical "experiments" demonstrate that the addition of Ti dopants lead to metastable structures which are local minima in the energy landscape with very similar energies. The results and conclusions for Sr-exchanged, Ti-substituted SOMS (not shown) are similar.

These DFT results are consistent with the experimental finding that water is more mobile in Ti-substituted SOMS and in the Sr-exchanged SOMS than in the as-synthesized end member system, and is predominantly solvating the cations in the pores. In the absence of Ti, the water configuration is highly ordered and stable. The introduction of Ti dopants lead to disordered water structures and the existence of multiple local minima in the energy landscape, which should in turn leads to faster water librational and diffusive motion.

Molecular Dynamics Simulations

An overall picture of the equilibrium dynamics for the various SOMS materials can be obtained through the comparative analysis and correlation of power spectra (derived from the classical molecular dynamics simulations) with observed spectroscopic evidence from inelastic neutron scattering and NMR techniques.

Power spectra are derived from velocity auto correlation functions (VACF) and large scale molecular dynamics simulations.[33-35] The atomic positions and velocities from the simulation trajectories were processed to identify correlated motions for the occluded water in all structures and the hydroxyl groups in the Ti-doped SOMS models. The time domain correlations were then Fourier transformed to obtain the frequency domain response corresponding to the power spectrum. The results indicate a distinction in the bend and stretch vibrational regions between the Sr-and Na-SOMS that also exists for both the end member and Ti-doped materials (Figure 7).
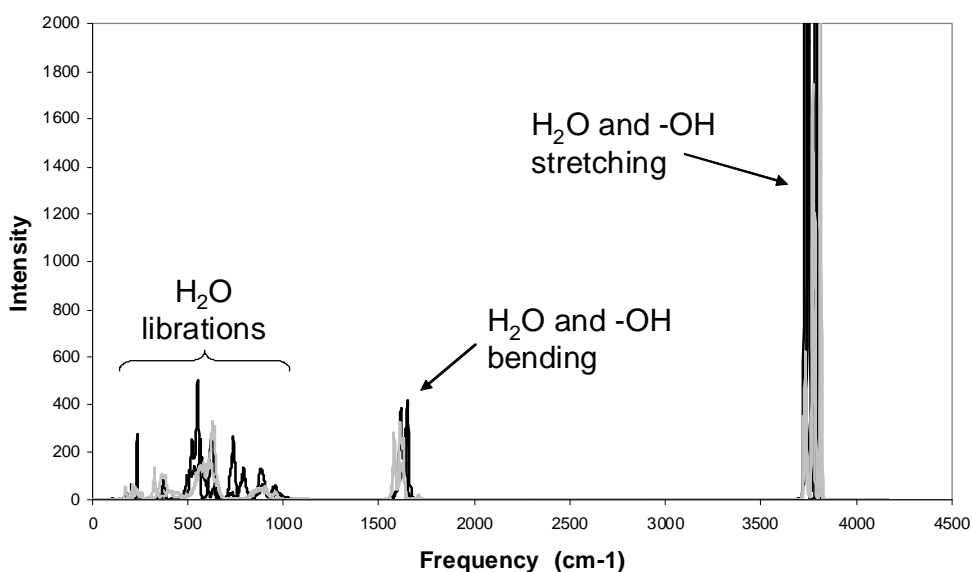
Figure 7. Comparison of entire power spectra derived from molecular dynamics simulations for all modes of water and hydroxyl in Na-SOMS and Na-Ti-SOMS (black) and Sr-SOMS and Sr-Ti-SOMS (gray).

Significant differences in the power spectra are observed for the SOMS structures having different pore cations are clearly observed (Figure 7). Power spectra for the Na-SOMS exhibit a shift (≈ 50 cm^{-1}) of the bend (deformation) peaks to higher frequencies (relative to the Sr-SOMS) and a shift (≈ 50 cm^{-1}) of the stretch peaks to lower frequencies. The models also suggest that substitution of Ti for Nb for either Na- or Sr-SOMS leads to similar shifts of the power spectra and a more liquid-like environment in the channel, consistent with the DFT results. In part, this response is related to the charge compensating hydroxyl group that contributes to the formation of a more stable hydrogen-bonded configuration. However, it is important to emphasize that the small highly-charged ions such a Sr^{2+} are less polarizable than the monovalent Na^{+}, and have larger hydration energies. In such a case, water-ion interactions dominate over the weaker water-SOMS and water-water interactions, and therefore have the strongest influence on occluded water properties.

In general, the power spectra results, which are consistent with INS vibrational spectra and NMR observations, indicate channel water behaves differently depending on the channel cation; the water may be more constrained for ions like Na^+ and more liquid-like for Sr^{2+} as the channel cation. Additionally, atomic trajectories obtained from the simulations for $SrNb_2O_6 \cdot H_2O$ and $SrNb_{1.6}Ti_{0.4}O_{5.6}(OH)_{0.4} \cdot H_2O$ systems exhibit noticeable differences in the power spectra for isolated channel water compared to water associated with Sr^{2+}. The deformation (bending) region for hydroxyl (≈ 1500 to 1750 cm^{-1}) is typically quite broad in the INS data relative to the more dominant modes for metal-water interactions and librational modes for water (see Figure 3). However, analysis of the power spectra clearly indicates the different environment for water in the SOMS pore with and without the exchangeable cation. The most sensitive discriminator for this behavior is found in the deformation mode of water where we observe a shift of approximately 40 cm^{-1} (see Figure 8). The exchange of divalent Sr^{2+} for Na^+ in SOMS requires only half the number of occupied channel sites, and therefore generates free water that can directly interact with the framework. Power spectra derived from trajectories for SOMS models with a monovalent ion like Na^+ exhibit peaks representing equivalent pore environments in both the SOMS and Ti-doped SOMS structures.
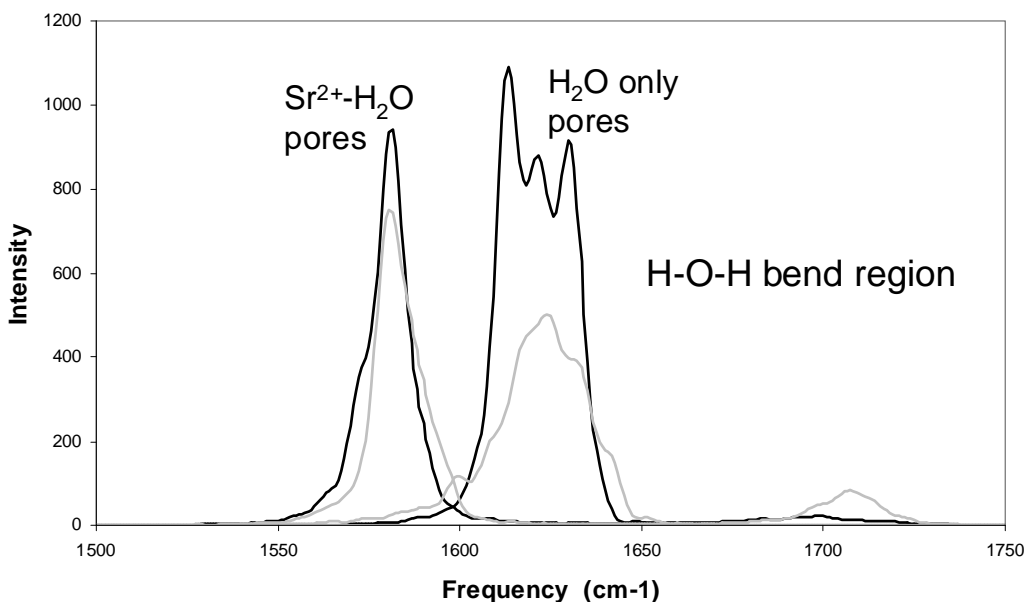
Figure 8: Comparison of power spectra derived from molecular dynamics simulations for bend modes of occluded water in Sr-SOMS (black) and Sr-Ti-SOMS (gray) indicating difference between isolated water and Sr-associated water in channels (pores).

Conclusion

We are using a variety of different analytical techniques to help elucidate the role of occluded water in ion exchange selectivity of molecular sieves, in particular the Sandia Octahedral Molecular Sieves (SOMS). Inelastic neutron scattering has allowed us to probe the nature of hydrogen bonding of water molecules in the SOMS materials. INS shows that in the low selectivity as-synthesized end member, the water exhibits an ice-like extended hydrogen bonding nature. The ^{1}H MAS NMR data confirms the INS data, that there is a great difference in the

mobility between the $Na_2Nb_2O_6 \cdot H_2O$ end member (low selectivity) and the $Na_2Nb_{1.6}Ti_{0.4}O_{5.6}(OH)_{0.4} \cdot H_2O$ material (high selectivity). The occluded water molecules in the end member are very rigid, almost immobile. This is in contrast to the water molecules of the 20%Ti SOMS where they have very high mobility. It appears that in molecular sieves in which the water is mobile, there is a cation solvation effect associated with the water, thereby allowing greater mobility of the cation. Contrary to this, when there is little water mobility, the cation is locked into its crystallographic site while the water is forming relatively rigid hydrogen bonding with itself throughout the channels. In both the 20%Ti-SOMS and the Sr-exchanged samples, the effective free volumes of the pores are decreased. This is due to cation size and charge balancing framework $-O_fH$ molecules present in the pore. The result is a disruption of the extended H-bonding network, further resulting in the disruption of possibly "ice-like" structural formations. On-going studies are focused on studies of the occluded water molecules in heavily hydrated zeolite systems with overall high ion exchange capacities. Furthermore, we are further developing and greatly expanding our research with molecular dynamics simulations involving a full exploration of the power spectra of occluded water molecules.

References

1. Klafter, J.; Blumem, A.; Drake, J.M. Relaxation and Diffusion in Restricted Geometry; Klafter, J.; Drake, J.M., Eds.; New York: Wiley, 1989.

2. Arndt, M.; Stannarius, R.; Gorbatschow, W.; Kremer, R. Phys. Rev. E: Stat., Nonlinear, Soft Matter 1996, 54, 5377.

3. (a) Breck, D.W. Zeolite Molecular Sieves, New York: Wiley, 1974; (b) Sherry, H. S. "Ion Exchange". Handbook of Zeolite Science and Technology, edited by S.M. Auerbach, K. A. Carrado, P.K. Dutta, New York: Marcel Dekker, 2003.

4. (a) Yang, S.Y.; Navrotsky, A.; Wilkin, R. Am. Mineral. 2001, 86, 438.; (b) Sun, P.P.; Deore, S.; Navrotsky, A. Micropor. Mesopor. Mater. 2006, 91, 15.

5. Corsaro, C.; Crupi,V.; Majolino, D.; Parker, S.F.; Venuti, V.; Wanderlingh, U. J. Phys. Chem. A, 2006, 110, 1190.

6. Hunger, J.; Beta, I.A.; Bohlig, H; Ling, C.; Jobic, H.; Hunger, B. J. Phys. Chem. B, 2006, 110(1), 342.

7. Beta, I. A.; Bohlig, H.; Hunger, B. Phys. Chem. Chem. Phys., 2004, 6, 1975.

8. Crupi, V.; Majolino, D.; Migliardo, P.; Venuti, V.; Wanderlingh, U.; Mizota, T.; Telling, M. J. Phys. Chem., 2004, 108, 4314.

9. Jobic, H.; Tuel, A.; Krossner, M.; Sauer, J. J. Phys. Chem. 1996, 100, 19545.

10. Line, C.M.B.; Kearley, G.J. *J. Chem. Phys.* **2000**, *112*, 9058.

11. Higgins, F.M.; de Leeuw, N. H.; Parker, S. C. *J. Mater. Chem.* **2002**, *12*, 124.

12. (a) Nyman, M.D.; Tripathi, A.; Parise, J.B.; Maxwell, R.S.; Harrison, W.T.A.; Nenoff, T.M. *J. Am. Chem. Soc.* *2001*, **123**, 1529. (b) Nyman, M.D.; Tripathi, A.; Parise, J.B.; Maxwell, R.S.; Nenoff, T.M. *J. Am. Chem. Soc.* 2002, *124*, 1704. (c) Nenoff, T. M.; Nyman M. "Niobate-based octahedral molecular sieves" US Patent # 6,596,254, 2003.

13. Pless, J.D.; Garino, T.J.; Maslar, J. E.; Nenoff, T. M. *Chem. Mater.*, **2007**, *19*, 4855.

14. JCPDS, Joint Committee of Powder Diffraction Standards database, International Centre for Diffraction Data (ICDD).

15. Holland, G.P.; Cherry, B.R.; Alam, T.M. *J. Magn. Reson.* **2004**, *167*, 161.

16 Alam, T.M.; Nyman, M.; Cherry, B.R.; Segall, J.M.; Lybarger, L.E. *J. Am. Chem. Soc.* **2004**, *126*, 5610.

17. Alam, T.M.; Nyman, M.; McIntyre, S. K. *J. Phys. Chem. A* **2007**, *111*, 1792.

18. Alam, T.M.; Pless, J.D.; Nenoff, T.M. "Probing Water Dynamics in Octahedral Molecular Sieves: High Speed ^{1}H MAS NMR Investigations". *Magnetic Resonance in Material Science*, edited by J. Herberg, Y. Wu, P. Grandinetti, S. Hayes, I. Farnan (Mater. Res. Soc. Symp. Proc. 984E, Warrendale, PA, 2007), 0984-MM03-03.

19. Perdew, J.P.; Burke, K.; Ernzerhof, M. *Phys. Rev. Lett.* **1996**, *77*, 3865.

20. Blochl, P.E. *Phys. Rev. B*, **1994**, *50*, 17953.

21. Kresse, G.; Joubert, D. *Phys. Rev. B* **1999**, *59*, 1758.

22. Kresse, G.; Furthmuller, J. *Phys. Rev. B* **1996**, *54*, 11169; *Comp. Mater. Sci.* **1996**, *6*, 15.

23. Berendsen, H.J.C., Postma, J.P.M., van Gunsteren, W.F., and Hermans, J. "Interaction models for water in relation to protein hydration." In B. Pullman, Ed. *Intermolecular Forces*, **1981**, p. 331.

24. Teleman, O.; Jonsson, B.; Engstrom, S. *Mol. Phys.*, **1987**, *60*(1), 193.

25. Åqvist, J., *J. Phys. Chem.*, **1990**, *94*, 8021.

26. Halgren, T.A., *J. Am. Chem. Soc.* **1992**, *114*(20), 7827.

27. Frenkel, D.; Smit, B. *Understanding Molecular Simulations: From Algorithms to Applications*, second edition, Academic Press, San Diego, **2002**.

28. Rietveld, H. M. *J. Appl. Crystallogr.* **1969**, *2*, 65.

29. Larson, A. C.; Von Dreele, R. B.; *GSAS-General Structure Analysis System*; Los Alamos National Laboratory Report No. LAUR 86-748: Los Alamos National Laboratory: Los Alamos, NM, 2000.

30. Nenoff, T.M.; Ockwig, N. W.; Pless, J.D.; Alam, T.M.; M. Hartl, M.; Daemon, L.L. *Stud. Surf. Sci. Catal.*, **2007**, in press.

31. J-C. Li, A.I. Kolesnikov, *J. Molecular Liquids* **2002**, *100*/1, 1.

32. Corsaro, C.; Crupi, V.; Longo, F.; Majolino, D.; Venuti, V.; Wanderlingh, U. *J. Phys.: Condens. Mater.* **2005**, *17*, 7925.

33. Bopp, P. *Pure Appl. Chem.*, **1987**, *59*, 1071.

34. Marti, J. *J. Chem. Phys.*, **1999**, *110*, 6876.

35. Bougeard, D.; Smirnov, K.S., *Phys. Chem. Chem. Phys.*, **2007**, *9*, 226.

Molecular Dynamics Studies of Nanoconfined Water in Clinoptilolite and Heulandite Zeolites

Abstract

The complete periodic series of alkali and alkaline earth cation variants (Li$^+$, Na$^+$, K$^+$, Rb$^+$, Cs$^+$, Mg^{2+}, Ca^{2+}, Sr^{2+}, and Ba^{2+}) of clinoptilolite (Si/Al=5) and heulandite (Si/Al=3.5) aluminosilicate zeolites are examined by large-scale molecular dynamics utilizing a flexible SPC water and aluminosilicate force field. Calculated hydration enthalpies, radial distribution functions, and ion coordination environments are used to describe the energetic and structural components of extra-framework species while power spectra are used to examine the intermolecular dynamics. These data are correlated to evaluate the impact of ion-zeolite, ion-water, and water-zeolite interactions on the behavior of nanoconfined water. Analysis of the correlated data clearly indicates that charge density of extra-framework cations appears to have the greatest influence on librational motions, while the anionic charge of the framework (i.e. Si/Al ratios) has a lesser impact.

Introduction

Understanding the behavior of confined molecular species in microporous materials is a challenging topic which spans a wide variety of both experimental and theoretical arenas.[1-4] Nanoconfined water is arguably the most important species in porous materials to investigate because of its ubiquitous nature and tremendous impact across many industrially significant and interdisciplinary processes. The structural and dynamical properties of bulk water are now mostly well understood in a wide range of temperatures and pressures. It is also well known that the bulk properties of water are significantly modified when confined on a molecular scale.[5] However, despite its relatively simple molecular structure, the complex collective behavior of water remains a major challenge for current scientific understanding and levels of theory.[6] Quantifying the behavior of water in such confined systems is the first step towards understanding its role in macroscopic phenomena (i.e. species mobility and ion exchange) and ultimately provides the fundamental foundation for understanding, modifying, and directing such properties. This is particularly true for zeolitic systems, where several focused studies on water in these systems has provided valuable insight to our greater understanding.[7-12]

Zeolites, derived from the Greek words *zein* "to boil" and *lithos* "a stone", are metastable microcrystalline aluminosilicate minerals which liberate occluded water molecules upon heating.[13] Largely defined by J. V. Smith[14a,b] and D. W. Breck,[14c] these framework type minerals have structures that enclose channels and/or cavities which may be occupied by charge-compensating ions and water molecules. The enclosed species often possess significant freedom of movement which permits ion exchange and reversible dehydration behaviors. These aluminosilicate materials are built up from corner sharing TO$_4$ tetrahedral units (where T is either Si or Al) with a generalized formula of X$_{x/n}$[(AlO$_2$)$_x$(SiO$_2$)$_y$] where X is the charge balancing counter-ion, n is the charge of the counter-ion, x is the number of charge-deficient alumina sites, and y is the number of charge-neutral silica sites. For every AlO$_4$ tetrahedron, the framework possesses a charge of -1 which must be balanced by the presence of additional extra-framework cations X$_{x/n}^{n+}$ that occupy the pores/channels of the zeolite. These cation species are quite often

exchangeable as they are small enough to move through the zeolite network of channels and pores. The pores and channels result from progressive connections of two adjacent TO_4 units through a bridging oxygen atom to form T-O-T linkages. The wide angular flexibility of these T-O-T linkages (~100º to ~180º) gives rise to topological and compositional zeolites variants. Zeolites are characterized by internal voids, channels, pores, and/or cavities of well-defined size in the nanometer range, $\approx$ 4-13 Å, accessible through apertures of well-defined molecular dimensions.[15] Within these zeolitic pores, the behavior of water molecules is the direct response of complex equilibria among four distinct types of interactions: (1) H_2O-H_2O; (2) Ion-H_2O; (3) H_2O-Framework; and (4) Ion-Framework. The effect of these interactions (hydrogen bonds, electrostatics, and ion-dipole) produce localized restrictions which alter the behavior of zeolite water from that of bulk water. An additional type of interaction, namely Ion-Ion electrostatic repulsions, may impact the water structure by spreading out the localized water attractors but this effect is probably less significant due to the effective screening of the zeolite framework, and therefore was not investigated in this study. Spectroscopically, the molecular behavior of nanoconfined water is manifested by changes in the intermolecular librational/rotational (300-1100 cm^{-1}) modes, and to a lesser extent, the intramolecular bending (~1600 cm^{-1}), and stretching (3300-3700 cm^{-1}) modes. An overall analysis of the equilibrium dynamics of water in zeolites can be obtained through computational chemical analysis and correlation of power spectra obtained from the trajectories of our large-scale molecular dynamics simulations.

In the last two decades, computer simulations, theoretical treatments, and experiments on the structural and dynamic properties of water in different local microscopic environments have been performed on a wide variety of frequently used adsorbents such as: clay minerals,[16] polymeric membranes,[17] various types of silica gels,[18] zeolites,[10] and activated charcoals.[19] The most prominent methods to extract information on structure and intra- and inter-molecular behavior of bulk and confined water are molecular dynamics (MD),[20-25] neutron[26] and X-ray diffraction,[27] incoherent quasi-elastic and incoherent inelastic neutron scattering (IQENS and IINS, respectively),[25,28-31] Raman scattering,[32] microwave and IR spectroscopies,[33] and nuclear magnetic resonance (NMR).[25,34] Many of these studies include multiple, and often complimentary, methods to probe the role of water in connection with structural, dynamical, and thermodynamic properties which have led to an impressive body of literature. However, there are numerous contradictory results which are continually challenging and improving our current levels of theory and understanding.

In this contribution, we investigate changes in the dynamic behavior of confined water molecules through their intermolecular interactions within the pores of the isostructural zeolitic frameworks—heulandite and clinoptilolite—and their counterbalancing cations. This highly variable system was specifically targeted to avoid the challenging topic of zeolite structural variations and their impact on H_2O interactions, but still address several fundamental basic science questions relating to the role of framework charge and cation type on confined water dynamics. Unlike the work of R. A. Jackson, C. R. A. Catlow, and colleagues,[35] our studies focus on the rotational (and consequently spectroscopically observable) behavior of water rather than hydration and dehydration processes, cation mobility, or framework stability.

Model and Simulation Description

The models of these systems were constructed to encompass a large compositional phase space to facilitate the multidimensional analysis of the dynamic behavior of water in the heulandite class of zeolites over a range of compositional variants. Specifically, the trajectories generated from these MD simulations were analyzed to provide energetic properties (hydration enthalpies), structural characteristics (radial distribution functions and ion coordination environments), and dynamical behaviors (power spectra). Consistent with our recent simulation study of sodalite,[36] the framework atoms in our models do not have their positions fixed and the atomic interactions are evaluated through non-bonded potentials. The non-bonded van der Waals interactions are modeled with 6-12 Lennard-Jones potential terms[37] while the electrostatics through Coulombic potential terms and handled through an Ewald summation method.[38] This allows for a dynamically active zeolite framework which possesses some degree of flexibility without imposing the typical rigid body restrictions suffered by many prior zeolite models and allows for an increased computational efficiency without using explicitly defined framework bonding parameters. This is further enhanced through the use of a flexible SPC-based water model,[39] which has harmonic bending and stretching terms included. These bending and stretching terms are the only explicitly-defined bonded interactions utilized in the force field. Lennard-Jones parameters for cation-water interactions were obtained from simulation studies of aqueous systems that utilized the SPC water model.[40] Geometric combination rules[41] were used to derive the off-diagonal Lennard-Jones interaction parameters for the various zeolite systems. The incorporation of combination rules and Lennard-Jones functions provides a relatively simple, yet accurate, method to evaluate the large number of atomic interactions associated with the simulations, and avoids the explicit requirements of Buckingham and other more complicated potential forms.

Heulandite and clinoptilolite are isostructural crystalline frameworks (both with the HEU framework type) with varying Si/Al ratios ranging from 2.5 to 6. Those with Si/Al ratios < 4 are defined as heulandite (HEU), while those with ratios > 4 are referred to as clinoptilolite (CLI). The structure itself is built up from rings of tetrahedral centers (T rings) which are interspersed by bridging oxygen atoms. In the HEU framework type, these rings define three distinct types of channels—one defined by 10T rings and two others by 8T rings—which are interconnected to form a layered array of channels (Figure 1). One of the 8T channels (**1**, 3.6 x 4.6 Å) and the 10T channel (**2**, 3.1 x 7.5 Å) run parallel to the *c*-axis while the remaining 8T channel (**3**, 2.8 x 4.7 Å) is parallel to the *a*-axis and intersects the first two channels to form an interconnected plane of channels. Both materials crystallize in the monoclinic space group *C2/m* with slightly different unit cells parameters.[42]
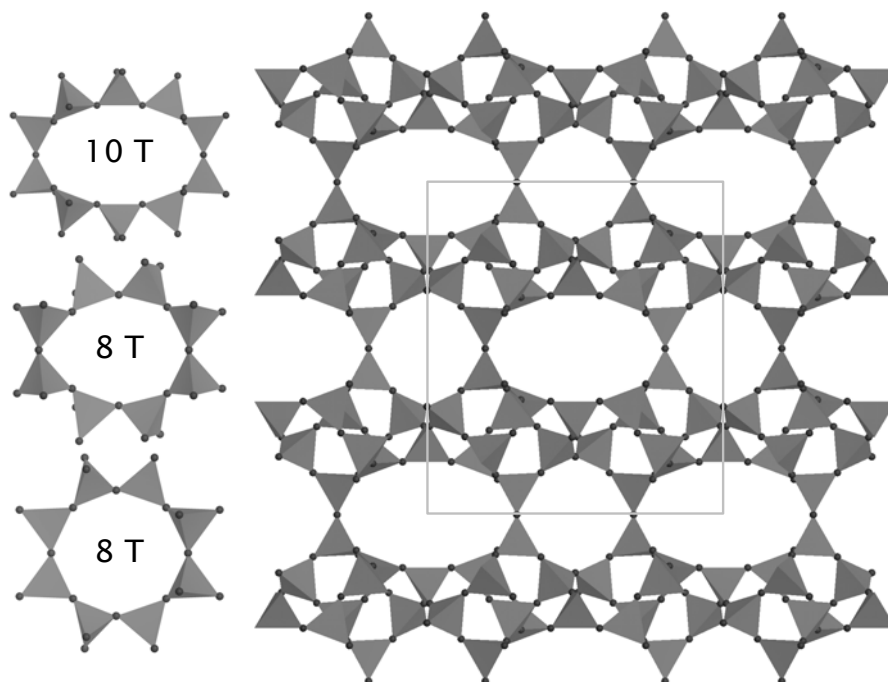
Figure 1. The two-dimensional pore system created by the intersection of a single 10T and two 8T channels. The 10T (upper left) and 8T (lower left) channels are parallel to the crystallographic *c*-axis and intersected by the remaining 8T channel which is parallel to the crystallographic *a*-axis. Polyhedra represent silicon (or aluminum) atoms while oxygen atoms are represented by small spheres.

For compatibility with the Large-scale Atomic/Molecular Massively Parallel Simulator (LAMMPS) molecular dynamics code,[43] the crystallographic symmetry restrictions were removed and the unit cell was transformed from monoclinic *C2/m* to orthogonal *P*1 with unit cell parameters of a = 15.92, *b* = 17.95, and *c* = 7.44 Å. Our heulandite models have a fixed Si/Al substitution ratio of 3.5 whereas the clinoptilolite models have a Si/Al ratio of 5. This yields idealized heulandite and clinoptilolite formula (where *X* is a monopositive cation) of $X_8Si_{28}Al_8O_{72} \cdot 24H_2O$ and $X_6Si_{30}Al_6O_{72} \cdot 24H_2O$, respectively. The idealized structural formula includes the maximum pore/channel content of 24 water molecules. For better statistics, each model was expanded to include 20 unit cells [2*a* x 2*b* x 5*c*] to give a supercell of dimensions 31.83 x 35.90 x 37.18 Å containing a maximum of 2,360 unique atoms when fully hydrated. The distribution of all aluminum sites throughout the supercell was randomly determined through virtual crystal approximation (the order-disorder subroutine of Cerius[2] software)[44] following Lowenstein's substitution rule and held fixed across each model of the series.[45] Initial cation locations were extracted from crystallographic references[46], while the initial water configurations were determined using a cartesian hybrid Monte Carlo algorithm.[47]

All MD simulations were performed using the LAMMPS code[43] with the modified zeolite force field used previously (Table 1).[36] Simulations of the fully hydrated system using an isothermal-isobaric ensemble (*NPT*) revealed less than 0.2 Å (~ 1%) fluctuations along any given axis and on this basis we assume optimal unit cell parameters (Table 2). Equilibrations were performed with a canonical ensemble (*NVT*) over 250 ps at 300 K applying the Nosé-Hoover thermostat.[48] Radial distribution functions (RDF), running coordination numbers, and energy evaluations were

calculated from constant *NVT* production runs performed over 500 ps at 300 K, while power spectra were calculated through Fourier transformation of velocity auto-correlation functions (VACF) that were compiled from 40 ps *NVT* trajectories with individual frames saved every 2 fs.[49]

Table 1. The partial charges, bond terms, and Lennard-Jones potentials of all species in the alkali and alkaline earth heulandite and clinoptilolite simulations.

Species	FF Type	Charge (e)	σ (nm)	ε (kcal/mol)
H water	h*	+0.41	-	-
O water	o*	-0.82	3.553	1.554×10^{-1}
zeolitic Si	sz	+2.4	8.186	1.147×10^{-9}
zeolitic Al	az	+1.4	0.831	$2.565 \times 10^{+3}$
zeolitic O	oz	-1.2	12.654	2.305×10^{-8}
ionic Li	li+	+1.0	4.726	9.026×10^{-7}
ionic Na	na+	+1.0	2.553	1.115×10^{-1}
ionic K	k+	+1.0	3.742	1.000×10^{-1}
ionic Rb	rb+	+1.0	4.050	1.000×10^{-1}
ionic Cs	cs+	+1.0	4.300	1.000×10^{-1}
ionic Mg	mg++	+2.0	1.846	8.750×10^{-1}
ionic Ca	ca++	+2.0	3.224	9.999×10^{-2}
ionic Sr	sr++	+2.0	3.886	1.000×10^{-1}
ionic Ba	ba++	+2.0	4.284	4.710×10^{-2}

Bond Stretching Parameters			
$E_{ij} = k_1 (r - r_o)^2$			
species *i*	species *j*	k_1 (kcal/mol Å^2)	r_o (Å)
o*	h*	553.9350	1.000

Angle Bending Parameters				
$E_{ijk} = k_2 (\theta - \theta_o)^2$				
species *i*	species *j*	species *k*	k_2 (kcal/mol rad^2)	θ_o (deg)
h*	o*	h*	45.7530	109.47

Table 2. Comparison of experimental and calculated fully hydrated lattice parameters (Å). The Δ_{max} value represents the maximum deviation from the experimental cell parameters.

	V (Å^3)	a (Å)	b (Å)	c (Å)	Δ_{max} (Å), axis
Exp.[a]	2107.87	15.81 (15)	17.92 (5)	7.40 (1)	
Li-CLI	2106.52	15.83	17.91	7.43	+0.03, c
Na-CLI	2111.51	15.88	17.92	7.42	+0.07, a
K-CLI	2131.77	15.95	17.94	7.45	+0.14, a
Rb-CLI	2144.08	15.96	17.96	7.48	+0.15, a
Cs-CLI	2146.43	15.99	17.97	7.47	+0.18, a
Mg-CLI	2084.29	15.86	17.88	7.34	-0.06, c
Ca-CLI	2127.42	15.93	17.95	7.44	+0.12, a
Sr-CLI	2149.37	15.98	18.03	7.46	+0.17, a
Ba-CLI	2157.86	15.97	18.04	7.49	+0.16, a
Exp.[a]	2110.86	15.79 (58)	17.92 (21)	7.46 (13)	
Li-HEU	2094.53	15.80	17.89	7.41	-0.05, c
Na-HEU	2105.66	15.87	17.93	7.40	+0.08, a
K-HEU	2121.85	15.94	17.94	7.42	+0.15, a
Rb-HEU	2143.41	15.98	17.98	7.46	+0.19, a
Cs-HEU	2140.39	15.97	17.99	7.45	+0.18, a
Mg-HEU	2111.35	15.87	17.93	7.42	+0.09, a
Ca-HEU	2131.80	15.92	17.95	7.46	+0.13, a
Sr-HEU	2149.34	15.96	17.98	7.49	+0.17, a
Ba-HEU	2152.36	15.97	17.97	7.50	+0.18, a

[a]Transformed from the experimental monoclinic $C2/c$ cell[42] to the orthogonal $P1$ simulation cell for LAMMPS compatibility.

Molecular simulations in this study emphasize the dynamical behavior of the zeolites through the use of MD methods. Static calculations such as energy minimization were initially used in the development of the force field parameters and in the preliminary analysis of the zeolite framework structure. However, structural minimizations are limited to 0 K and fail to identify any dynamical aspects of cation hydration and of the zeolite framework which controls much of the molecular behavior at 300 K. We report dynamical averages for the lattice parameters for each of the zeolite systems and use MD to identify the key vibrational signatures associated with the dynamics of the pore water.

Results and Discussion

We have performed large scale molecular dynamics simulations on eighteen unique zeolite-ion pairs (Li-CLI, Na-CLI, K-CLI, Rb-CLI, Cs-CLI, Mg-CLI, Ca-CLI, Sr-CLI, Ba-CLI, Li-HEU, Na-HEU, K-HEU, Rb-HEU, Cs-HEU, Mg-HEU, Ca-HEU, Sr-HEU, and Ba-HEU) using a procedure outlined above. To maintain charge neutrality, models containing divalent alkaline earth ions have only half the number of ions and these were placed in their respective crystallographically defined positions.[46] For validation purposes we have compared

experimental and calculated free ion hydration enthalpies (Table 3), Ion-O$_{Water}$ distances (Table 4), and coordination environments for all ions in this study.

Table 3. Experimental and calculated hydration enthalpies, ΔH_{hyd} (kcal/mol).

	Li$^+$	Na$^+$	K$^+$	Rb$^+$	Cs$^+$	Mg^{2+}	Ca^{2+}	Sr^{2+}	Ba^{2+}
Ion (*exp*)	-124	-97	-77	-71	-66	-459	-377	-345	-312
Ion (*calc*)[a]	-127	-101	-69	-66	-62	-433	-358	-311	-314
CLI (*calc*)[b]	-16.0	-14.2	-12.8	-12.4	-12.2	-98.8	-18.4	-17.6	-16.8
HEU (*calc*)[b]	-18.1	-15.2	-13.0	-12.6	-11.9	-95.0	-15.5	-15.3	-15.1

[a]Calculated on a per mol ion basis with standard deviations of ±37 kcal/mol.
[b]Calculated on a per mol H$_2$O basis with standard deviations of ±0.2 kcal/mol.

Table 4. Comparison of experimental and calculated ion-O distances (Å).

	Li$^+$	Na$^+$	K$^+$	Rb$^+$	Cs$^+$	Mg^{2+}	Ca^{2+}	Sr^{2+}	Ba^{2+}
Pure H$_2$O (*exp*)[50]	2.10	2.41	2.80	2.92	3.14	2.07	2.33	2.60	2.90
Pure H$_2$O (*calc*)	1.88	2.33	2.83	2.98	3.18	2.23	2.60	2.98	2.93
CLI-O$_{Water}$ (*calc*)[a]	1.88	2.29	2.82	2.94	3.06	1.99	2.43	2.68	2.75
HEU-O$_{Water}$ (*calc*)[a]	1.89	2.28	2.81	2.92	3.02	1.98	2.91	3.15	3.19

[a]Standard deviations are ±0.01 Å.

Table 5. Experimental and calculated ion coordination environments (first sphere only).

		Li$^+$	Na$^+$	K$^+$	Rb$^+$	Cs$^+$	Mg^{2+}	Ca^{2+}	Sr^{2+}	Ba^{2+}
	Ion-O$_{Water}$ (*exp*)Error! Bookmark not defined.	4.0	6.0	6.0	-	8.0	6.0	6.0	7.9	9.5
	Ion-O$_{Water}$ (*calc*)	4.0	5.8	5.9	9.0	9.0	5.8	6.8	9.0	8.0
C	**Ion-O$_{Water}$**	2.2	3.0	3.7	3.9	4.4	4.2	4.2	4.7	4.7
L	**Ion-O$_{Framework}$**	1.6	1.6	3.5	4.6	4.8	1.4	2.4	2.5	2.6
I	**Ion-O Total C.N.**	**3.8**	**4.6**	**7.2**	**8.5**	**9.2**	**5.6**	**6.6**	**7.2**	**7.3**
H	**Ion-O$_{Water}$**	1.9	3.0	3.7	3.7	4.0	3.7	3.3	4.2	4.1
E	**Ion-O$_{Framework}$**	1.9	1.8	3.5	4.2	5.4	1.8	7.6	7.9	7.4
U	**Ion-O Total C.N.**	**3.8**	**4.8**	**7.2**	**8.1**	**9.4**	**5.5**	**10.6**	**12.1**	**11.5**

Force Field Parameter Validation

The force field was validated through comparison of experimental and calculated hydration enthalpies, Ion-O$_W$ distances, and coordination environments, which are tabulated in the first two rows of Tables 3, 4, and 5. Hydration enthalpies (ΔH_{hyd}) of the solvated free ions were calculated through the following equation:

$$\Delta H_{hyd}^{ion} = \left\langle U_{water+ion} \right\rangle - \left\langle U_{water} \right\rangle$$

where $<U_{water+ion}>$ and $<U_{water}>$ are the respective mean potential energies. Although most of the calculated ΔH_{hyd} values are slightly higher (Table 3) than those observed experimentally, Li^+ and Na^+ both show slightly decreased hydration enthalpies. The maximum deviations in these data occur for alkali K^+ and alkaline earth Sr^{2+}, which show elevated values of 8 (10.4%) and 34 (9.8%) kcal/mol, respectively, relative to the experimental data. The distances between the water oxygen (O_W) and individual ions were extracted from RDF data and the coordination environments by integration of the resulting curves. The calculated Ion-O_W distances from the bulk solvation simulations are generally in good agreement with experimental evidence with a majority of the distances being slightly overestimated but with Li^+ and Na^+ both being slightly under estimated, perhaps indicating a slight deficiency in the force field. Finally, the first coordination sphere of each ion shows good correlation with experimental values and very small deviations for the smaller, higher charge density ions and more significant deviations for the larger ions with lower charge densities. Despite the slight deviations in overall values, there is a strong agreement between experimental and calculated data. The periodic trends are still quite clear and show that the higher charge density divalent cations are much more strongly hydrated then their monovalent counterparts. The tabulated data in the first two rows of Tables 3, 4, and 5 for hydration enthalpies, Ion-O_W distances, and first coordination sphere environments illustrate these periodic trends quite clearly.

Radial Distribution Functions and Hydration Enthalpies
The overall hydration enthalpies in the zeolite-ion-water systems are composed of three types of energy contributions: the self solvation ($U_{water+water}$), individual ion hydration ($U_{ion+water}$), and zeolite hydration ($U_{framework+water}$) energies which cannot be decoupled without making significant assumptions. Therefore, we have elected to calculate these hydration enthalpies simply on a per mol H_2O basis through the following relation:

$$\Delta H_{hyd}^{ion+framework} = \frac{\left\langle U_{water+ion+framework} \right\rangle - \left\langle U_{ion+framework} \right\rangle}{nH_2O} \tag{1}$$

where $<U_{water+ion+framework}>$ and $<U_{ion+framework}>$ are the respective mean potential energies while n is the total number of water molecules in the system. These values are compiled in the second two rows of Table 3. For comparison purposes, the data can be separated into four distinct types: CLI with alkali ions (CLI_{mono}), CLI with alkaline earth ions (CLI_{di}), HEU with alkali ions (HEU_{mono}), and HEU with alkaline earth ions (HEU_{di}). Each of these series shows that larger ions have less exothermic hydration enthalpies associated with the zeolite, and follow the trend $Li^+ > Na^+ > K^+ > Rb^+ > Cs^+$ for the alkalis and $Mg^{2+} >> Ca^{2+} > Sr^{2+} > Ba^{2+}$ for the alkaline earths. In addition, the zeolite hydration enthalpies for the alkaline earth series are generally stronger than their counterparts in the alkali series. However, when we compare the hydration enthalpies for identical ions in the CLI versus HEU systems, we see some distinct differences. In the alkali series, the more-charged HEU zeolite has more exothermic hydration enthalpies over the CLI system. This suggests that increasing the charge of the zeolite framework (by decreasing the Si/Al ratio) does indeed have an impact on the overall hydration enthalpy of the zeolite. However, when we examine the alkaline earth series we see this trend is completely inverted with the less-charged CLI zeolite having larger exothermic hydration enthalpies. When both observations are considered, the simulation data indicate that increasing ion charge density has a more significant impact on the overall hydration enthalpy than increasing charge on the zeolite

framework itself. This is consistent with the calculated Ion-O_{Water} distances where there are equivalent bond lengths across the entire alkali ion series regardless of the surrounding zeolite environment.

In the divalent HEU series we observe increased coordinating distances between the ion and the water oxygen (Ion-O_{Water}) whereas the CLI_{di} series shows decreased distances when compared against our bulk solvation results. Interestingly, the data for the CLI_{di} series universally deviate to shorter ion-water distances relative to the bulk solvation results while the entire HEU series shows increased bond distances with the exception of Mg^{2+}.

This can be rationalized by consideration of the overall charge on the zeolite framework. For example, in the CLI_{di} series the framework has a lower negative charge and therefore has less influence on the Ion-O_{Water} bond distances and therefore the ion-water interactions are dominant (i.e. short ion-water distances). Conversely, in the HEU system the framework has a greater negative charge and the ion-water interactions are subsequently disrupted by stronger ion-zeolite interactions at the charge deficient Al sites which subsequently results in weaker ion-water interactions (i.e. greater ion-water distances).

Coordination Environments

Analysis of the individual ion coordination environments focuses on the first coordination sphere. The coordination environments are detailed by accounting for contributions of $O_{Framework}$ and O_{Water} to the first coordination sphere of the ions in either CLI or the more negatively-charged HEU framework (Table 5). These contribution values are averaged over all ions within the 20-unit cell model and not each ion individually. As before, the data are separated into four groups (CLI_{mono}, CLI_{di} HEU_{mono}, and HEU_{di}) for comparison purposes. There is good consistency between the monovalent series and the calculated solvation values for the coordination numbers of Li^+, Rb^+, and Cs^+ in bulk water. In either zeolite, the coordination environment of Na^+ appears lowered while those of K^+ are elevated. Likewise, in the divalent series the coordination numbers for Mg^{2+} are close to the accepted value of six across all calculations, as is Ca^{2+} in CLI. In Sr- and Ba-CLI, the calculated ion coordination numbers are somewhat lower when compared against the reference solvation calculation. However, the HEU_{di} series shows significantly higher coordination numbers for Ca^{2+}, Sr^{2+}, and Ba^{2+} than expected from the reference. Further analysis of the simulation data indicates that the $O_{Framework}$ contribution to the first coordination sphere of any given ion is increased in the Heulandite models. The increased $O_{Framework}$ contribution appears to systematically lower the contribution of O_{Water} to a small degree in the monovalent cases, and more extensively in the divalent cases. Simulation studies indicate that the level of contribution is largely determined by electrostatic considerations. Heulandite has a greater number of charge deficient Al sites (a lower Si/Al ratio) than clinoptilolite, which increases the overall negative charge of the framework, specifically on the neighboring $O_{Framework}$ sites. The effect is an increase in the interaction between the ion and zeolite. This evidence suggests a significant link between charge density (ion or framework) and the extent of ion hydration.

Power Spectra and Libration Edge

The vibrational power spectrum of each hydrated ion-zeolite pair was calculated to study the *inter*molecular interactions of water, in particular the librational (rotational) region of the

spectrum which occurs from 300 to 1100 cm^{-1}. On a molecular level, the broad peak(s) in this region of the spectrum have non-zero angular momentum components which are commonly referred to as the 'normal' wagging, twisting, and bending modes of water. In cases where water is heavily restricted or isolated (through hydrogen bonding or sterics), these modes can become pronounced and are readily observed through IINS experiments.[50,53] However, despite significant efforts, their exact assignment (in terms of discrete wagging, twisting, and bending) is still somewhat speculative because changes in local environment can have dramatic effects on peak positions, widths, and intensities. Generally though, frequency increases and peak width decreases as rotational restrictions are increased through hydrogen bonding or related steric effects. Additionally, the rotational modes are quite low in energy so thermal contributions result in extensive peak broadening which often requires IINS experiments to routinely be performed at 10K. In cases of heavily hydrated materials, the libration modes are not discrete due to the many different co-existing water configurations. This results in a confluence of discrete wagging, twisting, and bending modes, to form a single extremely broad (~500 cm^{-1}) feature which renders most data sets very difficult to interpret. Furthermore, because deconvolution of such broad features into individual components has questionable accuracy, the leading edge, often referred to as the librational edge, is commonly (Figure 2) reported in literature.
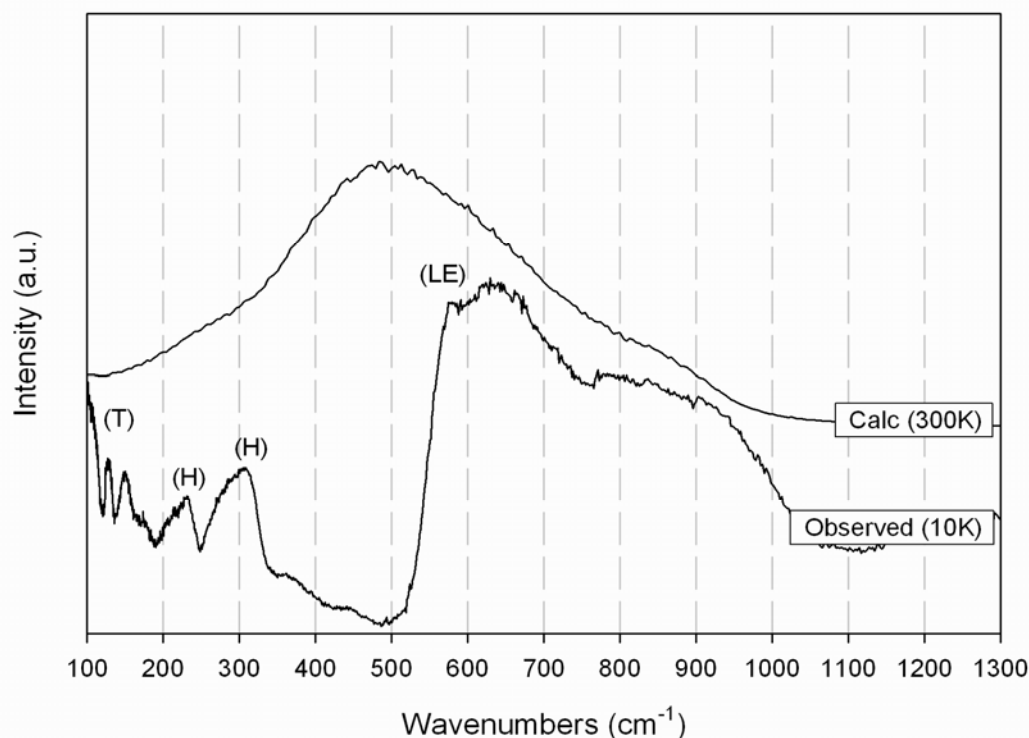
Figure 2. The upper plot is the calculated power spectrum of liquid water at 300 K. The lower plot is the observed IINS spectrum for Ice Ih at 10K.[52] LE: librational edge, H: hydrogen-bond bending and stretching, T: translational modes.[53] (1 cm^{-1} = 0.1240 meV).

The power spectra of confined water in each ion-zeolite system at 300K was calculated and illustrated in Figure 3. Water libration data of the monovalent (upper) versus divalent (lower)

ion effects in the clinoptilolite series are compared against librational data from the heulandite series (monovalents and divalents). Comparison across the monovalent series (Figure 3, upper left and right) shows strikingly similar power spectra (on a per ion basis) and nearly identical trends in libration shifts which increase frequency as a function of decreasing ion charge density ($Li^+ < Na^+ < K^+ < Rb^+ < Cs^+$). Comparison across the divalent series (Figure 3, lower left and right) reveals a completely different trend for the CLI series versus the HEU series. In the CLI_{di} series, a shift to lower frequency as a function of increasing ion charge density ($Ba^{2+} < Sr^{2+} < Ca^{2+} < Mg^{2+}$) is observed. However in the HEU_{di} series, a slightly increasing librational frequencies as ion charge density decreases ($Mg^{2+} < Ca^{2+} < Sr^{2+} < Ba^{2+}$) is observed. Within the CLI series (Figure 3, upper and lower left) opposite trends in the libration shifts are observed. CLI_{mono} shows an increasing trend while CLI_{di} shows a decreasing trend in frequency shifts as a function of the ion charge densities. Within the HEU series (Figure 3, upper and lower right) a similar trend of librational shifts to higher frequencies as a function of decreasing ion charge density is observed, albeit with a smaller magnitude than the HEU_{di} series.
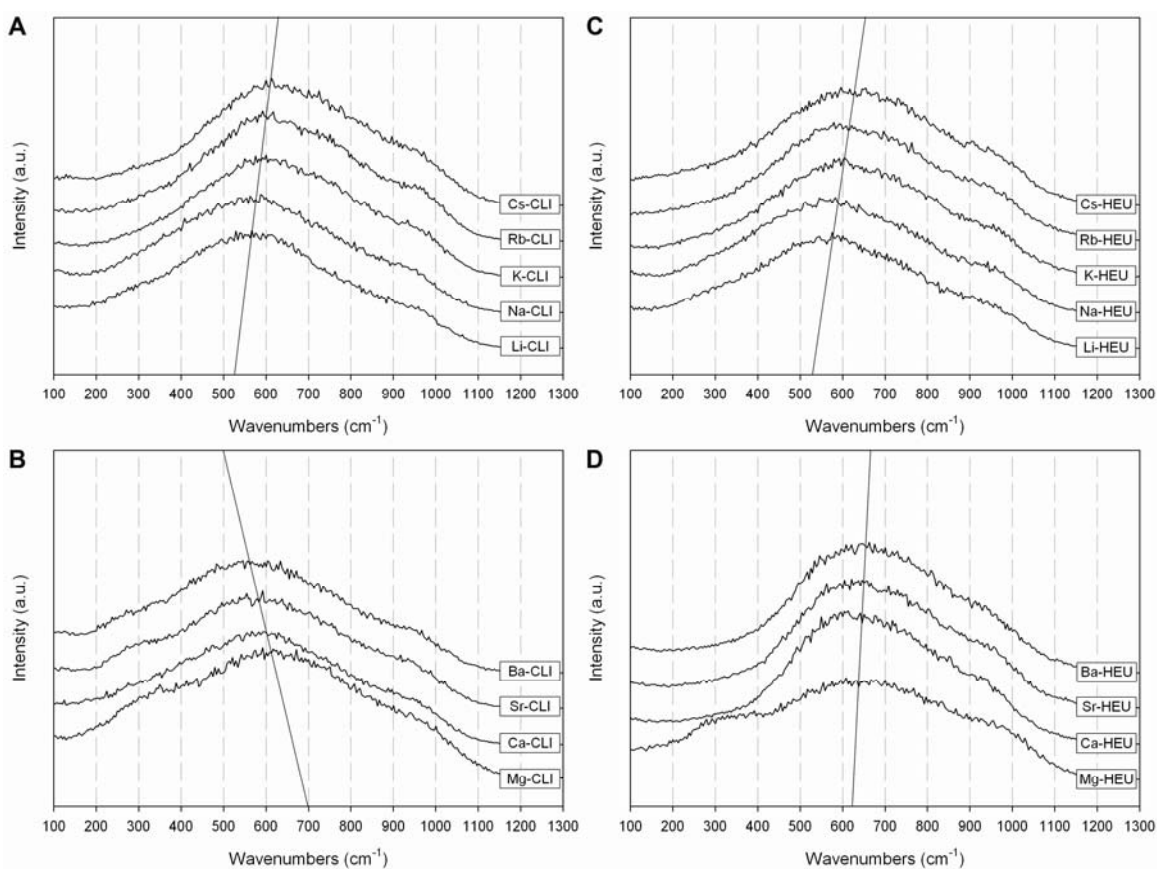
Figure 3. Librational region of the power spectra for water at 300 K confined in: (A) clinoptilolite with alkali ions, (B) clinoptilolite with alkaline earth ions, (C) heulandite with alkali ions, and (D) heulandite with alkaline earth ions. Lines indicate the general trend in the shift in peak positions.

Further examination of the libration shifts (Figure 4) clearly indicates that the rotations of nano-confined water in a charged zeolite are affected by both the cationic charge density and the anionic field strength of the zeolite itself. In the upper Figure 4, the shifts are higher in magnitude for the more negatively-charged heulandite which indicates that the greater

233

electrostatic field of the zeolite is producing more restricted rotations. This effect becomes more pronounced with decreasing cationic charge density. In the lower Figure 4, the alkaline earth series exhibits the same trend for the heulandite system. However, the trend starts at higher initial wavenumber indicating that the higher cationic field strength is further restricting rotational motion of confined water. Finally, the alkaline earth clinoptilolite series (lower Figure 4) exhibits a unique trend when compared against the others. Here the rotational motion of the confined water increases (as indicated by decreasing wavenumbers) with decreasing charge density. The explanation of this trend remains speculative, however the data suggest that it arises from a shift in ion-water-zeolite equilibria towards the stronger ion-water interactions over the diminished ion-zeolite or zeolite-water interactions. Another mitigating factor to consider in this explanation is the contributions of water-water and water-zeolite interactions in pores where there are no or very few ions present (i.e. alkaline earth clinoptilolite).
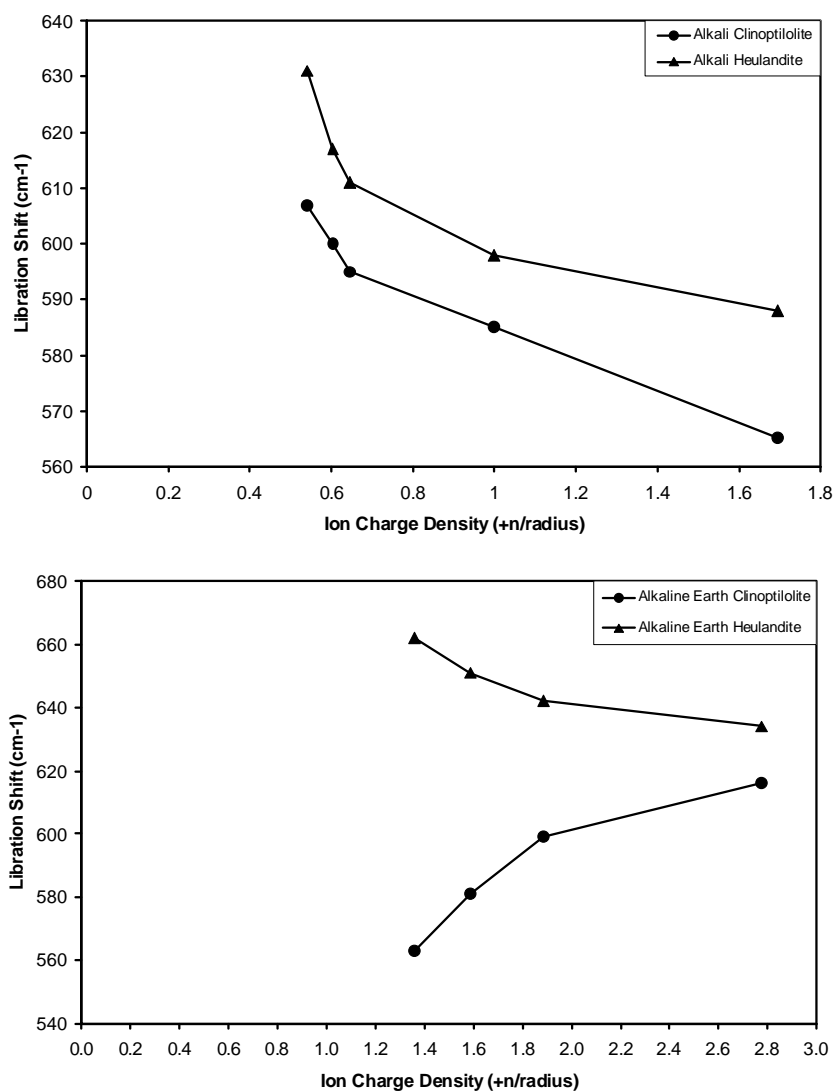
Figure 4. Librational (cm^{-1}) shifts of the alkali (upper) and alkaline earth (lower) series versus ion charge density. Clinoptilolite data represented by filled circles and heulandite data represented by filled triangles.

234

The cumulative interpretation of the power spectra suggests several key elements affecting the dynamical behavior of nanoconfined water. First, both the cation charge density and the anionic field strength (i.e. Si/Al ratio) have significant impact on the dynamics. Second, the balance between cation charge density and framework field strength has a marked impact on the librational signatures of a given zeolite system. The data clearly show that alteration of the ion-water-zeolite equilibria conditions changes the dynamical intermolecular behavior of nanoconfined water and results in different solvating environments for cations within a negatively-charged zeolitic pore.

Conclusions

We have examined the complete alkali and alkaline earth series of cation variants of clinoptilolite (Si/Al=5) and heulandite (Si/Al=3.5) using large scale molecular dynamics (MD) utilizing a flexible SPC water and aluminosilicate force field. Hydration enthalpies, radial distribution functions, and local ion coordination environments demonstrate the energetic and structural influence of zeolite electrostatic fields (Si/Al ratios). These contributions to the dynamic intermolecular behavior of nanoconfined water are manifested in librational region of the power spectra. Correlation of these data confirm the importance of ion-zeolite, ion-water and, water-zeolite equilibria on the rotational behavior of water. Analysis of these data clearly indicate that charge density of extra-framework cations have the greatest influence on librational motions, while the anionic charge of the framework (i.e. Si/Al ratios) has a lesser impact. The combined influence of these two variables provides a basic foundation to understand the influence of cation charge density and anionic field strength, and the delicate balance between these electrostatic fields. Furthermore, the modifications of the ion-water-zeolite equilibria conditions changes the intermolecular behavior of nanoconfined water, which is manifested through shifts in the libration (rotational) region of the power spectra. Future investigation necessarily includes (1) comparison of our simulated power spectra against the observed experimental IINS data,[52] (2) thermodynamic studies of ion-exchange and hydration processes, and (3) structural analysis of hydrogen-bonded water networks in the zeolite systems as a function of cation identity and degree of Si/Al substitution.

References

1. Klafter, J.; Blumen, A.; Drake, J. M. in Relaxation and Diffusion in Restricted Geometry; Klafter, J.; Drake, J. M., Eds.; New York: Wiley, 1989.

2. Rupley, J. A.; Careri, G.; Adv. Protein Chem. 1991, 41, 37.

3. Arndt, M.; Stannarius, R.; Gorbatschow, W.; Kremer, F. Phys. Rev. E: Stat., Nonlinear, Soft Matter 1996, 54, 5377.

4. Proceedings of the First International Workshop of Dynamics in Confinement; Frick, B.; Zorn, R.; Buttner, H., Eds.; EDP Science: Les Ulis, France, 2000.

5. Rovere, M. In J. Phys. Condens. Matter.- Special Section of Water in Confined Geometries 2004, 16, S5297-S5470. (a) Crupi, V.; Majolino, D.; Venuti, V. J. Phys. Condens. Matter.

2004, 16, S5297. (b) Swenson, J. J. Phys. Condens. Matter. 2004, 16, S5317. (c) Puibasset, J.; Pellenq R. J. M. J. Phys. Condens. Matter. 2004, 16, S5329. (d)Brovchenko, I.; Geiger, A.; Oleinikova, A. J. Phys. Condens. Matter. 2004, 16, S5345. (e) Zangi, R. J. Phys. Condens. Matter. 2004, 16, S5371. (f) Jedlovsky, P. J. Phys. Condens. Matter. 2004, 16, S5389. (g) Liu, L.; Faraone, A.; Mou, C. Y.; Yen, C. W. Chen, S. H. J. Phys. Condens. Matter. 2004, 16, S5403. (h) Klein, J.; Raviv, U.; Perkin, S.; Kampf, N.; Chai, L.; Giasson, S. J. Phys. Condens. Matter. 2004, 16, S5437. (i) Webber, B.; Dore, J. J. Phys. Condens. Matter. 2004, 16, S5449.

6. Angell, C. A. in Water: A Comprehensive Treatise; Franks, F. Ed.; Plenum Press; New York, 1981.

7. Mizota, T.; satake, N.; Fujiwara, K.; Nakayama, N. Steam, Water, and Hydrothermal Systems: Physics, and Chemistry Meetings the Needs of Indutry, Proceedings of the 13th ICPWS; Tremaine, P. R.; Hill, P. G.; Irish, D. E.; Balakrishnan, P. V.; Eds.; NCR Research Press: Ottawa, Ontario, 2000.

8. Beta, I. A.; Bohling, H.; Hunger, B. Phys. Chem. Chem. Phys., 2004, 6, 1975.

9. Jobic, H.; Tuel, A.; Krossner, M.; Sauer, J. J. Phys. Chem. 1996, 100, 19545.

10. Crupi, V.; Majolino, D.; Migliardo, P.; Venuti, V.; Wanderlingh, U.; Mizota, T.; Telling, M. *J. Phys. Chem. B.* 2004, **108**, 4314.

11. Line, C. M. B.; Kearley, G. J. *J. Chem. Phys.* 2000, **112**, 9058.

12. Line, C. M. B.; Kearley, G. J. *Chem. Phys.* 1998, **234**, 207.

13. Cronstedt, A. F. Kong Vetenskaps Acad. Handl. Stockholm 1756, **12**, 120.

14. a) Smith, J. V. *Mineral. Soc. Am. Spec. Pap.* 1963, **1**, 281. (b) Smith, J. V., in *Zeolite Chemistry and Catalysis* (Edited by J. A. Rabo), Vol. 171, A.C.S. Series (1976). (c) Breck, D. W. *Zeolite Molecular Sieves. Wiley,* New York (1974).

15. Higgins, F. M.; de Leeuw, N. H.; Parker, S. C. *J. Mat. Chem.* 2002, **12**, 124.

16. Soper, A. K. in *Hydrogen Bond Network, NATO ASI Series C: Mathematical and Physical Science*; Bellissent-Funel, Dore, J. C., Eds.; Kluwer Academic, Dordecht, 1994.

17. Wiggins, P. M. *Prog. Poly. Sci.* 1988, **13**, 1.

18. Crupi, V.; Majolino, D.; Migliardo, P.; Venuti, V.; Wanderlingh, U.; Mizota, T.; Telling, M. *J. Phys. Chem. B.* 2002, **106**, 10884.

19. Bellissent-Funel, M. C.; Dorbez-Sridi, R.; Bosio, L. *J. Chem. Phys.* 1996, **104**, 1.

20. Gallo, P.; Ricci, M. A.; Rovere, M.; *J. Chem. Phys.* 2002, **116**, 342.

21. Gallo, P.; Rapinesi, M.; Rovere, M.; *J. Chem. Phys.* 2002, **117**, 369.

22. Murad, S.; Jia, W.; Krishnamurthy, M. *Mol. Phys.* 2004, **102**, 2103.

23. Demontis, P.; Stara, G.; Suffritti, G. B. *J. Chem. Phys.* 2004, **120**, 9233.

24. Shirono, K.; Endo, A.; Daiguji, H. *J. Phys. Chem. B* 2005, **109**, 3446.

25. Nenoff, T. M.; Ockwig, N. W.; Cygan, R. T.; Alam, T. M.; Leung, K.; Pless, J. D.; Xu, H.; Hartl, M. A.; Daemen, L. L. *J. Phys. Chem. C.* 2007, **111**, 13212.

26. Crupi, V.; Majolino, D.; Migliardo, P.; Venuti, V.; Bellissent-Funel, M. C. *Mol. Phys.* 2003, **101**, 3323.

27. Fourzi, A.; Dorbez-Sridi, R.; Oumezzine, M. *J. Chem. Phys.* 2002, **116**, 791.

28. Kolesnikov, A. I.; Li, J. C. *Physica B* 1997, **234**, 34 and references therein.

29. Bellissent-Funel, M. C.; Lal, J.; Bosio, L. *J. Chem. Phys.* 1993, **98**, 4246.

30. Crupi, V.; Majolino, D.; Migliardo, P.; Venuti, V.; Diaonoux, A. J. *Appl. Phys., A Mater. Sci. Process. 2002*, **74**, S555.

31. Venturini, F.; Gallo, P.; Ricci, M. A.; Bizzari, A. R.; Cannistraro, S. *J. Chem. Phys.* 2001, **114**, 10010.

32. Crupi, V.; Magazu, S.; Maisano, G.; Majolino, D.; Migliardo, P. *J. Mol. Liq.* 1999, **80**, 133.

33. Kaatze, U.; Uhlendorf, V.; *Z. Phys. Chem. (N. F.)* 1981, **126**, 151.

34. Polnazek, C. F.; Bryant, R. G.; *J. Chem. Phys.* 1984, **81**, 4038.

35. (a) Jackson, R., A.; Catlow, C. R. A. *Mol. Sim.* 1988, **1**, 207. (b) Ooms, G.; van Santen, R. A.; den Ouden, C. J. J.; Jackson, R. A.; Catlow, C. R. A. *J. Phys. Chem.* 1988, **92**, 4462. (c) Aloisi, G.; Barnes, P.; Catlow, C. R. A.; Jackson, R. A.; Richards, A. J. *J. Chem. Phys.* 1990, **93**, 3573. (d) Channon, Y. M.; Catlow, C. R. A.; Gorman, A. M.; Jackson, R. A. *J. Phys. Chem. B.* 1998, **102**, 4045. (e) Johnson, M.; O'Connor, D.; Barnes, P.; Catlow, C. R. A; Owens, S. L.; Sankar, G.; Bell, R.; Teat, S. J.; Stephenson, R. *J. Phys. Chem. B.* 2003, **107**, 942.

36. (a) Moloy, E. C.; Cygan, R. T.; Bonhomme, F.; Teter, D. M.; Navrotsky, A. *Chem. Mater.* 2004, **16**, 2121. (b) Teleman, O.; Jonsson, B.; Engstrom, S. *Mol. Phys.* 1987, **60**, 193.

37. Lennard-Jones, J. E. Cohesion. *Proceedings of the Physical Society* 1931, **43**, 461.

38. Fraser, L. M.; Foulkes, W. M. C.; Rajagopal, G.; Needs, R. J.; Kenny, S.; Williamson, A. *J. Phys. Rev. B* 1996, **53**, 1814.

39. (a) Berendsen, H. J. C.; Postma, J. P. M.; van Gunsteren, W. F.; Hermans, J. In *Intermolecular Forces*; Pullmann, B., Ed.; Reidel: Dordrecht, 1981; p 331. (b) Robinson, G. W.; Zhu, S.-B.; Singh, S.; Evans, M. W. In *Water in Biology, Chemistry and Physics: Experimental Overviews and Computational Methodologies*, (World Scientific, Singapore, 1996).

40. (a) Smith, D. E.; Dang, L. X. *J. Chem. Phys.* 1994, **100**, 3757. (b) Aqvist, J. *H. Phys. Chem.* 1990, **94**, 8021. (c) Koneshan, S.; Rasaiah, J. C.; Lynden-Bell, R. M.; Lee, S. H. *J. Phys. Chem. B.* , 1998, **102**, 4193. (d) Palmer, B. J.; Pfund, D. M.; Fulton, J. L. *J. Phys. Chem.* 1996, **100**, 13393.

41. Halgren, T. A. *J. Am. Chem. Soc.* 1992, **114**, 7827.

42. Clinoptilolite: $a = 17.66$ (7), $b = 17.92$ (5), $c = 7.40$ (1) Å, and $\beta = 116.43$ (14) °. Heulandite: $a = 17.62$ (24), $b = 17.92$ (21), $c = 7.46$ (13) Å, and $\beta = 116.34$ (53)°.

43. (a) Plimpton, S. J. *J. Comp. Phys.* 1995, **117**, 1. (b) Plimpton, S. J.; Pollock, R.; Stevens, M. *Proceedings of the English SIAM Conference on Parallel Processing for Scientific Computing*; Minneapolis, MN, USA, 1997. (c) the LAMMPS code is freely available from http://lammps.sandia.gov.

44. Winkler, B.; Pickard, C. J.; Milman, V. *Chem. Phys. Lett.* 2002, **362**, 266.

45. Lowenstein, W. *Am. Mineral.* 1954, **39**, 92.

46. Yang, P.; Armbruster, T. *J. Solid State Chem.* 1996, **123**, 140.

47. (a) Implemented through the 'Amorphous Cell' module of Materials Studio. (b) Forrest, B. M.; Suter, U. W. *J. Chem. Phys.* 1994, **101**, 2616 and references therein.

48. (a) Nose, S. *Mol. Phys.* 1984, **52**, 255. (b) Hoover, W. G. *Phys. Rev. A.* 1985, **31**, 1695. (c) Allen, M. P. and Tildesley, *Computer Simulation of Liquids,* Oxford University Press, New York, 1987.

49. (a) Li, Y.; Lin, S.-T.; Goddard, W. A., III *J. Am. Chem. Soc.* 2004, **126**, 1872. (b) Maurin, G.; Bell, R. G.; Devautour, S.; Henn, F.; Giuntini, J. C. *Phys. Chem. Chem. Phys.* 2004, **6**, 182. (c) Praprotnik, M.; Janezic, D.; Mavri, J. *J. Chem. Phys. A* 2004, **108**, 11056.

50. Li, J. C. *J. Chem. Phys.* 1996, **105**, 6733.

51. Ohtaki, H.; Radnai, T. *Chem. Rev.* 1993, **93**, 1157.

52. Data collected at LANL-LANSCE on the Filter Difference Spectrometer (FDS) beamline.

53. Li, J. C.; Ross, D. K. *Nature* 1993, **365**, 327.

Incoherent Inelastic Neutron Scattering Studies of Nanoconfined Water in Clinoptilolite and Heulandite Zeolites

Abstract

In a continued effort studying the role of water in ion exchange process of zeolites, a synthetic series of alkali and alkaline earth cation variants (Na^+, K^+, Rb^+, Mg^{2+}, and Ca^{2+}) of the hydrated clinoptilolite (Si/Al $\approx$ 5) and heulandite (Si/Al $\approx$ 3.5) aluminosilicate zeolites is examined by incoherent inelastic neutron scattering (IINS). The low-frequency librational modes of water reveal the impact of nanoconfinement and framework charge within these isostructural aluminosilicate structures. The experimental IINS spectra are correlated with power spectra derived through molecular dynamics simulations. The impact of ion-zeolite, ion-water, and water-zeolite interactions on the hindered rotations (librations) of water molecules is explored as a function of Si/Al substitution, cation identity, and sub-nanometer confinement. The results indicate that electrostatic charge on the overall framework has a stronger influence than charge density of a given ion in the channel and that these effects become more pronounced as the charge difference between ion and zeolite is increased.

Introduction

Currently, the structural and dynamical behavior of bulk water is relatively well understood and documented.[1-8] However, there are comparatively few efforts focused on the behavior of water under Ångstrom-level confinement. The study of nanoconfined molecular species is a surprisingly difficult topic which relies on a variety of experimental methods and continues to challenge our theoretical understanding.[9-16] Nanoconfined water is arguably the most important molecular species in porous materials because of its tremendous impact across many industrially significant and interdisciplinary processes. It is reasonable to assume that the properties of confined and bulk water are similar. However, there are a growing number of reports which clearly indicate that such assumptions should be reconsidered.[17] The molecular structure of water is deceptively simple while the collective behavior of these species is quite complex, especially under nanoconfinement. It remains a major challenge for current scientific understanding and levels of theory.[18] Quantification of confined molecular behavior is the foundation necessary to understand macroscopic phenomena and ultimately provides the basis for understanding, modifying, and directing important macroscopic observables and physical properties. There are many porous systems of interest including zeolites, which are perhaps the most well studied within the context of confined water.[19-26]

Zeolites are aluminosilicate framework type minerals which commonly contain water and may include a wide variety of charge-compensating and exchangeable ions. These minerals are built up from corner sharing tetrahedral units (where TO_4 is either Si or Al) with a generalized formula of $X_{x/n}[(AlO_2)_x(SiO_2)_y]$ where X is the charge balancing counterion, n is the charge of the counter-ion, x is the number of charge-deficient alumina sites, and y is the number of charge-neutral silica sites. Each AlO_4 tetrahedral substitution imparts a framework charge of -1 that must be balanced by the presence of additional extra-framework cations ($X^{n+}_{x/n}$). These cations

occupy cavities within the zeolite structure and are generally exchangeable. Progressive connection of adjacent TO_4 units through bridging oxygens gives rise to topological and compositional variants. The wide angular flexibility of the T-O-T linkages (~100º to ~180º) results in a surprising range of channel or pore dimensions. Typically the internal voids, channels, pores, and/or cavities of zeolites are well-defined in the nanometer range from 4 to13 Å.[27] The molecular species trapped within a zeolite framework are not covalently bonded to the aluminosilicate architecture, and, therefore, possess significant mobility and may be exchanged or removed from the structure without disrupting or destroying the surrounding structure.

The multiple intramolecular vibrational and intermolecular librational/rotational modes of water give it distinct spectroscopic signatures. The *intramolecular* bending and stretching modes commonly occur at ~1600 cm^{-1} and 3300-3700 cm^{-1}, respectively, and the *intermolecular* librational/rotational modes occur from 300 to 1100 cm^{-1}. The low frequency (librational) modes are extremely sensitive to localized hydrogen bonding and steric restrictions from nanoscale confinement and consequently have more pronounced spectroscopic shifts. Thus, librational/rotational spectroscopy is a vital diagnostic tool for examining water behavior within porous media.

Additionally, the structural and dynamical properties of water in different localized environments have been probed using a wide variety of theoretical and experimental approaches.[22,25,26,28-31] Among the most commonly employed methods to probe the intra- and intermolecular behavior of water are: Raman scattering,[32] microwave and infrared spectroscopies,[33] nuclear magnetic resonance (NMR),[34,40] molecular dynamics (MD),[35-40] X-ray diffraction,[41] neutron diffraction,[42] and incoherent quasi-elastic and incoherent inelastic neutron scattering (IQENS and IINS, respectively).[40,43-46] There is an impressive body of literature on the role of water in thermodynamic, dynamical, and structural processes and the properties which have been probed through a variety of, often complementary, methods. Although these methods and studies provide internally consistent results, there are many conflicting studies and conclusions which are fueling the continuous revision of our theoretical understanding surrounding the behavior of nanoconfined water.

The complex interactions and equilibria which exist between four distinct interactions control the dynamic behavior of nanoconfined water. In no particular order, these are: (1) H_2O-H_2O; (2) Ion-H_2O; (3) H_2O-Framework; and (4) Ion-Framework. Although Ion-Ion electrostatic repulsions may have an impact by separation of localized water attractors, this effect is essentially negligible due to charge screening of the surrounding zeolite framework. Other studies on occluded water have presented evidence for the presence of ice-like water in small pore zeolitic systems with highly constrained waters exhibiting ion-H_2O and H_2O-framework interactions.[9-11,40] Furthermore, hydration and dehydration processes, cation mobility, and framework stability have been studied in mesoporous systems.[47] However, the heulandite and clinoptilolite systems are considered relatively large pored zeolites. Therefore, we can only consider water-water interactions a minor contribution. Our present study focuses on the librational (hindered rotational motion) behavior of water rather than hydration and dehydration processes, cation mobility, or framework stability which have been previously investigated for a variety of mesoporous materials by several other research teams.[48]

In this contribution, we probe changes in the librational behavior of confined water molecules in a series of synthetic larger pored heulandite and clinoptilolite zeolites through low temperature IINS studies. This is an experimental extension to complement and validate our previous MD simulations.[12] The two zeolites were specifically targeted to avoid the challenging topic of zeolite structural variations and their impact on H_2O interactions, but still address several fundamental questions relating to the role of framework charge and cation type on confined water dynamics. Heulandite and clinoptilolite are isostructural crystalline frameworks (both with the HEU framework type) with varying Si/Al ratios ranging from 2.5 to 6. Those with Si/Al ratios < 4 are defined as heulandite (HEU), while those with ratios > 4 are referred to as clinoptilolite (CLI). This framework is composed of three distinct types of channels—one defined by 10T rings and two others by 8T rings—which are interconnected to form a layered array of channels. One of the 8T channels (3.6 x 4.6 Å) and the 10T channel (3.1 x 7.5 Å) run parallel to the *c*-axis. Additionally, an interconnected plane of channels is formed by the remaining 8T channel (2.8 x 4.7 Å) which runs parallel to the *a*-axis and intersects the first two channels. Both materials crystallize in the monoclinic space group *C2/m* with slightly different unit cell parameters.[49]

Experimental

Chemical sources were aluminum hydroxide, USP, Pfaltz and Bauer, Inc.; Ludox LS colloidal silica 30% (w/w) silica, sodium hydroxide, potassium hydroxide, rubidium hydroxide (50 % aqueous solution), magnesium carbonate, and calcium carbonate from Aldrich Chemical Corporation.

Synthetic preparations of the zeolite phases were adapted from those reported by Zhao, Szostak, and Kevan.[50] Crystallizations were carried out in Teflon-lined stainless steel autoclaves under autogeneous pressure from a gel. A typical synthesis yields 8.27g of good quality crystal crystalline powder. Dried aluminum hydroxide ($Al(OH)_3$, 0.78 g) was added to 6 M aqueous solution of sodium hydroxide (3.41g). The mixture was vigorously stirred for 1 hr after which colloidal silica (Ludox LS, 10g) was added. The mixture was stirred for an additional 1 hr and the placed into a Teflon-lined steel autoclave. The autoclave was heated to 145°C at a rate 2°C/minute and held for 156 hours. Reactant molar compositions, reaction conditions, final pH values of the post-synthesis mother liquid, and resulting Si/Al ratios are summarized in Table 1. Sample hydration was performed by placing fully dehydrated samples in a hydration chamber (85ºC, 100% relative humidity) for 6 hours. Thermal gravimetric analysis (TGA) of all samples revealed ~22 water molecules (~90% hydrated) per idealized formula unit (heulandite: $X_8Si_{28}Al_8O_{72} \cdot 24H_2O$ and clinoptilolite: $X_6Si_{30}Al_6O_{72} \cdot 24H_2O$). The potassium endmember of clinoptilolite was produced following the same procedure however using potassium hydroxide rather than sodium hydroxide. The rubidium analog of clinoptilolite was synthesized through the use of commercially available 50 % w/w aqueous rubidium hydroxide rubidium solution. Our initial attempts to synthesize heulandite were quite unsuccessful until 5% w/w of a natural sample (calcium heulandite from the Nasik deposit near Maharashtra, India) was added to the reactions as a nucleating seed material. Phase purity was confirmed by X-ray powder diffraction (XRPD) while Si/Al ratios and composition were determined by scanning electron microscopy energy dispersive spectroscopy (SEM-EDS) and elemental analysis (EA).[51-53]

Table 1. Synthetic parameters for the preparation of alkali and alkali earth members of the clinoptilolite (CLI_{mono} and CLI_{di} respectively) and heulandite (HEU_{mono} and HEU_{di} respectively) series.

Sample	Reactant Composition	Temp (°C)	Time (hr)	pH[b]	Si/Al[c]
Na-CLI	$NaOH/Al(OH)_3/SiO_2/H_2O$ 15 9 50 521	145	156	11.6	5.0
K-CLI	$KOH/Al(OH)_3/SiO_2/H_2O$ 15 9 50 537	185	96	10.1	5.1
Rb-CLI	$RbOH/Al(OH)_3/SiO_2/H_2O$ 15 9 50 593	185	120	10.7	5.4
Mg-CLI	$MgCO_3/Al(OH)_3/SiO_2/H_2O$ 14 9 50 604	205	178	9.9	4.8
Ca-CLI	$CaCO_3/Al(OH)_3/SiO_2/H_2O$ 14 9 50 616	205	180	9.8	4.7
Na-HEU[a]	$NaOH/Al(OH)_3/SiO_2/H_2O$ 18 10 38 616	135	132	11.4	3.7
K-HEU[a]	$KOH/Al(OH)_3/SiO_2/H_2O$ 18 10 38 616	185	90	9.6	3.5
Rb-HEU[a]	$RbOH/Al(OH)_3/SiO_2/H_2O$ 18 10 38 616	185	108	10.1	3.4
Mg-HEU[a]	$MgCO_3/Al(OH)_3/SiO_2/H_2O$ 16 10 45 616	200	172	9.7	3.1
Ca-HEU[a]	$CaCO_3/Al(OH)_3/SiO_2/H_2O$ 16 10 45 616	200	178	9.8	3.3

[a]Required addition of 5 % (w/w) seed crystals of natural heulandite, from the Nasik deposit near Maharashtra, India.
[b]pH of post synthesis mother liquor.
[c]measured by SEM-EDS, ± 5%.

### *Incoherent Inelastic Neutron Scattering (IINS)*

The Filter Difference Spectrometer (FDS) of the Los Alamos Neutron Science Center (LANSCE) is used for vibrational and rotational spectroscopy by incoherent inelastic neutron scattering. The instrument is designed for high count rates using a large three steradian (9848.4 deg.[2]) solid-angle detector.

Neutrons are a unique probe for the study of molecular dynamics in hydrogen containing solids and liquids. In particular, incoherent inelastic neutron scattering is ideally suited for molecular rotational modes because of its sensitivity to *intermolecular* motions relative to the higher frequency *intramolecular* vibrations. Of particular interest for this study are the low frequency librational modes of water molecules which arise from hindered rotations within a given channel. While Si, Al, and O have very low incoherent scattering cross section, ^1H has a very large incoherent neutron scattering cross section (80 barns). On this basis IINS represents the ideal probe for examining the behavior of nanoconfined water in microporous aluminosilicate zeolites. In fact, the *IINS spectrum is completely dominated by the scattering contributions from hydrogen*

with minimal contribution from other species. In addition, nucleus-neutron interactions do not have any of the photon-electron selection rules and therefore all modes are readily observed.

The IINS spectrum of each hydrated zeolite sample was measured to specifically examine the *inter*molecular interactions of water as manifested by changes in the librational (rotational) spectrum which usually occur from 300 to 1100 cm^{-1}. The librational spectrum arises from molecular motions which have a non-zero angular moment component. This produces three distinctly different rotational modes for molecular water (rocking, twisting, and wagging) ranging from 500 to 1000 cm^{-1} which are typically broad and often merge into a single broad feature rendering the discrete rotational modes indistinguishable from one another. The librational modes are highly dependent on the local environment, position, and ordering of water. Sharp librational features are typically observed in cases where water is highly ordered in a crystalline lattice while broadening of the librational signals is a direct consequence of disordered 'bulk-like' water where multiple energetically close configurations coexist and produce a continuum of librational features. Broadening also arises from the Debye-Waller[54] factor, however this is relatively small compared to the intrinsic width of the librational modes.

The confluence of libration modes produces a single extremely broad (~500 cm^{-1}) feature rendering many data sets very difficult to interpret, however, for these data deconvolution with a single coalescence was rigorously fit.[55] In cases where water is heavily restricted or isolated (through hydrogen bonding or related steric effects), these modes can become noticeably sharp, pronounced, and readily observable in IINS experiments.[56,58] Therefore, changes in local environment can have dramatic effects on peak positions, widths, and intensities. Generally, though, frequency increases and peak width decreases as rotational restrictions are increased through hydrogen bonding or steric effects. Despite significant experimental and theoretical efforts, the absolute assignment of discrete wagging, twisting, and rocking modes remains problematic. Often the onset of the librational features, referred to as the librational edge, is the only definitive spectroscopic assignment which is quantified in IINS experiments of ice Ih (Figure 1). However, even merged, the intensities of the soft librational features are significant and can be quantitatively predicted because of the simplicity of neutron-nucleus interactions.[57]
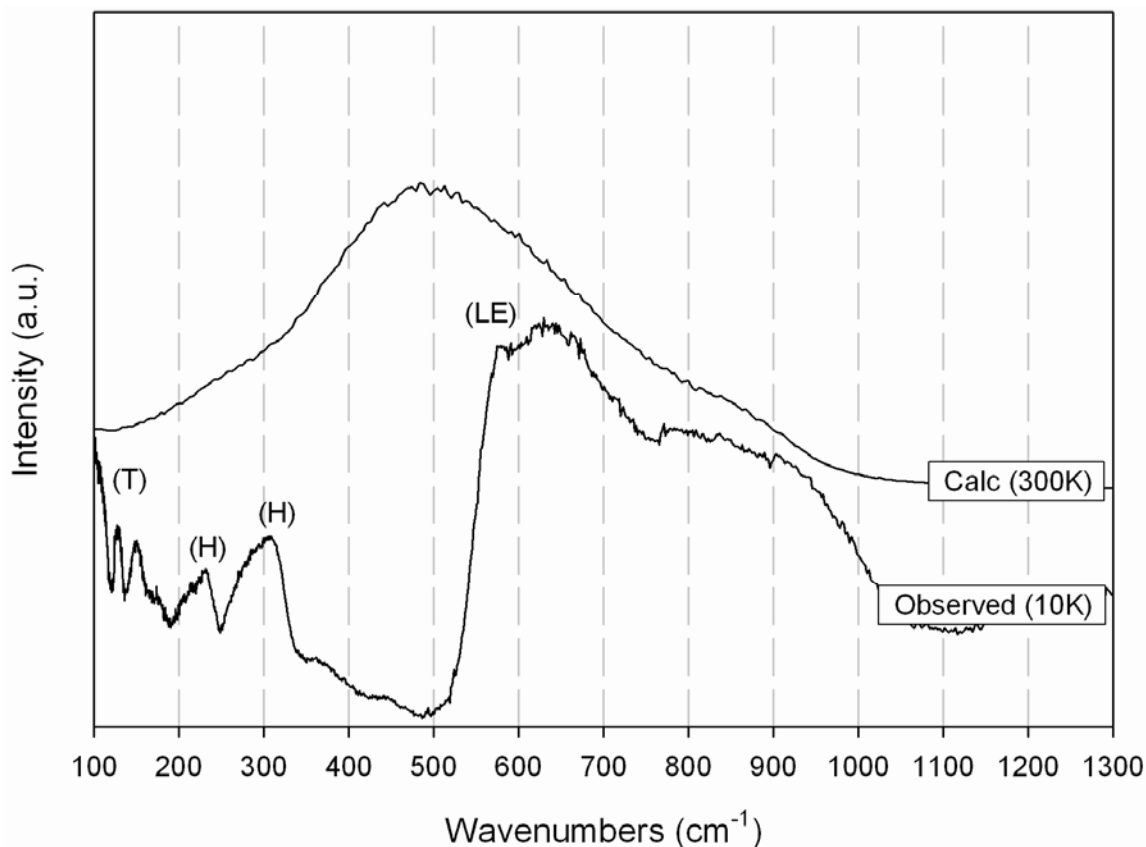
Figure 1. The upper plot denotes the low frequency regions of the power spectrum of liquid water at 300 K derived from MD simulations. The lower plot is the observed IINS spectrum for Ice Ih at 10K. LE: librational edge, H: hydrogen-bond bending and stretching, T: translational modes.[58] ($1 \text{ cm}^{-1} = 0.1240$ meV).

The librational spectra of each ion-zeolite pair (Na^+, K^+, Rb^+, Mg^{2+}, Ca^{2+} of CLI and HEU) were measured at 10 K (Figure 2A-D). The libration IINS spectra for the clinoptilolite series (Figure 2A and 2B, CLI_{mono} and CLI_{di} respectively) are compared, then the heulandite series (Figure 2C and 2D, HEU_{mono} and HEU_{di} respectively) follow by a cross comparison of (1) monovalent series versus the divalent series, and (2) between the observed IINS data and simulated power spectra[12] for each zeolite ion pair.

A
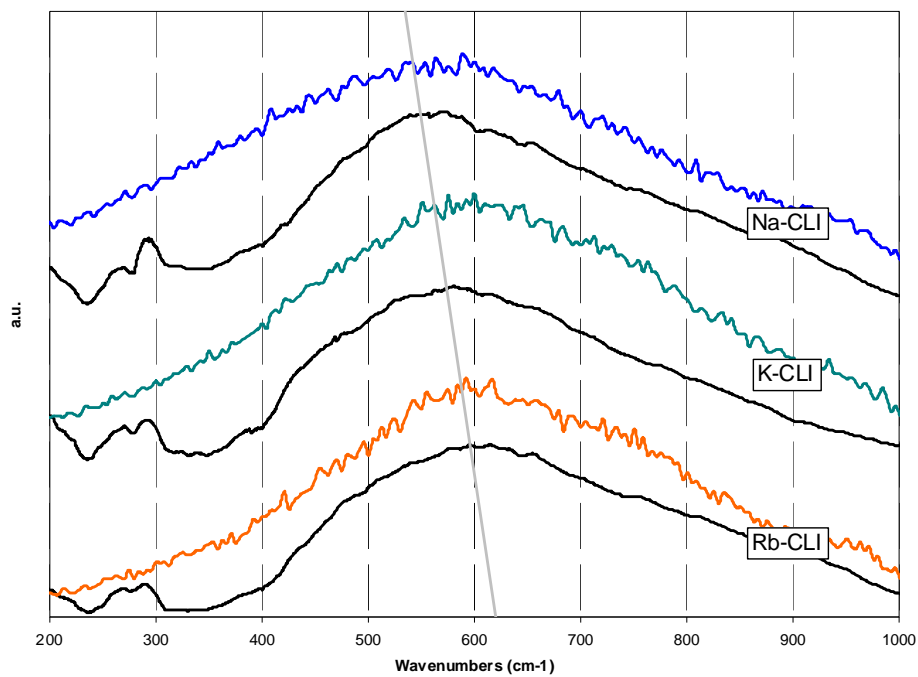
B
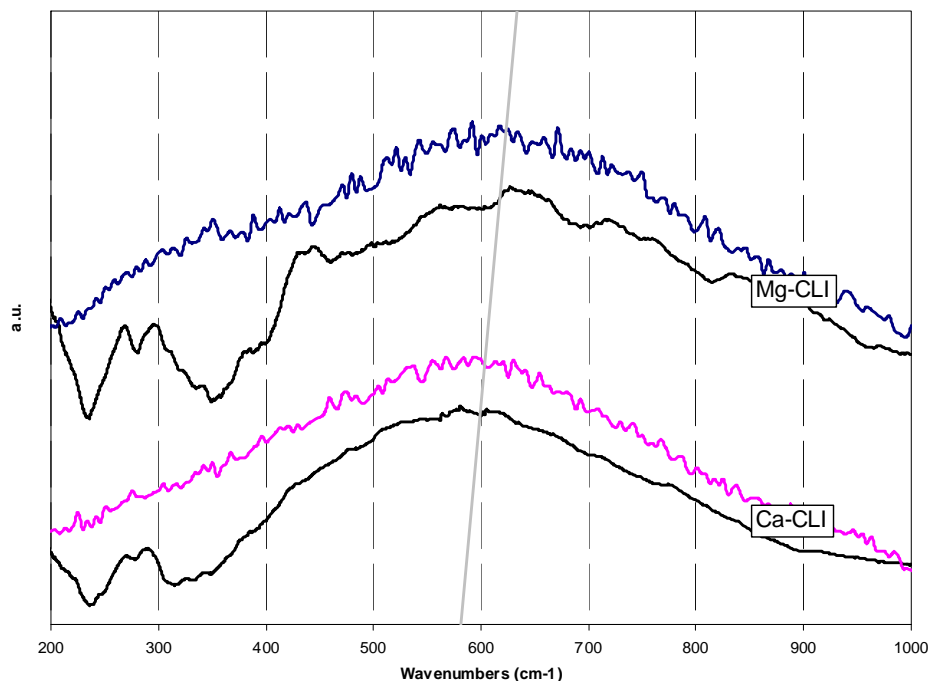
C
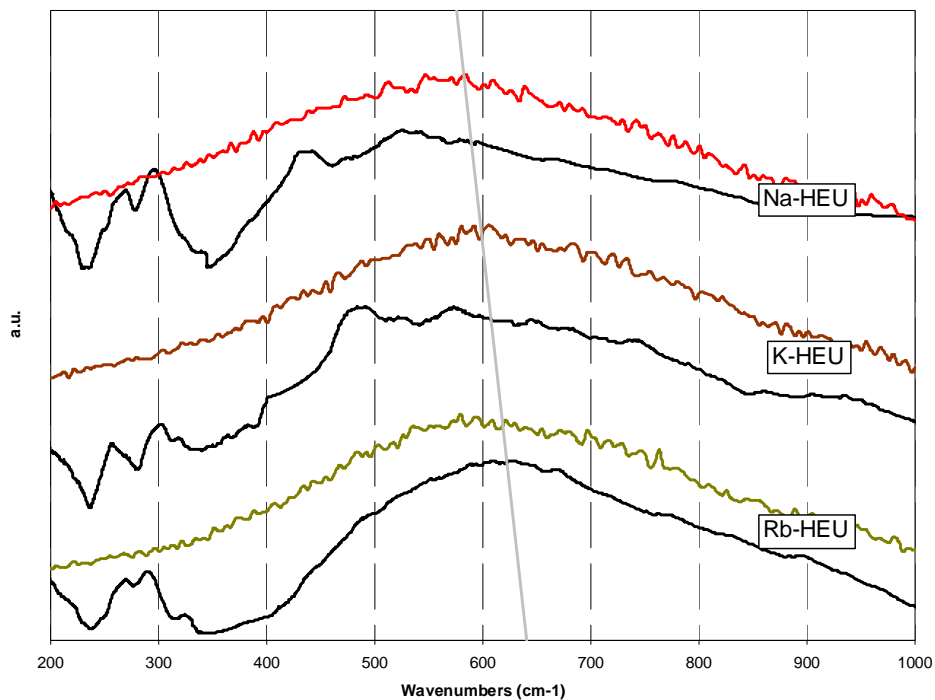
D
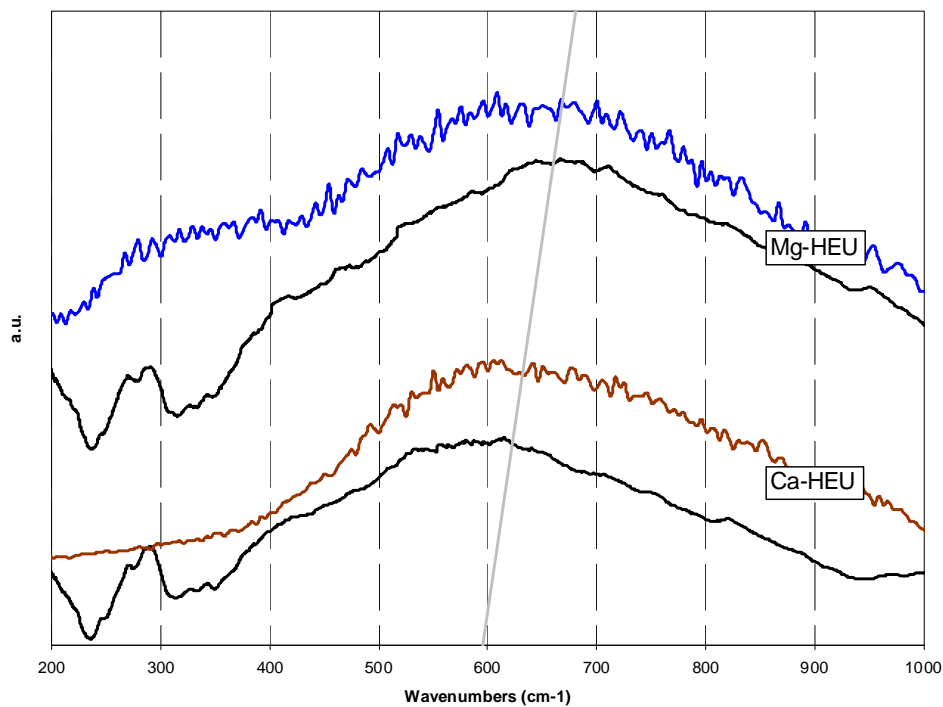
Figure 2. Simulated and measured librational region of the IINS spectra at 10 K confined in: (A) clinoptilolite with alkali ions (CLI_{mono}), (B) clinoptilolite with alkaline earth ions (CLI_{di}), (C) heulandite with alkali ions (HEU_{mono}), and (D) heulandite with alkaline earth ions (HEU_{di}). The simulated data are derived from molecular dynamics trajectories at 300 K. Gray line represents the general trend in each respective data set (values determined through single peak deconvolution[55]).

Each IINS spectrum in the CLI_{mono} series shows a single broad librational feature with no uniquely distinguishable wagging, rocking, or twisting modes. The data shows a rough linear trend in librational shift ranging from 591 cm^{-1} for Na^{+1} to 637 cm^{-1} for Rb^{+1}. This trend corresponds to a shift to higher frequency as the extra framework cation charge density decreases. The IINS spectra of the CLI_{di} series show a single broad librational feature with no uniquely distinguishable wagging, rocking, or twisting modes. The data show a trend in librational shift ranging from 651 cm^{-1} for Mg^{+2} to 633 cm^{-1} for Ca^{+2}. This trend is opposite of that observed for the CLI_{mono}, with shifts to higher frequency observed with increasing extra framework cation charge density.

The IINS spectra for the HEU_{mono} series also show a single broad librational feature with no uniquely identifiable wagging, rocking, or twisting modes. The observed trend (similar to that of CLI_{mono}) in the HEU_{mono} librational data is observed with shifts to higher frequency as a function of charge density decreases on the extra framework cations. Both IINS spectra in the HEU_{di} series show single broad librational features with no discrete wagging, rocking, or twisting modes. In the HEU_{di} series the observed libration peak is shifted to higher frequency as the charge density of the extra framework cation is increased, similar to the trend observed for the CLI_{di} series).

Comparison of the IINS data for the monovalent series (both CLI and HEU) shows nearly equivalent librational spectra (on a per ion basis) and virtually identical trends in librational shifts which increase in frequency as a function of decreasing ion charge density ($Na^{+} < K^{+} < Rb^{+}$) for either zeolite. The IINS data for the divalent endmembers (both CLI and HEU) also shows a significant degree of similarity in overall trend however the HEU_{di} data are shifted to higher overall frequency.

Comparison of the divalent endmembers (Figures 2C and 2D) reveals a significant difference between the trends in power spectra and observed librational spectra for CLI_{di} versus HEU_{di}. In the power spectra of the CLI_{di} system, increasing ion charge density ($Ba^{2+} < Sr^{2+} < Ca^{2+} < Mg^{2+}$) results in a shift of the librational maxima to higher frequency ($Ba^{2+} < Sr^{2+} < Ca^{2+} < Mg^{2+}$).

Correlation and comparison of IINS with MD power spectra
We further examined the trends in the IINS spectra by placing them within the context of our recent MD simulations[12] of nanoconfined water in aluminosilicate zeolites (Figure 3) and the derived power spectra. Although the entire series of cation-substituted zeolites was not experimentally measured, the correspondence of experimental and theoretical data do strongly suggest that trends can be established for librational interpretations and that they are indeed affected by the balance between the strength of zeolite, ion, and water interactions. Furthermore, the excellent correlation of IINS and MD results indicates that the interpretation of these results is reasonable and valid. However, cation charge density and framework charge are undoubtedly not the only variables which affect librational motions of nanoconfined water.
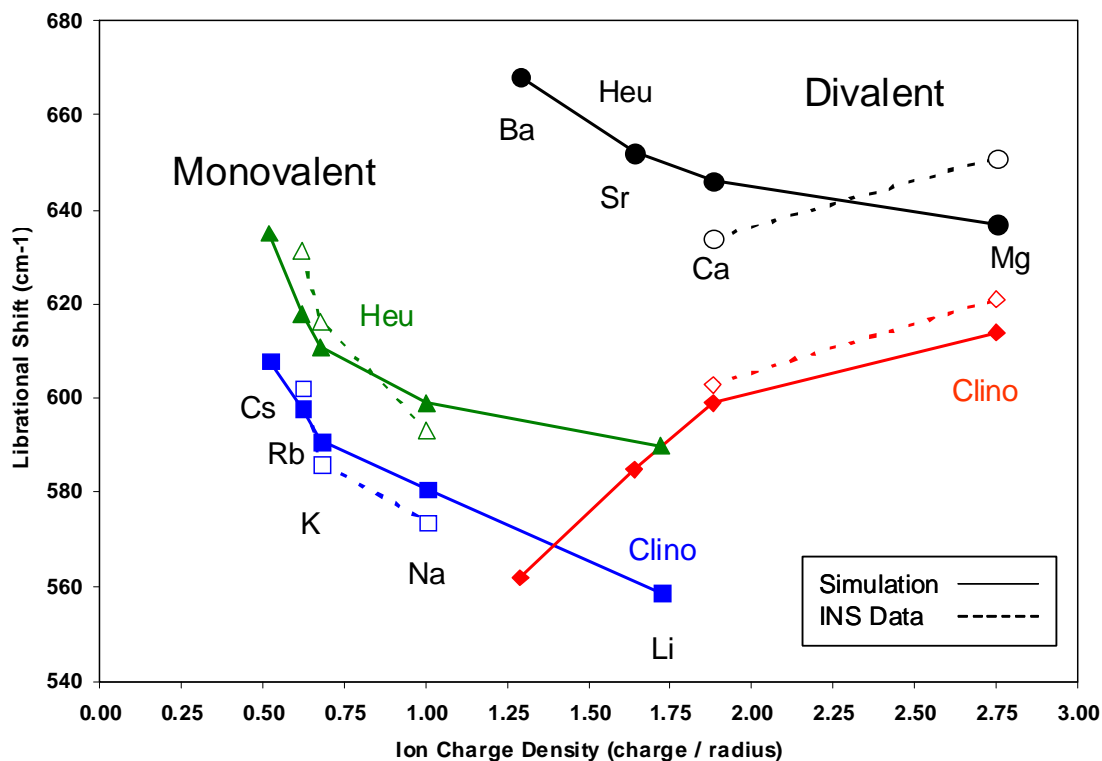
Figure 3. Librational shifts (cm^{-1}) of the alkali (subscript mono) and alkaline earth (subscript di) series versus ion charge density. Theoretical values of clinoptilolite (CLI) and heulandite (HEU) librational shifts are represented by solid lines while the shifts observed by IINS are represented dotted lines.

The general interpretation of the correlated IINS and power spectra suggests that both the cation charge density and the anionic field strength (i.e. Si/Al ratio) have significant impacts on the rotational motion of nanoconfined water. Furthermore, the balance between cation charge density and framework anionic field strength has a marked impact on the librational signatures of a given paired zeolite-ion system. The experimental data clearly illustrate that with the alteration of ion-water-zeolite equilibria conditions (which modify the librational signatures of nanoconfined water) a different localized environment results due to the cations within a negatively-charged zeolitic pore. The results also indicate that electrostatic charge on the overall framework has a stronger influence than charge density of a given ion in the channel and that these effects become more pronounced as the charge difference between ion and zeolite is increased. It is interesting to note that a shift to lower frequencies (in the power spectra) in the alkaline series follows an inverse trend of increasing enthalpies of hydration for the given cation (ΔH_{hyd}: $Cs^{1+} < Rb^{1+} < K^{1+} < Na^{1+} < Li^{1+}$; Libration shift: $Cs^{1+} > Rb^{1+} > K^{1+} > Na^{1+} > Li^{1+}$). This observation is reversed in the alkaline earth series, with decreasing frequencies as a function of hydration enthalpy (ΔH_{hyd}: $Ba^{2+} < Sr^{2+} < Ca^{2+} < Mg^{2+}$; Libration shift: $Ba^{2+} < Sr^{2+} < Ca^{2+} < Mg^{2+}$).

Similarities and difference in trends exist when comparing the zeolite experimental IINS data and MD derived power spectra. Comparison between the CLI series (Figures 2A, 2B, and 3) reveals a reversal in the libration shift trends between the monovalent and divalent series. In the observed IINS spectra, the CLI$_{mono}$ series exhibits a decreasing trend with monovalent cations,

while showing an increasing trend in librational edge frequency as a function of increasing ion charge densities. This behavior is also observed in the comparison of the IINS data for the HEU_{mono} and HEU_{di} series (Figures 2C, 2D, and 3). In our prior report,[12] the HEU system did have the smallest magnitude frequency shift of all the zeolite-ion combinations studied. This suggests that this system is near an inversion of the equilibrium between the ion-water and zeolite-water interactions where the energy of interaction changes from being dominated by the ion to being dominated by the zeolite).

Comparison of IINS spectra of CLI_{di} and HEU_{di} reveals a good agreement in trends between the two zeolite systems with frequency increasing as a function of increasing charge density ($Ca^{2+} < Mg^{2+}$). The data suggest that this behavior arises from a shift in ion-water-zeolite equilibria towards the stronger ion-water interactions over the diminished ion-zeolite or zeolite-water interactions. An additional contributing factor may be the more effective role of water-water and water-zeolite interactions in channels, especially in the divalent series where there are fewer counterbalancing extra-framework cations than the more densely populated monovalent series.[40]

In some systems all three libration modes may not be observed, for example if a particular mode is completely unhindered. Unfortunately, our MD simulations were not able to fully addressed this issue since there were multiple different, but closely related (energetically and structurally), 'bulk-like' water configurations and as such precluded any direct assignment of discrete wagging, twisting, of rocking modes in the librational spectra. Density functional theory (DFT) studies and normal mode analysis of small water clusters revealed that discrete librational modes are not distinguishable unless there are very few waters or the system is nearly static. None of the HEU or CLI systems we examined fit either of those criteria and thus discrete assignments cannot be made with any degree of certainty. However, we suspect that all three librational modes are present and close in frequency in these systems and none are strongly suppressed due to interactions with the framework.

Conclusions

We have examined a subset of the alkali and alkaline earth series of cation analogs of clinoptilolite (Si/Al≈5) and heulandite (Si/Al≈3.5) frameworks using incoherent inelastic neutron scattering. Coupled with our prior MD studies, we have demonstrated that ion charge density and the electrostatic field of the zeolite (Si/Al ratios) have a strong impact on the dynamical intermolecular behavior of nanoconfined water. This impact is manifested and observable in librational region on the IINS spectra by shifting the data to higher frequencies. Furthermore, charge density of framework (i.e. Si/Al ratios) has the greatest influence on librational motions, while the identity and charge of the extra-framework cations is of less significance. Correlation of these data confirm the importance of ion-zeolite, ion-water and, water-zeolite equilibria on the rotational motions of water. The librational peaks in the IINS spectra for heulandite (the more negatively charged framework) are shifted to higher frequencies for the HEU_{mono} from the CLI_{mono}. The trend in the IINS spectra indicate that the increased electrostatic field associated with the zeolite channel produces more heavily restricted water molecules rotations (e.g. recognized by a shift to higher frequencies). This behavior becomes more pronounced as cation charge density increases. The HEU_{di} series exhibits the same general trend in the observed data, although this behavior occurs at a higher frequency. This behavior suggests that the higher

cation field strength is further restricting rotational motion of confined water. The notable reversal between experimental and simulated spectra for the HEU$_{di}$ series is possibly due to a shift in equilibrium from being dominated by water-water to water-framework although we do not fully understand this phenomenon yet.

The combined effect of these two variables provides a basic foundation to understand the influence of exchangeable cation charge density and anionic field strength of the framework, and the effects that these opposing electrostatic fields have on the librational behavior. While the electrostatic field of the framework has the greatest effect it is the overall differential between cation charge density and anion framework charge which is the core phenomena which alters the librational dynamics of nanoconfined water. Furthermore, the balance between these fields is the foundational reason for ion exchange capacities and potential ion exchange rates. Future investigations could potentially include a combination of the thermodynamics of ion-exchange and hydration processes, plus the structural analysis of hydrogen-bonded networks within these zeolite systems.

References

1. Head-Gordon, T.; Hura, G. Chem. Rev. 2002, 102, 2651 and reference therein.

2. Kalinichev, A.G. In Reviews in Mineralology and Geochemistry, Cygan, R. T., Kubicki J. D.; Ed., 2001, Vol. 42 and reference therein.

3. Jedlovsky, P.; Brodholt, J.P.; Bruni, F.; Ricci, M.A.; Soper, A.K.; Vallauri, R. J. Chem. Phys. 1998, 108, 8528.

4. Soper, K. Chem. Phys. 2000, 258, 121.

5. Ricci, M.A.; Soper, A.K. Physica A. 2002, 304, 43.

6. Soper, A.K.; Ricci, M.A. Phys. Rev. Lett. 2000, 84, 2881.

7. (a) Guillot, B. J. Mol. Liq. 2002, 101, 217. (b) Guillot, B. J. Mol. Liq. 2002, 101, 219.

8. Head- Gordon, T.; Johnson, M.E. P. Natl. Acad. Sci USA, 2006, 103, 7973.

9. Wang, K.; Kalinichev, A.G.; Kirkpatrick R.J.; Geochim. Cosmochim. Ac. 2004, 16, 3351.

10. Ricci, M.A.; Bruni, F.; Gallo, P.; Rovere, M. ; Soper, A.K. *J. Phys. Condens. Matter.* **2000,** *12*, 345.

11. Ricci, M.A.; Rovere, M. *J. Phys. IV*. **2000**, *10*, 187.

12. Ockwig, N.W.; Cygan, R.T.; Nenoff, T.M.; Daemen, L.L.; Hartl, M.A.; Criscenti, L.J. *Phys. Chem. Chem. Phys.*, **2008**, *10*, 800.

13. Klafter, J.; Blumen, A.; Drake, J.M. In *Relaxation and Diffusion in Restricted Geometry*; Klafter, J.; Drake, J.M., Eds.; New York: Wiley, 1989.

14. Rupley, J.A.; Careri, G.; *Adv. Protein Chem.* **1991**, *41*, 37.

15. Arndt, M.; Stannarius, R.; Gorbatschow, W.; Kremer, F. *Phys. Rev. E: Stat., Nonlinear, Soft Matter* **1996**, *54*, 5377.

16. *Proceedings of the First International Workshop of Dynamics in Confinement*; Frick, B.; Zorn, R.; Buttner, H., Eds.; EDP Science: Les Ulis, France, 2000.

17. Rovere, M. In J. Phys. Condens. Matter.- Special Section of Water in Confined Geometries **2004**, 16, S5297-S5470. (a) Crupi, V.; Majolino, D.; Venuti, V. J. Phys. Condens. Matter. **2004**, 16, S5297. (b) Swenson, J. J. Phys. Condens. Matter. **2004**, 16, S5317. (c) Puibasset, J.; Pellenq R.J.M. J. Phys. Condens. Matter. **2004**, 16, S5329. (d) Brovchenko, I.; Geiger, A.; Oleinikova, A. J. Phys. Condens. Matter. **2004**, 16, S5345. (e) Zangi, R. J. Phys. Condens. Matter. **2004**, 16, S5371. (f) Jedlovsky, P. J. Phys. Condens. Matter. **2004**, 16, S5389. (g) Liu, L.; Faraone, A.; Mou, C.Y.; Yen, C.W. Chen, S.H. J. Phys. Condens. Matter. **2004**, 16, S5403. (h) Klein, J.; Raviv, U.; Perkin, S.; Kampf, N.; Chai, L.; Giasson, S. J. Phys. Condens. Matter. **2004**, 16, S5437. (i) Webber, B.; Dore, J. J. Phys. Condens. Matter. **2004**, 16, S5449.

18. Angell, C. A. In *Water: A Comprehensive Treatise*; Franks, F. Ed.; Plenum Press; New York, 1981.

19. Mizota, T.; Satake, N.; Fujiwara, K.; Nakayama, N. *Steam, Water, and Hydrothermal Systems: Physics, and Chemistry Meetings the Needs of Indutry, Proceedings of the 13th ICPWS*; Tremaine, P.R.; Hill, P.G.; Irish, D.E.; Balakrishnan, P.V.; Eds.; NCR Research Press: Ottawa, Ontario, 2000.

20. Beta, I.A.; Bohling, H.; Hunger, B. *Phys. Chem. Chem. Phys.*, **2004**, *6*, 1975.

21. Jobic, H.; Tuel, A.; Krossner, M.; Sauer, J. *J. Phys. Chem.* **1996**, *100*, 19545.

22. Crupi, V.; Majolino, D.; Migliardo, P.; Venuti, V.; Wanderlingh, U.; Mizota, T.; Telling, M. *J. Phys. Chem. B.* **2004**, *108*, 4314.

23. Line, C.M.B.; Kearley, G.J. *J. Chem. Phys.* **2000**, *112*, 9058.

24. Line, C.M.B.; Kearley, G.J. *Chem. Phys.* **1998**, *234*, 207.

25. Celestian, A.J.; Parise, J.B.; Smith, R.I.; Toby, B.H.; Clearfield, A. *Inorg. Chem.* **2007**, *46*, 1081.

26. Celestian, A.J., Kubicki, J.D., Hanson, J., Clearfield, A., Parise, J.B. *J. Amer. Chem. Soc.* **2008**, (Currently Under Review).

27. Higgins, F.M.; de Leeuw, N.H.; Parker, S.C. *J. Mat. Chem.* **2002**, *12*, 124.

28. Soper, A.K. in *Hydrogen Bond Network, NATO ASI Series C: Mathematical and Physical Science*; Bellissent-Funel, M.C.; Dore, J.C., Eds.; Kluwer Academic, Dordecht, 1994.

29. Wiggins, P.M. *Prog. Poly. Sci.* **1988**, *13*, 1.

30. Crupi, V.; Majolino, D.; Migliardo, P.; Venuti, V.; Wanderlingh, U.; Mizota, T.; Telling, M. *J. Phys. Chem. B.* **2002**, *106*, 10884.

31. Bellissent-Funel, M.C.; Dorbez-Sridi, R.; Bosio, L. *J. Chem. Phys.* **1996**, *104*, 1.

32. Crupi, V.; Magazu, S.; Maisano, G.; Majolino, D.; Migliardo, P. *J. Mol. Liq.* **1999**, *80*, 133.

33. Kaatze, U.; Uhlendorf, V.; *Z. Phys. Chem. (N. F.)* **1981**, *126*, 151.

34. Polnazek, C.F.; Bryant, R.G.; *J. Chem. Phys.* **1984**, *81*, 4038.

35. Gallo, P.; Ricci, M.A.; Rovere, M.; *J. Chem. Phys.* **2002**, *116*, 342.

36. Gallo, P.; Rapinesi, M.; Rovere, M.; *J. Chem. Phys.* **2002**, *117*, 369.

37. Murad, S.; Jia, W.; Krishnamurthy, M. *Mol. Phys.* **2004**, *102*, 2103.

38. Demontis, P.; Stara, G.; Suffritti, G.B. *J. Chem. Phys.* **2004**, *120*, 9233.

39. Shirono, K.; Endo, A.; Daiguji, H. *J. Phys. Chem. B* **2005**, *109*, 3446.

40. Nenoff, T.M.; Ockwig, N.W.; Cygan, R.T.; Alam, T.M.; Leung, K.; Pless, J.D.; Xu, H.; Hartl, M.A.; Daemen, L.L. *J. Phys. Chem. C.* **2007**, *111*, 13212.

41. Fourzi, A.; Dorbez-Sridi, R.; Oumezzine, M. *J. Chem. Phys.* **2002**, *116*, 791.

42. Crupi, V.; Majolino, D.; Migliardo, P.; Venuti, V.; Bellissent-Funel, M.C. *Mol. Phys.* **2003**, *101*, 3323.

43. Kolesnikov, A.I.; Li, J.C. *Physica B* **1997**, *234*, 34 and references therein.

44. Bellissent-Funel, M. C.; Lal, J.; Bosio, L. *J. Chem. Phys.* **1993**, *98*, 4246.

45. Crupi, V.; Majolino, D.; Migliardo, P.; Venuti, V.; Diaonoux, A. J. *Appl. Phys., A Mater. Sci. Process. 2002*, *74*, S555.

46. Venturini, F.; Gallo, P.; Ricci, M. A.; Bizzari, A. R.; Cannistraro, S. *J. Chem. Phys.* **2001**, *114*, 10010.

47. (a) Anandan, S.; Okazaki, M. *Microporous Mesoporous Mater.*, **2005**, *87*, 77. (b) Brühwiler, D.; Calzaferri, G. *Microporous Mesoporous Mater.*, **2004**, *72*, 1. (c) Ma, Y.; Tong, W.; Zhou, H.; Suib, S.L. *Microporous Mesoporous Mater.*, **2000**, *37*, 243.

48. (a) Carey, J.W.; Bish, D.L. *Amer. Min.*, **1996**, *81*, 952. (b) Wilkin, R.T.; Barnes, H.L. *Phys. Chem. Minerals*, 1999, **26**, 468. (c) Yang, P.; Stolz, J.; Armbruster, T.; Gunter, M.E. *Amer. Min.* **1997**, *82*, 517. (d) Doebelin, N.; Armbruster, T. *Microporous Mesoporous Mater.*, **2003**, *61*, 85. (e) Ruiz-Salvador, A. R.; Gómez, A.; Lewis, D.W.; Catlow, C.R.A.; Rodriguez-Albelo, L.M.; Montero, L.; Rodriguez-Fuentes, G. *Phys. Chem. Chem. Phys.*, **2000**, *2*, 1803. (f) Ruiz-Salvador, A.R.; Lewis, D.W.; Rubayo-Soneira, J.; Rodriguez-Fuentes, G.; Sierra, L.R.; Catlow, C.R.A. *J. Phys. Chem. B* **1998**, *102*, 8417. (g) Ruiz-Salvador, A.R.; Gómez, A.; Lewis, D.W.; Rodriguez-Fuentes, G.; Montero, L. *Phys. Chem. Chem. Phys.*, **1999**, *1*, 1679.

49. Clinoptilolite: $a = 17.66\,(7)$, $b = 17.92\,(5)$, $c = 7.40\,(1)$ Å, and $\beta = 116.43\,(14)$ °. Heulandite: $a = 17.62\,(24)$, $b = 17.92\,(21)$, $c = 7.46\,(13)$ Å, and $\beta = 116.34\,(53)$°.

50. Zhao, D.; Szostak, R.; Kevan, K. *J. Mat. Chem.*, **1998**, *8*, 233.

51. Elemental analysis performed by Galbraith Laboratories, Inc., Knoxsville, TN.

52. Clinoptilolite series elemental analysis results. Na-CLI (Calc, %): Na, 5.10; Al, 5.99; Si, 31.17; H, 1.69. K-CLI (Calc, %): K, 8.25; Al, 5.70; Si, 30.24; H, 1.63. Rb-CLI (Calc, %): Rb, 15.78; Al, 4.98; Si, 28.01; H, 1.50, Mg-CLI (Calc, %): Mg, 2.86; Al, 6.34; Si, 31.69; H, 1.73. Ca-CLI (Calc, %) Ca, 4.70; Al, 6.33; Si, 30.89; H, 1.70. Na-CLI (Obs., %): Na, 5.19; Al, 5.91; Si, 31.22; H, 1.81. K-CLI (Obs., %): K, 8.32; Al, 5.76; Si, 30.92; H, 1.78. Rb-CLI (Obs., %): Rb, 15.39; Al, 5.37; Si, 28.33; H, 1.71. Mg-CLI (Obs., %): Mg, 2.55; Al, 6.17; Si, 32.16; H, 2.01. Ca-CLI (Obs., %): Ca, 4.71; Al, 6.62; Si, 31.36; H, 1.29.

53. Heulandite series elemental analysis results. Na-HEU (Calc, %): Na, 6.43; Al, 7.54; Si, 29.06; H, 1.67. K-HEU (Calc, %): K, 10.87; Al, 7.51; Si, 27.35; H, 1.59. Rb-HEU (Calc, %): Rb, 21.44; Al, 6.77; Si, 23.95; H, 1.40, Mg-HEU (Calc, %): Mg, 4.00; Al, 8.88; Si, 28.65; H, 1.71. Ca-HEU (Calc, %) Ca, 6.14; Al, 8.27; Si, 28.42; H, 1.67. Na-HEU (Obs., %): Na, 6.57 ; Al, 7.81; Si, 30.12; H, 2.00 ; Ca, 0.03; Fe, 0.01. K-HEU (Obs., %): K, 10.61; Al, 7.54; Si, 28.15; H, 1.98; Ca, 0.05; Fe 0.02,. Rb-HEU (Obs., %): Rb, 20.37; Al, 6.18; Si, 23.44; H, 2.13; Ca, 0.11; Fe, 0.07. Mg-HEU (Obs., %): Mg, 4.92; Al, 9.00; Si, 27.99; H, 1.83; Ca, 0.03; Fe, 0.03. Ca-HEU (Obs., %): Ca, 6.38; Al, 8.64; Si, 28.87; H, 1.99; Fe, 0.05.

54. (a) Debye, P. *Ann. d. Phys.* **1913**, *348*, 49. (b) Waller, I. *Z. Phys.* **1923**, *17*, 398.

55. PeakFit v4.12 software suite with an error of ± 5 cm^{-1}.

56. Li, J.C. *J. Chem. Phys.* **1996**, *105*, 6733.

57. (a) Yildrim, T. *Chem. Phys.* **2000**, *261*, 205. (b) Payne, M.C.; Teter, M.P.; Arias, D.C.; Joannopoulos, J.D. *Rev. mod. Phys.* **1992**, *64*, 1045. (c) Lovesey, S. In *Theory of Neutron Scattering in Condensed Matter*; 3rd Ed.; Oxford University Press; New York, 1987.

58. Li, J.C.; Ross, D.K. *Nature* **1993**, *365*, 327.

Appendix

Sum Frequency Generation Spectra of Nylon Thin Films

The ordering of water on model nylon films was monitored as a function of salt content using a combination of sum-frequency generation (SFG) infrared spectroscopy, low angle neutron scattering measurements, and measurements of the viscoelastic properties of the interfacial water using the interfacial force microscope. All three techniques indicate that in deionized water, nylon perturbs the "liquid-like" structure of bulk water, creating a zone of interfacial water that is around 4-nm thick, exhibits "ice-like" structural features, and is much more viscous than bulk water. When salts such as NaCl, LiCl, and $MgCl_2$ are added, the results indicate that there is a competition between the Nylon surface and dissolved ions for ordering the water, and that salts eventually disrupt the ordered structures that are present at the surface.

The influence of both Nylon and dissolved salts on the molecular structure of the interfacial water is most clearly seen in the vibration spectra obtained at the immediate Nylon-water interface using SFG methods (Figure 1). Within the frequency window associated with the O-H stretches of water, two peaks are predominant: a peak near 3200 cm^{-1} which is attributed to "ice-like" water, and a peak near 3500 cm^{-1} which is attributed to "liquid-like" water. On bare quartz, the "liquid-like" peak dominates. However, on the model Nylon surface, the "ice-like" peak is predominant, indicating that the Nylon surface structures the interfacial water differently than as with quartz. As salts such as NaCl are added to the deionized water, the peaks associated with the interfacial water decrease in intensity, at eventually disappear (at 1 M NaCl and higher concentrations). However, the relative amounts of "ice-like" and "liquid-like" water do not appear to change with salt content above either the bare quartz or Nylon terminated surfaces. Divalent salts such as $MgCl_2$ cause significant decreases in the SFG signal at significantly lower concentrations than for monovalent salts such as NaCl. Our interpretation for the observed results is that as the salt content increases, and the electrical double layer collapses into the surface, hydrated ions (which do not generate a SFG signal) increasingly occupy space at the immediate surface. The hydrated ions displace ordered water, but do not change the ordering above the Nylon in areas that are not occupied by adsorbed ions. The drop in the SFG signal with water content is mirrored by a disappearance of the 3-4 nm thick layer of low density "ice-like" water seen in neutron scattering, as well as the disappearance of the high viscosity layer of interfacial water detected via the IFM. These results indicate that the ability of the Nylon surface to sort ions from water may be highly dependent on salt content, and that at the highest salt contents, the ordering of water may be compromised.
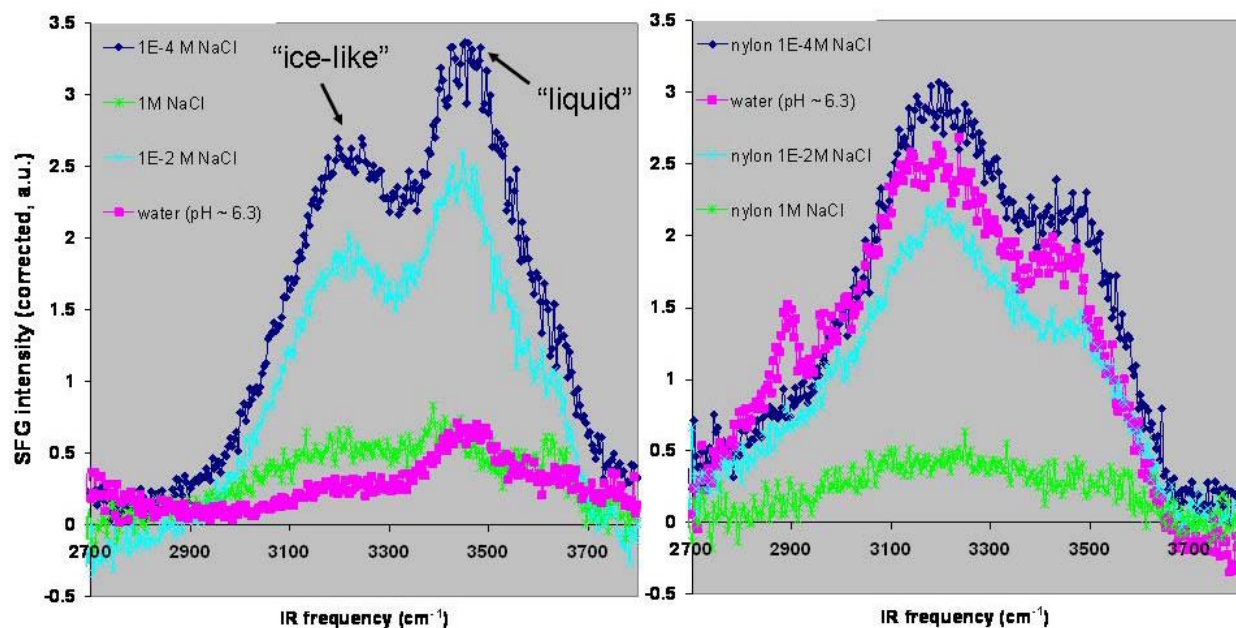
Figure 1. SFG spectra of (left) water and NaCl solutions on quartz at pH 6.3 and (right) water on self-assembled monolayer of Nylon at pH 6.3.

## Molecular Dynamics Simulations of Nylon-Water Interactions

We studied the water interaction with nylon self-assembled monolayers (SAMs) by performing atomistic molecular dynamics simulations. The original idea was to determine if two dimensional water layers can form in the SAM at the horizontal layers of hydrophilic amide groups within the nylon monomers. The systems consisted of two-monomer nylon with silane end group that bonds to a silicon oxide substrate. The simulations used the OPLS force-field and the TIP3P model for water. Two different setups were used for the initial placement of water. To study the water diffusion into the nylon SAM a slab of water was placed above the SAM. To study the diffusion of water within the SAM, water at low concentrations was placed randomly within the SAM. In both cases, molecular dynamics simulations followed the water.

For water diffusing into to the SAM from above, the simulations show that water molecules can penetrate the SAM. The spacing of the SAM molecules is about 5Å and the simulations show that there is sufficient space for water molecules to diffuse between the nylon molecules into the SAM. Some of the water molecules individually diffuse into the SAM and remain isolated. Other molecules diffuse in as a group that is hydrogen bonded together (Figure 2). The water molecules do not form a two-dimensional structure at the amide group positions. In fact the waters do not aggregate at the amides. Instead the hydrogen bonded groups of water span from one amide region to another. As always the interpretation of the results must have in mind that the simulations only treat time scales of order 10 ns. The equilibration of the system on much longer time scales, which is the experimental time scale, can result in a different organization of the water molecules.

258
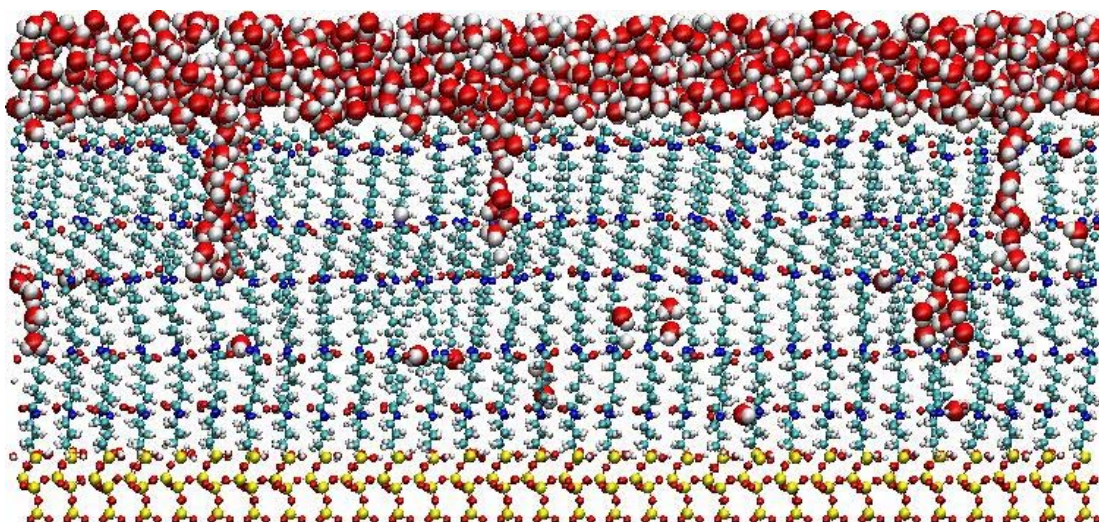
Figure 2. Image of water penetrating nylon SAM. Colors: O (red), H (white), N (blue), C (cyan).

Another way to examine the water diffusion and to get an idea of how far the water molecules can move within the SAM is to start the waters within the SAM. Figure 3 shows a snapshot after 12 ns of a molecular dynamics simulation of 100 waters in a SAM with 100 nylon chains. Some of the waters have diffused to the top of the SAM and form a water cluster that extends away from the SAM. Some of the waters have aggregated within the SAM to form small clusters. Again there appears to be a preference for forming clusters of water instead of hydrogen bonding within an amide layer. However, we must caution that the time scales for forming any structure is unknown and may be well beyond what can be simulated here. The present simulation shows that the water will diffuse within the SAM and that for a two monomer nylon SAM the water can diffuse to the top of the SAM within 12 ns.
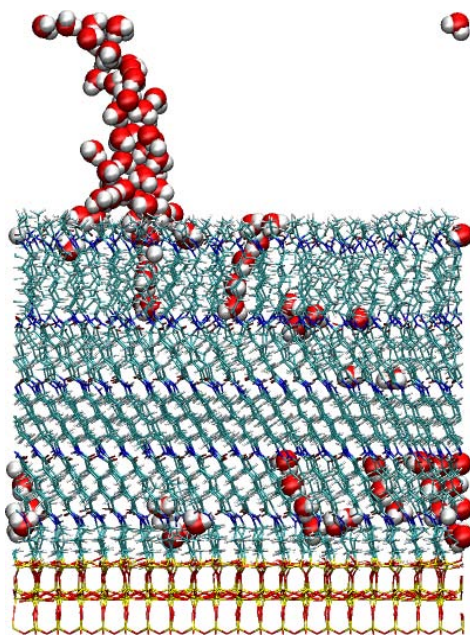

Figure 3. Image of system after water initially placed within SAM has diffused. Colors as in Figure 2.

Tracking the Evolution of Thin Ice Films on Pt with Molecular-Layer Resolution

Despite its importance little is known about water-solid interactions. In fact, to this day, the best theoretical models often fail to reproduce the most basic phenomena. Understanding the water-solid interaction would imply, for example, that one can correctly predict wetting behavior, which is not the case for many systems. Whether water wets a given substrate is determined by the balance between the energies of the exposed surfaces and the energy of the water-solid interface. Thus, experimentally tracking wetting/dewetting phenomena is a direct way to quantify the water-solid interaction.

To obtain the most detailed information one would like to monitor wetting/dewetting in real-space at a molecular level. A promising approach to do this in a well-defined way is to study ice films prepared in ultra-high vacuum. We chose a Pt(111) substrate as a relatively simple model case. Pt(111) does not dissociate water, but does bind it strongly enough to form a 2-d wetting layer accessible to Scanning tunneling microscopy (STM). That clean and atomically flat Pt(111) surfaces can be prepared offers the prospect of well-defined, reproducible experiments. The equilibrium structure of ice/Pt(111) comprises isolated 3D ice crystals on a Pt(111) surface covered by a bilayer of water molecules. That is, ice dewets Pt. The processes by which the dewetting occurs are not known. For instance, it is not clear whether the driving force for dewetting is large enough to nucleate the new layers required for ice crystals to grow taller.

Microscopic techniques that had proved powerful to address such basic questions for metals, e.g., TEM, SEM or LEEM, all failed in studying ice, because they use electrons, which immediately destroy the ice. STM has not been successful either in studying multilayer ice because it requires an electric current to flow between STM tip and sample. But ice, as an insulator, cannot, under normal conditions, supply the electrons needed for imaging. Recently we discovered conditions where the needed electrons are extracted from the valence band of ice, making nondestructive imaging possible.[1] Figure 4, depicting an ice film grown on Pt at 140 K, illustrates the success of this novel approach. At 1nm mean film thickness (left) individual nanometer-sized ice crystals are embedded in a molecularly thin wetting layer (black). Upon depositing more water these crystals coalesce into a continuous film at around 4 nm average thickness (right).
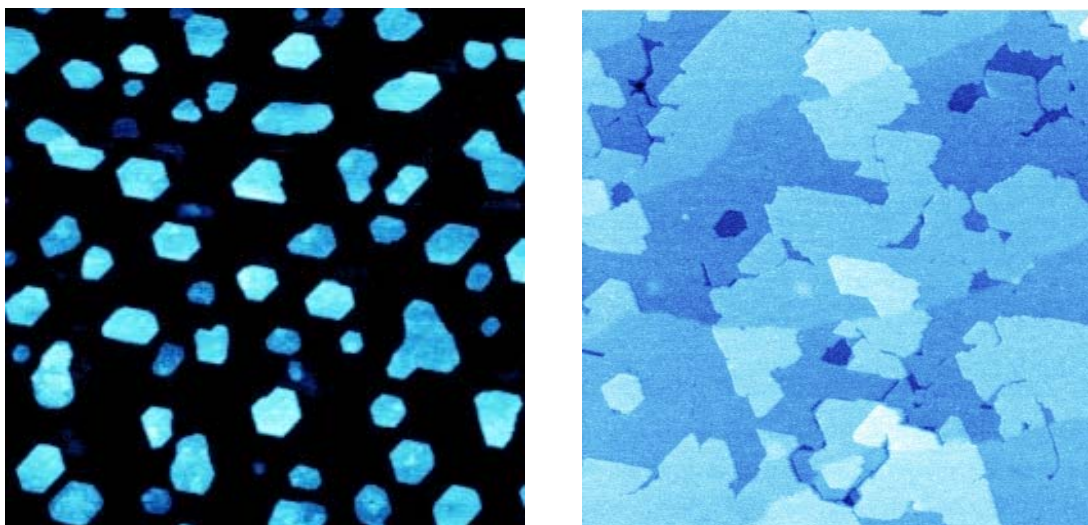
Figure 4. 500nm × 500nm STM images of water (ice) films grown at 140 K onto a Pt(111) substrate. At 1 nm mean film thickness (left image) the film consists of individual ~3nm high crystals, which are embedded in a one molecular layer thick wetting layer. At 4 nm thickness the multi-layer ice covers completely the substrate. The sharp edges are molecular-height (~0.37 nm) surface steps. The slightly blurred edges are buried (0.23nm high) Pt substrate steps.

To probe the stability of ice/Pt(111) we monitored with STM how the morphology changes when a 1 nm thick film (equivalent to the film in left side of Figure 4) is annealed for 1 hour at 140 K. The image sequence in Figure 5 reveals that the ice crystals grow thicker to expose more of the wetting-layer covered Pt surface. This means that the driving force for dewetting is strong enough to cause nucleation of new layers, in contrast to metal/metal systems where such nucleation does not occur. The results show that the rate at which new layers nucleate, and not surface diffusion, determines how fast individual crystallite shapes equilibrate. Applying nucleation theory to measured growth rates versus crystallite dimensions, we obtain new bounds on the energetics both of step formation on ice and of the Pt-ice interface.[2] Although understanding dewetting-induced nucleation is crucial for predicting the stability of thin films, it had not been characterized before in any system. This new insight into ice-film energetics provides a benchmark against which first principles calculations could be tested and improved.
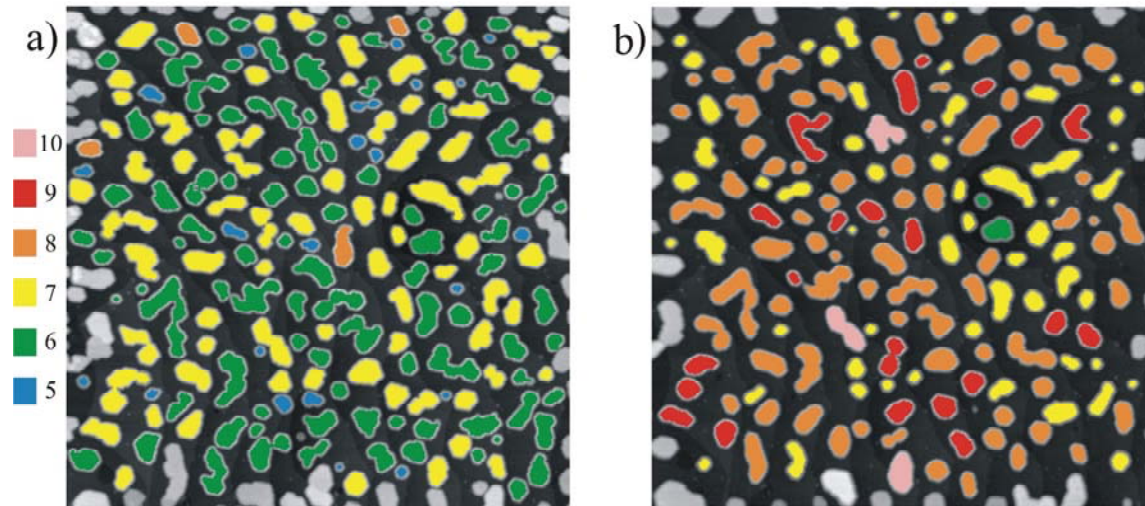
Figure 5. Nucleation limited dewetting: (a) 1μm² image of an ice film grown at 140 K with the height of each three-dimensional crystallite colored differently; (b) Image of the same surface region after annealing at 140 K for one hour.

1. Thürmer, K. and Bartelt, N.C. (2008) Growth of multilayer ice films and the formation of cubic ice imaged with STM. Physical Review B **77**, 195425.

2. Thürmer, K. and Bartelt, N.C. Nucleation-limited dewetting of ice films on Pt(111). Physical Review Letters **100**, 186101 (2008).

Distribution

1   Joshua A. Anderson
Department of Physics and Astronomy
Iowa State University
Ames, IA 50011

1   Curt Brown
Research and Development Office
U.S. Bureau of Reclamation
Denver Federal Center
PO Box 25007 (86-69000)
Denver, CO 80225-0007

1   Joseph L. Cecchi
Department of Chemical and Nuclear Engineering
MSC01 1140
1 University of New Mexico
Albuquerque, NM 87131-0001

1   Zhu Chen
Center for Micro-Engineered Materials
Department of Chemical and Nuclear Engineering
MSC01 1120
1 University of New Mexico
Albuquerque, NM 87131-0001

1   Jacalyn S. Clawson
GlaxoSmithKline
5 Moore Dr.
Durham, NC 27709

1   Luke L. Daemen
Manuel Lujan, Jr. Neutron Scattering Center
LANSCE-LC, MS-H805
Los Alamos National Laboratory
Los Alamos, NM 87545

1   Darren R. Dunphy
Department of Chemical and Nuclear Engineering
MSC01 1120
1 University of New Mexico
Albuquerque, NM 87131-0001

1 Benjamin L. Frankamp
  Bend Research
  64550 Research Road
  Bend, OR 97701-8599

1 Henry Gerung
  Center for Micro-Engineered Materials
  Department of Chemical and Nuclear Engineering
  MSC01 1120
  1 University of New Mexico
  Albuquerque, NM 87131-0001

1 Monica A. Hartl
  Manuel Lujan, Jr. Neutron Scattering Center
  LANSCE-LC, MS-H805
  Los Alamos National Laboratory
  Los Alamos, NM 87545

1 Gregory P. Holland
  Magnetic Resonance Research Center
  Department of Chemistry and Biochemistry
  Arizona State University
  Tempe, AZ 85287

1 David J. Kissel
  Center for Micro-Engineered Materials
  Department of Chemical and Nuclear Engineering
  MSC01 1120
  1 University of New Mexico
  Albuquerque, NM 87131-0001

1 Nanguo Liu
  Dow Corning Corporation
  3901 S. Saginaw Rd.
  Midland, MI 48640

1 Christian D. Lorenz
  Kings College London
  Materials Research Group
  Department of Mechanical Engineering
  London WC2R 2LS, England
  United Kingdom

1 Ryan C. Major
  Hysitron, Inc.
  10025 Valley View Road
  Minneapolis, MN 55344

1 Matthew J. McGrath
 Department of Chemistry
 Smith Hall
 University of Minnesota
 207 Pleasant St. SE
 Minneapolis, MN 55455-0431

1 Jason D. Pless
 Catalytic Solutions, Inc.
 1640 Fiske Pl.
 Oxnard, CA 93033

1 Kevin Price
 Water Treatment Engineering Research
 U.S. Bureau of Reclamation
 Denver Federal Center
 PO Box 25007 (86-68230)
 Denver, CO 80225-0007

1 Mark A. Shannon
 WaterCAMPWS
 Department of Mechanical Science and Engineering
 University of Illinois
 1206 West Greene St.
 Urbana, IL 61801

1 J. Ilja Siepmann
 Department of Chemistry
 B-8, 139 Smith Hall
 University of Minnesota
 207 Pleasant St. SE
 Minneapolis, MN 55455-0431

1 Alex Travesset
 Department of Physics and Astronomy
 503 Physics Hall
 Iowa State University
 Ames IA 50011

1 Nicholas B. Woodward
 Geoscience Research Program
 Office of Basic Energy Sciences
 U.S. Department of Energy
 19901 Germantown Rd.
 Germantown, MD 20874-1290

1   George K. Xomeritakis
UOP LLC
25 East Algonquin Road
P.O. Box 5017
Des Plaines, IL 60017-5017

1   Hongwu Xu
Manuel Lujan, Jr. Neutron Scattering Center
LANSCE-LC, MS-H805
Los Alamos National Laboratory
Los Alamos, NM 87545

1   Xiaoyang Zhu
Department of Chemistry
239 Smith Hall
University of Minnesota
207 Pleasant St. SE
Minneapolis, MN 55455-0431

1	MS 0125	J. P. VanDevender, 12101
1	MS 0351	R. H. Stulen, 1000
1	MS 0351	W. R. Cieslak, 1010
1	MS 0614	C. J. Orendorff, 2546
1	MS 0724	L. E. Shephard, 6000
1	MS 0734	B. J. Kelley, 6327
1	MS 0735	J. A. Merson, 6310
1	MS 0735	R. E. Finley, 6313
1	MS 0754	P. V. Brady, 6310
1	MS 0754	S. J. Altman, 6316
1	MS 0754	L. J. Criscenti, 6316
7	MS 0754	R. T. Cygan, 6316
1	MS 0754	J. A. Greathouse, 6316
1	MS 0754	T. M. Mayer, 6316
1	MS 0754	M. D. Nyman, 6316
1	MS 0754	N. W. Ockwig, 6316
1	MS 0754	M. J. Rigali, 6316
1	MS 0886	T. M. Alam, 1816
1	MS 0887	D. M. Dimos, 1800
1	MS 0895	S. B. Rempe, 8331
1	MS 1078	W. Hermina, 1710
1	MS 1104	M. L. Tatro, 6200
1	MS 1304	D. L. Huber, 1132
1	MS 1315	M. J. Stevens, 8331
1	MS 1315	N. D. Shinn, 1131
1	MS 1322	J. B. Aidun, 1435
1	MS 1322	P. S. Crozier, 1435
1	MS 1349	C. J. Brinker, 1002

1	MS 1349	Y.-B. Jiang, 18151
1	MS 1411	A. R. Roach, 1814
1	MS 1411	F. B. van Swol, 1814
1	MS 1411	B. C. Bunker, 1816
1	MS 1413	S. Varma, 8331
1	MS 1415	C. Gutierrez, 1114
1	MS 1415	J. E. Houston, 1114
1	MS 1415	K. Leung, 1114
1	MS 1415	T. M. Nenoff, 1114
1	MS 1415	P. J. Feibelman, 1130
1	MS 1427	J. M. Phillips, 1100
1	MS 1455	M. Farrow, 2555
1	MS 9291	S. Singh, 8755
1	MS 9161	K. Thuermer, 8756
1	MS 0123	D. Chavez, LDRD Office, 1011
1	MS 0899	Technical Library, 9536 (electronic copy)